IntechOpen

Multi-purposeful Application of Geospatial Data

Edited by Rustam B. Rustamov, Sabina Hasanova and Mahfuza H. Zeynalova

MULTI-PURPOSEFUL APPLICATION OF GEOSPATIAL DATA

Edited by **Rustam B. Rustamov, Sabina Hasanova** and **Mahfuza H. Zeynalova**

Multi-purposeful Application of Geospatial Data
http://dx.doi.org/10.5772/intechopen.69713
Edited by Rustam B. Rustamov, Sabina Hasanova and Mahfuza H. Zeynalova

Contributors

Junghyun Lee, Antônio Teixeira, Janice Leivas, Carlos Ronquim, Gustavo Bayma, Jonathan Becedas, María Del Mar Núñez, David González, Zina Mitraka, Lingli Zhu, Suomalainen Juha, Jingbin Liu, Juha Hyyppä, Harri Kaartinen, Henrik Haggren, Olumuyiwa Idowu Ojo, Masengo Francois Ilunga, Biswajit Nath, Zheng Niu, Shukla Acharjee, Nabansu Chattopadhyay, Swati Chandras, Nivedita Tidke, Heri Andreas, Hasanuddin Zainal Abidin, Irwan Gumilar, Dina Anggreni Sarsito, Dhota Pradipta, Noor Nabilah Abdullah, Nurul Hazrina Idris

Notice

First published in London, United Kingdom, 2018 by IntechOpen
eBook (PDF) Published by IntechOpen, 2019
IntechOpen is the global imprint of INTECHOPEN LIMITED, registered in England and Wales, registration number: 11086078, The Shard, 25th floor, 32 London Bridge Street
London, SE19SG – United Kingdom
Printed in Croatia

British Library Cataloguing-in-Publication Data
A catalogue record for this book is available from the British Library

Additional hard and PDF copies can be obtained from orders@intechopen.com

Multi-purposeful Application of Geospatial Data
Edited by Rustam B. Rustamov, Sabina Hasanova and Mahfuza H. Zeynalova

p. cm.

Print ISBN 978-1-78923-108-3

Online ISBN 978-1-78923-109-0

eBook (PDF) ISBN 978-1-83881-410-6

Meet the editors

Associate Prof. Dr. Rustam B. Rustamov was born on May 25, 1955, in Azerbaijan. He is a freelance expert on space science and technology. In the past, he was in charge of the Azerbaijan National Aerospace Agency activities as an Acting Director General. Rustam B. Rustamov graduated with a PhD degree from the Russian Physical-Technical Institute (S. Petersburg). Rustam B. Rustamov was invited for the work at the European Space Agency within the Framework of the United Nations Program on Space Applications at the European Space Research and Technology Center, the Netherlands. He is a Cambridge Scholars Publishing International Editorial Advisory Board member on Astronomy, Astrophysics and Space Science, London, UK. He is an author of 12 books published by the famous European and US publishers and more than 120 scientific papers.

Sabina N. Hasanova was born on November 11, 1988, in Baku, Azerbaijan. She completed her bachelor degree at the Azerbaijan Architecture and Construction University, Baku, Azerbaijan, and owns a master's degree from IE Business School in Architectural Management and Design. She is a young successful specialist heading for the innovative ideas. She is supported by her purposefulness and willingness to achieve a new summit in oil and gas sectors taking engineering obligations with successful integration and running scientific research activities. Sabina N. Hasanova is the author of four books published in the US and Europe publication houses and a number of scientific papers published in recognized international journals. Currently, she works for British Petroleum (BP) as a Geographical Information System Specialist.

Dr. Mahfuza H. Zeynalova was born on January 28, 1962, in Baku, Azerbaijan. She completed her higher education in 1982 at the Azerbaijan State Pedagogical Institute, Azerbaijan. She is a Doctor of Philosophy since 2012. Currently, Mahfuza H. Zeynalova works at the National Museum of History of the Azerbaijan National Academy of Sciences as the Deputy Director in Scientific Fond Affairs. She is an author of 1 monograph and 30 scientific papers. Mahfuza H. Zeynalova is a member of the International Committee of Museum (ICOM).

Contents

Preface

Up-to-date advances in space technology play a vital role in our daily lives. Undoubtedly, the use of a remote sensing method with further Geographic Information System (GIS) development as the final product of the image processing stage is driven by user needs. The fact is that the capabilities of GIS to integrate digital information into combined databases and to provide fundamental and advanced data analysis as well as visualization techniques has led to the larger application of GIS in wider spheres. There is no doubt that GIS is an excellent data source for government authorities at the decision-making stage in different areas of engineering, construction, and scientific research activities.

Today, GIS applications and uses are a convenient way for GIS to store data in digital database form and then represent it visually in a mapped hardware format. It makes the use of maps easier because final processing can communicate through Google Maps, Bing Maps, Yahoo Maps, etc.

GIS has an important place in planning and decision making for telecom industries. It enables wireless telecommunication development and management for the integration of geographic data into the network system design, process optimization, and any other required actions necessary for normal function and operation.

The demand of today's circumstances is to measure and assess human, technological, and other impacts that provide negative influences to Earth's ecological conditions and environments. There are a huge number of human activities that produce potential adverse ecological/environmental effects, which include the construction and operation of highways, railroads, pipelines, airports, radioactive waste disposal, and many others. The performance of GIS technology by integrating various GIS layers and by assessing natural features is the way to achieve specific information on the scale and characteristics of environmental impacts.

Natural disasters need to be controlled for the safety of human life and the protection of property. It is important to manage and mitigate natural disaster processes to minimize their consequences. Today, modern GIS technology developments are used to protect natural disaster impacts. GIS helps to assess and estimate risk and develop risk management systems with further diversification of natural or manmade disasters. It is the way to successfully implement preventive and protective actions, which can be executed by using GIS technological advances.

One common natural disaster is the hazardous landslide, which can be successfully monitored by a remote sensing method with further GIS development. It is the method that accurately divides landslide areas into zones. The evaluation of a landslide hazard is a complex task due to the collection, manipulation, and integration of spatial data into various geologi-

cal, structural, surface cover, and slope characteristic information systems of the selected area for further hazard zonation. With the support of GIS it gives the opportunity to provide risk assessment and reduce losses of human life and property.

Undoubtedly, flood damage prediction, forecasting, and estimation by using GIS technology advances the impact of achieving high accuracy. This achievement helps state authorities to take action when there is the threat of a natural flood. By delivering information resources to government representatives within flood risk areas, flood level potential in the surrounding area can be evaluated, making it possible to estimate and assess the consequencies of flood damage.

A GIS application in agriculture can observe and collect data regarding land cover/land use for the assessment of effective and efficient utilization of land by farmers, as well as successful management of agriculture activities. It contains such activities as analysis of soil data and what needs to be done to maintain high productivity of agricultural products. In the meantime, it can reveal sudden changes in land use/land cover caused by drought or deforestation, for example.

Space technology applications in navigation encourage the selection of the route and the scheduling of time for a selected destination. Today, Global Positioning Systems (GPS) are available to safely navigate waterways.

This book covers the above-mentioned areas of space technology application. It has brought together advances in space technology with the aim of applying geospatial data applications to Earth studies.

We encourage the interest of our potential readers in this book.

Rustam B. Rustamov
Institute of Physics of the Azerbaijan National Academy of Sciences
Azerbaijan

Sabina Hasanova
BP (British Petroleum) South Caucasus Pipeline Expansion Project
Azerbaijan

Mahfuza H. Zeynalova
Museum of History of Azerbaijan
Azerbaijan

Section 1

Satellite Instrumentation Development

Chapter 1

Introduction to Navigation Systems

Junghyun Lee

Additional information is available at the end of the chapter

http://dx.doi.org/10.5772/intechopen.71047

Abstract

Navigation is the method for determining position, speed, and direction of the object. That is mainly classified into two groups: physical model-based methods (PMMs) and external data-based methods (EDMs). Examples of PMMs are inertial navigation systems (INS) and dead-reckoning navigation. They determine the existing position of an object by measuring various changes in its state, such as velocity and acceleration. Representative EDMs is the global navigation satellite system (GNSS). In the case of spacecraft, auxiliary navigation systems using data compression were proposed. In the case of low earth orbit satellites, the deviations between nominal and real orbit are compressed in the form of Fourier coefficients by using the periodic characteristics of the trajectory. In the event of Deep space explorer, B-spline based orbit compression and transmission was proposed.

Keywords: navigation, GNSS, INS, B-spline, data compression

1. Introduction

Navigation refers to the method of determining aspects such as position, speed, and direction during travel. In the pre-modern era, direction and position were determined using an altazimuth, a compass, and a map; these are now considered primitive forms of navigation. As a result of modern developments in science and technology, exact positions and speeds are determined using equipment such as artificial satellites, global navigation satellite system (GNSS), inertial navigation systems (INS), etc. In the modern sense, navigation is mechanical devices equipped in ground vehicles, ships, and aircraft to determine their positions.

Navigation is classified into two categories in this study: physical model-based methods (PMMs) and external data-based methods (EDMs). Examples of PMMs are inertial navigation systems (INS) and dead-reckoning navigation. They determine the existing position of an object by measuring various changes in its state, such as velocity and acceleration. The global

navigation satellite system (GNSS) is an excellent representative of EDMs. Methods to determine longitude and latitude using polar stars or the sun considered as EDMs, which is utilized in the spacecraft nowadays. PMM and EDM have duality. The accuracy of PMMs is exponentially proportional to the cost, and the error increases over time. However, information can be obtained for three axes (X, Y, and Z); this is a stable configuration as no communication problems are incurred. EDMs are relatively cheap and the accuracy is pre-defined according to sensor. However, there may be some restrictions on communication. The navigation equipment in ground vehicles and the orbit propagator in spacecraft are designed to complement each other, considering the properties of tools such as the INS/GNSS.

In the case of spacecraft, auxiliary navigation systems using data compression were proposed due to the unpredictable space environment and limited communication. The orbital equation used in spacecraft is represented by a nonlinear differential equation containing multiple perturbation terms, which makes the determination of orbit numerically complex. Generally, a precise determination of orbit is made on the ground, and the information is then transmitted to the spacecraft periodically. However, Deep space communication is restrictive and expensive. Therefore, the cost of communication can be reduced by compressing orbital data. For Low Earth Orbit satellites, the deviations between nominal and real orbit are compressed in the form of Fourier coefficients by using the periodic characteristics of the trajectory [1, 2]. Deep space explorer orbit compression and transmission were proposed using B-spline [3].

2. Navigation system

2.1. PMMs

Representative PMMs include dead-reckoning navigation (DR) and the inertial navigation system (INS). They determine the current position by measuring the vehicle's own velocity and acceleration in addition to initial position data. Due to the nature of PMMs, the error increases with time.

2.1.1. Dead-reckoning navigation (DR)

Dead-reckoning navigation is a method of estimating the current position using the moving direction, velocity, and time. It considers errors according to true north and magnetic north. In the case of ground vehicles, only their own velocity needs to be considered, but aircraft and ships must calculate positions by considering ocean currents, wind, and so on. In fact, all navigation systems currently use this dead-reckoning method. Because the accuracy of this method decreases as time and distance increase, celestial navigation is used to determine the accurate position, and then the dead-reckoning method is used from that point forward. The traditional dead-reckoning method used a plotter (a protractor attached to a straight ruler) or a flight computer to determine position. At present, it is calculated automatically using an electronic flight computer.

2.1.2. Inertial navigation system (INS)

The Inertial Navigation System is a stand-alone navigation system that continuously calculates the position, direction, and velocity of the main body through its own accelerometer, rotation sensor, and arithmetic unit, without receiving any external information [4]. Although GPS offers a precise navigation system, it has limitations in space, deep seas, tunnels, and similar places because the GPS operates only when it can receive signals from the satellite. Furthermore, INS can avoid GPS jamming issues. Because an INS is a PMM, the error increases with time. Moreover, the price increases exponentially as the precision is enhanced. One critical factor in an INS is the accurate entry of the initial position and velocity. After that, the data measured by the accelerometer and rotation sensor are integrated consecutively. The accelerometer provides position data whereas the rotation sensor (gyroscope) provides attitude data. **Figure 1** shows an example of a strapdown inertial navigation system. Velocity and position data can be obtained by integrating the acceleration twice. It is strapped with an accelerometer that considers the acceleration of the tangent and vector components.

2.2. EDMs

EDMs include GNSS, which is represented by GPS. The application scope is very broad, and includes ground vehicles, ships, and airplanes. In this chapter, the use of GNSS for satellites and deep space probes is explained. Defining the current position and velocity of a satellite is called "orbit determination." The orbit determination problem can be largely divided into a system model part, a measurement model part, and an estimation technique part. Each can be explained as follows. First, the system model is a mathematical model that represents the orbital motion and various specific variables. It has to be approximated to some degree because many assumptions are included in the process of deriving the equation of motion. Second, for the measurement model, the GPS navigation solution or the tracking data (line of sight, elevation angle, azimuth angle, etc.) of the ground station is used. Here, the measurement values cannot be the true values due to sensor errors and other reasons, and always include some errors. Third, the estimation technique part estimates the optimum prediction values, that is, the position and velocity of the satellite using the approximated system model

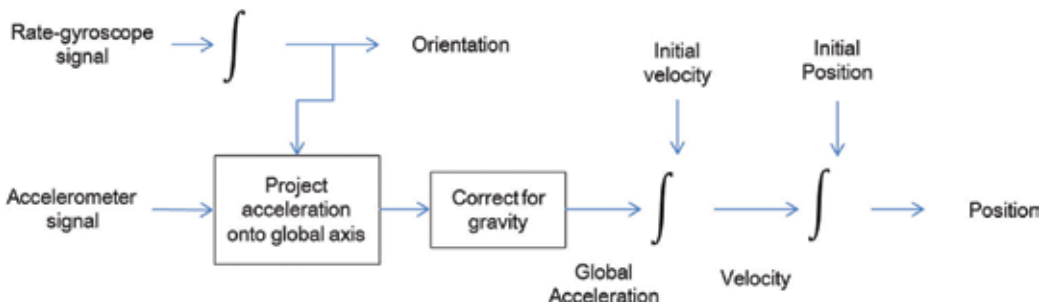

Figure 1. Principle of strapdown inertial navigation systems [5].

and inaccurate measurement values. Among these estimation techniques, the batch mode and the sequential model, such as the Kalman Filter, are widely used [6].

2.2.1. Data estimation method

2.2.1.1. Least squares estimation

Least squares estimation is also known as the "batch filter." The state equation and measurement equation are as follows:

$$z_k = h_k^T x + v_k \tag{1}$$

The least squares estimation method estimates the state variable θ, which minimizes the error, that is, the difference between the mathematically predicted value $h_k^T \theta$ and the actual measured value (z_k). This can be expressed as follows:

$$L(x) = \frac{1}{n} E\left[\frac{1}{2}\sum_{k=1}^{n}\left(z_k - h_k^T x\right)^2\right] = \frac{1}{2n} E\left[\sum_{k=1}^{n}\left(z_k - h_k^T x\right)^2\right] = \frac{1}{2n}\left(Z_n - H_n X\right)^T\left(Z_n - H_n X\right) \tag{2}$$

Eq. (2) is a convex shape for the state variable, and the following condition must be met to obtain the minimum value:

$$\frac{\partial L(x)}{\partial x} = 0 = -H_n{}^T\left(Z_n - H_n X\right) \tag{3}$$

In the above equation, X represents the optimum prediction result. Ultimately, Eq. (3) can be rearranged as follows, which is called the Normal Equation:

$$\hat{X} = \left(H_n{}^T H_n\right)^{-1} H_n{}^T Z_n \tag{4}$$

The weighted least square estimation can be also used, which uses a weight matrix to prevent the distortion of estimation results by observation values that contain large errors. This batch estimation method is performed after all the data required for estimation is obtained, and multiple reiterative calculations are required to converge to the desired value.

2.2.1.2. Kalman filter algorithm

Unlike the aforementioned batch filter, the Kalman filter is used often as a sequential method. The Kalman filter algorithm estimates the optimum prediction value in real time by appropriately mixing predictions made by a mathematical model with measured values from sensors [7]. In the mathematical propagation, which is the first step for the Kalman filter, it is possible to propagate to the target point through an analytical method using appropriate numerical integration or a state transition matrix, assuming that the initial conditions of the orbit are given by the mean and covariance matrix at a random point. The mathematical model is represented by the following state equation:

$$x_{k+1} = \Phi_k x_k + w_k \tag{5}$$

This forms a state-space equation together with Eq. (1).

The covariances of the measurement error and the system error can be expressed as R and Q, respectively. The error was assumed as zero-mean Gaussian white noise. First, the covariances of the estimates and deviations in the system can be obtained by the following:

$$\hat{x}_k^- = \Phi \hat{x}_{k-1}^- \tag{6}$$

$$P_k^- = \Phi P_{k-1}^- \Phi + Q \tag{7}$$

Second, in the measurement and processing step, the actual measurement is performed. The measured value is expressed as z according to Eq. (1). Finally, in the update step, we must determine which value must be given a greater weight depending on the reliability of the mathematical prediction and the actual measurement. For this purpose, the Kalman gain is defined as follows:

$$k_k = \frac{P_k^- h_k}{h_k P_k^- h_k^T + R} \tag{8}$$

Accordingly, the weights of the system estimates and measurements are considered. The measurements are updated as follows:

$$\hat{x}_k = \hat{x}_k^- + k_k\left(z_k + h_k \hat{x}_k^-\right) \tag{9}$$

$$P_k = \left(I - k_k h_k\right) P_k^- \tag{10}$$

The degree of update of the Kalman filter is automatically adjusted according to the reliability of the measurement. If the reliability of measurement is good and X is very small, the Kalman gain increases and more weight is given to the measurement than the mathematical prediction; otherwise, the mathematical prediction is preferred. In this way, the process of stochastically finding the optimum estimate using the Kalman gain, which is a weighting factor, is repeated in real time. The typical Kalman filter algorithm is shown in **Figure 2**.

As explained above, the Kalman filter method estimates the value of the state variable in real time by stochastically filtering through a system model after receiving measurements mixed with noise. The estimated value is the orbit.

2.2.2. GNSS

The global navigation satellite system (GNSS) estimates positions through the GNSS dedicated satellite orbiting the earth. The global positioning system (GPS) is open to the public and is frequently used. The satellite has a precise time and sends its own position and time information every moment. As shown in Eq. (11) the GPS receiver calculates the straight distance between the satellite and the receiver considering the incoming velocity of signals [8]. The position is determined by a sphere whose diameter is the distance to the satellite if there

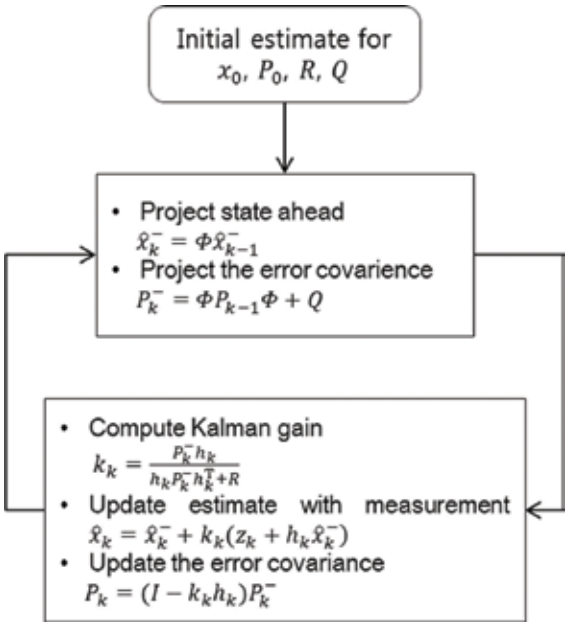

Figure 2. Kalman filter algorithm.

is one satellite, by a circle in space if there are two satellites, and by one point if there are three satellites (**Figure 3**). **Figure 3** illustrates the typical satellite orbit determination method. This orbit determination algorithm can be implemented by a computer installed in the ground station or in the satellite, according to the satellite operation scenario. In other words, an appropriate model and algorithm should be chosen depending on the performing entity. This concept can be expanded to ships, ground vehicles, airplanes, etc.

$$r = \sqrt{(X - X_s)^2 + (X - X_s)^2 + (X - X_s)^2} + s \tag{11}$$

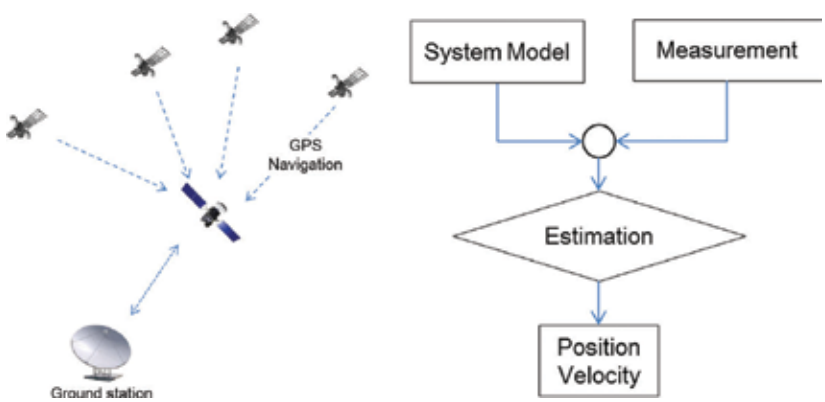

Figure 3. Orbit termination scheme via GPS.

The GNSS is comprised of a space part, a ground control part, and a user part, which have an organic relationship with one another (**Figure 4**). The space part consists of approximately 30 clustered satellites in a space orbit. When satellites reach the end of their life, new satellites are launched to maintain a constant number. The measurement error decreases as the number of satellites increases, and more satellites are also added due to communication interruptions by the Earth. Techniques such as SBAS and DGPS are used to enhance accuracy. The ground control part constitutes control facilities on the ground that monitor and adjust the correct rotation of the satellites around the orbit. The GPS has one main control station and four unmanned monitor stations. They monitor if satellites are moving in a given orbit, and perform orbital maneuvering if any satellite moves out of the orbit. The user part consists of general users and GPS receivers that can be purchased.

2.3. GPS/INS coupling system

The INS and GPS are complementary. The INS detects the navigation information (position, velocity, and attitude) of moving bodies using an accelerometer and gyroscope. The precision and cost of an INS are exponentially proportional and its error increases with time. However, it is more stable than other systems because it can obtain information about three axes, X, Y, and Z, and has no communication problems. It has the advantage of not being affected by the external environment, and providing highly accurate and continuous navigation data for short voyage durations. The GPS is a system that determines the position and velocity of moving

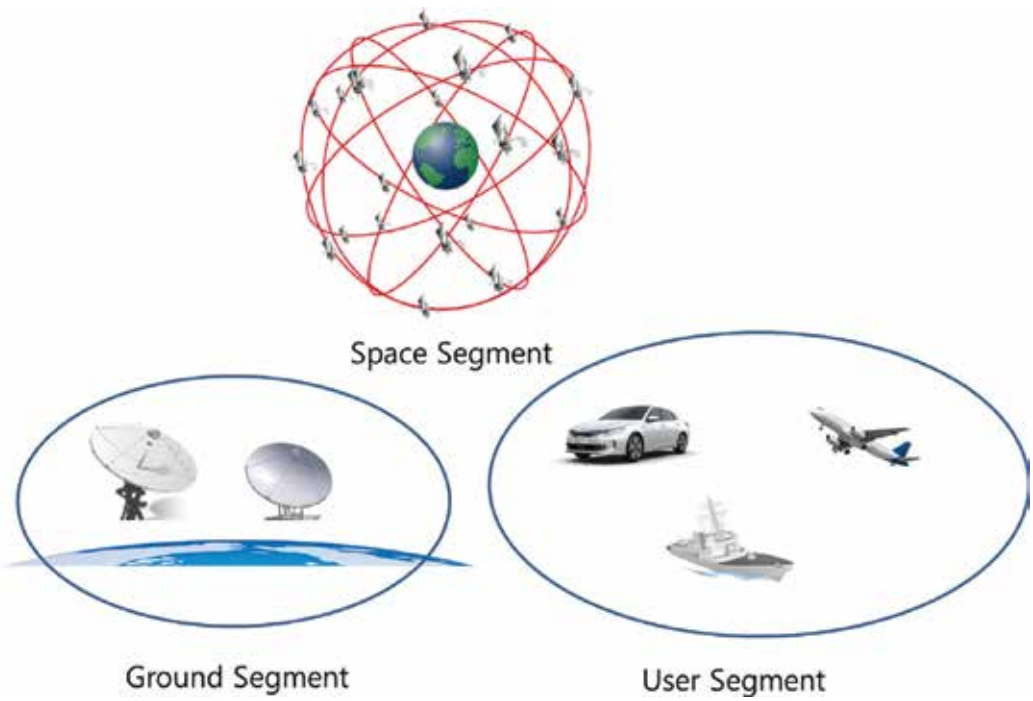

Figure 4. Components of GPS systems.

bodies by measuring the pseudo range to moving bodies from at least 4 of the 24 satellites orbiting the Earth. The GPS is relatively low-priced, does not accumulate errors with time, and the error range is fixed. However, its disadvantage is that the performance drops if there is severe jamming, or the number of visible satellites is less than four. Furthermore, visibility and communication may become restricted [9].

If you design a navigation system using only one method, high costs are required to obtain the desired performance. However, high-performing sensors can be obtained at low cost if you consider complementary performance. Thus, the navigation system of ground equipment and the orbiter of a space probe are designed to complement each other. We can design navigation systems more effectively by using the INS and performing periodic calibrations with GPS. Furthermore, this can make the overall navigation system more robust than if using only one method [10]. Current research is attempting to integrate these two systems, using integration methods that can be largely divided into tight and loose INS/GPS integration systems [11]. One characteristic of these integration systems is that the performance can be enhanced by improving the tracking performance of the code and carrier tracking loops of the GPS receiver.

The structure of the tightly coupled INS/GPS integration system is shown in **Figure 5**. Data measured from the GPS receiver (pseudo range, pseudo range rate) and the INS data (position, velocity, attitude) include many errors. The INS and GPS do not perform separate filtering, but these errors are estimated by one Kalman filter. The loosely coupled INS/GPS integration system is shown in **Figure 6**. In this system, INS and GPS perform measuring and filtering separately.

2.3.1. Comparison of integration systems

The loosely coupled system can be smaller and faster than the tightly coupled system. However, noises also become amplified. The performance of loosely coupled and tightly coupled integration is the same if the GPS availability is good throughout the test run. When GPS availability is poor, as in an urban canyon, tightly coupled integration performs better than loosely coupled integration. The positional accuracy is best when both code and Doppler measurements are used, and is worst when only Doppler measurements are used. The velocity accuracy is also best when both code and Doppler measurements are used, and worst when code only measurement is used.

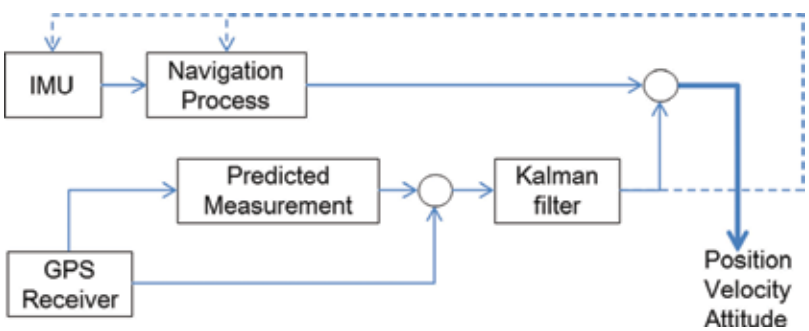

Figure 5. Tightly coupled INS/GPS integration systems.

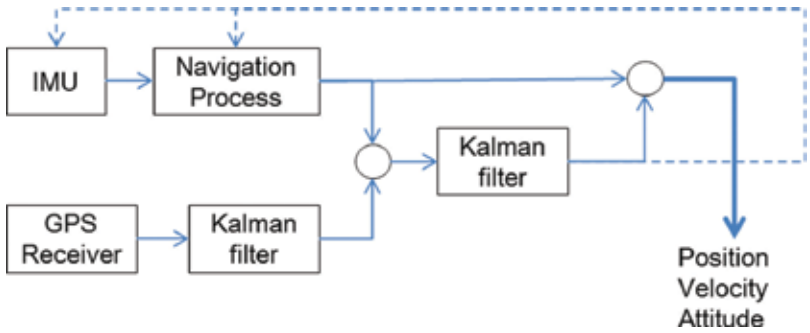

Figure 6. Loosely coupled INS/GPS integration systems.

3. Auxiliary navigation system using data compression technique

The analysis of space orbital motion generally means the integration of the nonlinear orbital motion equation. For this analysis, special perturbation [12], which is a numerical method, or general perturbation, which is an analytical method, is used. Special perturbation has a small error due to numerical integration during orbit propagation, but requires a high-performance onboard computer. General perturbation has a small computational load during orbit propagation, but the numerical integration error increases substantially with time. To improve this shortcoming, low-orbit satellites generate a residual, which is the difference between the reference orbit and the true orbit. The residuals, which exhibit periodic characteristics, are approximated using the coefficients of trigonometric and Fourier functions, before being transmitted to the satellites along with the reference orbital elements. The satellite computer can improve the precision of orbit propagation and greatly reduce the computational load by generating a reconstruction orbit [13, 14] using coefficients and reference orbital elements received from the ground station.

However, the approximation method using residuals cannot be applied to deep space probes for the Moon and Mars because they do not rotate around the Earth repeatedly, like satellites. As a solution, an auxiliary navigation system using B-spline data compression has been proposed [3]. The data compression rate must be increased because deep space communication is expensive and limited in communication time. For Earth and lunar orbits where takeoff and landing occur, intensive control and communication are essential due to the danger and unpredictability. However, in the transition segment, which is stable and accounts for the majority of navigation, communication time can be saved, and stable navigation data can be received by sending compressed orbit data calculated on the ground to the probes.

3.1. Satellite orbit compression using the Fourier technique

Satellite orbit compression using the Fourier technique, and development of an auxiliary navigation system using this technique, have mainly been studied using a low-orbit satellite model [1, 2, 12, 15]. The overall operation concept of an onboard orbit propagator is

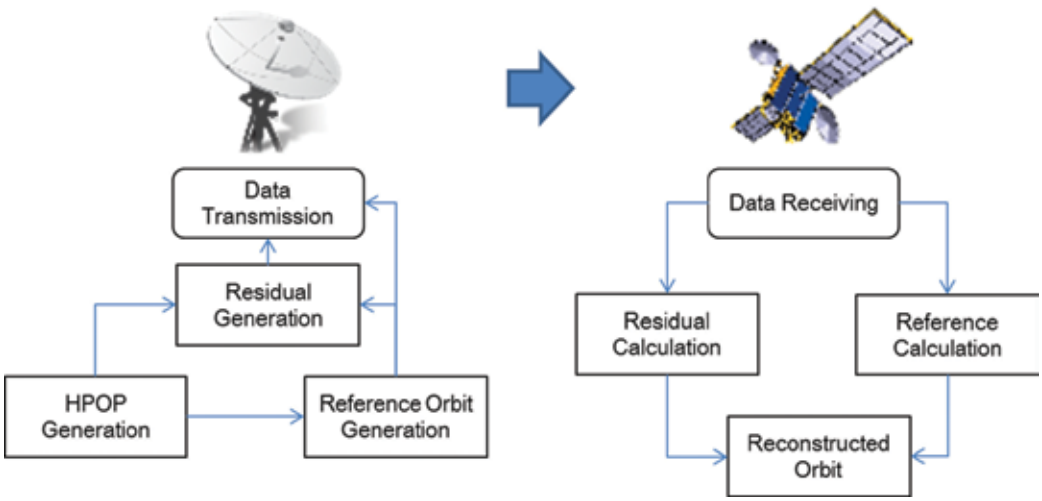

Figure 7. Diagram of onboard orbit propagator operation.

shown in **Figure 7**. First, an actual orbit is created through accurate modeling and numerical integration of orbital motions, which is available on the ground. Then, a reference orbit is created that is sufficiently close and has a known solution. After defining the residual, which is the difference between the reference orbit and the actual orbit, a few approximate functions are obtained by reflecting the characteristics of orbital motion. The corresponding coefficients are sent to the satellite. The satellite determines the position and velocity of the satellite by substituting the pre-embedded numbers in the onboard computer (Orbit Reconstruction).

The orbit precision predicted through such orbit reconstruction is closely related to the selection of the reference orbit and residual reproduction function. However, the selection criteria for the reference orbit and residual reproduction function must be based on the calculation power of the satellite onboard computer, the data transmission protocol between the ground station and the satellite, and the required precision of the orbit propagation result.

3.1.1. Creation of reference orbit

Essentially, orbit data is created by numerical integration using the initial time, position, and velocity data on the ECI coordinate system, as well as precise orbit modeling. The data determined in this way is converted to orbit elements, and the reference orbit is established. The general reference orbit can be expressed in first or second order polynomials, as shown below, and the coefficients are interpolated using the least squares method.

$$n(t) = n_0 + n_1 t + n_2 t^2 \tag{12}$$

$$e(t) = e_0 + e_1 t + e_2 t^2 \tag{13}$$

$$i(t) = i_0 + i_1 t + i_2 t^2 \tag{14}$$

$$\Omega(t) = \Omega_0 + \Omega_1 t + \Omega_2 t^2 \tag{15}$$

$$\omega(t) = \omega_0 + \omega_1 t + \omega_2 t^2 \tag{16}$$

$$M(t) = M_0 + M_1 t + M_2 t^2 \tag{17}$$

where n is the mean motion, e is the eccentricity, i is the inclination angle, Ω is the right ascension of ascending node, ω is the argument of perigee, and M is the mean anomaly.

Here, the coefficients are determined using the least squares curve fit or a similar technique based on the precise orbit prediction data of actual orbits created by numerical integration. However, in the case of a near-circular orbit, the argument of perigee cannot be defined or the curve fitting may be inaccurate. Therefore, instead of ω and M, $u = \omega + f$ can be used, which is an argument of latitude of the orbit.

3.1.2. Residual reproduction

The residual means the difference between the actual orbit data and the designed reference orbit (**Figure 8**). The Fourier series coefficient must be determined, and the least squares regression is used for this purpose.

$$r - r^* = \delta r = b_0 + \sum b_k \sin(ku) + \sum b_k \cos(ku) \tag{18}$$

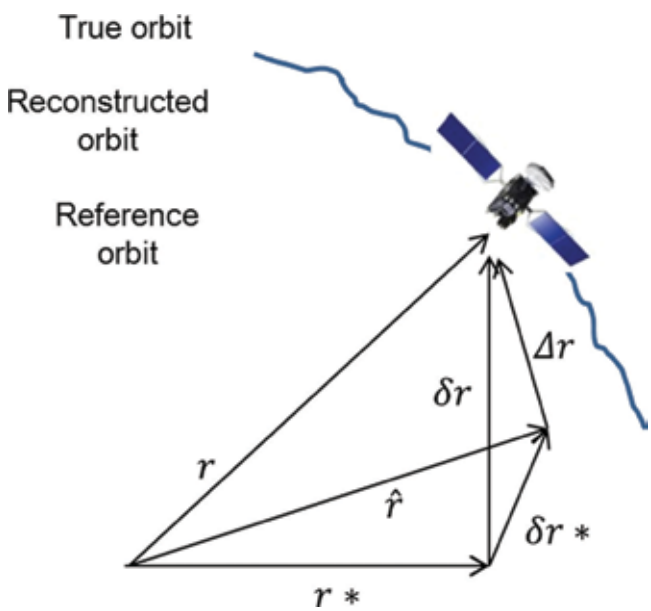

Figure 8. Definition of various orbits.

3.1.3. Orbit reconstruction

The coefficients determined above are uploaded from the ground station to the satellite through communication. Using the reference orbit coefficient and residual coefficient received from the ground station, the onboard computer in the satellite reconstructs the orbit. Eqs. (12)–(18) are stored in the satellite computer, and orbit data is created if the current time is inputted. The velocity data is indirectly calculated from the position data, or can be directly created using the same method. The compressed orbit elements are converted to velocity and position data through the DCM, etc., and vary with the characteristics of the orbit.

3.2. Lunar probe orbit compression using a B-spline

Deep space probes that explore the Moon, Mars, and minor planets stay in the Earth's orbit after being launched by a launch vehicle. After staying in Earth's orbit for some time, they escape it by burning the engine to reach the target planet. In the case of lunar exploration satellites, they activate trans-lunar injection (TLI) in the parking orbit of the Earth to enter the lunar transfer orbit. Once a lunar exploration satellite enters the lunar transfer orbit, the satellite is tracked with ground antennae around the world, and orbit determination is performed by processing the obtained tracking data. Communication with a lunar probe corresponds to deep space communication, and a representative example is the Deep Space Network (DSN). Four antennae are in currently in operation at three locations (Goldstone, Madrid, and Canberra) [16–18]. The antennae and communication range of DSN are shown in **Figure 9**. The orbit data must be compressed as much as possible because communication is very limited in both time and range. Therefore, an algorithm for efficient orbit data compression should be developed.

3.2.1. Ground control station data compression

After orbit determination, the coordinates and velocity data of the calculated orbit are compressed as control points through the proposed procedure based on a B-spline. Compared to the conventional method, this method can stably compress even bulky data at a higher compression rate. This data is sent to the probe in the form of compressed parameters. The

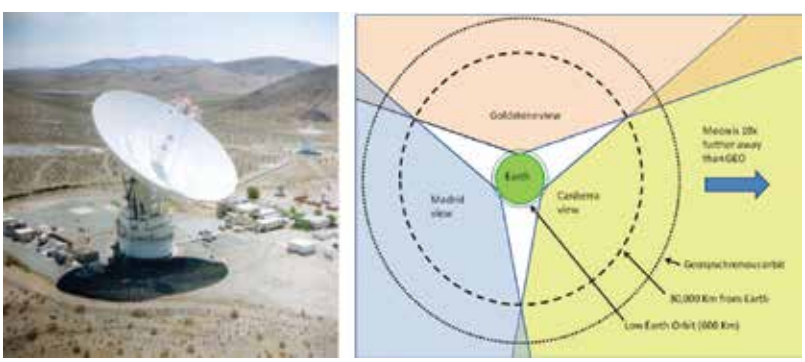

Figure 9. Deep space network facility.

probe reconstructs the orbit based on the received parameters. Methods by which the lunar exploration satellite leaves the earth orbit and enters the lunar orbit include direct transfer, phasing loop transfer, and weak stability boundary (WSB).

The B-spline approximation method creates a three-dimensional curve with position and velocity data over time (4-D), excluding time, and then time is reconstructed by linear interpolation using the B-spline. The initial degree and control points are given, and the parameters are estimated based on the given point data. Control points are obtained from the estimated parameters and corresponding points, and the curve is reconstructed. After performing linear interpolation for the reconstructed data in line with the time, it is compared with the original data, and the control points and degrees are increased until they enter the error range.

Then, the drive command is given with the position and velocity data of the x, y, and z axes for time t. The position data can be expressed by (t, X, Y, Z) and the velocity data by (t, Vx, Vy, Vz). The next step is parameterization, where the parameter values corresponding to the given points are estimated. When a point (=1,2,…,n) is given on a secondary plane, the parameter values can be obtained as follows: si = si-1 + Δi/L, (i = 2,3,…,n), Δi = |pi-pi-1|α, and L = $\sum$ Δi, where s is the parameter and s1 = 0. In these equations, 1/2 or 1 can be used for α.

Next, adjustment points are calculated. The method of obtaining the curve using given points and calculated parameter values is as follows. A k-order B-spline curve with nc adjustment points is given as follows:

$$\mathbf{c}(s) = \sum_{i=1}^{n} \mathbf{b}_i N_{i,k}(s) \tag{19}$$

where b_i is the adjustment point, and $N_{i,k}$ is the k-order B-spline basis function. Here, if nc-3 is rt., the vector becomes T = (j = 1,…,rt). The k-order B-spline basis function is defined as follows:

$$\begin{aligned} N_{i,0}(s) &= \begin{cases} 1 & if\ u_i \le s < u_{i+1} \\ 0 & otherwise \end{cases}, \\ N_{i,k}(s) &= \frac{s-u_i}{u_{i+k}-u_i} N_{k-1}(s) + \frac{u_{i+k+1}-s}{u_{i+p+1}-u_{i+1}} N_{i+1,k-1}(s). \end{aligned} \tag{20}$$

where u_i is the value of the ith knot vector. If the given points are $\mathbf{p}_i$ (i = 1~n) and the parameter value corresponding to each point is s_i, the following equation must be satisfied:

$$\mathbf{p}_i \simeq \mathbf{c}(s_i) = \sum_{i=1}^{n} \mathbf{b}_i N_{i,k}(s_i) \tag{21}$$

This becomes n simultaneous equations consisting of n_c unknown numbers, which can be solved by singular value decomposition [19]. The optimal value for the error between the reconstructed value **c** and the original value **p** can be derived by adjusting the control points and degrees.

3.2.2. Orbit reconstruction

The optimal solution is calculated using the B-spline method (**Figure 10**). To apply the B-spline-based approximation method to the orbit of a deep space probe, some changes

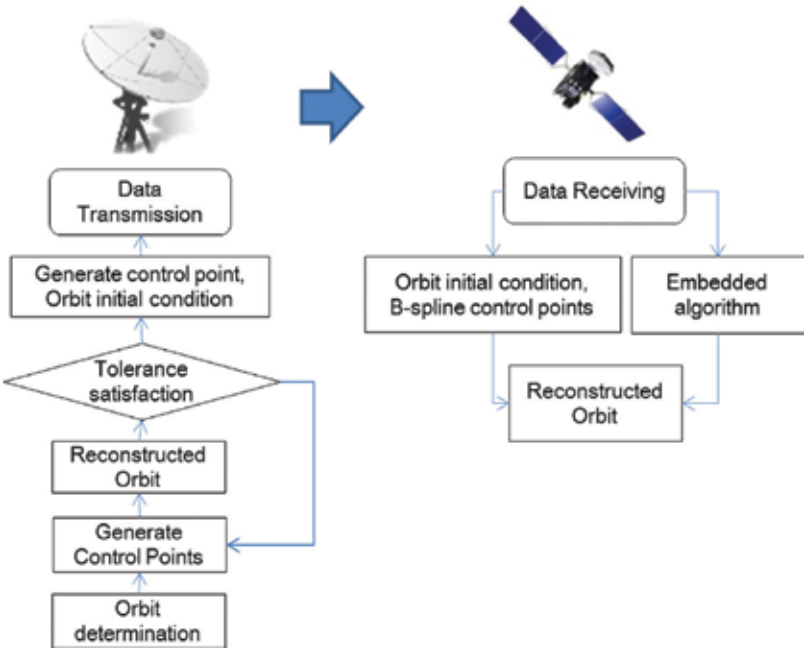

Figure 10. Diagram of data compression via the B-spline method.

need to be made to the system currently in use. The transmission data include the number of calculated coefficients: n_c; the calculated coefficients: b_i; and the section beginning and end times: t_s, t_e. Two system changes are required: knot vector creation and basis function evaluation.

For the former, the B-spline method requires a knot vector for calculation. This knot vector can be set in such a way that it will be automatically calculated in the probe without being transmitted from the ground to the satellite. For the latter, the B-spline method uses the basis function introduced in Section 3.2.1. Therefore, the ground control system and satellites must have a function for calculating the B-spline basis function $N_{i,k}$ and calculating the B-spline curve.

4. Conclusion

In this study, we examined the general operation of satellite navigation systems. Basic navigation methods were defined and described in detail. The navigation methods were classified into PMMs and EDMs, and integration of these two methods was proposed. An auxiliary navigation system using data compression was also described. Regarding the navigation system, we suggested a novel method for designing an organic system, rather than a simple navigation device, according to its purpose, cost, and performance.

Author details

Junghyun Lee

Address all correspondence to: yanggwa82@gmail.com

Defense Agency for Technology and Quality, Jinju, South Korea

References

[1] Kim K, Noh T, Jeon S, Kim J, Ki C. Performance Analysis of Onboard Orbit Propagator using LEO Spacecraft GPS Data. The Korean Society For Aeronautical and Space Sciences, South Korea; 2011. pp. 569-575

[2] Jung O. Relative Orbit Propagator and Its Applications [Master's Degree Thesis]. Jeonju: Chonbuk National University; 2004

[3] Lee J, Choi S, Ko K. Onboard orbit propagator and orbit data compression for lunar explorer using B-spline. International Journal of Aeronautical and Space Sciences. 2016;**17**:240-252

[4] Siouris G. Aerospace Avionics Systems: A Modern Synthesis, 2nd, Academic Press: The United States; 1993

[5] Woodman OJ. An Introduction to Inertial Navigation. University of Cambridge, Computer Laboratory: The United Kingdom; 2007

[6] Spall JC. Introduction to Stochastic Search and Optimization. 1st. Wiley-Interscience: The United States; 2003

[7] Kim P. Kalman Filter for Beginners: With MATLAB Examples. CreateSpace: The United States; 2011

[8] Yamaguchi S, Tanaka T. GPS standard positioning using Kalman filter. In: SICE-ICASE 2006; 18-21 October 2006; Busan. IEEE; 2006. p. 1351-1354

[9] Kaplan E, Hegarty C. Understanding GPS: Principles and Applications. Artech House: The United Kingdom; 2005

[10] Angrisano A. GNSS/INS integration methods [PhD thesis]. Naples: Universita'degli Studi di Napoli Parthenope; 2010

[11] Cheol-Kwan Y, Duk-Sun S. Analysis for stability and performance of INS/GPS integration system. In: Proceedings of the KIEE Conference. 1998. p. 445-447

[12] Ok Chul J, Tae Soo N, Sang Ryool L. A study on autonomous update of onboard orbit propagator. Journal of The Korean Society for Aeronautical and Space Sciences. 2003;**31**:51-59

[13] Salama AH. On-board ephemeris representation for Topex/Poseidon. In: AIAA/AAS Astrodynamics Conference; 20-22 August 1990. Portland: American Institute of Aeronautics and Astronautics; 1990. p. 674-679

[14] Segerman AM, Coffey SL. Ephemeris compression using multiple Fourier series. The Journal of the Astronautical Sciences. 1998;**46**:343-359

[15] Cho D, Choi Y, Noh TM, Bang H, Lee C. Onboard Orbit Propagator Using Only GPS Signal for STSAT-3. The Korean Society For Aeronautical and Space Sciences; 2010. p. 955-959

[16] Clement BJ, Johnston MD. The deep space network scheduling problem. In: Proceedings of the National Conference on Artificial Intelligence; 9-13 July 2005; Pittsburgh. AAAI; 2005. p. 1514-1520

[17] Clement BJ, Johnston MD. Design of a deep space network scheduling application. In: Proceedings of the International Workshop on Planning and Scheduling for Space; 22-25 October 2006; Baltimore. 2006

[18] Tai WS, Bhanji AM, Luers EB, Shen Y. Deep Space Network Services Catalog. Ed: Document, 2015

[19] Press WH, Teukolsky SA, Vetterling WT, Flannery BP. Numerical Recipes in C vol. 2. Citeseer; 1996

Chapter 2

A Review: Remote Sensing Sensors

Lingli Zhu, Juha Suomalainen, Jingbin Liu,
Juha Hyyppä, Harri Kaartinen and Henrik Haggren

Additional information is available at the end of the chapter

http://dx.doi.org/10.5772/intechopen.71049

Abstract

The cost of launching satellites is getting lower and lower due to the reusability of rockets (NASA, 2015) and using single missions to launch multiple satellites (up to 37, Russia, 2014). In addition, low-orbit satellite constellations have been employed in recent years. These trends indicate that satellite remote sensing has a promising future in acquiring high-resolution data with a low cost and in integrating high-resolution satellite imagery with ground-based sensor data for new applications. These facts have motivated us to develop a comprehensive survey of remote sensing sensor development, including the characteristics of sensors with respect to electromagnetic spectrums (EMSs), imaging and non-imaging sensors, potential research areas, current practices, and the future development of remote sensors.

Keywords: remote sensing, satellite, sensors, electromagnetic spectrum, spectrum of materials, imaging sensors, non-imaging sensors

1. Introduction

In 2015, one of the most remarkable events in the space industry was when SpaceX realized the reusability of its rocket for the first time. Additionally, in June 2014, Russia used 1 rocket to launch 37 satellites at the same time. At present, many countries have the capability to launch multiple satellites in one mission. For example, NASA and the US Air Force launched 29 satellites in a single mission in 2013. At that time, the mission represented the most satellites ever launched at one time [1]. In 2015 and 2016, China and India launched 20 satellites in single mission, respectively. At present, six organizations have the capability to launch multiple satellites in a single mission: Russia, USA, China, India, Japan, and ESA. This trend indicates that in the future, the cost of sending satellites to space will greatly decrease. More and more remote sensing resources are becoming available. It is of great importance to have

a comprehensive survey of the available remote sensing technology and to utilize inter- or trans-disciplinary knowledge and technology to create new applications.

Remote sensing is considered a primary means of acquiring spatial data. Remote sensing measures electromagnetic radiation that interacts with the atmosphere and objects. Interactions of electromagnetic radiation with the surface of the Earth can provide information not only on the distance between the sensor and the object but also on the direction, intensity, wavelength, and polarization of the electromagnetic radiation [2]. These measurements can offer positional information about the objects and clues as to the characteristics of the surface materials.

Satellite remote sensing consists of one or multiple remote sensing instruments located on a satellite or satellite constellation collecting information about an object or phenomenon on the Earth surface without being in direct physical contact with the object or phenomenon. Compared to airborne and terrestrial platforms, spaceborne platforms are the most stable carrier. Satellites can be classified by their orbital geometry and timing. Three types of orbits are typically used in remote sensing satellites, such as geostationary, equatorial, and sun-synchronous orbits. A geostationary satellite has a period of rotation equal to that of Earth (24 hours) so the satellite always stays over the same location on Earth. Communications and weather satellites often use geostationary orbits with many of them located over the equator. In an equatorial orbit, a satellite circles the Earth at a low inclination (the angle between the orbital plane and the equatorial plane). The Space Shuttle uses an equatorial orbit with an inclination of 57°. Sun-synchronous satellites have orbits with high inclination angles, passing nearly over the poles. Orbits are timed so that the satellite always passes over the equator at the same local sun time. In this way, these satellites maintain the same relative position with the sun for all of its orbits. Many remote sensing satellites are sun synchronous, which ensures repeatable sun illumination conditions during specific seasons. Because a sun-synchronous orbit does not pass directly over the poles, it is not always possible to acquire data for the extreme polar regions. The frequency at which a satellite sensor can acquire data of the entire Earth depends on the sensor and orbital characteristics [3]. For most remote sensing satellites, the total coverage frequency ranges from twice a day to once every 16 days. Another orbital characteristic is altitude. The space shuttle has a low orbital altitude of 300 km, whereas other common remote sensing satellites typically maintain higher orbits ranging from 600 to 1000 km.

The interaction between a sensor and the surface of the Earth has two modes: active or passive. Passive sensors utilize solar radiation to illuminate the Earth's surface and detect the reflection from the surface. They typically record electromagnetic waves in the range of visible (~430–720 nm) and near-infrared (NIR) (~750–950 nm) light. Some systems, such as SPOT 5, are also designed to acquire images in middle-infrared (MIR) wavelengths (1580–1750 nm). The power measured by passive sensors is a function of the surface composition, physical temperature, surface roughness, and other physical characteristics of the Earth [4]. Examples of passive satellite sensors are those aboard the Landsat, SPOT, Pléiades, EROS, GeoEye, and WorldView satellites. Active sensors provide their own source of energy to illuminate the objects and measure the observations. These sensors use electromagnetic waves in the range of visible light and near-infrared (e.g., a laser rangefinder or a laser altimeter) and radar waves

(e.g., synthetic aperture radar (SAR)). A laser rangefinder uses a laser beam to determine the distance between the sensor and the object and is typically used in airborne and ground-based laser scanning. A laser altimeter uses a laser beam to determine the altitude of an object above a fixed level and is typically utilized in satellite and aerial platforms. SAR uses microwaves to illuminate a ground target with a side-looking geometry and measures the backscatter and travel time of the transmitted waves reflected by objects on the ground. The distance that the SAR device travels over a target in the time taken for the radar pulses to return to the antenna produces the SAR image. SAR can be mounted on a moving platform, such as spaceborne and airborne platforms. According to the combination of frequency bands and polarization modes used in data acquisition, sensors can be categorized as single frequency (L-band, C-band, or X-band), multiple frequency (a combination of two or more frequency bands), single polarization (VV, HH, or HV), and multiple polarization (a combination of two or more polarization modes). Currently, there are three commercial SAR missions in space: Germany's TerraSAR-X and TanDEM-X (X-band with a ~3.5 cm wavelength), Italy's COSMO-SkyMed (X-band with ~3.5 cm wavelength), and Canada's RADARSAT-2 (C-band with ~6 cm wavelength). In addition, ESA's ERS-1, ERS-2, and Envisat also carried SAR, although these missions have ended. The latest SAR satellites from ESA include Sentinel-1A, Sentinel-1B, and Sentinel-3A. Typical SAR parameters are repeat frequency, pulse repetition frequency, bandwidth, polarization, incidence angle, imaging mode, and orbit direction [5].

As sensor technology has advanced, the integration of passive and active sensors into one system has emerged. This trend makes it unclear difficult to categorize sensors in the traditional way, into passive sensors and active sensors. In this paper, we introduce the sensors in terms of imaging or non-imaging functionality. Imaging sensors typically employ optical imaging systems, thermal imaging systems, or SAR. Optical imaging systems use the visible, near-infrared, and shortwave infrared spectrums and typically produce panchromatic, multispectral, and hyperspectral imagery. Thermal imaging systems employ mid to longwave infrared wavelengths. Non-imaging sensors include microwave radiometers, microwave altimeters, magnetic sensors, gravimeters, Fourier spectrometers, laser rangefinders, and laser altimeters [6].

It has been decades since Landsat-1, the first Earth resources technology satellite, was launched in 1972. Satellite platforms have evolved from a single satellite to multi-satellite constellations. Sensors have experienced unprecedented development over the years, from 1972 with the first multispectral satellite, Landsat-1, with four spectral bands to 1997 with the first hyperspectral satellite, Lewis, with 384 spectral bands. Spatial resolution has also significantly improved over the decades, from 80 m in Landsat-1 to 31 cm in Worldview-3. A number of studies on satellite imagery processing methods and applications have been conducted. A few papers providing sensor overviews have been published, including [7–9]. Blais [7] reviewed the range sensors developed over the past two decades. The studied range sensors include single point and laser scanners, slit scanners, pattern projections, and time-of-flight systems. In addition, commercial systems related to range sensors were reviewed. Melesse et al. [18] provided a survey of remote sensing sensors for typical environmental and natural resources mapping purposes, such as urban studies, hydrological modeling, land-cover and floodplain mapping, fractional vegetation cover and impervious surface area mapping, surface energy flux and micro-topography correlation, remotely sensed-based rainfall, and potential evapotranspiration for estimating

crop water requirement satisfaction indexes. Recently, a survey on remote sensing platforms and sensors was provided by Toth and Jóźków [9]. The authors gave a general review in current remote sensing platforms, including satellites, airborne platforms, UAVs, ground-based mobile and static platforms, sensor georeferencing and supporting navigation infrastructure, and provided a short summary of imaging sensors.

In the literature, we found that overviews of remote sensing sensors were quite rare. One reason for this finding was that this topic is fairly broad. Usually, one can find detailed knowledge from thick books or a very simple overview from some webpages. As most readers need to obtain relevant knowledge within a reasonable time period and with a modest depth, the contribution of our paper is valuable. In this paper, we review the history of remote sensing, the interaction of the electromagnetic spectrum (EMS) and objects, imaging sensors and non-imaging sensors (e.g., laser rangefinders/altimeters), and commonly used satellites and their characteristics. In addition, future trends and potential applications are addressed. Although this paper is mainly about satellite sensors, there is no apparent boundary between satellite sensors and airborne, UAV-based, or ground-based sensors except that satellite sensors have more interaction with the atmosphere. Therefore, we use the term "remote sensing sensors" generally.

2. Remarkable development in spaceborne remote sensing

Although the term 'remote sensing' was introduced in 1960. However, in practice, remote sensing has a long history. In the 1600s, Galileo used optical enhancements to survey celestial bodies [10]. An early exploration of prisms was conducted by Sir Isaac Newton in 1666. Newton discovered that a prism dispersed light into a spectrum of red, orange, yellow, green, blue, indigo, and violet and recombined the spectrum into white light. One hundred years later, in 1800, Sir William Herschel explored the thermal infrared electromagnetic radiation for the first time in the world. Herschel measured the temperature of light that had been split with a prism into the spectrum of visible colors. In the following decades, some attempts were made with aerial photographs using cameras attached to balloons. However, the results were not satisfactory until 1858, when Gasper Felix Tournachon took the first aerial photograph successfully from a captive balloon from an altitude of 1200 feet over Paris. Later, in 1889 in Labruguiere, France, Arthur Batut attached a camera and an altimeter to kites for the first time so that the image scale could be determined. Therefore, he is considered to be the father of kite aerial photography. Then, at the beginning of the twentieth century, the camera was able to be miniaturized (e.g., 70 g) so that it was easily carried by pigeons. The Bavarian Pigeon Corps took the first aerial photos using a camera attached to a pigeon in 1903. During the First World War, the use of aerial photography grew. Later, in 1936, Albert W. Stevens took the first photograph of the actual curvature of the earth from a free balloon at an altitude of 72,000 feet. The first space photograph from V-2 rockets was acquired in 1946. **Table 1** addresses the evolution of the remote sensing, excluding the early development stage. The table starts with the use of aerial photographs for surveying and mapping as well for military use. The milestones in this evolution (see **Table 1**) were referenced to [7, 10]. Additionally, recent developments in microsatellites and satellite constellations are also listed in **Table 1**.

Phases	Time series	Remarks
Airborne remote sensing	During the First and Second World Wars	The use of photographs for surveying, mapping, reconnaissance and military surveillance
Rudimentary spaceborne satellite remote sensing	In the late 1950s	The launch of Sputnik 1 by Russia in 1957 and Explorer 1 by US in 1958
Spy satellite remote sensing	During the Cold War (1947–1991)	Remote sensing for military use spilled over into mapping and environment applications
Meteorological satellite sensor remote sensing	1960~	The launch of the first meteorological satellite (TIROS-1) by the US in 1960. Since then, data in digital formats and the use of computer hardware and software
Landsat	1972~	Landsat 1, 2, and 3 carrying a multispectral scanner; Landsat 4 and 5 carried a Thematic Mapper sensor; Landsat 7 carries an Enhanced Thematic Mapper; Landsat 8 carries the Operational Land Imager. Landsat satellites have high resolution and global coverage. Applications were initially local and have become global since then
European Space Agency's first Earth observing satellite program	1991~	The European Space Agency launched the first satellite ERS-1 in 1991, which carried a variety of earth observation instruments: a radar altimeter, ATSR-1, SAR, wind scatterometer, and microwave radiometer. A successor, ERS-2, was launched in 1995
Earth observing system (EOS)	Since the launch of the Terra satellite in 1999	Terra/Aqua satellites carrying sensors, such as MODIS and taking measurements of pollution in the troposphere (MOPITT). Global coverage, frequent repeat coverage, a high level of processing, easy and mostly free access to data
New millennium	Around the same time as EOS	Next generation of satellites and sensors, such as Earth Observing-1, acquiring the first spaceborne hyperspectral data
Private industry/ commercial satellite systems	2000~	1. Very high-resolution data, such as IKONOS and Quickbird satellites 2. A revolutionary means of data acquisition: daily coverage of any spot on earth at a high resolution, such as Rapideye 3. Google streaming technology allows rapid data access to very high-resolution images 4. The launch of GeoEye-1 in 2008 for very high-resolution imagery (0.41 m)
Microsatellite era and satellite constellations	2008~	1. Small satellites and satellite constellation (RapidEye and Terra Bella, formerly Skybox): RapidEye was launched in August, 2008, with five EOS. These are the first commercial satellites to include the Red-Edge band, which is sensitive to changes in chlorophyll content. On March 8, 2016, Skybox imaging was renamed to Terra Bella. Satellites provided the ability to capture the first-ever commercial high-resolution video of Earth from a satellite and the ability to capture high-resolution color and near-infrared imagery 2. For the first time, Russia carried out a single mission to launch 37 satellites in June of 2014 3. ESA launched the first satellite of the Sentinel constellation in April of 2014. 4. SpaceX reusable rocket capacity since December of 2015 5. Current satellites in high revisiting period, large coverage, and high spatial resolution, up to 31 cm

Table 1. Evolution and advancement in remote sensing satellites and sensors.

3. Characteristics of materials in electromagnetic spectrum (EMS)

Remote sensors remotely interact with objects on the surface of the Earth. Objects on the surface of the Earth generally include terrain, buildings, road, vegetation, and water. The typical materials of these objects that interact with the EMS are categorized into groups: transparent and opaque (partly or fully absorbed).

3.1. Electromagnetic spectrum

Figure 1 contains the EMS range from gamma rays to radio waves. In remote sensing, typical applications include the visible light (380–780 nm), infrared (780 nm–0.1 mm), and microwave (0.1 mm–1 m) ranges. This paper treats the terahertz (0.1–1 mm) range as an independent spectral band separate from microwaves. Remote sensing sensors interact with objects remotely. Between sensors and the earth surface, there is atmosphere. It is estimated that only 67% of sunlight directly heats the Earth [11]. The remainder of the light is absorbed and reflected by the atmosphere. The Earth's atmosphere strongly absorbs infrared and UV radiation. In visible light, typical remote sensing applications include the blue (450–495 nm), green (495–570 nm), and red (620–750 nm) spectral bands for panchromatic or multispectral or hyperspectral imaging. Current bathymetric and ice LIDAR generally uses green light (e.g., NASA's HSRL-1 LIDAR, with a spectrum of 532 nm). However, new experiments have shown that in the blue spectrum, such as at 440 nm, the absorption coefficient for water is approximately an order of

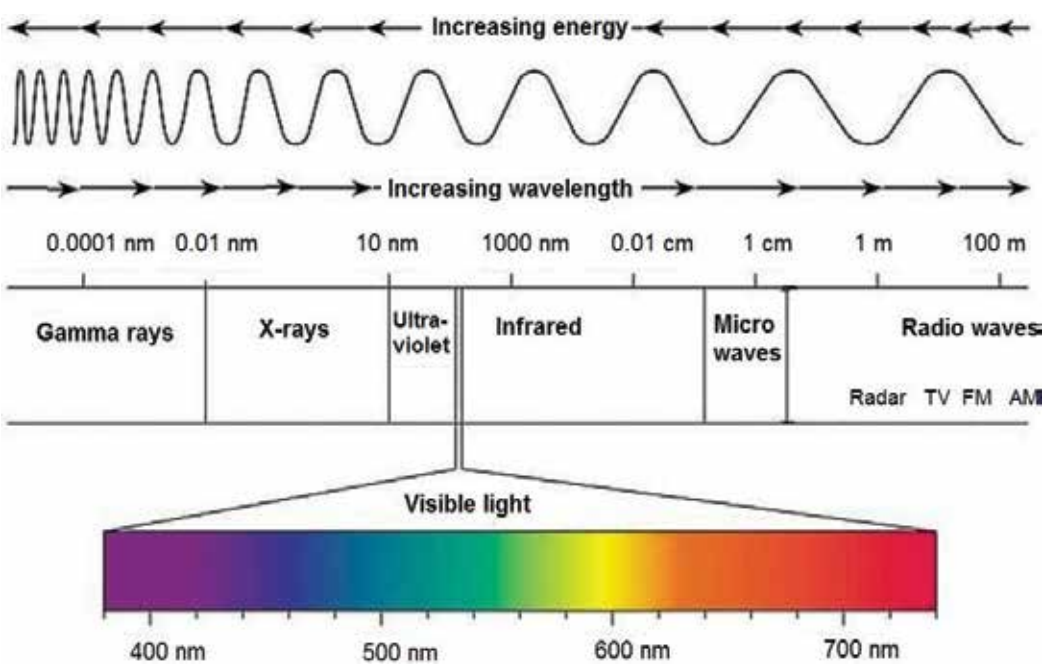

Figure 1. The electromagnetic spectrum. Image from UC Davis ChemWiki, CC-BY-NC-SA 3.0.

magnitude smaller than at 532 nm, and 420–460 nm light can penetrate relatively clear water and ice much deeper, offering substantial improvements in sensing through water for the same optical power output, thus reducing power requirements [11]. The red spectrum together with near-infrared (NIR) is typically used for vegetation applications. For example, the Normalized Difference Vegetation Index (NDVI) is used to evaluate targets that may or may not contain live green vegetation. Infrared is invisible radiant energy. Usually, infrared is divided into different regions: near IR (NIR, 0.75–1.4 μm), shortwave IR (SWIR, 1.4–3 μm), mid-IR (MIR, 3–8 μm), longwave IR (LWIR, 8–15 μm), and far IR (FIR, 15–1000 μm). Alternatively, according to the ISO 20473 scheme, another division is proposed as NIR (0.78–3 μm), MIR (3–50 μm), and FIR (50–1000 μm). Most of the infrared radiation in sunlight is in the NIR range. Most of the thermal radiation emitted by objects near room temperature is infrared [14]. In nature, on the surface of the Earth, almost all thermal radiation consists of infrared in the mid-infrared region, which is a much longer wavelength than that in sunlight. Of these natural thermal radiation processes, only lightning and natural fires are hot enough to produce much visible energy, and fires produce far more infrared than visible light energy. NIR is mainly used in medical imaging and physiological diagnostics. One typical application of MIR and FIR is thermal imaging, for example, night vision devices. In the MIR and FIR spectrum bands, water shows high absorption, and biological systems are highly transmissive.

With regard to the terahertz spectrum band, terahertz frequencies are useful for investigating biological molecules. Unlike more commonly used forms of radiated energy, this range has rarely been studied, partly because no one knew how to make these frequencies bright enough [12] and because practical applications have been impeded by the fact that ambient moisture interferes with wave transmission [13]. Nevertheless, terahertz light (also called T-rays) has remarkable properties. T-rays are safe, non-ionizing electromagnetic radiation. This light poses little or no health threat and can pass through clothing, paper, cardboard, wood, masonry, plastic, and ceramics. This light can also penetrate fog and clouds. THz radiation transmits through almost anything except for not metal and liquid (e.g., water). T-rays can be used to reveal explosives or other dangerous substances in packaging, corrugated cardboard, clothing, shoes, backpacks, and book bags. However, the technique cannot detect materials that might be concealed in body cavities [14].

The terahertz region is technically the boundary between electronics and opt-photonics [15]. The wavelengths of T-rays—shorter than microwaves, longer than infrared—correspond with biomolecular vibrations. This light can provide imaging and sensing technologies not available through conventional technologies, such as microwaves [16]. For example, T-rays can penetrate fabrics. Many common materials and living tissues are semi-transparent and have 'terahertz fingerprints', permitting them to be imaged, identified, and analyzed [17]. In addition, terahertz radiation has the unique ability to non-destructively image physical structures and perform spectroscopic analysis without any contact with valuable and delicate paintings, manuscripts, and artifacts. In addition, terahertz radiation can be utilized to measure objects that are opaque in the visible and near-infrared regions. Terahertz pulsed imaging techniques operate in much the same way as ultrasound and radar to accurately locate embedded or distant objects [18]. Current commercial terahertz instruments include Terahertz 3D medical imaging, security scanning systems, and terahertz spectroscopy. The latest breakthrough research (9.2016) on

terahertz applications was that MIT invented a terahertz camera that can read a closed book. This camera can distinguish ink from a blank region on paper. The article indicates that 'In its current form the terahertz camera can accurately calculate distance to a depth of about 20 pages' [19]. It is expected that in the future, this technology can be used to explore and catalog historical documents without actually having to touch or open them and risk damage.

Regarding microwaves, shorter microwaves are typically used in remote sensing. For example, this region is used for radar, and the wavelength is just a few inches long. Microwaves are typically used for obtaining information on the atmosphere, land, and ocean, such as Doppler radar, which is used in weather forecasts, and for gathering unique information on sea wind and wave direction, which are derived from frequency characteristics, including the Doppler effect, polarization, back scattering, that cannot be observed by visible and infrared sensors [20]. In addition, microwave energy can penetrate haze, light rain and snow, clouds, and smoke [21]. Microwave sensors work in any weather condition and at any time.

3.2. Objects and spectrum

When light encounters an object, they can interact in several different ways: transmission, reflection, and absorption. The interaction depends on the wavelength of the light and the nature of the material of the object.

Most materials exhibit all three properties when interacting with light: partly transmission, partly reflection, and partly absorption. According to the dominant optical property, we categorize objects into two typical types: transparent materials and opaque materials.

Transparent material allows light to pass through the material without being scattered or absorbed. Typical transparent objects include plate glass and clean water. **Figure 2** shows the transmission spectrum of soda-lime glass with a 2-mm thickness. Soda-lime glass is typically used in windows (also called flat glass) and glass containers. From **Figure 2**, it can be seen that soda-lime glass nearly blocks UV radiation. Nevertheless, it has high transmittance in the

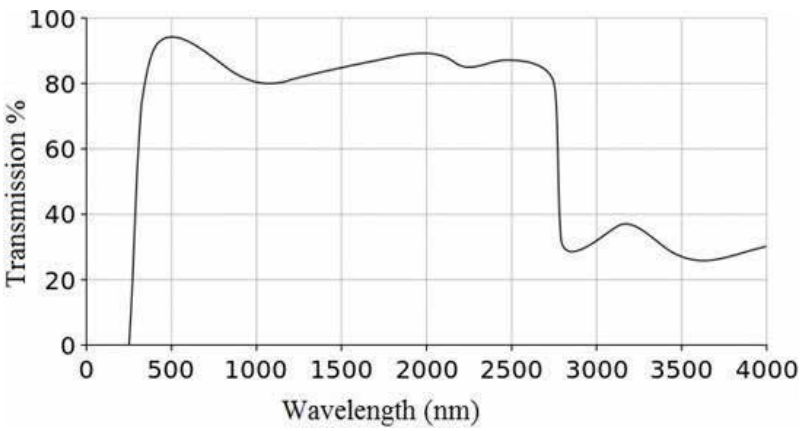

Figure 2. Transmission spectrum of soda-lime glass with a 2-mm thickness. Obtained from Wikipedia [22].

visible light and NIR wavelengths. It is easy to understand that when a laser scanner with a wavelength of 905, 1064, or 1550 nm hits a flat glass window or a glassy balcony, over 80% of the laser energy passes through the glass and hits the objects behind the window. Another typical example of transmissive material is clear water. Water transmittance is very high in the blue-green part of the spectrum but diminishes rapidly in the near-infrared wavelengths (see **Figure 3**). Absorption, on the other hand, is notably low in the shorter visible wavelengths (less than 418 nm) but increases abruptly in the range of 418–742 nm. A laser beam with a wavelength of 532 nm (green laser) is typically applied in bathymetric measurements as this wavelength has a high water transmittance. According to the Beer-Lambert law, the relation between absorbance and transmittance is as follows: Absorbance = −log (Transmittance).

Opacity occurs because of the reflection and absorption of light waves off the surface of an object. The reflectance of light depends on the material of the surface that the light encounters. There are two types of reflection: one is specular reflection and another is diffuse reflection. Specular reflection is when light from a single incoming direction is reflected in a single outgoing direction. Diffuse reflection is the reflection of light from a surface such that an incident ray is reflected at many angles rather than at just one angle, as in the case of specular reflection. Most objects have mixed reflective properties [24]. Representative reflective materials include metals, such as aluminum, gold, and silver. From **Figure 4**, it can be seen that aluminum has a high reflectivity over various wavelengths. In the visible light and NIR wavelengths, the reflectance of aluminum reaches up to 92%, while this value increases to 98% in MIR and FIR. Silver has a higher reflectance than aluminum when the wavelength is longer than 450 nm. At a

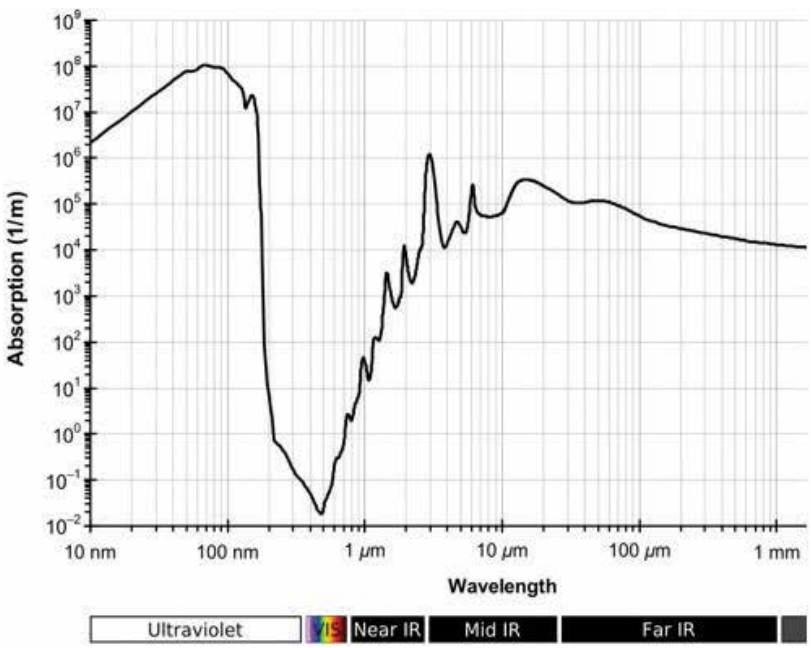

Figure 3. Liquid water absorption spectrum. Obtained from Wikipedia [23].

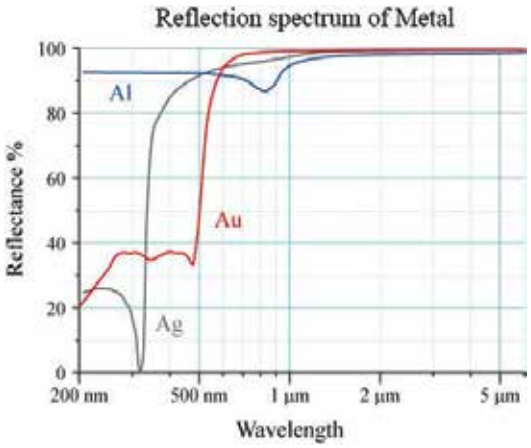

Figure 4. Reflective spectrum of metals: aluminum, gold, and silver.

wavelength of 310 nm, the reflectance of aluminum is zero [25]. The reflectance of gold significantly increases at a wavelength of approximately 500 nm, reaching a very high reflectance starting in the infrared. This figure indicates that regardless of the wavelength at which the sensor operates, it is inevitable to encounter high reflection from aluminum surfaces.

The physical characteristics of the material determine what type of electromagnetic waves will and will not pass through it. **Figure 5** shows examples of the reflection spectrums of dry bare soil, green vegetation, and clear water. The reflection of dry bare soil increase as the wavelength increases from 400 to 1800 nm. Green vegetation has a high reflectance in the red light and near-infrared regions. These characteristics have been applied for distinguishing green vegetation from other objects. In addition, the previous figure shows that water has a low absorbance in the visible light region. **Figure 5** shows that water reflects visible light at a low rate (<5%). Indirectly, the figure indicates that water has a high transmittance in the visible light range.

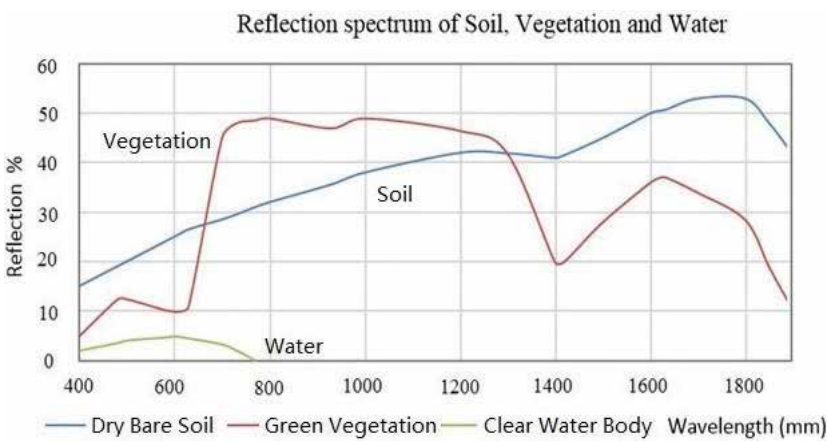

Figure 5. Examples of reflective materials. Image referenced from Wikimedia [26].

4. Spaceborne sensors

Spaceborne sensors have been developed for over 40 years. Currently, approximately 50 countries are operating remote sensing satellites [9]. There are more than 1000 remote sensing satellites available in space, and among these, approximately 593 are from the USA, over 135 are from Russia, and approximately 192 are from China [27].

Conventionally, remote sensors are divided into two groups: passive sensors and active sensors, as we described in the first section. However, as sensor technology has advanced, nothing has been absolute. For example, an imaging camera is usually regarded as a passive sensor. However, in 2013, a new approach that integrates active and passive infrared imaging capability into a single chip was developed. This sensor enables lighter, simpler dual-mode active/passive cameras with lower power dissipation [28]. Alternatively, remote sensing sensors can be classified into imaging sensors and non-imaging sensors. In terms of their spectral characteristics, the imaging sensors include optical imaging sensors, thermal imaging sensors, and radar imaging sensors. **Figure 6** illustrates the category in terms of imaging sensors and non-imaging sensors.

4.1. Optical imaging sensors

Optical imaging sensors operate in the visible and reflective IR ranges. Typical optical imaging systems on space platform include panchromatic systems, multispectral systems, and hyperspectral systems. In a panchromatic system, the sensor is a monospectral channel detector that is sensitive to radiation within a broad wavelength range. The image is black and white or gray scale. A multispectral sensor is a multichannel detector with a few spectral bands. Each channel is sensitive to radiation within a narrow wavelength band. The resulting image is a multilayer image that contains both the brightness and spectral (color) information of the targets being observed. A hyperspectral sensor collects and processes information from 10 to 100 of spectral bands. A hyperspectral image consists of a set of images. Each narrow spectral band forms an image. The resulting images can be utilized to recognize objects, identify materials, and detect elemental components. **Table 2** gives a more detailed description of

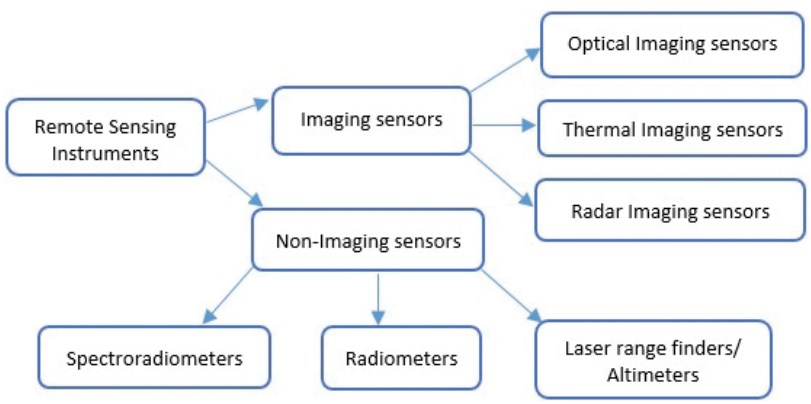

Figure 6. Spaceborne remote sensing sensors.

	Panchromatic systems	Multispectral systems	Hyperspectral systems
Spectral range (nm)	~430–720	~430–720 ~750–950	~470–2000
Satellites	QuickBird, SPOT, IKONOS	SPOT, QuickBird, IKONOS	TRW Lewis, EO-1
Spectral band	Monospectral, black and white, gray-scale image	Several spectral bands	10 to 100 of spectral bands
Spatial resolution	Submeter	Up to 1–2 m	Up to 2 m
Applications	Earth observation and reconnaissance applications	Red-green-blue (true color): visual analysis; Green-red-infrared: vegetation and camouflage detection; Blue-NIR-MIR: visualizing water depth, vegetation coverage, soil moisture content, and the presence of fires, all in a single image	(i) Agriculture; (ii) eye care; (iii) food processing; (iv) mineralogy; (v) surveillance; (vi) physics; (vii) astronomy; (viii) chemical imaging; (ix) environment
Advantages	High applicability in (i) imaging multiple targets; (ii) mosaic strips to large area; (iii) stereo and tristereo acquisition; (iv) linear feature acquisition, such as coastlines, pipelines, roads, and borders		
Disadvantages	Affected by sun illumination and cloud coverage. Polar areas with seasonal changes in sun illumination and the equatorial belt with persistent cloud coverage		

Table 2. Satellite optical imaging systems.

these optical imaging systems. It can be seen that when a light is split into multiple spectrums, the greater the number of spectrums is, the lower the imaging resolution will be. That is, a panchromatic image usually presents a higher resolution than a multispectral/hyperspectral image. Pan-sharpening technique was introduced by Padwick et al. in 2010 [29] for improving the quality of multispectral images. This method combines the visual information of the multispectral data with the spatial information of the panchromatic data, resulting in a higher resolution color product equal to the panchromatic resolution.

4.2. Thermal IR imaging sensors

A thermal sensor typically operates in the electromagnetic spectrum between the mid-to-far-infrared and microwave ranges, roughly between 9 and 14 μm. Any object with a temperature above zero can emit infrared radiation and produce a thermal image. A warm object emits more thermal energy than a cooler object. Therefore, the object becomes more visible in an image. This is especially useful in tracking a living creature, including animals and the human body, and detecting volcanos and forest fires because a thermal image is independent from the lights in a scene and is available whether it is daytime or nighttime. Commonly used thermal imaging sensors include IR imaging radiometers, imaging spectroradiometers, and IR imaging cameras. Currently, the satellite IR sensors in use include ASTER, MODIS, ASAA, and IRIS. **Table 3** lists the thermal IR sensors and their applications.

Sensor	Operational wave band	Definition	Satellites sensors	Applications
IR imaging radiometer	UV, mid-to-far-infrared, or microwave	Measures the intensity of electromagnetic radiation	ASTER	Volcanological, mineralogical, and hydrothermal studies, forest fires, glacier, limnological and climatological studies and DEM
Imaging spectroradiometer	Infrared	Measure the intensity of radiation in multiple spectrums	MODIS, ASAS, IRIS	Sea surface temperature, cloud characteristics, ocean color, vegetation, trace chemical species in the atmosphere
Infrared imaging camera	Mid-far infrared	Measure reflected energy from the surface		Volcanology, determining thunderstorm intensity, identifying fog and low clouds

Table 3. Thermal IR sensors.

4.3. Radar imaging sensors

A radar (microwave) imaging sensor is usually an active sensor, operating in an electromagnetic spectrum range of 1 mm–1 m. The sensor transmits light to the ground, and the energy is reflected from the target to the radar antenna to produce an image at microwave wavelengths. The radar moves along a flight path, and the area illuminated by the radar, or footprint, is moved along the surface in a swath. Each pixel in the radar image represents the radar backscatter for that area on the ground. A microwave instrument can operate in cloudy or foggy weather and can also penetrate sand, water, and walls. Unlike infrared data that help us identify different minerals and vegetation types from reflected sunlight, radar only shows the difference in the surface roughness and geometry and the moisture content of the ground (the complex dielectric constant). Radar and infrared sensors are complimentary instruments and are often used together to study the same types of Earth surfaces [30]. Frequently used microwave spectrum bands for remote sensing include the X-band, C-band, S-band, L-band, and P-band. Specific characteristics of each band can be found in **Table 4**.

Conventional passive microwave imaging instruments (such as cameras or imaging radiometers) provide imagery with a relatively coarse spatial resolution when compared to an optical instrument. The diffraction-limited angular resolution of a camera aperture is directly proportional to the wavelength and inversely proportional to the aperture dimension [33]. To achieve a similar spatial resolution as optical instruments, a large antenna aperture (e.g., tens of kilometers) is needed. Clearly, it is not feasible to carry such a large antenna on a space platform. SAR is an active microwave instrument that resolves the above problem. SAR utilizes the motion of the spacecraft to emulate a large antenna from the small craft itself. The longer the antenna is, the narrower the beam is. A fine ground resolution usually results from a narrow beam width. At present, a synthesized aperture can be several orders of magnitude larger than the transmitter and receiver antenna. It has become possible to produce an SAR image with a half meter of accuracy [32].

Band	Frequency (GHz)	Wavelength (cm)	Key characteristics
Ka	40–27	0.75–1.11	Usually for astronomical observations
K	27–18	1.11–1.67	Used for radar, satellite communications, astronomical observations, automotive radar
Ku	18–12	1.67–2.5	Typically used for satellite communications
X	12.5–8	2.4–3.75	Widely used for military reconnaissance, mapping and surveillance
C	4–8	3.75–7.5	Penetration capability of vegetation or solids is limited and restricted to the top layers. Useful for sea-ice surveillance
S	4–2	7.5–15	Used for medium-range meteorological applications, for example, rainfall measurement, airport surveillance
L	2–1	15–30	Penetrates vegetation to support observation applications over vegetated surfaces and for monitoring ice sheet and glacier dynamics
P	1–0.3	30–100	So far, only for research and experimental applications. Significant penetration capabilities regarding vegetation canopy, sea ice, soil, and glaciers

Referenced from Born and Wolf [31].

Table 4. Commonly used frequency and spectrum bands of radar imaging sensors.

Specifically, SAR uses microwaves to illuminate a ground target with a side-looking geometry and measures the backscatter and traveling time of the transmitted waves reflected by objects on the ground. The distance the SAR device travels over a target in the time taken for the radar pulses to return to the antenna produces the SAR image. Typically, SAR is mounted on a moving platform, such as a spaceborne or airborne platform. According to the combination of frequency bands and polarization modes used in data acquisition, SAR can be categorized into [33]:

- Single frequency (L-band, C-band, or X-band);
- Multiple frequency (Combination of two or more frequency bands);
- Single polarization (VV, HH, or HV);
- Multiple polarization (Combination of two or more polarization modes).

The main parameters of designing and operating SAR include the power of electromagnetic energy, frequency, phase, polarization, incident angle, spatial resolution, and swath width. There are different types of SAR techniques, including ultra-wideband SAR, terahertz SAR, differential interferometry (D-InSAR), and interferometric SAR (InSAR). Ultra-wideband SAR utilizes a very wide range of frequencies of radio waves. This method results in a better resolution and more spectral information on target reflectivity. Therefore, this approach can be applied for scanning a smaller object or a closer area. Terahertz radiation works in the spectral range from 0.3 to 10 THz, typically between infrared and microwave. Typical characteristics of this wavelength range include its transmission through plastics, ceramics, and even papers. Terahertz radiation is extraordinarily sensitive to water content. If the material has even a small

amount of water content, it will be fairly absorptive to terahertz light. Therefore, this radiation can be applied in detecting lake shores or coastlines. InSAR, also called interferometric SAR, is a technique that produces measurements from two or more SAR images. This technique is widely applied in DEM production and monitoring glaciers, earthquakes, and volcanic eruptions [34]. D-InSAR requires taking at least two images with the addition of a DEM. The DEM can be acquired from GPS measurements. This method is mainly used for monitoring subsidence movements, slope stability analysis, landslides, glacier movement, and 3D ground movement [35]. Doppler radar is used to acquire a distant object's velocity relative to the radar. The main applications of this technique include aviation, sounding satellites, and meteorology. In general, SAR can reach a spatial resolution on the order of a millimeter.

Sensor	Operational wave band	Definition	Application
Radiometer	Ultraviolet, IR, microwave	To measure the amount of electromagnetic energy present within a specific wavelength range	Calculating various surface and atmospheric parameters
Altimeter	IR, microwave/ radiowave, sonic	To measure the altitude of an object above a fixed level	Mapping ocean-surface topography and the hills and valleys of the sea surface
Spectrometer	Visible, IR, microwave	To measure the spectral content of the incident electromagnetic radiation	Multispectral and hyperspectral imaging
Spectro-radiometer	Visible, IR, microwave	To measure the intensity of radiation in multiple spectrums	Monitoring sea surface temperature, cloud characteristics, ocean color, vegetation, trace chemical species in the atmosphere
LIDAR	Ultraviolet, visible, NIR	To measure distance and intensity	Ocean, land, 3D topographic mapping
		Doppler LIDAR: measure the wave number for speed; Polarization effects of LIDAR: shape	Meteorology, cloud measurements, wind profiling and air quality monitoring
Sonar	Acoustic	Measure the distance to an object; determine the depth of water beneath ships and boats	Navigation, communication and security (e.g., vessels) and underwater object detection. For example, handheld sonar for a diver
Sodar	Acoustic	As a wind profiler, sodar systems measure wind speeds at various heights above the ground and the thermodynamic structure of the lower layer of the atmosphere	Meteorology: atmospheric research, wind monitoring (typically in a range from 50 to 200 m above ground level)
A radio acoustic sounding system (RASS)	Radio wave and acoustic wave	Measuring the atmospheric lapse rate using backscattering of radio waves from an acoustic wave front to measure the speed of sound at various heights above the ground	Is added to a radar wind profiler or to a sodar system

Table 5. Non-imaging sensors.

4.4. Non-imaging sensors

A non-imaging sensor measures a signal based on the intensity of the whole field of view, mainly as a profile recorder. In contrast with imaging sensors, this type of sensor does not record how the input varies across the field of view. In the remote sensing field, the commonly used non-imaging sensors include radiometers, altimeters, spectrometers, spectroradiometers, and LIDAR. **Table 5** provides detailed information about conventional non-imaging sensors. In the remote sensing field, non-imaging sensors typically work in the visible, IR, and microwave spectral bands. The applications for non-imaging sensors mainly focus on height, temperature, wind speed, and other atmospheric parameter measurements.

Lasers have been applied in measuring the distance and height of targets in the remote sensing field. We generally call a laser scanning system as LIDAR (light detection and ranging) system. Satellite LIDAR, airborne LIDAR, mobile mapping LIDAR, and terrestrial LIDAR are different carrier platforms. Laser sources include solid-state lasers, liquid lasers, gas lasers, semiconductor lasers, and chemical lasers (see **Table 6**). Typical laser sources for laser rangefinders and laser altimeters include semiconductor laser and solid-state lasers. Semiconductor lasers typically produce light sources at wavelengths of 400–500 nm and 850–1500 nm. Solid-state lasers generate light at wavelengths of 700–820 nm, 1064 nm, and 2000 nm. Satellite or airborne LIDAR systems are typically operated at wavelengths of 905 , 1064 and 1550 nm. One of the main considerations for wavelength selection is the atmospheric transmission between the sensor and the surface of the Earth. Lower transmittance at a given wavelength means less solar radiation at that wavelength. The transmittance at 905 nm is approximately 0.6, while the wavelengths of 1064 and 1550 nm have similar transmittances of approximately 0.85. In addition, wavelength selection can also be a cost issue. Diode lasers at 905 nm are inexpensive compared to Nd:YAG solid-state lasers at 1064 nm and diode lasers at 1550 nm. In 2007, the cost of diode lasers at 1550 nm was 2.5 times higher than lasers at 905 nm. However, the wavelength

Laser types	Pump source	Typical applications
Gas laser	Electrical discharge	Interferometry, holography, spectroscopy, material processing
Chemical laser	Chemical reaction	Military use
Dye laser	Other laser, flashlamp	Research, laser medicine
Metal-vapor laser	Electrical discharge	Printing and typesetting applications, fluorescence excitation examination, scientific research
Solid-state laser	Flashlamp, laser diode, Fiber laser, Nd: YAG.	Material processing, rangefinding, laser target designation
Semiconductor laser	Electrical current	Telecommunications, holography, printing, weapons, machining

Table 6. Typical laser sources.

Name	wavelength (nm)	Laser sources	Typical applications
UV laser	355	Gas laser	Cutting and drilling
Violet laser	405	Semiconductor laser or solid-state laser	Laser printing, data recording, laser microscopy, laser projection displays, spectroscopic measurements
Blue laser	488	Solid-state laser	Environmental monitoring, medical diagnostics, handheld projectors and displays, telecommunications
Green laser	532	Solid-state laser (Nd:YAG)	Bathymetric measurement
Red laser	640	Semiconductor laser	Vegetation measurement
NIR laser	1064	Semiconductor laser or solid-state laser (fiber laser)	Airborne laser scanning
NIR laser	1550	Semiconductor laser or solid-state laser (fiber laser)	Airborne laser scanning

Referenced from Hey [36].

Table 7. Commonly used laser wavelength.

of 1550 nm is a good candidate for use in invisible wavelength eye-safe LIDAR. The higher absorption of 1550 nm light by water makes it eye safe, and this absorption is approximately 175 times greater than that of 905 nm light. In addition, the solar background level of light at 1550 nm is approximately 50% lower than that of light at 905 nm. Making measurements at 1550 nm also results in a higher signal to noise ratio compared to using a beam at 905 nm. All in all, when ignoring the cost issue, a wavelength of 1550 nm has a clear advantage over light at 905 nm [36].

In general, at a wavelength of 1064 nm, vegetation has stronger reflectance than soil, while at a wavelength of 1550 nm, soil shows greater a reflectance than vegetation. Taking measurements with different wavelengths is beneficial for object classification. Green lasers with a wavelength of 532 nm are usually pumped by a solid-state laser (Nd:YAG). This type of laser is widely used for bathymetric measurement. **Table 7** lists the typical applications of different laser light wavelengths.

4.5. Commonly used remote sensing satellites

So far, more than 1000 remote sensing satellites have been launched. These satellites have been updated with new generation satellites. The few spectral sensors from the earliest missions have been upgraded to hyperspectral sensors with hundreds of spectral bands. The spatial and spectral resolutions have been improved on the order of 100-fold. Revisit times have been shortened from months to daily. In addition, more and more remote sensing data are available as open data sources. **Table 8** gives an overview of the commonly used remote sensing satellites and their parameters.

Mission	Country	Launch year	Sensors	Height of orbit (km)	Swath (km)	Revisit (day)	Channels	Spatial resolution
Landsat	USA	1972, 1975, 1978,1982, 1984,1993, 1999,2013, 2020	Panchromatic and multispectral sensor	705	185, 183	16	7–11	120 m, 100 m, 60 m, 30 m, 15 m
SPOT	USA	1986, 1990, 1993, 1998, 2002, 2012	Imaging spectroradiometer	694	60	1–3	Panchromatic, B, G, R, NIR	2.5 m, 5 m, 10 m, 20 m
ERS	ESA	1991, 1995	IR radiometer, microwave sounder, Radiometer, SAR	782–785	5–100 km (AMI) - 500 km (ATSR)	3, 35, 336	SAR	26 m across track and 6–30 m along track
RADARSAT	Canada	1995, 2007, 2018	SAR	793–821, 798, 592.7	45–100, 18–500, 5–500	1	SAR	8–100 m, 3–100 m, 3–100 m
MODIS	USA	1999, 2002	Imaging spectroradiometer	705	2330	1	36	1000 m, 500 m, 250 m
IKONOS	USA	1999	Imaging spectroradiometer	681	11.3	3	Panchromatic, B, G, R, NIR	Panchromatic:80 cm B, G, R, NIR:3.2 m
QuickBird	USA	2000, 2001	Imaging spectroradiometer	482, 450	16.8–18	2.4–5.9	Panchromatic, B, G, R, NIR	Panchromatic:65 cm/61 cm B, G, R, NIR:2.62 m/2.44 m
Envisat	ESA	2002	ASAR, MERIS, AATSR, RA-2, MWR, GOMOS, MIPAS, SCIAMACHY, DORIS, LRR	790	1150 km, 100 km, 400 km	35 days	15 bands (VIS, NIR), C-band	300 m, 30–150 m
GeoEye	USA	2008	Imaging spectroradiometer	681	15.2	8.3	Panchromatic, B, G, R, NIR	Panchromatic:41 cm B, G, R, NIR: 1.65 m

Mission	Country	Launch year	Sensors	Height of orbit (km)	Swath (km)	Revisit (day)	Channels	Spatial resolution
WorldView	USA	2007 2009 2014 2016.9	Imaging spectroradiometer, Laser altimeter	496, 770, 617, 681	17.6 km 16.4 km 13.1 km 14.5 km	1.7 1.1 <1 3	Panchromatic; Panchromatic and eight multispectrum; Panchromatic and eight multispectrum; Panchromatic, B, G, R, NIR	Panchromatic 0.5 m; Panchromatic and stereo images:0.46 m multispectral: 1.84 m; Panchromatic 0.34 m and multispectral 1.36 m
Sentinel 1–6	ESA	2014, 2015, 2016, 2017, 2021	Radar and super-spectral imaging	693, 786, 814	250 km 290 km, 250 km,	12, 10, 27	C-SAR, 12 bands (VIS, NIR, SWIR), 21 bands (VIS, NIR), S-band & X-band	5–20 m, 5–40 m, 10 m & 20 m & 60 m

Referenced from Refs. [37–40].

Table 8. Remote sensing satellites.

http://dx.doi.org/10.5772/intechopen.71049

5. Future and discussions

A common expectation from the remote sensing community is the ability to acquire data at high resolutions (spatial, spectral, radiometric, and temporal), at low cost, with open resource support and for the creation of new applications by the integration of spatial/aerial and ground-based sensors.

The development of smaller, cheaper satellite technologies in recent years has led many companies to explore new ways of using low Earth orbit satellites. Many companies have focused on remote imaging, for example, to gather optical or infrared imagery. In the future, a low-cost communications network between low Earth orbit satellites can be established to form a spatial remote sensing network. This network would integrate with a large number of distributed ground sensors to establish ground-space remote sensing. In addition, satellites can easily cover large swaths of territory, thereby supplementing ground-based platforms. Thus, data distribution and sharing would become very easy.

Openness and sharing resources can promote the utilization of remote sensing and maximize its output. In recent years, open remote sensing resources have made great progress. Beginning on April 1, 2016, all Earth imagery from a widely used Japanese remote sensing instrument operating aboard NASA's Terra spacecraft since late 1999 has been available to users everywhere at no cost [41]. On April 8, 2016, ESA announced that an amazing 40-cm resolution WorldView-2 European cities dataset would be available for download through the Lite Dissemination Server. These data are made available free of charge. This dataset was collected by ESA, in collaboration with European Space Imaging, over the most populated areas in Europe at 40-cm resolution. These data products were acquired between February 2011 and October 2013. The dataset is available to ESA member states (including Canada) and European Union Member states [42]. In open remote sensing resources, NASA (USA) was a pioneer in sharing its imagery data. NASA has been cooperating with the open source community, and many NASA projects are also open source. NASA has also set up a special website to present these projects. In addition, some commercial companies like DigiGlobal (USA) have also partly opened their data to the public. In the future, more and more open resources will become available.

Future applications in remote sensing will combine the available resources from space/aerial/UAV platforms with ground-based data. The prerequisites of such resource integration are as follows: (i) the spatial resolution of satellite data is high enough to match ground-based data; for example, both spatial data and ground data are in the same order of accuracy. WorldView-3 has achieved a 30-cm spatial resolution, which is comparable with ground-based sub-centimeter data accuracy (e.g., 2 cm in mobile laser point cloud); (ii) cloud-based calculation supports big datasets from crowd-sourced remote sensing resources. The current situation shows promising support for the integration of multiple sources of remote sensing data. We expect to see new applications developing in the coming years.

6. Conclusions

This paper investigated remote sensing sensor technology both broadly and in depth. First, we reviewed some fundamental knowledge about the electromagnetic spectrum and the interaction of objects and the spectrum. It helps to understand that when a sensor is operated in a certain wavelength how environmental objects will react to it. In addition, we also highlighted the terahertz region of the spectrum. Since little research has been done on this range, in the future, research efforts on new applications of terahertz radiation may be worth exploring. On the interaction of sensors with the environment, typical examples in glass, metal, water, soil, and vegetation were provided. Remote sensors were presented in terms of imaging sensors and non-imaging sensors. Optical imaging sensors and thermal imaging sensors, radar imaging sensors, and laser scanning were highlighted. In addition, commonly used remote sensing satellites, especially those from NASA and ESA, were detailed in terms of launched time, sensors, swath width, spectrum bands, revisit time and spatial resolution.

Acknowledgements

We would like to thank TEKES for its funding support in the project of COMBAT and also the financial support from EU project 6Aika.

Author details

Lingli Zhu[1]*, Juha Suomalainen[1], Jingbin Liu[1,3], Juha Hyyppä[1], Harri Kaartinen[1] and Henrik Haggren[2]

*Address all correspondence to: lingli.zhu@nls.fi

1 Finnish Geospatial Research Institute FGI, National Land Survey of Finland, Masala, Finland

2 Aalto University School of Engineering, Aalto, Finland

3 Wuhan University, Wuhan, China

References

[1] Space. Record-Setting Rocket Launch on Nov. 19: The 29 Satellites [Internet]. 2013. Available from: http://www.space.com/23646-ors3-rocket-launch-satellites-description.html [Accessed: Feb 27, 2017]

[2] Microimages. Introduction to RSE [Internet]. 2012. Available from: http://www.microimages.com/documentation/Tutorials/introrse.pdf [Accessed: Feb 27, 2017]

[3] NASA. Earth Satellite Orbits [Internet]. 2012. Available from: http://earthobservatory.nasa.gov/Features/OrbitsCatalog/page2.php [Accessed: Mar 2, 2017]

[4] NASA. Passive Sensors [Internet]. 2012. Available from: https://www.nasa.gov/directorates/heo/scan/communications/outreach/funfacts/txt_passive_active.html [Accessed: Mar 3, 2017]

[5] Earth Imaging Journal Exploring the Benefits of Active Vs. Passive Spaceborne Systems [Internet]. 2013. Available from: http://eijournal.com/print/articles/exploring-the-benefits-of-active-vs-passive-spaceborne-systems [Accessed: Mar 8, 2017]

[6] Japan Association of Remote Sensing. Sensors [Internet]. 2010. Available from: http://www.jars1974.net/pdf/03_Chapter02.pdf [Accessed: Mar 20, 2017]

[7] Blais F. Review of 20 years of range sensor development. Journal of Electronic Imaging. 2004;**13**(1):231-240

[8] Melesse AM, Weng Q, Thenkabail PS, Senay GB. Remote sensing sensors and applications in environmental resources mapping and modelling. Sensors. 2007;**7**(12):3209-3241

[9] Toth C, Jóźków G. Remote sensing platforms and sensors: A survey. ISPRS Journal of Photogrammetry and Remote Sensing. 2016;**115**(May):22-36

[10] Barry Rice. A Brief History of Remote Sensing [Internet]. 2008. Available from: http://www.sarracenia.com/astronomy/remotesensing/primer0120.html [Accessed: Mar 28, 2017]

[11] An Introduction to Solar System Astronomy. The Earth's Atmosphere [Internet]. 2007. Available from: http://www.astronomy.ohio-state.edu/~pogge/Ast161/Unit5/atmos.html [Accessed: Mar 30, 2017]

[12] TechPort. New Technology Reports: Available from: techport.nasa.gov [Accessed: Mar 30, 2017]

[13] Wikipedia. Infrared [Internet]. 2008. Available from: https://en.wikipedia.org/wiki/Infrared [Accessed: Mar 30, 2017]

[14] Lightsources. Terahertz Radiation or T-Rays [Internet]. 2010. http://www.lightsources.org/terahertz-radiation-or-t-rays [Accessed: Apr 3, 2017]

[15] PHYS. A Revolutionary Breakthrough in Terahertz Remote Sensing [Internet]. 2010. Available from: http://phys.org/news/2010-07-revolutionary-breakthrough-terahertz-remote.html#jCp [Accessed: Apr 4, 2017]

[16] KASAI Y. Introduction to terahertz-wave remote sensing. Journal of the National Institute of Information and Communications Technology. 2008;**55**(1):65-67

[17] Amir F. (2011). Advanced Physical Modelling of Step Graded Gunn Diode for High Power TeraHertz Sources. [thesis].

[18] Wagh MP, Sonawane YH, Joshi OU. Terahertz technology: A boon to tablet analysis. Indian Journal of Pharmaceutical Sciences. 2009;**71**(3):235

[19] GIZMODO. MIT Invented a Camera that can Read Closed Books [Internet]. 2016. Available from: http://gizmodo.com/mit-invented-a-camera-that-can-read-closed-books-1786522492 [Accessed: Apr 10, 2017]

[20] Japan Association of Remote Sensing. Chapter 3 Microwave Remote Sensing [Internet]. 2010. Available from: http://wtlab.iis.u-tokyo.ac.jp/~wataru/lecture/rsgis/rsnote/cp3/cp3-1.htm [Accessed: Apr 18, 2017]

[21] NASA. Microwaves [Internet]. 2011. Available from: http://science.hq.nasa.gov/kids/imagers/ems/micro.html [Accessed: Apr 18, 2017]

[22] Wikipedia. Soda-Lime Glass [Internet]. 2010. Available from: https://en.wikipedia.org/wiki/Soda-lime_glass [Accessed: Apr 20, 2017]

[23] Wikipedia. Electromagnetic_Absorption_by_Water [Internet]. 2017. Available from: https://en.wikipedia.org/wiki/Electromagnetic_absorption_by_water [Accessed: Apr 20, 2017]

[24] Wikipedia. Specular_Reflection [Internet]. 2017. Available from: https://en.wikipedia.org/wiki/Specular_reflection [Accessed: Apr 20, 2017]

[25] More RM, editor. Laser Interactions with Atoms, Solids and Plasmas. Vol. 327. Springer Science & Business Media. Berlin/Heidelberg, Germany; 2013

[26] Wikimedia. File: Image-Metal-Reflectance.png [Internet]. 2010. Available from: https://commons.wikimedia.org/w/index.php?curid=1729695 [Accessed: Apr 21, 2017]

[27] UCSUSA. UCS Satellite Database [Internet]. 2017. Available from: http://www.ucsusa.org/nuclear-weapons/space-weapons/satellite-database#.WagRxrIjGpo [Accessed: Aug 25, 2017]

[28] Photonics. Active and Passive Modes in one IR Camera [Internet]. 2013. Available from: http://www.photonics.com/Article.aspx?AID=52832 [Accessed: Apr 21, 2017]

[29] Padwick C, Deskevich M, Pacifici F, Smallwood, S, 2010. Worldview-2 Pan-Sharpening. ASPRS 2010 Annual Conference, San Diego, California, April 26-30, 2010

[30] Earth Imaging Journal. Radar [Internet]. 2012. Available from: http://eijournal.com/wp-content/uploads/2012/10/radar_table2.jpg [Accessed: Apr 27, 2017]

[31] Born M, Wolf E. (1980). Principles of Optics: Electromagnetic Theory of Propagation, Interference and Diffraction of Light. Sixth Edition. Copyright © 1980 Elsevier Ltd., Pergamon, ISBN: 978-0-08-026482-0. pp 836

[32] Jackson CR, Apel JR. Synthetic Aperture Radar: Marine user's Manual. US Department of Commerce, National Oceanic and Atmospheric Administration, National Environmental Satellite, Data, and Information Serve, Office of Research and Applications; Washington, D. C.; 2004. p. 1-7

[33] Natural Resources Canada. Polarization in Radar Systems [Internet]. 2010. Available from: http://www.nrcan.gc.ca/earth-sciences/geomatics/satellite-imagery-air-photos/satellite-imagery-products/educational-resources/9567 [Accessed: Apr 28, 2017]

[34] Wikipedia. Synthetic Aperture Radar [Internet]. 2010. Available from: https://en.wikipedia.org/wiki/Synthetic_aperture_radar [Accessed: May 5, 2017]

[35] Permanet. Differential Interferometry Synthetic Aperture Radar (DInSAR) [Internet]. 2010. Available from: http://www.permanet-alpinespace.eu/archive/pdf/WP6_1_dinsar.pdf [Accessed: May 9, 2017]

[36] Hey JDV. A novel LIDAR ceilometer: Design, implementation and characterisation. In: Weber SM, editor. Handbook of Laser Wavelengths. CRC Press, Florida, United States; 2014, 1998. p. 784 ISBN 9780849335082

[37] Wikipedia. Remote Sensing Satellite and Data Overview [Internet]. 2017. Available from: https://en.wikipedia.org/wiki/Remote_sensing_satellite_and_data_overview [Accessed: May 11, 2017]

[38] NASA. Missions [Internet]. 2010. Available from: http://www.nasa.gov/missions [Accessed: May 16, 2017]

[39] ESA. Latest Mission Operations News [Internet]. 2017. Available from: https://earth.esa.int/web/guest/missions/esa-operational-eo-missions/ers [Accessed: May 16, 2017]

[40] ESA. Sentinel [Internet]. 2016. Available from: https://sentinel.esa.int/web/sentinel/home [Accessed: May 16, 2017]

[41] Jet Propulsion Laboratory. NASA, Japan Make ASTER Earth Data Available at no Cost [Internet]. 2016. Available from: http://www.jpl.nasa.gov/news/news.php?feature=6253 [Accessed: May 18, 2017]

[42] ESA. WorldView-2 European Cities Dataset 40cm Resolution [Internet]. 2016. Available from: https://earth.esa.int/web/guest/content/-/article/worldview-2-european-cities-dataset-40cm-resolution [Accessed: May 18, 2017]

Section 2

Diversity Forms of Satellite and Satellite Data Applications

Chapter 3

Validation and Quality Assessment of Sea Levels from SARAL/AltiKa Satellite Altimetry over the Marginal Seas at the Southeast Asia

Noor Nabilah Abdullah and Nurul Hazrina Idris

Additional information is available at the end of the chapter

http://dx.doi.org/10.5772/intechopen.74399

Abstract

In this study, high resolution (40 Hz) sea levels derived from the advanced SARAL/AltiKa satellite altimetry are validated over the Southeast Asia coastal regions. The parameter of sea level is derived based on three standard retracking algorithms of MLE-4, Ice-1, and Ice-2. The assessments of quantity and quality of the retracked sea levels are conducted to identify the optimum retracker over the study regions, which are the Andaman Sea, the Strait of Malacca, the South China Sea, the Gulf of Thailand, and the Sulu Sea. The quantitative analysis involves the computation of percentage of data availability and the minimum distance of sea level anomaly (SLA) to the coastline. The qualitative analysis involves the absolute validation with tide gauge. In general, AltiKa measurement can get as close as ~1 km to the coastline with ≥85% data availability. The Ice-1 retracker has shown an excellent performance with percentage of data availability ≥90% and minimum distance as close as 0.9 km to the coastline. In term of quality of the data, 3 out of 6 validation site show that Ice-1 retracker is superior than the other retracker with temporal correlation up to 0.89 and RMS error up to 8 cm.

Keywords: SARAL/AltiKa, coastal sea level, validation, retracking, Southeast Asia

1. Introduction

Satellite altimeter occupies the radar technology at vertical incidence. It measures the two-way travel time of pulses, which corresponds to the distance between the satellite and the ocean surface. The time between the transmission of the pulses to the reception of the reflected echoes is proportional to the satellite's orbital height. Through the magnitude and shape of

the echoes (or waveform), geophysical information about the ocean surfaces (i.e., sea level, wave height, and wind speed) can be retrieved (**Figure 1**).

There are two types of radar altimetry: pulse-limited and beam-limited. The pulse-limited altimeter dictates the shape of returning signals by the length (width) of the pulse; meanwhile, the beam-limited dictates the shape of returning signals by the width of the beam (cf. [1]). The technology of pulse-limited altimeter has been used over the past 30 years, on-board of various altimetry missions such as ERS series, Jason series, and SARAL/AltiKa. Contrary, the beam-limited altimeter is considered as an advanced technology, which carries delay-Doppler altimeter instrument on-board of Cryosat-2 and Sentinel 3A satellites. With the advanced technology, the improvement can be seen in terms of the along-track spatial resolution, the noise ratio, and the sensitivity rate to the sea states [1].

The altimetry data have been beneficial for measuring ocean geophysical parameters, particularly the sea levels. They have been embedded in several ocean modeling systems such as the Australian national coastal modeling hindcast/forecast systems (e.g., BLUElink), and Regional Ocean Modeling System in Alaska, the United States of America. The altimetry can provide highly accurate sea level measurement (in cm level) over the open ocean due to proper modeling of ocean state qualities (e.g., tides) and accurate measurement of atmospheric refractions [2]. The altimetry is capable of providing accurate information of ocean properties up to 4 cm in height measurements [3, 4] and 2–3 cm in mean sea level variations [5].

However, in coastal regions, altimetry and its applications face many challenges (e.g., [2, 6–9]) due to various reasons. The accuracy of measurements decreases abruptly as the altimeter approaches the coast, where the sea conditions can diverge drastically over time and space. In addition, the altimetric waveforms within a footprint are usually corrupted by land, resulting in complicated ocean signals.

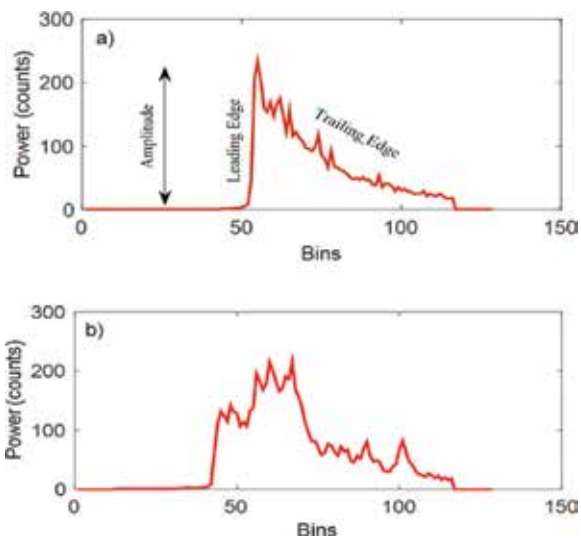

Figure 1. Examples of returned waveforms. (a) Brown-shaped waveform over homogeneous ocean surface. (b) Non-brown waveform over complex coastal area.

http://dx.doi.org/10.5772/intechopen.74399

Figure 1 shows the altimetric waveforms over the open and coastal oceans. The waveform shape over the open ocean (**Figure 1a**) follows the Brown [10] model. It features a sharp increase of leading edge, following a decreasing plateau. From the shape, several ocean parameters can be deduced. The parameter of wind speed can be deduced from the waveform amplitude, the sea level from the mid-point of leading edge, and the significant wave height from the slope of leading edge. Satellite instrumentation parameters can also be deduced: thermal noise and antenna mispointing angle (based on the slope of trailing edge). In **Figure 1b**, the land impact is clearly seen in the waveform, which features high amplitude on the waveform trailing edge. In case of corrupted waveforms, the processor tracker on-board of the satellite cannot properly determine the ocean parameters. Therefore, an efficient signal post-processing called as "the retracking" should be performed on the ground to optimize the accuracy of the estimation [8]. This is because the leading edge of waveform deviates from the on-board tracking gate [8], thus reducing the accuracy of measurements.

Waveform retracking can be conducted based on the physical (e.g., MLE4, OCE3, and Red3) or empirical (e.g., Ice1 and Offset Centre of Gravity (OCOG)) retrackers. The former fits the waveforms to an ocean surface model (e.g., [10]) to retrieve the optimized parameters (e.g., [10–13, 14]), and the latter retrieves the parameters based on the empirical assumption about the signals (e.g., [15, 16]).

Due to the low quality of altimeter geophysical retrieval over coastal oceans, data are usually systematically flagged and rejected. The coastal water is poorly observed, particularly within ~10 km of the shoreline [17, 18]. The no data gaps over coastal regions have been improved with the advanced altimetric technology such as AltiKa and Sentinel 3A altimetry mission. The AltiKa satellite operates with a Ka-band (~35.8 GHz) frequency signal. It produces a finer spatial resolution when compared to Ku-band (~13.5 GHz). With the smaller size footprint (~8 km in diameter compared to 20 km for Jason-2 and 15 km for Envisat) [19] and higher spatial resolution along the satellite track (40 Hz, compared to 20 Hz for Jason-2), the AltiKa can bring measurements closer to the coastline and produces excellent data coverage (~99%) [20, 21].

This chapter provides a necessary step to derive accurate sea level anomaly (SLA) from AltiKa satellite altimetry. The framework developed in this chapter should enable the derivation of accurate sea levels over the Southeast Asia regions. The launched of the AltiKa satellite mission promises a significant refinement of coastal altimetry, with advanced instruments, an improved retracking algorithm, and geophysical corrections [7, 19, 20, 22, 23]. The validation and calibration of the satellite mission are compulsory to find the level of confidence on the data quality before it can be used in any applications. Global calibrations for AltiKa have been conducted by Centre National d'Etudes Spatiales (CNES), Indian Space Research Organization (ISRO), and many other researchers (e.g., [5, 19, 20, 24, 25]). However, limited research focuses on the regional validation over the Southeast Asia (e.g., [24, 26–29]). The regional validation is important because the ocean characteristics of the region are significantly different than the other oceans, such as the Pacific and Atlantic Ocean. It is characterized by marginal and semi-closed oceans that contain many small islands and a broad range of topographic features, thus producing complicated waveform patterns when they enter the altimeter footprints. Therefore, this study is conducted to quantify the quality of sea levels derived from the AltiKa over the Southeast Asia region.

This chapter presents the quality assessment, and the validation of AltiKa sea levels against tide gauges over the Southeast Asia coastal region. The quality assessment identifies how close the data can get to the coastline and how much data can be recovered through three retracking algorithms (i.e., MLE-4, Ice-1, and Ice-2) [30–32] Southeast. It is noted that the three retracking algorithms are the standard retrackers available from the Sensor Geophysical Data Records (SGDR). The assessments are conducted by computing: (1) the percentage of data availability over the Southeast coastal region; (2) the minimum distance of the AltiKa retracked sea level data to the coastline; and (3) the root mean square (RMS) error and temporal correlation of the retracked sea levels with tide gauges.

Section 2 presents the data description and processing procedures involved in the quality assessment and validation; Section 3 reports on the data qualitative assessment, which includes both the percentage of data availability and the minimum distance of sea level to the coastline; Section 4 reports on the validation of retracked sea levels against the tide gauge; and Section 5 concludes the chapter.

2. Data description and processing procedures

The experimental region encompasses the Southeast Asia, which comprises of the Andaman Sea, the Strait of Malacca, the Gulf of Thailand, the South China Sea, and the Sulu Sea (**Figure 2**). It covers an area of about 20°N–5°S and 95°E–126°E.

The data utilized in this study are acquired from several agencies. The altimeter data are available at the Archiving, Validation and Interpretation of Satellite Oceanographic Data (AVISO) ftp site (ftp://avisoftp.cnes.fr). SGDR product, which comprises of 40 Hz of data from cycles 1 to 19 (April 2013–December 2014), are utilized. Hourly tide gauge measurements are supplied by the Department of Survey and Mapping Malaysia (DSMM) and the University of Hawaii Sea Level Centre (UHSLC); https://uhslc.soest.hawaii.edu). There are six tide gauge stations used in this study, which are Geting, Langkawi, Bintulu, Lubang, Ko Taphao Noi, and Vung Tau (**Figure 2**). The hourly tide gauge data are acquired from March 2013 to December 2014.

For altimeter data, two processing steps are involved in the derivation of sea level: (1) by applying the range correction and (2) by correcting the impact of atmosphere and ocean geophysical. The range corrections are obtained from MLE-4, Ice-1, and Ice-2 retracking algorithms. The MLE-4 and Ice-2 algorithms are based on the theoretical model of scattering surface of Brown [10], and Ice-1 is the empirical method of the OCOG [15]. The geophysical amendments correct the SLAs by isolating the ocean dynamic height contributors of ocean tides, atmospheric refraction, and atmospheric pressure loading such as sea state bias (SSB) and inverse barometer.

The SLA from AltiKa is derived from Eq. (1) [33];

$$SLA = H - \left(R_{obs} - R_{retracked} - \Delta R_{wet} - \Delta R_{dry} - \Delta R_{iono} - \Delta R_{ssb} - mssh\right) - h_{ot} - h_{solid} - h_{pole} - h_{load} - h_{iny} - h_{hf} \quad (1)$$

http://dx.doi.org/10.5772/intechopen.74399

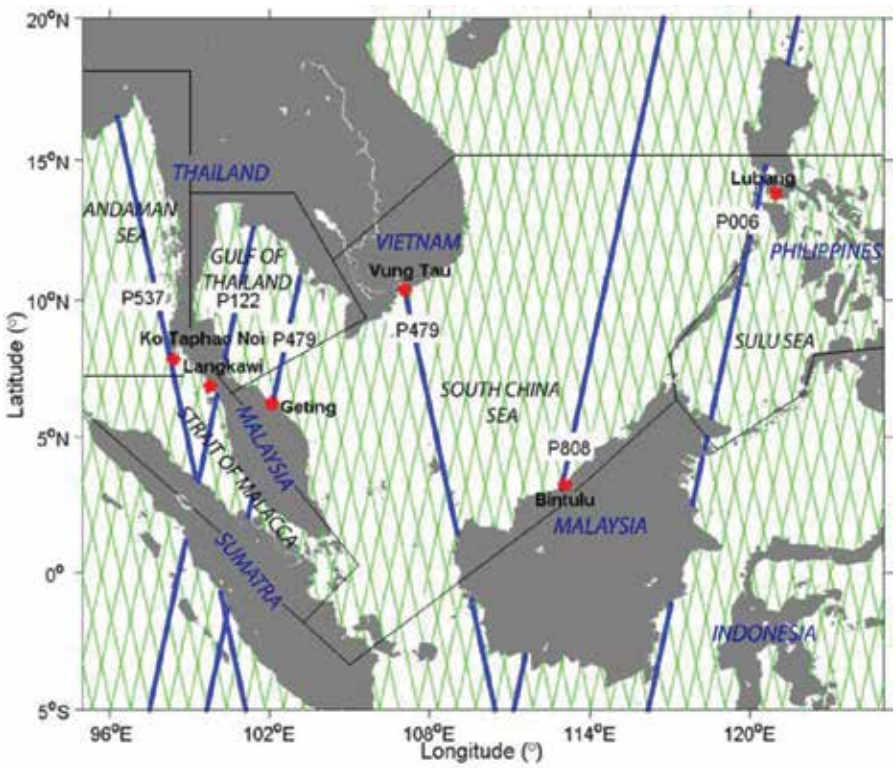

Figure 2. The region of the study area. Red marks indicate the tide gauge stations and green lines indicate the AltiKa ground passes. The blue lines are the AltiKa ground passes used for validation with tide gauge.

where H is satellite altitude, R_{obs} is the observed range, $R_{retracked}$ is the range corrections from the retracking algorithm (i.e., MLE-4, Ice-1 and Ice-2), R_{dry} and R_{wet} are dry and wet tropospheric corrections, R_{iono} is ionospheric correction, R_{ssb} is sea state bias correction, $mssh$ is mean sea surface height, h_{ot} is ocean tides, h_{solid} is solid earth tides, h_{pole} is pole tides, h_{load} is tidal loading, h_{iny} is inverse barometer height correction, and h_{hf} is high frequency fluctuations. The correction of R_{dry} and R_{wet} are based on the European Centre for Medium-Range Weather Forecasts, R_{iono} is from the Global Ionospheric Map, R_{ssb} is from the Hybrid sea state bias [34], and h_{ot} is from the FES2012 model. Due to limited number of data samples (~1.5 years) used in this study, the global FES2012 tidal model is used rather than a coastal tidal model such as the pointwise tide model (e.g., [35]). The use of pointwise tide modeling for resolving tidal signals requires at least 3 years of datasets to ensure that the individual constituents are separated due to the Rayleigh criterion [36]). It is noted that the use of the global tidal model to resolve coastal tidal signals may produce inaccurate results because tidal signals in the coastal regions are more complex than in the deep ocean.

The tide gauge data is processed to extract a non-tidal sea level time series, so that the physical contents are comparable to the satellite altimetry. The sea level measured by the tide gauge is different from the sea level measured by the satellite altimeter. The tide gauge measures the

changes in sea level over time relative to a datum, which is mean sea surface height (MSSH). Meanwhile, the altimeter measures the sea level above the reference ellipsoid.

The tide gauge is designed to estimate tides. In order to find the non-tidal sea level, high-frequency tidal effects on the tide gauge data need to be removed. Tidal signals from the tide gauge are removed using a harmonic analysis method [37, 38]. Harmonic analysis is a mathematical process which separates the observed tide into basic harmonic constituents. This method can determine the amplitude and phase of tidal constituents from a long-time series observation. It models the tidal signals as the sum of a finite set of sinusoids at specific frequencies related to astronomical parameters. If the amplitude and phase of each constituent is known, it can be removed from the sea level measurement [37].

3. Qualitative assessment

This section investigates the quantity of retracked SLAs from the three retrackers (i.e., MLE-4, Ice-1, and Ice-2) that are available from the AVISO SGDR product. The quantity is computed in terms of the percentage of data availability over the region (Section 3.1) and the minimum distance to the coastline (Section 3.2). These assessments are conducted to evaluate the amount of data that can be recovered through those three retracking algorithms.

3.1. Data availability of SARAL/AltiKa-retracked SLA over the coastal region

Figures 3–8 show the percentage of data availability over the regions. In general, the AltiKa shows an outstanding data recovery with ≥80% of data availability for all retrackers (see **Figures 1–3**). The spatial plot around the Strait of Malacca shows that the data availability is considerably high (≥70%) for most all passes of all retrackers, considering the complexity of the region with its narrow strait. However, several passes on the Andaman Sea show data availability of ≤70%. The percentage of data also degrades significantly over the eastern part of the Southeast Asia, around the Sulu Sea, near the Philippines coastal water. The data availability is ≤50% for several passes.

The close-up of the most complex area around Singapore, near the Riau Archipelago, and the Sulu Sea near the Philippines, are shown in **Figures 6–8**. The percentage of data around the Riau Archipelago is considerably high (≥70%) even though it is located in shallow water and surrounded by small islands. On the other hand, data over the Philippines coastal water degrades significantly with the percentage of data availability ≤50% for several passes.

Figure 9 indicates the mean percentage of retracked SLA data availability within 30 km of the coastline for the five tested regions. Of all regions, the South China Sea has the highest (≥88%) percentage, with the MLE-4, Ice-1, and Ice-2 retrackers providing 88, 90, and 89% of data, respectively. The South China Sea has less complex coastal topography when compared to the other regions. Hence, the contamination of land within the altimeter footprint may not be severe in this region, making the retracking of sea level work efficiently and producing outstanding data coverage.

http://dx.doi.org/10.5772/intechopen.74399

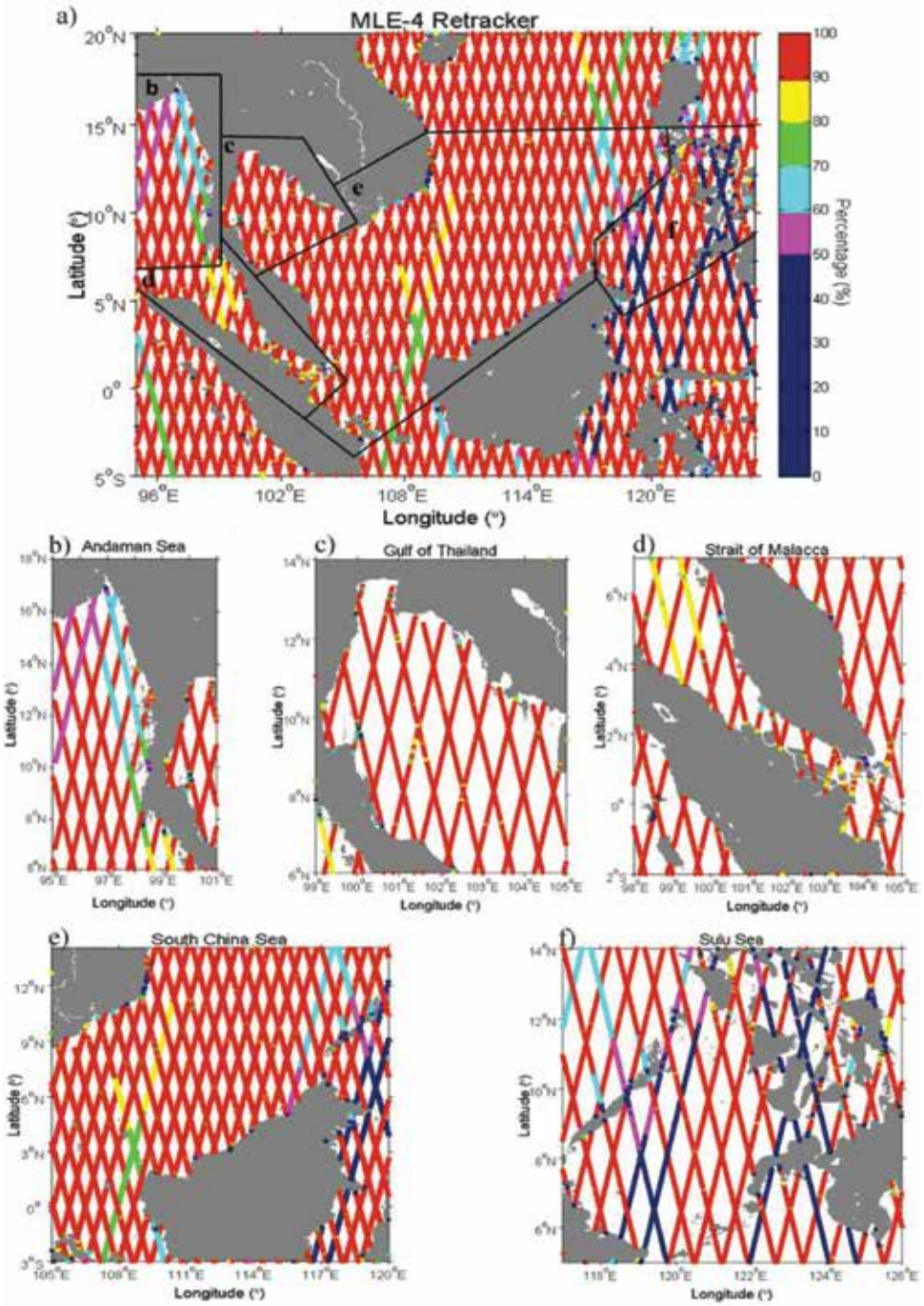

Figure 3. (a) The data availability (in unit %) for MLE-4 retracked SLAs over the Southeast Asia. Close up for (b) the Andaman Sea, (c) the Gulf of Thailand, (d) the Strait of Malacca, (e) the South China Sea, and (f) the Sulu Sea.

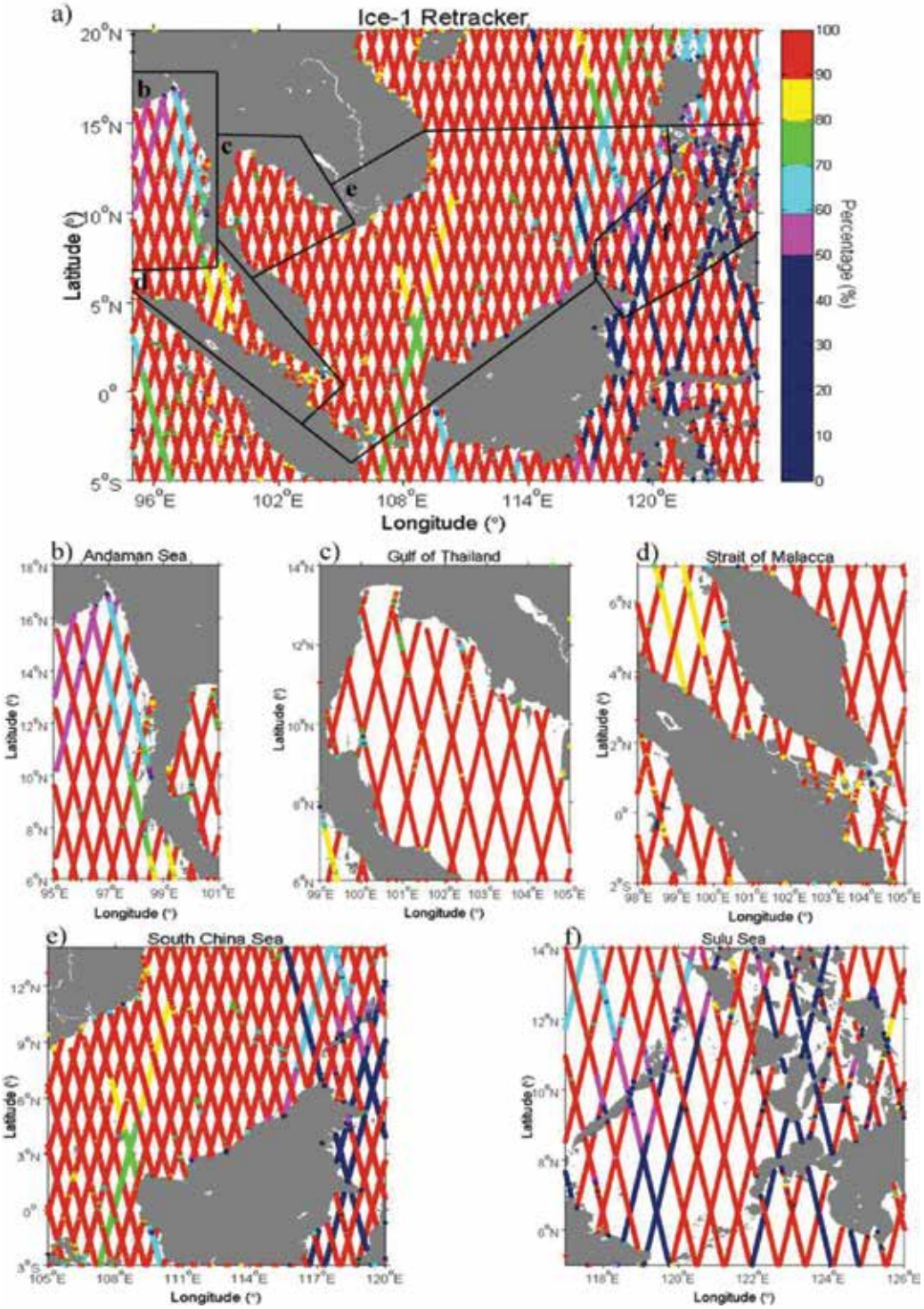

Figure 4. (a) The data availability (in unit %) for Ice-1 retracked SLAs over the Southeast Asia. Close up for (b) the Andaman Sea, (c) the Gulf of Thailand, (d) the Strait of Malacca, (e) the South China Sea, and (f) the Sulu Sea.

http://dx.doi.org/10.5772/intechopen.74399

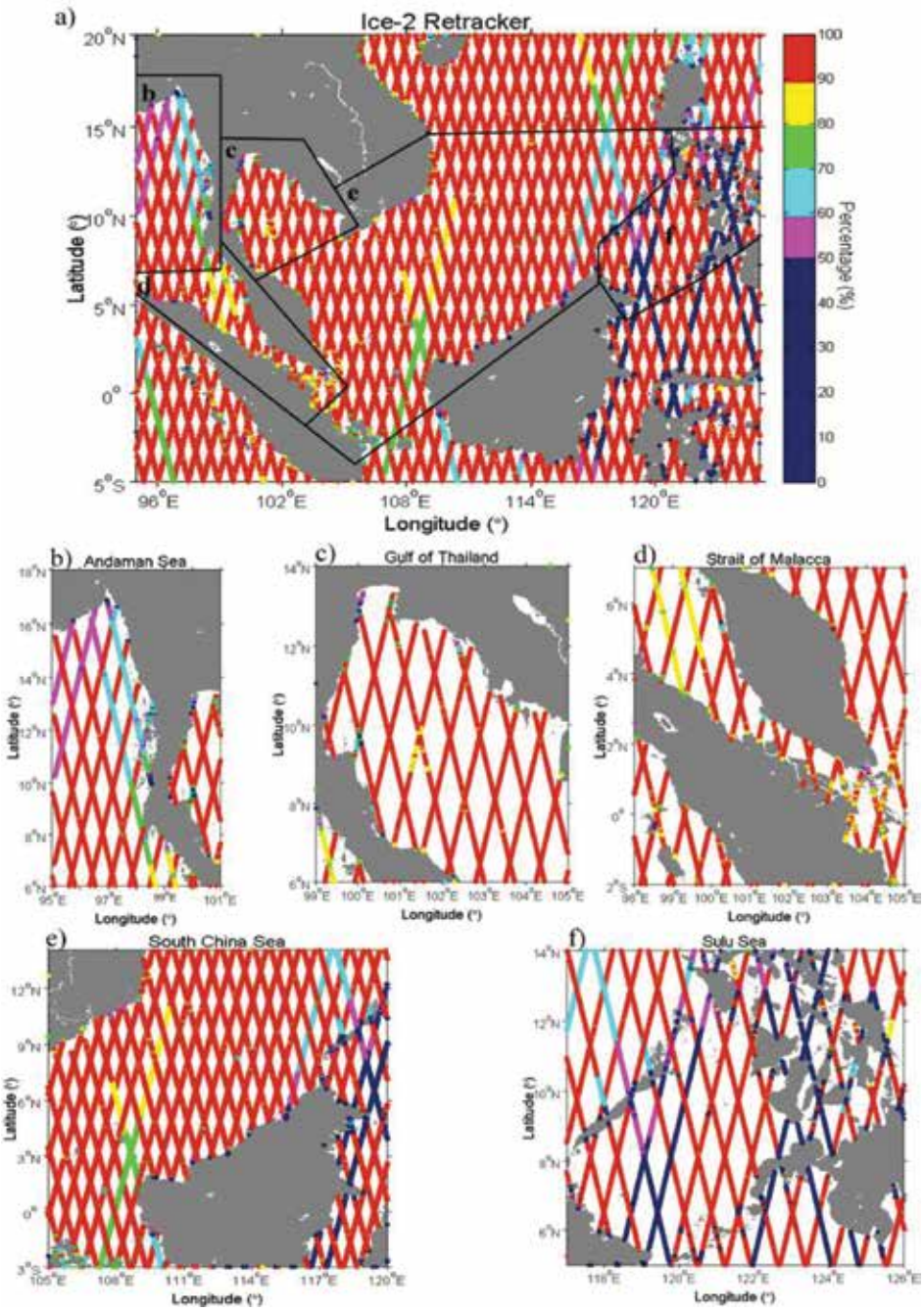

Figure 5. (a) The data availability (in unit %) for Ice-2 retracked SLAs over the Southeast Asia. Close up for (b) the Andaman Sea, (c) the Gulf of Thailand, (d) the Strait of Malacca, (e) the South China Sea, and (f) the Sulu Sea.

In contrast, the Sulu Sea has the lowest (≤68%) percentage of data coverage, with the MLE-4, Ice-1 and Ice-2 retrackers providing 64, 68, and 65% of data, respectively. The Sulu Sea is surrounded by many small islands, narrow straits, and shallow water with rough bottom topography. It is

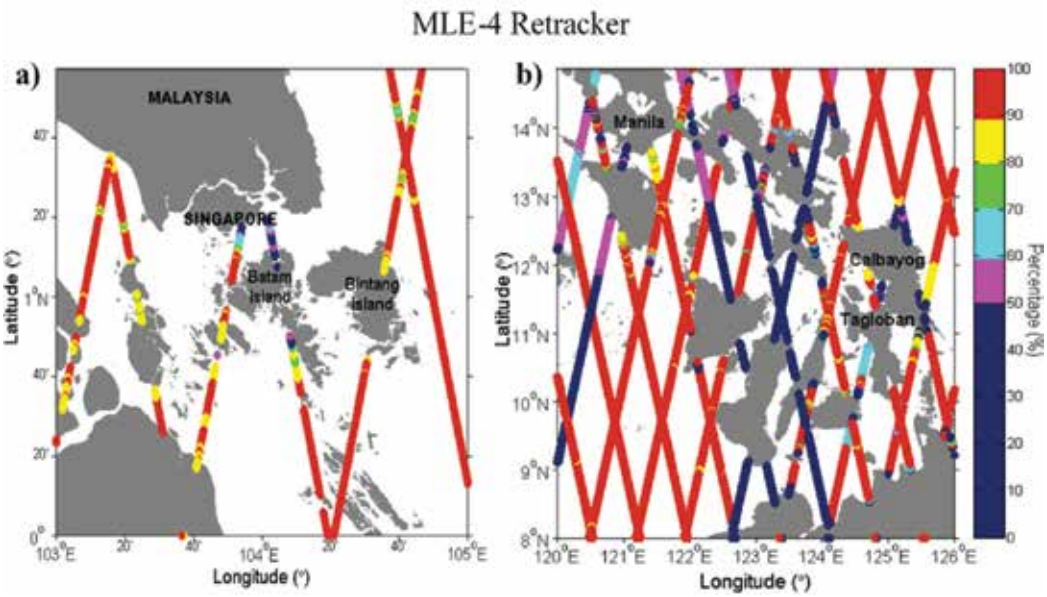

Figure 6. The data availability (in unit %) for MLE-4 retracked SLAs. Close up for area (a) near the Riau Archipelago and (b) over the Philippines coastal water.

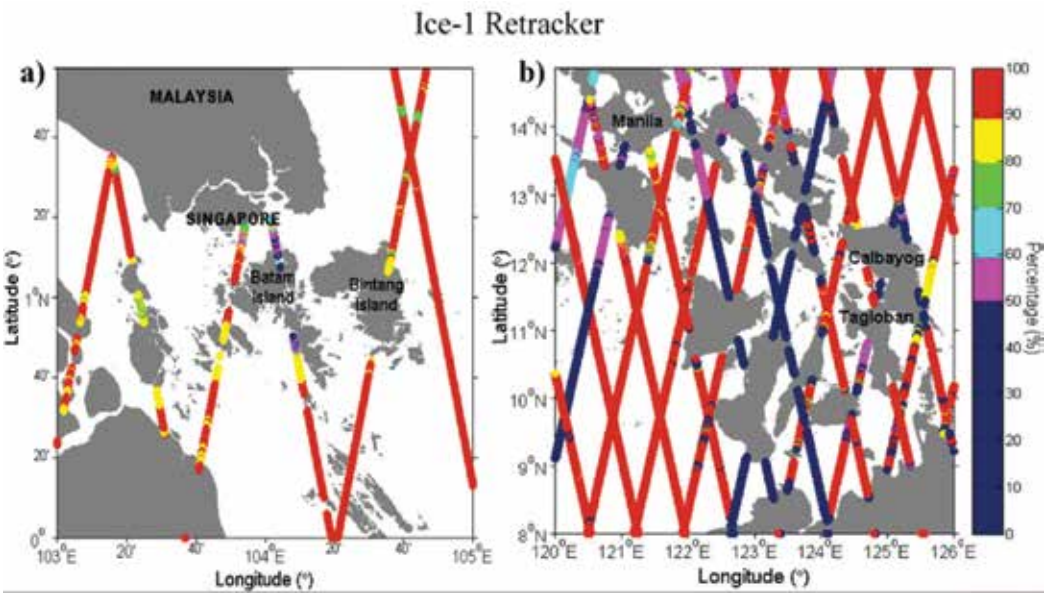

Figure 7. The data availability (in unit %) for Ice-1 retracked SLAs. Close up for area (a) near the Riau Archipelago and (b) over the Philippines coastal water.

one of the most complex archipelagos in the world [39]. This area also suffers from rapid changes in sea-state and quasi periodic-variation of surface roughness [40]. The altimetric waveforms could be severely corrupted due to the high complexity of the coastal topography, thus producing invalid estimations of geophysical information [8], particularly SLAs.

http://dx.doi.org/10.5772/intechopen.74399

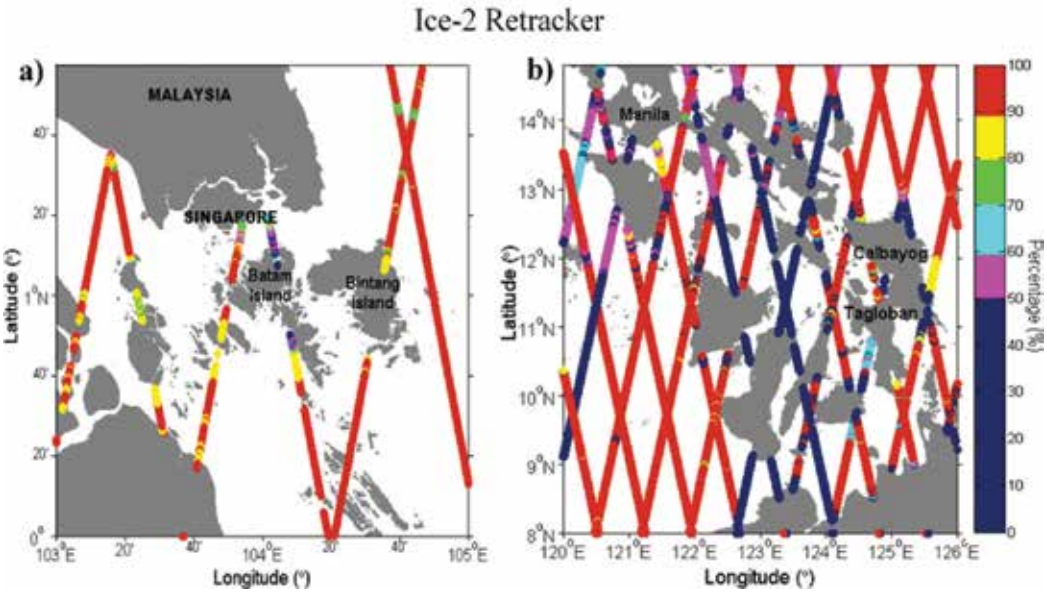

Figure 8. The data availability (in unit %) for Ice-2 retracked SLAs. Close up for area (a) near the Riau Archipelago and (b) over the Philippines coastal water.

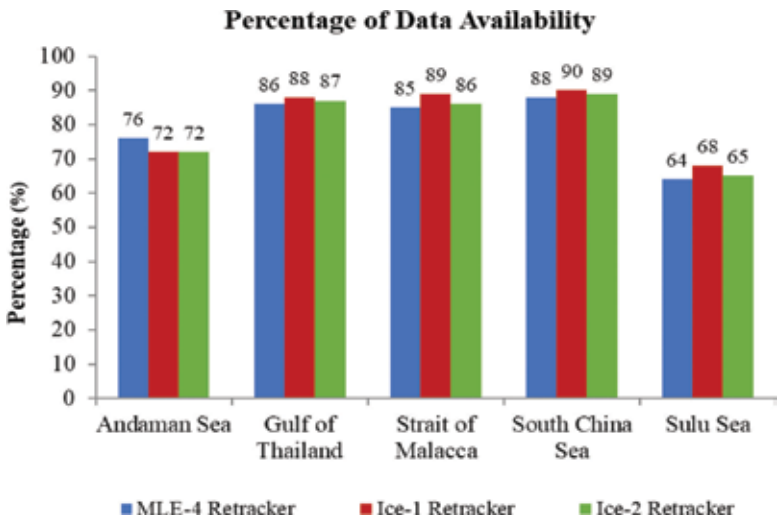

Figure 9. Mean percentage of AltiKa data availability over five experimental regions computed within 30 km of the coastline. It is computed from 18 passes for the Andaman Sea and the Strait of Malacca, 16 passes for the Gulf of Thailand, 30 passes for the South China Sea, and 17 passes for the Sulu Sea.

For the Andaman Sea, the Gulf of Thailand, and the Straits of Malacca, the AltiKa shows satisfactory results in data coverage with >72% data availability. Based on the result in **Figure 9**, 4 out of 5 regions have good data availability with more than 70% data coverage, thanks to the smaller AltiKa footprint size that has contributed to segregating the type of surface in transition zones (from water to land and from land to water) over coastal regions.

It is comprehended that the Ice-1 retracker always outperforms the MLE-4 and Ice-2 retrackers, except for the Andaman Sea where the performance of the Ice-1 and Ice-2 retrackers are similar. In contrast, the MLE-4 always underperforms compared to the other retrackers, except in the Andaman Sea where the percentage is slightly superior than those of other two retrackers.

3.2. The minimum distance of the SARAL/AltiKa retracked SLAs to the coastline

The quality of the AltiKa retracked SLAs over the coastal region is further investigated by computing the minimum distance of the available data to the coastline. **Figure 10** shows an example of the minimum distance of retracked AltiKa data computed from several passes over the Southeast Asia region. In general, the AltiKa SLAs data becomes available within 2 km from the coastline.

Figure 11 shows the mean minimum distance of the retracked AltiKa data computed over the five experimental regions. The total number of satellite passes included in the calculation is similar to the number of passes utilized in the computation of data availability. As shown in **Figure 11**, the AltiKa data over the South China Sea region have the lowest mean minimum distance compared to the other regions. The data are available within a distance of ≤3.2 km from the coastline. The Sulu Sea shows the opposite result, with the highest mean minimum distance ≥4 km from the coastline.

The finer spatial resolution with ~174 m along-track sampling in the Ka-band AltiKa (compared to the Jason-2 with ~300 m along-track sampling) enables high-density coastal observations, thus bringing the AltiKa measurements closer to the coastline. Based on previous research [21], this has confirmed that the AltiKa provides a significant improvement in accuracy and data availability up to ~3 km from the coastline. This is overwhelmingly better than the Jason-2 and Envisat which generally provide data beyond ~7–10 km from the coastline [18, 41, 42].

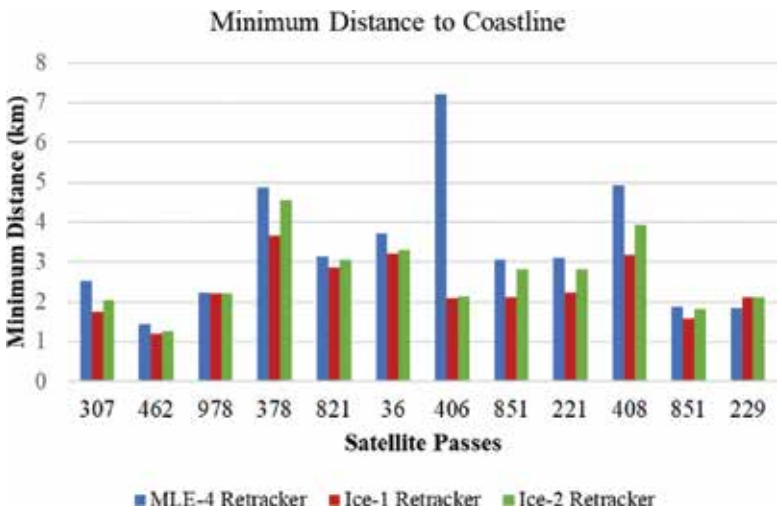

Figure 10. Mean of minimum distance of AltiKa MLE-4, Ice-1, and Ice-2 retracked SLAs to the coastline for several passes over the Southeast Asia coastal regions, computed from 19 cycles.

http://dx.doi.org/10.5772/intechopen.74399

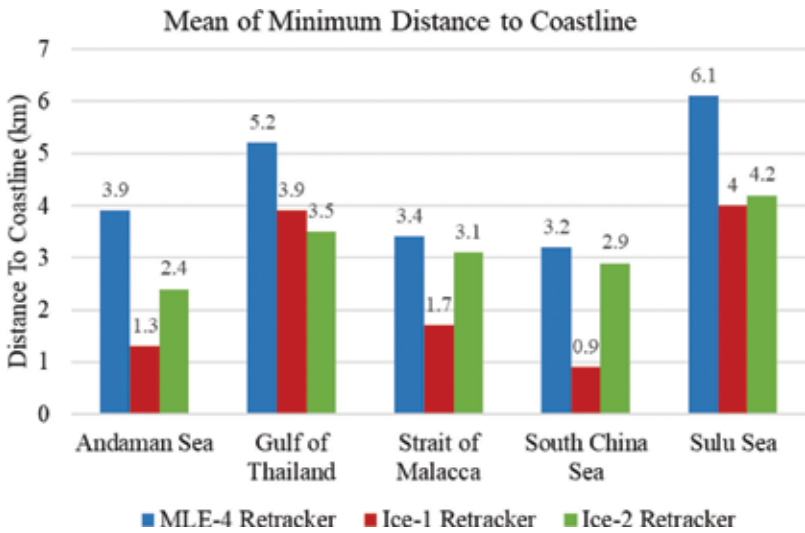

Figure 11. Mean of minimum distance of AltiKa for MLE-4, Ice-1 and Ice-2 retracked SLAs to the coastline over five experimental regions, computed from 19 cycles.

The overall inspection shows that the Ice-1 retracker performs better than other retrackers within a minimum distance of ≤4 km from the coastline, except for in the Gulf of Thailand. Over this region, the Ice-2 retracker is better than the other retrackers. The Ice-1 retracker is based on the OCOG, which is well-adapted to the rapidly changing surface like the continental sea shelf [8]. The MLE-4 retracker underperforms when compared to the other retrackers, with a mean minimum distance of ≥3.2 km from the coastline. The MLE-4 retracker is the standard ocean retracker, which relies on the waveform's physical shape to fit the waveform to the theoretical Brown-shape [8, 12]. The Ice-2 retracker underperforms when compared to Ice-1 for most of the regions. However, the Ice-2 is better than the MLE-4 retracker. This is because the Ice-2 retracker is an adaptation of Brown's model, with slight modifications, and was purposely developed for continental ice regions, making it more adaptable for coastal waveforms.

4. Validation against tide gauge

To validate the AltiKa retracked SLA, the temporal correlation and RMS error between the SLAs from the retracking algorithms and tide gauges are calculated. In this study, the mean value of temporal correlation and RMS errors are computed for distances ≤5 km from the coastline. **Figure 12** shows the result for retracked SLAs from the MLE-4 Ice-1 and Ice-2 corresponding to the six tide gauge stations.

For the validation near Bintulu tide gauge, the MLE-4 retracker has better performance than those of Ice-1 and Ice2 retrackers with a correlation of 0.53 and RMS error of 8 cm. The performance of Ice-1 and Ice-2 retrackers is significantly low with correlation ≤4 and RMS error ≥13 cm. Near Geting station, the performance of three retrackers are nearly similar, with

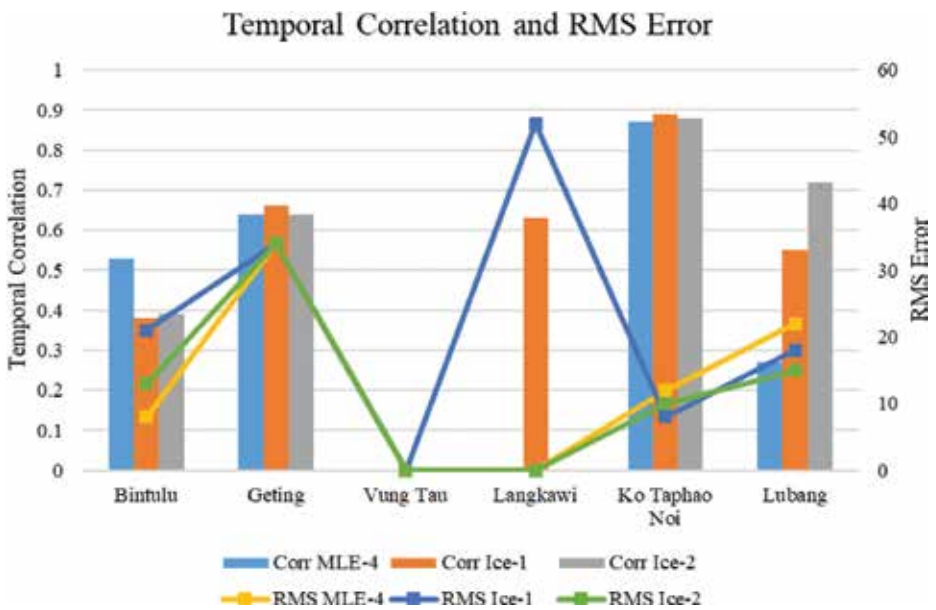

Figure 12. The temporal correlation and RMS error for MLE-4, Ice-1, and Ice-2 for distance within 5 km from coastline.

temporal correlation of 0.64 for MLE-4 and Ice-2 retrackers and 0.66 for Ice-1 retracker, and RMS error of 34 cm for all retrackers. Similar situation is shown near the Ko Taphao Noi tide gauge. The performance of three retracker are nearly similar with temporal correlation between 0.87 and 0.89 and RMS error between 8 and 12 cm. Near Vung Tau tide gauge, there is no data available for distance within 5 km from coastline. This is because, within this distance, satellite track crosses over a bay, thus producing complicated waveforms. The data over this area are unable to be retrieved from the three retracking algorithms. Near Langkawi tide gauge, the Ice-1 is the only retracker that can recover data. The temporal correlation and RMS error are 0.63 and 52 cm, respectively. Near Lubang tide gauge, Ice-2 is the optimum retracker based on the highest temporal correlation of 0.72 and RMS error 15 cm. The MLE-4 retracker seems to be the most inferior for this region, with a temporal correlation of 0.27 and an RMS error of 22 cm.

5. Summary

The AltiKa shows an excellent retracked SLA data coverage over the coastal water, with ≥85% data availability for most locations of the experimental regions (three out of five regions). AltiKa measurements also can get as close as ~1 km from the coastline. This is extremely better than the performance of previous missions (i.e., Jason-2 and Envisat), which can generally provide measurements beyond ~7–10 km from the coastline.

For overall results, it shows that the Ice-1 is the optimum retracker over the Southeast Asia coastal region, with the percentage of data availability up to 90% and the minimum distance

as close as 0.9 km from the coastline. Nevertheless, the amount of data that can be recovered through the retracking algorithm depends on the coastal topography and sea states, in which different coastal characteristics have different impacts on the altimetric signals. Thus, this makes the performance of each retracker differ between different locations.

Acknowledgements

The research is supported by Research University Grant Tier 1 (vot 17H59). We would like to acknowledge the Ministry of Higher Education Malaysia for providing research funding. This acknowledgement also goes to the Achieving, Validating, and Interpretation of Satellite Oceanography (AVISO) data team for providing SARAL/AltiKa data, the Department of Survey and Mapping Malaysia (DSSM) and the University of Hawaii Sea Level Centre (UHSLC) for providing tide gauge data. Special thanks to Dr. Angela Maharaj from University of New South Wales, Australia for her constructive comment about this book chapter.

Author details

Noor Nabilah Abdullah[1] and Nurul Hazrina Idris[1,2]*

*Address all correspondence to: nurulhazrina@utm.my

1 Faculty of Geoinformation and Real Estate, Universiti Teknologi Malaysia, Johor Bahru, Malaysia

2 Geoscience and Digital Earth Center, Research Institute for Sustainability and Environment, Universiti Teknologi Malaysia, Johor Bahru, Malaysia

References

[1] Cipollini P, Snaith H. A short course on altimetry. In: 3rd ESA Advanced Training on Ocean Remote Sensing; 23-27 September. Cork, Ireland; European Space Agency; 2013

[2] Anzenhofer M, Shum CK, Rentsh M, O.S. University. Coastal Altimetry and Application. Vol. 1. Columbus, Ohio: Department of Civil and Environmental Engineering and Geodetic Science; 1999

[3] Challenor PG, Read JF, Pollard RT, Tokmakin RT. Measuring surface current in drake passage fron altimetry and hydrography. Journal of Physical Oceanography. 1996;**26**: 2784-2758

[4] Fu LL, Cazenave A, Fu LL, Cazenave A. Satellite Altimetry and Earth Sciences: A Handbook of Techniques and Applications. San Diego, California: Academic Press; 2001

[5] Gómez-Enri J, Cipollini P, Gommenginger C, Martin-Puig C, Vignudelli S, Woodworth P, Benveniste J, Villares P. COASTALT: Improving radar altimetry products in the oceanic coastal area. Remote Sensing of the Ocean, Sea Ice, and Large Water Regions. 2008;**71050J**:1-10. DOI: 10.1117/12.802456

[6] Bouffard J, Pascual A, Ruiz S, Faugère Y, Tintoré J. Coastal and mesoscale dynamics characterization using altimetry and gliders: A case study in the Balearic Sea. Journal of Geophysical Research: Oceans. 2010;**115**:1-17

[7] Cipollini, P. The Coastal Zone: A Mission Target for Satellite Altimetry In Coastal Altimetry Workshop; 7-8 October; Boulder, Colorado; 2013. 72

[8] Gommenginger C, Thibaut P, Fenodlio-Marc L, Quartly G, Deng X, Gomez-Enri J, Challenor P, Gao Y. Retracking altimeter waveforms near the coasts. A review of retracking methods and some applications to coastal waveforms. In Vignudelli S et al. Coastal Altimetry. London, New York: Spring; 2011. pp. 61-101. DOI: 10.1007/978-3-642-12796-0_4

[9] Vignudelli S, Kostianoy AG, Cipollini P, Benveniste J. Coastal Altimetry. Berlin: Springer; 2011. DOI: 10.1007/978-3-642-12796-0.A

[10] Brown GS. The average impulse response of a rough surface and its applications. IEEE Journal of Oceanic Engineering. 1977:67-74

[11] Dinardo S, Benveniste J. Application of a modeified brown model to quasi specular echoes. In Coastal Altimetry Workshop; 17-18 September; Frascati, Italy. 2009

[12] Thibaut P, Poisson JC, Bronner E, Picot N. Relative performance of the MLE3 and MLE4 retracking algorithms on Jason-2 altimeter waveforms. Marine Geodesy. 2010;**33**:317-335. DOI: 10.1080/01490419.2010.491033

[13] Brown S. A novel near-land radiometer wet path-delay retrieval algorithm: Application to the Jason-2/OSTM Advanced microwave radiometer. IEEE Transactions on Geoscience and Remote Sensing. 2010;**38**:1986-1992. DOI: 10.1109/TGRS.2009.2037220

[14] Idris NH, Deng X, Md Din AH, Idris NH. CAWRES: A waveform retracking fuzzy expert system for optimizing coastal sea levels from Jason-1 and Jason-2 satellite altimetry data. Remote Sensing. 2017;**9**:603

[15] Wingham DJ, Rapley CG, Griffiths H. New techniques in satellite tracking systems. In: IGARSS. In 86 Symposium Digest; September; Zurich, Switzerland. 1986. pp. 185-190

[16] Villadsen H, Deng X, Andersen OB, Stenseng L, Nielsen K, Knudsen P. Improved inland water levels from SAR altimetry using novel empirical and physical retrackers. Journal of Hydrology. 2016;**537**:234-247

[17] Deng X, Featherstone WE, Hwang C, Berry PAM. Estimation of constamination of ERS-2 and POSEIDON satellite radar altimetry close to the coasts of Australia. Marine Geodesy. 2002;**25**:249-271. DOI: 10.1080/01490410214990

[18] Idris NH, Deng X. The retracking technique on multi-peak and quasi-specular waveforms for Jason-1 and Jason-2 missions near the coast. Marine Geodesy. 2012;**35**:217-237. DOI: 10.1080/01490419.2012.718679

[19] Verron J, Sengenes P, Lambin J, Noubel J, Steunou N, Guillot A, Picot N, Coutin-Faye S, Sharma R, Gairola RM, Murthy DVAR, Richman JG, Griffin D, Pascual A, Remy F, Gupta PK. The SARAL/AltiKa altimetry satellite mission. Marine Geodesy. 2015;**38**:2-21. DOI: 10.1080/01490419.2014.1000471

[20] Prandi P, Philipps S, Pignot V, Picot N. SARAL/AltiKa global statistical assessment and cross-calibration with Jason-2. Marine Geodesy. 2015;**38**:297-312. DOI: 10.1080/01490419.2014.995840

[21] Abdullah NN, Idris NH, Maharaj AM. The retracked sea levels from SARAL/AltiKa satellite altimetry: The case study around the Strait of Malacca and the South China Sea. International Journal of Geoinformatics. 2016;**12**:33-39

[22] Ratheesh S, Sharma R, Prasad KVSR, Basu S. Impact of SARAL/AltiKa-derived sea level anomaly in a data assimilative ocean prediction system for the Indian Ocean. Marine Geodesy. 2015;**38**:354-364. DOI: 10.1080/01490419.2014.988833

[23] Schwatke C, Dettmering D, Börgens E, Bosch W. Potential of SARAL/AltiKa for inland water applications. Marine Geodesy. 2015;**38**:626-643. DOI: 10.1080/01490419.2015.1008710

[24] Abdalla S. SARAL/AltiKa wind and wave products: Monitoring, validation and assimilation. Marine Geodesy. 2015;**38**:365-380. DOI: 10.1080/01490419.2014.1001049

[25] Tournadre J, Poisson J, Steunou N, Picard B. Validation of AltiKa matching pursuit rain flag. Marine Geodesy. 2015;**38**:107-123

[26] Abdullah NN, Idris NH, Idris NH. Performance of SARAL/Altika satellite altimetry mission over the Straits of Malacca and the South China Sea. In: IEEE Workshop on Geoscience and Remote Sensing; 16-17 November 2015. Kuala Lumpur, Malaysia; IEEE Geoscience and Remote Sensing Society Malaysia; 2015. pp. 86-89

[27] Idris NH, Maharaj A, Abdullah NN, Deng X, Andersen OB. A comparison of Saral/Altika coastal altimetry and in-situ observation across australasia and maritime continent. In: SARAL/AltiKa Workshop; 27-31 October 2014. Lake Constant, Germany: ESA Publication; 2014

[28] Idris NH, Maharaj A, Deng X, Abdullah NN, Idris NH, Wan Kadir WH. A comparison of Saral/Altika coastal altimetry and in-situ observation across australasia and maritime continent. In: Australia Coastal Ocean Modelling and Observations; 7-8 October 2014. Canberra, Australia: IMOS Australia; 2014

[29] Mohammed SB, Idris NH, Abdullah NN. Along-track high resolution sea levels from SARAL/Altika satellite altimetry data over the maritime continent In: IEEE Workshop on Geoscience and Remote Sensing; 16-17 November. Kuala Lumpur, Malaysia: IEEE Geoscience and Remote Sensing Society Malaysia; 2015. pp. 90-93

[30] Amarouche L, Thibaut P, Zanife OZ, Dumont JP, Vincent P, Steunou N. Improving the Jason-1 ground retracking to better account for attitude effects. Marine Geodesy. 2004;**27**:171-197. DOI: 10.1080/01490410490465210

[31] Lee H, Shum CK, Emery W, Calmant S, Deng X, Kuo C-Y, Roesler C, Yi Y. Validation of Jason-2 altimeter data by waveform retracking over California coastal ocean. Marine Geodesy. 2010;**33**:304-316. DOI: 10.1080/01490419.2010.488982

[32] Legresy B, Papa F, Remy F, Vinay G, Van Den Bosch M, Zanife O-Z. ENVISAT radar altimeter measurements over continental surfaces and ice caps using the ICE-2 retracking algorithm. Remote Sensing of Environment. 2005;**95**:150-163

[33] Andersen OB, Scharroo R. Range and geophysical corrections in coastal regions: And impications for mean surface determination. In: Vignudelli S et al., editors. Coastal Altimetry. London, New York: Springer; 2011. pp. 103-146. DOI: 101.1007/978-3-642-12796-0

[34] Wang D-P, Flagg CN, Donohue K, Rossby HT. Wavenumber spectrum in the gulf stream from shipboard ADCP observations and comparison with altimetry measurements. Journal of Physical Oceanography. 2010;**40**:840-844. DOI: 10.1175/2009jpo4330.1

[35] Idris NH, Deng X, Andersen OB. The importance of coastal altimetry retracking and detiding: A case study around the Great Barrier Reef, Australia. International Journal of Remote Sensing. 2014;**35**:1729-1740

[36] Andersen OB. Global ocean tides from ERS 1 and TOPEX/POSEIDON altimetry. Journal of Geophysical Research: Oceans. 1995;**100**:25249-25259

[37] Pawlowicz R, Beardsley B, Lentz S. Classical tidal harmonic analysis including error estimates in MATLAB using T_TIDE. Computers & Geosciences. 2002;**28**:929-937

[38] Schureman P. Manual of Harmonic Analysis and Prediction of Tides. US Government Printing Office; 1958

[39] Brown RM, Siler CD, Oliveros CH, Esselstyn JA, Diesmos AC, Hosner PA, Linkem CW, Barley AJ, Oaks JR, Sanguila MB. Evolutionary processes of diversification in a model Island Archipelago. Annual Review of Ecology, Evolution, and Systematics. 2013;**44**:411-435

[40] Apel JR, Holbrook JR, Liu AK, Tsai JJ. The Sulu Sea internal soliton experiment. Journal of Physical Oceanography. 1985;**15**:1625-1651

[41] Babu K, Shukla A, Suchandra A, Arun Kumar S, Bonnefond P, Testut L, Mehra P, Laurain O. Absolute calibration of SARAL/AltiKa in Kavaratti during its initial calibration-validation phase. Marine Geodesy. 2015;**38**:156-170

[42] Deng X, Featherstone WE. A coastal retracking system for satellite radar altimeter waveforms: Application to ERS-2 around Australia. Journal of Geophysical Research. 2006;**111**:12-28. DOI: 10.1029/2005jc003039

Section 3

Satellite Data in Remote Sensing and GIS Applications

Chapter 4

Geospatial Analysis for Irrigated Land Assessment, Modeling and Mapping

Olumuyiwa Idowu Ojo and
Masengo Francois Ilunga

Additional information is available at the end of the chapter

http://dx.doi.org/10.5772/intechopen.73314

Abstract

Assessment of irrigated lands by conventional means of survey requires a great deal of time, but the application of geospatial analysis using remote sensing data and GIS techniques minimize time consuming and offer the possibility rapid production of maps and models. This paper gave an overview of the techniques and methods in use at different scales. The presence of salt in the soils and its variation may be because of rise in water table and the difference in elevation in irrigated lands. The combined application of conventional methods with remote sensing and geographical information system techniques in detecting these problems in irrigated lands were examined. Different salinity indexes coupled with ground truthing with the proven results in assessing such problems were also examined thereby depicting indexes as good indicator of soil salinity and water logging, which may influence decision on reclamation of degraded land for proper agricultural land management. Irrigation and drainage managers, planners, farmers, and government agencies for smart agriculture can use models and maps generated through geospatial analysis.

Keywords: assessment, modeling, mapping, GIS, RS, irrigated land

1. Introduction

Irrigated agriculture is important to the national economy of a country as it contributes significantly to the production of food. The main objective of irrigated agriculture is to enhance crop production for food sufficiency, particularly in semi-arid and arid zones [1]. It has contributed positively to food security, poverty alleviation, and rural development. In addition, it protects plant against frost, suppresses growing of weeds in grain fields, and prevents soil consolidation. Most irrigation schemes are faced with problem of soil deterioration resulting

from increased level of soil salinity and rise in water table. Soil salinity affects soil chemical, physical, and biological characteristics of the soil, fertility, and sustainable productivity unless it is properly monitored. Geo-informatics involves a combination of special techniques, technologies and tools for the acquisition, processing, management, analysis, and presentation of geospatial data [2]. It is a combined method to GIS and remote sensing. Remote sensing and GIS are well established information tools, since they give reasonable pictures of the entire process in spatial and temporal terms. They both provide a cost effective and adequate understanding of landscape dynamics, detect, identify, map, and monitor differences in land use and land cover pattern over long period of time [3]. The application of Satellite Remote Sensing (SRS) and GIS has been proved useful and successful in many fields such as natural resources management, agriculture, and environmental issues and water resources. Remote sensing approaches are very effective for detecting, monitoring and control of soil salinity. Remotely sensed data are used to assess soil salinity either on bare soils with salt crust or through biophysical properties of vegetation as these are affected by salinity [4].

1.1. General background

Replace environmental land degradation has recently become a global, urgent issue, and is now being considered with high priority, especially in the developing countries in order to meet the food and fiber demands of accelerated population pressure with limited available resources. One of the goals of irrigation is to boost food production in a sustainable technique so that a fast growing global population could be fed. Sustainable irrigation scheme can only be achieved effectively by taking into consideration the environmental effectiveness and availability of funds to maintain the implemented project. The function of irrigation is to apply water to maintain crop evapotranspiration, the total amount of available water essential for economy, health, and welfare of a very large part of the world [5]. Analyses of information from Asia have also shown that yields per area, for most crops have increased between 100 and 400% because of irrigation [6]. Based on the management system of irrigation scheme, it can provide both positive as well as negative effects on vegetation cover. Well-planned irrigation scheme have good natural vegetation conservation and management plans. Several factors could influence the salinity levels of irrigated land. One of the factors is the irrigation method [7].

1.2. Importance of irrigation

Irrigation is undertaken to provide insurance against droughts, cooling of the soil and atmosphere and provide more favorable environment for plant growth. It can also wash out or dilute salts in the soil, reduce the hazards of piping, and soften tillage pans [8]. Generally, the goal is to supply the entire field uniformly with water, so that each plant has the amount of water it needs. In arid and semi-arid areas where there are less rainfall, irrigation is often used to grow cash crops, develop landscapes and vegetate disturbed soils. This is expected of the increase in world population and the need to expand agricultural land under the threat of climate change. It has contributed immensely in the production of food in industries.

http://dx.doi.org/10.5772/intechopen.73314

1.3. Impact of irrigation on vegetation and soil

The practice of irrigation sometimes has an adverse effect on environmental condition otherwise properly monitored, planned and managed. Past record claims that human activities have a strong effect on the natural environment and becoming the main cause of environmental degradation [9]. The expansion of irrigation project has many advantages. However, large-scale irrigation projects changes natural ecosystem. To undertake large irrigation projects, vegetation cover needs to be cleared and different construction activities needs to be done. Natural vegetation is an eminent parts of the ecosystem negatively affected with large-scale irrigation projects [10]. Soil being a vital natural resources, it has been assisting the increasing number of life on earth. As regards to increase in population, food demand also increased. This in turn put-size pressure on land/soil resource, areas of land that are formerly considered as marginal are now being cultivated [11].

2. Characterization of soil salinity

Mougenot et al. [12] argues that visible reflectance of leaves from plants growing on non-salt affected leaves before plant maturation is higher than after maturity. In addition, visible reflectance of leaves from plants growing on salt affected soil is lower than the visible reflectance of plants growing on non-salt affected soils. Near-infrared reflectance increases without water stress due to a succulent (cell thickening) effect and increases in other cases. Spatial information on soil moisture can be accessed through bands in the near- and middle-infrared spectral bands; this is confirmed by [13]. The study showed that near- to middle-infrared indices are indicators for chlorosis in stressed crops normalized difference for TM bands 4 and 5. This new ratio is however dull to color variations and provides an indication of leaf water potential. In addition [14] showed that chlorotic canopies could be distinguished from healthy canopies, as biophysical response to a salinity can be seen in low fractional vegetation cover, low leaf-area index (LAI), high albedo, low surface roughness and high surface resistance compared with healthy crops. This is because healthy vegetation absorbs most of the visible light hitting it and reflects a large portion of the near infrared light. However, sparse vegetation (right) reflects more visible light and less near infrared light [15]. Traditionally, electrical conductivity (EC) measured in dS/m is used to determine the soil salinity on a small field with the aid of hand-held conductivity meter, while on a large scale it is measured and mapped using electromagnetic (EM) conductivity meter [15]. These approaches (traditional and geospatial) are used to quantify the density of plant growth on the earth visible radiation minus near-infrared radiation divided by near-infrared radiation plus visible radiation resulting into vegetation indices [16]. **Table 1** gave the criteria for classifying soil salinity.

2.1. Geographical information system in soil salinity modeling

During the last decade, there has been a proliferation of geospatial data in natural resource management including in the disciplines of forestry, fishery management, geology, geomorphology,

Degree of salinity	Salinity ECe (dS/m)
Slight	4–8
Moderate	8.25
Strong	>25

Source: [15].

Table 1. Soil salinity classification.

hydrology, wildfire, and climate change [17]. Geographic Information System (GIS) enables the measurement and representation of geographic phenomena and thereafter transform this spatial information into various forms while interacting with social structures [18]. GIS has the benefit of its ability to interrelate spatially multiple types of information and data obtained from a range of sources. In addition based on the findings of [19], GIS technique has the capacity as an effective tool for spatial analyses and modeling of concentrations of air pollutants. GIS also has three basic key functions, which include database management, spatial analysis and visualization. Thus with these three components, this system (GIS) provides the capabilities of linking the concentration of the air pollutants with their geographic location [19]. From their study, it was also discovered that GIS technology could effectively represent the spatial relationships between sources and receptors as it can integrate with satellite remote sensing data in order to spatially analyze the relationship between the geographic location of air pollutants and the land use/land cover classes of the area. Models are representation of reality and they are created as a simplified, manageable view of reality, due to the inherent complexity of the earth and the diverse interactions in it. Models help to understand, describe, or predict how things work in the real world. Models are broadly classified into two namely representation and process models. Representation models are those that represent the objects in the landscape while those that attempt to simulate processes in the landscape are process models [20]. Representation models describe the objects in the landscape, such as buildings, streams, or forest while process models describe the interaction of the objects that are modeled in the representation model. There are different types of process models including suitability modeling, distance modeling and hydrological modeling [21].

2.2. Remote sensing for soil salinity mapping

The essence of remote sensing is the measuring and recording of the electromagnetic radiation emitted or reflected by the earth's surface [22]. For soil salinity investigation, this may be useful where salty soil, salt-affected vegetation, saline water, pond water and high water table area give contrasting reflectance with other landscape features so that they can be unambiguously distinguished. Remote Sensing (RS) is the art and science of obtaining information about an object, area or phenomenon through analysis of the data acquired by such device that is not in contact with the object, area or phenomenon under consideration. It is the measurement of object properties on Earth's surface using data acquired from aircraft and satellites. Rather than in situ, RS attempts to measure something at a distance. It involves measuring, recording and transmission of electromagnetic energy by the sensors mounted on aircraft or satellite reflected from or emitted by object from vantage point above the surface and relating

of such measurements to the nature and distribution of surface materials and atmospheric conditions. Remote sensing system operation involves the detection, collection and interpretation of data from distance by mean of sensors. The reflectance of electromagnetic radiations from the features at the earth surface is measured with the aid of a sensor, while the radiated energy is transmitted through space in waveform. For land resources survey using remote sensing, wavelengths between 0.4 and 2.4 nm are commonly used. Generally, the electromagnetic spectrum ranges from gamma rays, with wavelength of less than 0.03 nm, to radio energy with a wavelength of more than 30 cm. According to [12], the presence of salts at the terrain surface can be detected from remotely sensed data either directly on bare soils, with salt efflorescence and crust, or indirectly through vegetation type and growth as these are controlled or affected by salinity. Better understanding of the relationship can advance the use of remote sensing for soil studies between soil properties and surface reflectance. Salt affected soils in arid regions, especially when a salt crust whitish color is formed show a high reflectance. Effective application of remote sensing data requires one to have the technical expertise and understand the spectra characteristics of the particular features to be studied. In addition, an understanding of the behavior of different wavelength regions on different soil materials and surface conditions may increase the efficiency of the study of soil salinity based on remote sensing [23].

2.3. Mapping of waterlogging

The change in soil color and the change in soil reflectance properties caused excess soil moisture, which can be easily detected by remote sensing. Plant response is one means of detecting poorly drained soils in California mainly because of a build-up of the water table. On the other hand, Salman [24] reported that as result of excess organic matter, soil color is generally darker in poorly drained areas than well-drained soils. The visible bands in Landsat-MSS data can be used to classify this color. According to [25] as cited in [26] pointed out that color infrared photography could indicate drainage problems by soil moisture saturation or plant stress. Shallow water tables exhibit a rise in surface moisture, which can be detected from visible reflectance and microwave emissivity. The information about drainage basin area and drainage pattern can be obtained from satellite imagery. Water logging and problems associated with drainage can be examined through GIS by identifying the drainage network and its characteristics in a basin, besides the report on the presence of high water table, high morphology, soil color, plant stress and drainage water collection in lower spots [27].

2.4. Application to large areas

For relatively large areas, remote sensing is an essential tool for mapping and surveying salt-affected and waterlogged soils [28]. The understanding of the actual conditions at the earth surface makes it feasible to interpret the satellite images. However, because of lack of specific absorption bands and spectral confusion, it is complex to distinguish the degree of salinity through remote sensing approach [29] that separated different soil salinity level using Landsat imagery. Most authors are capable to differentiate only 2–3 classes (strong and medium) of salinity levels with errors between moderately saline and normal soils.

2.5. Techniques in monitoring soil salinity

The classification of salt affected soils, assessment of the percentage of severity particularly in its early stage is important in terms of sustainable agricultural management [30]. Various approaches have been employed by researchers to analyze and monitor soil salinity. The three major techniques commonly used in soil salinity determination include traditional method, Electromagnetic Induction method and Remote Sensing and GIS method. The traditional or conventional methods used for detecting soil properties include ground-based geophysics and laboratory analysis methods [31]. Adeniran et al. [5] used this method to determine electrical conductivity of soil in Omi irrigation scheme by carrying out chemical analysis of the soil samples. The disadvantages of traditional method includes; time consuming, costly since dense sampling is required to adequately characterize the spatial variability of an area and demanding when considering large areas [32, 33]. Remote sensing methods are suitable for detecting, monitoring and controlling soil salinity. Researchers have used GIS and RS techniques to model, assessed, and investigate land use and land cover pattern, detect, map, monitor and forecast soil salinity on an irrigation scheme [34]. Ojo et al. [15] stated the advantages of remote sensing and GIS method includes; time saving, wide range of coverage, facilitation of faster and long term monitoring. Electromagnetic Induction (EMI) was first employed in agriculture to detect saline soils by measuring its electrical conductivity [35]. Electromagnetic approaches are reliable means used for rapid determination of soil salinity [36]. Spatially varying soil types and properties are identified easily and map out quickly with the application of EMI as it offers unique benefit over traditional methods.

2.6. Soil mapping

There are varieties of methods to identify and map surface features using remotely sensed imagery. Techniques for mapping soil surface conditions, such as salinity and waterlogging are based on the presence or absence of spectral absorption features. Soil mapping include locating and identifying the various soils that occur, nature and properties, collecting information about soil location and recording this information on maps and in supporting documents to show their spatial distribution. Seghal et al. [37] applied Landsat MSS data for mapping salt affected soils in the frame of the reconnaissance soil map of Indian. Dwivedi [38] used Landsat MSS and TM data for more detailed mapping and monitoring of salt affected soils in the Indo-Gangetic alluvial plain. Landsat TM data have proved useful for mapping depositional environments on playas Tunisia [39]. Crowley [40] reported that gypsum and halite were likely to be the only evaporate phases detected and mapped on the Chott el Dyerid using TM data. Mehrjardi et al. [41] used Landsat TM+ taken in 2002 to map soil salinity in Ardakane Yazd by using an exponential model. They used band 3 of the images and soil salinity parameter in a regression analysis (R2 = 0.58) and reported a map accuracy of 0.87% and K coefficient equal to 0.47%. Various remote sensing data such as aerial photos, video, images, infrared thermography, visible and infrared multispectral, microwave and airborne geophysical data, is available for monitoring, classification and mapping out of saline soil [42]. According to [43] several authors have dealt with the study of soil salinization using satellite data, among them [12, 44–51]. In China, Peng [52] integrate

http://dx.doi.org/10.5772/intechopen.73314

Landsat TM data with the depth and mineralization rate of groundwater to create soil salinity map. In Israel, hyper-spectral airborne sensor data were processed to yield quantitative maps of soil salinity [53].

2.7. Landsat image

Landsat image consists of three separate instrument subsystem, each operating in a different spectral region, using a separate optical system [54]. These subsystems are the Visible and Near Infrared (VNIR), the Short Wave Infrared (SWIR), and the Thermal Infrared (TIR), respectively. Landsat data has 14 bands allocated in three spectral regions as VNIR (band 1, 2, 3) with 15 m resolution, SWIR (bands 4–9) with 30 m resolution and TIR (bands 10–14) with 90 m resolution [55].

2.8. Landsat platform characteristics

With the launching of the Landsat satellite in 1972, researchers began to use satellite data for monitoring environmental activities in different parts of the world [56]. Landsat provides basic tools for working with satellite imagery as automated geo-referencing and cloud detection. Landsat consist of functions for radiometric normalization and various approaches to atmospheric correction. It also includes useful functions such as bare soil line and tasseled cap calculations [57]. The physiological condition of a crop is shown best at TM 5 and TM7. Landsat 5 (TM) that was launched on 01/03/1984 and Landsat 7 (ETM+) on 15/04/1999, each revisit a location every 16 days, and the two orbits are staggered for images to be taken every 8 days. Due to a hardware failure on 31/05/2003, Landsat 7 scenes are now missing 22% of the pixels also severe problem occurs toward the edges of an image. Band attributes are largely coherent, but ETM+ added an additional band. Landsat images haves been converted to integer digital numbers (DN) before distribution to facilitates storage and display. Atmospheric correction, topographic correction and conversion to radiance or reflectance may be required. Minimal processing may be needed if a single image or images widely separated in time are used to examine gross changes. However, careful correction is needed to examine detailed comparison of vegetation indices from multiple images. The most accurate atmospheric corrections need ground data collected during the satellite image capturing. For retrospective studies, this is impossible to obtain, and less-accurate image-based correction method must be used [58]. Band Wavelength and resolution for Landsat 5 Thematic Mapper (TM) and Landsat 7 Thematic Mapper (TM) is shown in **Tables 2** and **3** respectively. Panah and Goossens [23] claimed that thermal band of Landsat (TM) imagery is a good source of information that may have a vital role in soil salinity studies and in detecting gypsiferous soils in arid region. The reflective bands 1, 3, 4 and 7 are the best band composition for preparing the color composite images [59].

2.9. Land use and land cover (LU/LC)

Land-use and land-cover change being one of the major driving forces of global ecological change, is vital to the sustainable development discussion. One of the most accurate methods

	PW	AW	R
Band 1: Blue	0.45–0.52	0.452–0.518	30
Band 2: Green	0.52–0.60	0.528–0.609	30
Band 3: Red	0.63–0.69	0.626–0.693	30
Band 4: Near Infrared (NIR)	0.76–0.90	0.776–0.94	30
Band 5: Middle Infrared (MIR)	1.55–1.75	1.567–1.784	30
Band 6: Thermal Infrared (TIR)	10.40–12.50	10.45–12.42	120
Band 7: Middle Infrared (SWIR)	2.08–2.35	2.097–2.349	30

Source: [57]. Planned wavelength (PW), Actual wavelength (AW), Resolution (R).

Table 2. Band Wavelength (urn) and resolution (m) for Landsat 5.

to comprehend how land was used in the past, the types of changes to be expected in future, and also the forces and processes behind the changes is LU/LC analysis [45]. Increase in population, which lead people to clear forest for agricultural purposes in conjunction with anthropogenic activities accounts for the changes in LU/LC [60]. Messay [61] used sequential satellite images and GIS technologies, in combination with field observations, to investigate the LU/LC changes in the district of Nonno. The author stated that the overall consequence of conversion and modification processes of the LU/LC is the severe decrease in quality of the natural environment in the area. Changes in land use and land-cover provide a wide range of effect on environmental and landscape qualities including quality water, land and air resources, processes of ecosystem and functions, and the climate system itself through greenhouse gas fluxes [62]. Land cover is a significant element in change studies, affecting many aspects of the environmental system. Accurate and updated change in land cover information is necessary to understand the main factor causing changes and its environmental consequences [3]. Significant land-cover and land-use variation occurred in areas where irrigation is being practice in response to the increase of saline soils from time to time affecting crop cultivation leading to change in land-use [63]. The baseline data required for adequate and good understanding on the land-use patterns of previous years and its impacts can be extracted from Land-cover analysis. It also helps to figure out the percentage of the past land-cover changes and the physical factors behind [64]. Changes in land-use that occurs especially through deforestation and improper cultivation practice may rapidly degrade the quality of soil, as ecologically sensitive constituents of the habitats are not able to buffer the adverse effects. As a result, severe deterioration of the soil quality may result, leading to a permanent degradation of land productivity, and land degradation increases agricultural costs to maintain soil [65]. One of the major impacts of Land-use and Land-cover changes in arid and semi-arid region is soil salinization, this occur mostly wherever irrigation is being practiced. The decrease in soil quality due to accumulation of salts and sodicity keeps increasing at an alarming rate of endangering agricultural ecosystem and its environment [66].

	PW	AW	R
Band 1: Blue	0.45–0.52	0.452–0.514	30
Band 2: Green	0.52–0.60	0.519–0.601	30
Band 3: Red	0.63–0.69	0.631–0.692	30
Band 4: Near Infrared (NIR)	0.77–0.90	0.772–0.898	30
Band 5: Middle Infrared (MIR)	1.55–1.75	1.547–1.748	30
Band 6: Thermal Infrared (TIR)	10.40–12.50	10.31–12.36	60
Band 7: Middle Infrared (SWIR)	2.09–2.35	2.097–2.346	30
Band 8: Panchromatic	0.52–0.90	0.515–0.896	15

Source: [57]. Band 8 (ETM+ only) is higher resolution visible light data.
Planned wavelength (PW), Actual wavelength (AW), Resolution (R).

Table 3. Band Wavelength (urn) and resolution (m) for Landsat 7.

2.10. Landsat index

Soil and green vegetation have different methods of reflectance characteristics. The mixture of soil, green vegetation and shade in the pixels make remote sensing of land cover a challenge. Stewar and Rogerson [67] used vegetation indices to minimize the impacts of soil background and biological aging materials. Vegetation indices such as salinity index (SI), Soil Adjusted Vegetation Index (SAVI), Enhanced Vegetation Index (EVI), Green Vegetation Index (GVI), Transformed Soil Adjusted Vegetation Index (TSAVI), Simple Ratio (SR), Normalized Salinity Differential Index (NSDI), and Normalized Differential Vegetation Index (NDVI) are used to classified salt affected land to give better results [68].

2.10.1. Salinity index (SI)

Salinity index is the fraction of red band to near infrared band (NIR). The equation below describes salinity index equation [69].

$$\mathrm{SI} = \frac{Band\ 3}{Band\ 4} \tag{1}$$

Lhissou et al. [70] cited that Al-khaier [71] reported the usefulness of the salinity index using ASTER (Advance Space borne Thermal Emission and Reflection Radiometer) sensor data in mapping salinity of irrigated farmland in Syria. Salinity Index (SI), and Normalized Differential Salinity Index (NDSI) give good results in detecting salt-affected lands; the spectral reflectance of NIR, which radioed with red hand, gives very spectral values for vegetation [72].

2.10.2. Normalized differential salinity index (NDSI)

NDSI is the ratio of the difference between the red band and NIR to the summation of the red band and NIR. Chandana et al. [73] used NDSI for identification of salt affected soils in

assessment of soil salinity level of Pambantota district, Southern Sri Lanka, based on remote sensing information of TM sensor of Landsat 7 satellite. The equation for calculating NDSI is given in Eq. (2) [74].

$$\text{NDSI} = \frac{Band\ 3 - Band\ 4}{Band\ 3 + Band\ 4} \tag{2}$$

2.10.3. Normalized different vegetation index (NDVI)

The vegetation cover of a place can be examined using Normalized different vegetation index (NDVI) method [75]. NDVI is expressed as the fractional difference between NIR and red band to the addition of the two. It may be calculated from reflectance measured in the visible and near infrared channels from satellite based remote sensing. According to [75] NDVI shows spatial and temporal change of vegetation cover. The use of NDVI helps to create better and visual interpretation of healthy vegetation in contrast to other features [73]. The amount of salt present in the soil can be measured using NDVI through stressed vegetation; Aldakheel et al. [73, 76] gave the mathematical expression of NDVI as:

$$\text{NDVI} = \frac{Band\ 4 - Band\ 3}{Band\ 3 + Band\ 4} \tag{3}$$

NDVI has been used many researches to work mask vegetation from non-vegetation, and to detect the spatio-temporal change in vegetation biomass. Panah and Goossens [23] used TM based NDVI as an indicator of vegetation cover to separate bare soil from vegetation cover 1990 and the MSS based NDVI was taken to separate bare soil from vegetation cover in 1975. In Egypt, Masoud and Koike [77] used vegetation indices to examine and monitored salinization from changes in surface characteristics and radiometric thermal temperature for specific years. Darvishsefat et al. [78] classified salt affected soils based on ETM+ images acquired for Hoze Soltan Ghom area using image proportional and principal component analysis method. They claimed that the methods used were not suitable for image classification of saline soils. Saha et al. [47] employed band 3, 4, 5, and 7 of TM images to classifying salt affected land of moorland in India with an accuracy of 95%. Landsat ETM+ was applied in preparation soil salinity assessment for Texaco in Mexico [79]. Combined spectral response index (COSRI) and an exponential model was used to derive a high correlation coefficient between soil characteristics and spectral values of the multiband index. They reported values between −0.885 and 0.857 for EC and sodium adsorption ratio SAR as a correlation coefficient respectively with derived variance of 82.6 and 75.1% for EC and SAR as respectively. Unsupervised image classification technique is largely automated while supervised classification method requires considerable human input in the classification process [80]. Classification of soil using different Band Combination is presented in **Table 4**.

2.10.4. Pixel purity index (PPI)

Pixel Purity Index (PPI) is a way of finding the most spectrally pure pixels in hyper-spectral and multispectral images [81]. The most spectrally pure pixels typically correspond to mixing

Band Combination	Classification	Total Accuracy	Total Accuracy (Medium and High Salinity)
1,2,3,4,5,7	Supervised (Maximum likelihood Classification)	57%	66.20%
1,3,7	Supervised (Maximum likelihood Classification)	51%	56.50%
1,3,4,7	Supervised (Maximum likelihood Classification)	54%	71.3%
1,3,4,7	Hybrid	50%	80.5%
1,2,3	Supervised (Maximum likelihood Classification)	40%	***
1,3,4,7	Hybrid (No salinity and High salinity)	62%	***

Source: [59].
*** No figure.

Table 4. Total Accuracy of soil classification based on different Band Combination.

end-members. The PPI values are calculated by projecting n-dimensional scatterplots onto a random unit vector repeatedly. The pure pixels in each projection are recorded and the total number of period at which each pure pixel was marked is noted [71]. The digital number (DN) of each PPI generated corresponds to the number of pixel occurrence, which is recorded as extreme. The PPI normally run on a Minimum Noise Fraction (MNF) transform result apart from the noise bands. Results of the unmixing model and conventional classification technique are then compared for identification of land quality reduction in region [82]. Number of iterations with different threshold limit is carried out interactively to separate the position of most pure pixels in the image. A threshold of two are fixed for the identification of pure pixels in the image which will be explained as, all the pixels having 2 DN values (maximum limit) greater than the extreme pixel is thought to be pure. Two different sets of iterations 1000 and 5000 is carried out on the data set while keeping the threshold at two. The more the number of iterations, the more the number of extreme pixels found with more variability in the data set [40]. The value in the PPI image indicates the number of times each pixel as extreme in some projection while PPI image with higher values indicate pixels that are closer "corners" to the n-dimensional data cloud, and are hence relatively purer than the pixels with lower value. Lastly, Region of interest (ROI) is generated for the PPI image keeping the minimum threshold limit at 50, after comparing the PPI image with calibrated image to get a better idea about the position of the pure pixels [83].

2.10.5. Digital analysis using surface vegetation index

Vegetation index is a spectral index that detects the presence of chlorophyll [84]. Various crop indices have been derived using the fact that chlorophyll strongly absorbs the light energy in the red part and highly reflects in the near-infrared part [85]. Several researches for specific analyses have proposed a number of vegetation indices. Many papers have explained the

detection of salinity through its effect on the vegetation. Richardson et al. [86] specified that an inverse relationship is observed between reflectance and salinity, as salt content induces less plant cover (decreasing of density, LAI and height) and sometimes slight salt deposition on surface associated with vegetation have similar reflectance as that of normal cropped area. Salt tolerant plants are good references of salinity level on salt marshes but necessitate good calibration [30]. Contrasted associations of vegetation and bare soils can be more useful for salinity detection than individual surface types. Remotely sensed imagery cannot be used to classify and assess soil profile. Spectral characteristics of the earth surface features that are indicative of subsurface conditions can be analyzed. Satellite multi-spectral data denote changes that aid in locating mapping units; they hold great promise for soil surveys and land-use planning [87]. Some relationships have been established to relate soil properties and spectral data while most of these properties have been from the surface soil, subsurface properties that influence some surface characteristics were considered. Satellite sensors observe only the ground surface, actually both subsurface and surface soil conditions are influenced by common genetic factors [88]. Both subsurface conditions and surface conditions are plant canopy. Therefore, when satellite imagery depicts a pattern based on a different spectral response, it is not unreasonable to attempt some inferences about subsurface soil patterns [70].

2.10.6. Image classification

There are many procedures commonly used for the classification of remote sensing images and this depends on the radiometric information in the image bands. The traditionally used classification method is a pixel-based approach and is one of the procedures based on conventional statistical techniques and it performs well. Pixel based approach is based on conventional statistical techniques, such as parallelepiped, maximum likelihood and minimum distance procedures [57]. In pixel-based classification, two kinds of traditional classification methods-unsupervised classification and supervised classification are used. Ideally, pixels are expected to be to a degree, more or less grouped in the multispectral space in clusters corresponding to different land cover types [89]. It is a classic classification approach that classifies an image pixel by pixel and one pixel can only be classified into one class, thus produces is a hard classification [67].

2.10.7. Classification of digital satellite data

The basic characteristics of digital image acquired by remote sensing method are composed of pixels. According to [24], the intensity of each pixel corresponds to the mean radiance measured electrically over the ground area corresponding to each pixel. Each pixel has digital number (DN) corresponding to the average radiance measured in this pixel. This number from quantizing the original electrical signal from the sensor result into positive integer values using a process termed analogue-to-digital signal conversion [90]. The DNs comprising of a digital image are recorded over numerical ranges as 0–255, 0–511, or higher. These ranges correspond to the set of integers that were recorded using 8-, 9-, and 10-bit binary computer coding scales, respectively. In such numerical formats, the image can be analyzed with the aid of computer [91]. A digital image is a 2-dimension array of elements; the corresponding

area on the earth's surface was stored in each element emitted from the energy. The spatial arrangement of the measurements defines the image or image space, depending on the sensor; data are recorded in n bands.

3. Conclusion

The chapter demonstrates possibility of use of high technology in particular remote sensing and GIS technology in land cover/land use and soil salinity monitoring with demonstration of advantages of use such technology in similar problem solving. Detection of soil salinity by conventional means of soil survey requires a great deal of time, but the application of geospatial analysis using remote sensing and GIS techniques minimize time consuming and offer the possibility assessment, modeling and mapping of irrigated land. The chapter also worked on general subjects with reflection of the cycle of satellite data use with a variety of application, indexes for registration and data processing stage. The fact is that the use of space technology advances in land classification are commonly used instrument for soil monitoring which is one of the suitable and flexible instrument from a wide point of view. The instrument makes it possible to perform results conveniently for users. In addition, the application of these indexes is a good indicator of soil salinity in irrigated lands, which may influence decision on reclamation of soil salinity and used as an input for agricultural land management. Irrigation managers, planners, farmers and government agencies for smart agriculture can use models and maps generated through geospatial analysis.

Acknowledgements

The authors would like to thank UNISA for providing their literature datasets.

Conflict of interest

The authors declared no potential conflicts of interest with respect to the research, authorship, and/or publication of this article.

Author details

Olumuyiwa Idowu Ojo* and Masengo Francois Ilunga

*Address all correspondence to: ojooi@unisa.ac.za

Department of Civil and Chemical Engineering, University of South Africa, Pretoria, South Africa

References

[1] Rhoades JD, Chanduvi F, Lesch S. Soil salinity assessment: Methods and interpretation of electrical conductivity measurements. FAO Irrigation and Drainage Paper. 1999;**57**: 1-148

[2] Ehlers M. Geoinformatics and digital earth initiatives: A German perspective. International Journal of Digital Earth. 2008;**1**:17-30 (2007)

[3] Rimal B. Application of remote sensing and GIS, land use / land cover change in Kathmandu Metropolitan city, Nepal. Journal of Theoretical and Applied Information Technology. 2011;**23**(2/3):80-86. Retrieved from: www.jatit.org

[4] Abd-elwahed MS. Assessment of soil salinity problems in agricultural areas through spatial and temporal remote sensing. Egyptian Journal of Basic and Applied Sciences. 2005;**4**(2):23-30

[5] Adeniran KA, Amodu MF, Adeniji FA. Water requirements of some selected crops in Kampe dam irrigation project. Australian Journal of Agricultural Engineering. 2010;**4**(1): 119-125

[6] FAO. World Food Summit. Agriculture and Food Security; 1996

[7] Pal le R, Preez CD, Strydom MG, Rensburg VL, Bennie ATP. Effect of irrigation on soil salinity profiles along the Lower Vaal River. Water SA. 2007;**33**(4):473-478

[8] Yahaya M. Development and challenges of Bakolori irrigation project in Sokoto State, Nigeria. Nordic Journal of African Studies. 2002;**11**(3):411-430

[9] Rietz DN, Haynes RJ, Chidoma S. Effects of soil salinity induced under irrigated sugarcane in the Zimbabwean Lowveld on soil microbial activity. Proceedings of the South Africa Sugar Technologists Associations. 2001;**75**:68-74

[10] Murray R, Grant C. The impact of irrigation on soil structure. The National Program for Sustainable Irrigation. Braddon, Australia: Land & Water Australia Publications; 2007. pp. 1-43

[11] Warrence BNJ, Bauder JW, Pearson KE. Basics of Salinity and Sodicity Effects on Soil Physical Properties. Bozeman: Department of Land Resources and Environmental Science, Montana State University; 2002. pp. 1-29

[12] Mougenot B, Epema GF, Pouget M. Remote sensing of salts affected soils. Remote Sensing Reviews. 1993;**7**:241-259

[13] Agbu PA, Fehrenbacher DI, Jansen IJ. Soil-property relationships with SPOT satellite digital data in East Central Illinois. Soil Science Society of America Journal. 1990;54:807-812

[14] Steven MD, Malthus TJ. Monitoring responses of vegetation to stress. In: Cracknell AP, Vaughan RA, editors. Proceedings of the 18th Annual Conference of the Remote Sensing Society. Nottingham, UK: Remote Sensing Society; 1992

[15] Ojo OI, Ochieng GM, Otieno FOA. Assessment of water logging and salinity problems in South Africa: An overview of Vaal hart's irrigation scheme. WIT Transactions on Ecology and the Environment. 2011;**153**(4):477-484

[16] Reza A, Sanaeinejad SH, Parisa MH, Marjan G, Atefeh K. Evaluation of vegetation cover and soil indices for saline land classification in Neyshabour Region using ETM+ Landsat. International Symposium on Geoinformatics for Spatial Infrastructure Development in Earth and Allied Sciences, Mashhad, Iran. 2008;**3**(1):1-10

[17] Miller DJ. Programs for DEM analysis. In: Landscape dynamics and forest management. General Technical Report. RMRS-GTR-101CD. Fort Collins, CO, USA: USDA Forest Service, Rocky Mountain Research Station, CD-ROM; 2003. http://www.fsl.orst.edu/clams/prj_wtr_millerprg.html. Last Accessed on October 28, 2017

[18] Keskar YM, Kumar S. Need of remote sensing and geographical information system in urban planning, a case of housing colony in Bhopal City, Madhya Pradesh, India. International Journal of Engineering Research and Technology. Oct. 2013;**2**(10):1752-1752. ISSN: 2278-0181

[19] Ejikeme JO, Igbokwe JI, Emengini EJ. Spatial analysis of impacts of fugitive emission concentration using GIS and remote sensing techniques: A case study of Onitsha Metropolis, Anambra State, Nigeria. International Journal of Engineering Research and Technology (IJERT). 2013;**2**(4):388-397

[20] Pradesh A, Haryana K, Karnataka D, Rajasthan B, Gujarat A. A Methodology for Identification of Waterlogging and Soil Salinity Conditions Using Remote Sensing. Joint Completion Report on IDNP Result; Switzerland: World Meteorological Organization; 2002. pp. 1-78

[21] Kiran VSS, Sankar GJ, Rao MJ. Application of remote sensing and GIS for modeling and assessment of land use / land cover changes in Krishna Delta. Environmental Management. 2000;**4**:21-70

[22] Nezami MT, Alipour ZT. Preparing of the soil salinity map using geo-statistics method in the Qazvin Plain. International Institute for Geo-Information Science and Earth Information Journal. 2012;**3**(2):36-41

[23] Panah SKA, Goossens R. Relationship between the Landsat TM, MSS DATA and soil salinity. Journal of Agricultural Science and Technology. 2001;**3**:21-31

[24] Salman A. Using State-of-the-Art Remote Sensing and GIS for Monitoring Waterlogging and Salinity. Lahore, Pakistan: International Water-Management Institute; 2000

[25] Baber JJ. Detecting crop conditions with low-altitude aerial photography: Causes and effects, non-uniformity of fertilizer application, poor water pattern, drainage needs. In: Johannsen CJ, Sanders JL, editors. Remote Sensing for Resource Management. Ankeny, Iowa: Soil Conservation Society of America. 1982. pp. 407-412

[26] IDNP. A Methodology for Identification of Waterlogging and Soil Salinity Conditions Using Remote Sensing. Karnal: CSSRI; Wageningen: Alterra-ILRI; 2002. p. 78

[27] Pattanaaik SK, Singh OP, Sahoo RN, Singh DK. Irrigation induced soil salinity mapping through principal component analysis of Remote Sensing data. Journal of Agricultural Physics. 2008;**8**:29-36

[28] Franco-Plata R. Using a GIS tool to map the spatial distribution of population for 2010 in the State of Mexico, Mexico. Journal of Geographic Information System. 2012;**04**(January): 1-11. http://doi.org/10.4236/jgis.2012.41001

[29] Abdalsatar A, Aldabaa A, Weindorf DC, Chakraborty S, Sharma A, Li B. Combination of proximal and remote sensing methods for rapid soil salinity quantification. Geoderma. 2015;**239-240**:34-46. http://doi.org/10.1016/j.geoderma.2014.09.011

[30] Farifteh J. Imaging Spectroscopy of salt-affected soils: Model-based integrated method. Journal of Management and Entrepreneurial Development. 2007;**3**(1):1-235

[31] Robbins CW, Wiegand CL. Field and Laboratory Measurements. New York: Agricultural Salinity Assessment and Management, American Society of Civil Engineering; 1990

[32] Brunner P. Generating soil electrical conductivity maps at regional level by integrating measurements on the ground and remote sensing data. International Journal of Remote Sensing. 2007;**28**(15):3341-3361

[33] Maina MM, Amin MSM, Aimrun W, Sani I. Soil salinity assessment of Kadawa Irrigation of the Kano River Irrigation Project (KRIP). Journal of Food, Agriculture and Environment. 2012;**10**(2):56-68

[34] Hussien IM, Zhu X, Zhou G, Ahmed N, Nimir E. Comparison of germination and seedling characteristics of wheat varieties from China and Sudan under salt stress. The American Society of Agronomy. 2016;**108**(1):103

[35] van der Lelij A. Use of Electromagnetic Induction Instrument (Type EM-38) for Mapping Soil Salinity. New South Wales, Australia: Water Resources Commission, Murrumbidgee Division; 1983

[36] Williams BG, Baker G. An electromagnetic induction technique for reconnaissance surveys of soil salinity hazards. Australian Journal of Soil Resources. 1982;**20**:107-118

[37] Seghal J, Saxena RK, Verma KS. Soil resources inventory of Indian using image interpretation techniques in remote sensing as a tool for soil scientist. In: Proceeding of the Fifth Symposium of the Working Group Remote Sensing ISSS. Budapest, Hungary. 1988. pp. 17-31

[38] Dwivedi RS. Monitoring and the study of effects of image scale on delineation of salt-affected soils in the Indo-Gangetic plains. International Journal of Remote Sensing. 1992;**13**:1527-1536

[39] Millington AC. Monitoring salt playa dynamics using Thematic Mapper data. IEEE Transactions on Geoscience and Remote Sensing. 1989;**27**:745-761

[40] Crowley J. Mapping playa evaporite minerals with AVIRIS data. A first report from Death Valley, California. Remote Sensing Environment. 1993;**44**:337-356

[41] Mehrjardi RT, Taze M, Sahebjalal E. Accuracy assessment of soil salinity map in Yazd-Ardakan Plain, Central Iran, based on Landsat ETM+ imagery. American-Eurasian Journal of Agriculture and Environmental Sciences. 2008;**3**(5):708-712

[42] Shrestha DP, Farshad A. Mapping salinity hazard: An integrated application of remote sensing and modeling-based techniques. In: Metternicht G, Zinck JA, editors. Remote Sensing of Soil Salinization; Impact of Land Management. Boca Raton, USA: CRC Press, Taylor & Francis Group LLC; 2009. pp 257-270

[43] Idoko A, Femi M, Rotimi M. Population growth and economic growth: The Nigerian experience. Journal of Management and Entrepreneurial Development. 2013;**3**(1):1-13

[44] Metternicht GI. Assessing temporal and spatial changes of salinity using fuzzy logic, remote sensing and GIS. Foundation of an expert system. Ecological Modelling. 2001; **144**(2-3):163-179

[45] Nanni RM, Alexander J, Damatte M. Spectral reflectance methodology in comparison to traditional soil analysis. Soil Science Society of America Journal. 2006;**70**:393-407

[46] Szabolcs I. Salt affected soils. Photographic and videographic observations for determining and mapping the response of cotton to soil salinity. Remote Sensing of Environment. 1987;**1**(49):212-213

[47] Saha SK, Kudra M, Bhan S. Digital processing of Landsat TM data for watershed mapping in parts of Aligarh District, Uttar Pradesh, India. International Journal of Remote Sensing. 1990;**11**:485-492

[48] Rao B, Venkataraman L. Mapping the magnitude of sodicity in part of the Indo-Gangetic plains of Uttar Pradesh, Northern India using Landsat data. International Journal of Remote Sensing. 1991;**12**:419-425

[49] Al-hassoun SA. Remote sensing of soil salinity in arid areas. International Journal of Civil & Environmental Engineering IJCEE-IJENS. 2011;**10**(02):11-20

[50] Vidal A, Tabet D, Ahmad MD, Asif S, Zimmer D, Strosser P. Salinity assessment in irrigation systems using remote sensing and geographical information systems - application to Chistian subdivison, Pakistan; Report R-47; Lahore, Pakistan: International Water Management Institute; 1998

[51] Wu J, Vincent B, Yang J, Bouarfa S, Vidal A. Remote sensing monitoring of changes in soil salinity: A case study in Inner Mongolia, China. Sensors. 2008. http://doi.org/10.3390/s8117035

[52] Peng W. Synthetic analysis for extracting information on soil salinity using remote sensing and GIS: A case study of Yanggao basin china. Environmental Management. 1998;**22**(1):153-159

[53] Ben-Dor E, Patkin K, Banin A, Karnieli A. Mapping of several soil properties using DAIS-7915 hyperspectral data: A case study over clayey soil in Israel. International Journal of Remote Sensing. 2002;**23**(6):1043-1062

[54] Janssen L, Gorte GH. Principle of Remote Sensing, chapter 12 Digital image classification. Enschede, the Netherlands: International Institute for Aerospace Survey and Earth Science, ITC; 2001

[55] Verma K, Saxena RK, Barthwal AK, Deshmukh SN. Remote sensing technique for mapping salt affected soils. International Journal of Remote Sensing. 1994;**15**(9):1901-1914

[56] Coker AE. The application of remote sensing technology to assess the effects of and monitor change in coal mining in Eastern Tennessee. In: Proceedings of the First Annual William Symposium. Falls Church. 1997. pp. 95-105

[57] Goslee SC. Analyzing remote sensing data in R: The Landsat package. Journal of Statistical Software. 2011;**43**(4):1-25. Retrieved from: http://www.jstatsoft.org

[58] Chander G, Markham BL, Helder D. Summary of current radiometric calibration coefficients for Landsat MSS, TM, ETM, and EO-I ALI sensor. Remote Sensing of Environment. 2009;**113**:893-903

[59] Sanaeinejad SH, Astaraei A, Mousavi PM, Ghaemi M. Selection of best band combination for soil salinity studies using ETM+ satellite images. World Academy of Science, Engineering and Technology. 2009;**54**:519-521

[60] Gebresamuel G, Singh BR, Dick O. Land-use changes and their impacts on soil degradation and surface runoff of two catchments of Northern Ethiopia. Acta Agriculturae Scandinavica, Section B — Soil & Plant Science. 2010;**60**:211-226

[61] Messay MT. Land-use/land-cover dynamics in Nonno district, central Ethiopia. Journal of Sustainable Development in Africa. 2011;**13**(1):123-141

[62] Lambin E, Rounsevell MDA, Geist HJ. Are agricultural land use model able to predict changes in land use intensity? Agriculture, Ecosystems and Environment. 2000;**82**:321-331

[63] Zewdu S, Suryabhagavan KV, Balakrishnan M. Land-use/land-cover dynamics in Sego Irrigation Farm, Southern Ethiopia: A comparison of temporal soil salinization using geospatial tools. Journal of the Saudi Society of Agricultural Sciences. King Saud University and Saudi Society of Agricultural Sciences. 2014:1-7. http://doi.org/10.1016/j.jssas. 2014.03.003

[64] Mengistu D, Salami A. Application of remote sensing and GIS in land use/land cover mapping and change detection in a part of southwestern Nigeria. African Journal of Environmental Science and Technology. 2007;**1**:99-109

[65] Abera Y, Belachew T. Effects of land use on soil organic carbon and nitrogen in soils of Bale, South Eastern Ethiopia. Tropical and Subtropical Agroecosystems, 2011;**14**:229-235

[66] Sonmez S, Buyuktas D, Okturen F, Citak S. Assessment of different soil to water ratios (1:1, 1:2.5, 1:5) in soil salinity studies. Geoderma Regional. 2008;**144**:361-369

[67] Stewar TFA, Rogerson PA. GIS and spatial analytical problems. International Journal of Geographical Information Systems. 1993;**7**(1):3-19. http://doi.org/10.1080/02693799308901936

[68] Gitelson AA, Chivkunova OB, Merzlyak MN. Assessing carotenoid content in plant leaves with reflectance spectroscopy, photochemistry and photobiology. International Journal of Pharmaceutics. 2002;**75**:272-281

[69] Tripathi NK, Rai BK, Dwivedi P. Spatial modelling of soil alkalinity in GIS environment using IRS data. In: Proceedings of 18th Asian Conference on Remote Sensing. 1997. pp. 20-24

[70] Lhissou R, El A, Chokmani K. Mapping soil salinity in irrigated land using optical remote sensing data. Eurasian Journal of Science. 2014;**3**:82-88

[71] Al-khaier F. Soil salinity detection using satellite remote sensing. African Journal of Environmental Science and Technology. 2003;**2**(4):7-20

[72] Amal MA, Benni JT. Monitoring and evaluation of soil salinity in term of spectral response using Landsat images and GIS in Mesopotamian plain. Journal of Iraqi Desert Studies Special Issue of First Scientific Conference. 2010;**2**(2):19-32

[73] Chandana PG, Weerasinghe KDN, Subasinghe S, Pathirana S. Remote sensing approach to identify salt-affected soils in Hambantota District. In: Proceedings of the Second Academic Sessions; 2004. pp. 128-133

[74] Ochieng GM, Ojo OI, Otieno FAO, Mwaka B. Use of remote sensing and geographical information system (GIS) for salinity assessment of Vaal-Harts irrigation scheme, South Africa. Environmental System Research. 2013;**2**(4):1-12

[75] Amdihun A. GIS and remote sensing integrated environmental impact assessment of irrigation project in Finchaa Valley area. International Journal of Digital Earth. 2000;**4**: 400-417

[76] Aldakheel Y, Elprince AM, Aatti MA. Mapping vegetation and saline soil using NDVI in arid irrigated lands. In: ASPRS 2006 Annual Conference; 2006. pp. 1-6 (1992)

[77] Masoud AA, Koike K. Arid land salinization detected by remotely sensed land cover changes: A case study in Siwa region, NW Egypt. Journal of Arid Environments. 2006;**66**(1): 151-167

[78] Darvishsefat AA, Damavandi MH, Jafari M, Zehtabiyan GR. Assessing of Landsat TM images for using in soil salinity classification. Journal of Desert. 2000;**5**(2):56-67

[79] Fernandez-Bucesa N, Siebea C, Cramb S, Palacio JL. Mapping soils salinity using a combined spectral response index for bare soil and vegetation: A case study in the former lake Texaco, Mexico. Journal of Arid Environments. 2006;**65**:644-667

[80] Al-Tamimi S, Al-Bakri J. Comparison between supervised and unsupervised classifications for mapping land use/cover in Ajloun area. Jordan Journal of Agricultural Sciences. 2005;**1**(1):73-83

[81] Bordman JW, Kruse FA. A geologic example using AVIRIS data, north Grapevine Mountains, Nevada. In: Proceedings, Tenth Thematic Conference on Geologic Remote Sensing, Environmental Research Institute of Michigan; 1994

[82] Aymn E, Garcia LA, Gates TK. A remote sensing - GIS approach to evaluate the effects of soil salinity on evapotranspiration. Hydrology Days. 2007;**2**(970):80523

[83] Oosterbaan R. Saline soils in brief. Journal of Agricultural Science and Technology. 2003; **10**(2):6-10

[84] Daniel AM, Ayobami TS. Application of remote sensing and GIS inland use / land cover mapping and change detection in a part of southwestern Nigeria. African Journal of Environmental Science and Technology. 2007;**3**(1):99-109

[85] Devia GK, Ganasri BP, Dwarakish GS. A review on hydrological models. Aquatic Procedia. 2015;**4**(ICWRCOE):1001-1007. http://doi.org/10.1016/j.aqpro.2015.02.126

[86] Richardson AJ, Gerbermann AH, Gausmann HW, Cuellar JA. Detection of saline soils with Skylab multi-spectral scanner data. Photogrammetric Engineering and Remote Sensing. 1976;**42**:679-684

[87] Garcia L, Eldeiry A, Elhaddad A. Estimating soil salinity using remote sensing data. In: Proceedings Central Plains Irrigation Conference; 2005, pp. 1-10 [Online]. Available at: http://www.ksre.ksu.edu/irrigate/OOW/P05/Garcia.accessed on July. 2017

[88] Ojo OI. Mapping and modeling of irrigation induced salinity of Vaal-Harts irrigation scheme in South Africa [Unpublished D.Tech thesis]. South Africa: Dept of Civil Engineering, Tshwane University of Technology; 2013

[89] Pitt JL, Provin T. Managing soil salinity. Texas A & M AgriLife Extension. 2001;**60**:3-12

[90] Ali RR, Kotb MM. Use of satellite data and GIS for soil mapping and capability assessment. 2010;**8**(8):104-115

[91] Ibrahim MM, Dafalla M, Elhag AM. Monitoring, predicting and quantifying soil salinity, sodicity and alkalinity in Sudan, using soil techniques, remote sensing and GIS analysis, case study: University of Khartoum top farm. International Journal of Scientific and Research Publications. 2013;**3**(3):1-7

Satellite Navigation System

Chapter 5

The Use of GNSS GPS Technology for Offshore Oil and Gas Platform Subsidence Monitoring

Heri Andreas, Hasanuddin Z. Abidin, Irwan Gumilar,
Dina A. Sarsito and Dhota Pradipta

Additional information is available at the end of the chapter

http://dx.doi.org/10.5772/intechopen.73565

Abstract

Due to oil and gas exploitation, offshore oil and gas platform may experience subsidence. Continuing subsidence may deform the platform infrastructures, adding the risk for any failure on the platform objects. The failure means disaster. Therefore the subsidence information is mandatory for risk assessment and safety requirement. Repeatedly or continuous monitoring of accurate positions on the platform by using global navigation satellite system global positioning system (GNSS GPS) technology may reveal the changing of even small positions which are representing subsidence on the platform. This chapter will be deeply discussed on the use of GNSS GPS technology for offshore oil and gas platform subsidence monitoring, especially in Indonesia, the archipelago country where long baseline between reference station in the land and monitoring station at the sea slightly exists. The capability and especially the high performance of this technology on deriving subsidence information along with data sample of long baseline will be highlighted.

Keywords: GNSS GPS, accuracy, oil and gas platform, subsidence, monitoring

1. Introduction

Nearly of today the global navigation satellite system global positioning system (GNSS GPS) technology has been played as remarkable tool for positioning and mapping and with high accuracy can be achieved in the easiest way [1–3]. By observing several satellites and measuring their distance, and with the known of their satellite coordinates and the distance from observation, in this case the coordinate on location at the earth can be calculated. In everywhere and in anytime worldwide when signals from the satellites are received by the receivers, in these cases the position in 3D or even 4D can be determined precisely and even with

precision in the order of millimeter. The GNSS (GPS) indeed become a revolution in positioning on the twentieth century.

Repeated or continuous monitoring of accurate positions on the objects (e.g., offshore oil and gas platform) may reveal the changing of positions which are representing deformation (e.g., subsidence). Due to oil and gas exploitation, offshore oil and gas platform may experience subsidence. The rates can vary from 1 to 10 cm per year and even more for certain places. This subsidence information is mandatory for risk assessment and safety requirement. Continuing subsidence may deform the platform infrastructures, adding the risk for any failure on the platform objects.

2. Oil and gas platform subsidence

People commonly use fuel for transportation, electricity, machine, housing, etc. The fuels are produced from oil and gas exploitation. First, we need to explore the existence of oil and gas through exploration using geoscience technique (e.g., geology and geophysics surveys). There are numerous oil and gas reservoirs onshore and offshore all around the world. Platforms are built around offshore reservoirs (**Figure 1**) and also onshore. Once we successfully locate the reservoirs, we do drilling and extract the oil and gas. As the extraction or exploitation continues, the reservoirs may deplete through time due to loss of pore pressure, etc. As consequences, the platform may experience subsidence.

Some platforms have trend of few centimeters per year while others in the order of 10 cm or event more; it depends on how much oil and gas are being exploited, pore pressure decreases, load from rock is there in the surrounding, is level of fluid injection, etc. This subsidence information as mentioned above is mandatory for risk assessment and safety requirement since disaster may occur from that situation.

Figure 2 shows the physical evidence of offshore oil and gas platform subsidence. From the first picture, we can see jacket walkway was missing, while from the second picture, we can see the landing boat is disappearing into the sea. The different elevation levels between decks are about 5–6 m. In this case by seeing the condition of jacket walkway and the landing boat,

Figure 1. Oil and gas platform offshore.

Figure 2. Subsidence evidence on oil and gas platform offshore.

the magnitude of subsidence is already quite large. It may be around 1–3 m. It is true that platform subsidence may reach 1–20 cm per year, especially on old oil and gas platform. The subsidence may continue through years. As mentioned before, continuing subsidence may deform the platform infrastructures, adding the risk for any failure on the platform objects. There are regulations for monitoring oil and gas platform both for onshore and offshore but especially offshore where the risk is higher.

Strategic position around plate boundary has made Indonesia rich of oil and gas resources, probably one of the largest in the world. Three major plates (e.g., Australia, Pacific, and Sunda Block) meet each other in Indonesia and formed many faults and basins area where usually we can found oil and gas resources. Millions of years of burned planktons getting heated by the mantle have turned them into an oil and also gas. Basin in eastern of Sumatera Island, eastern of Kalimantan, and northern of Java Island is rich in oil and gas resources both onshore and offshore. Bird head of Papua also potentially reserves huge amount of oil and gas. According to data released by Indonesia Ministry of Energy and Mineral Resources, the proven oil reservoirs in Indonesia are about 3306.97 MMS TB. Meanwhile the potential reservoirs are about 3994.20 MMS TB.

In spite of these potential resources, the areas of oil and gas in Indonesia especially the offshore area are prone to the risk of subsidence failure on the platform facilities. Along with this risk, the tilting and vibrations on the platform are also the risk. Huge oil and gas company is already realized about this situation, as well as the authorities. There are several regular programs on monitoring subsidence, tilting, and vibration on the platform. Nevertheless continues monitoring seems still beyond the agenda since it is relatively too expensive or people do not realize how important it is.

3. GNSS GPS for monitoring subsidence

The GNSS GPS principle of measurement is by observing of minimum four satellites and measuring their distance. With the known of their satellite coordinates from broadcast or precise

ephemeris and the distance from time synchronize of code data or phase calculation, in this case the coordinate on location at the earth can be calculated. This technology can measure accurately an object as small as an ant like depicted in **Figure 3**. From the figure, graph of position repetition within millimeter variation is seen. As mentioned previously the subsidence on the oil and gas platform can be vary for about 1–10 cm per year and even more. So, by using GNSS GPS technology, the accurate information of subsidence on the platform can be achieved confidently.

Once again we mention that the accurate subsidence information of oil and gas platform is mandatory for risk assessment and safety requirement. Monitoring program should be conducted regularly or even continuously. Continuing subsidence may deform the platform infrastructures, adding the risk for any failure on the platform objects. With surrounding full of gases and oil, the failure may cause fatality.

There are several methods on GNSS GPS positioning such as static method/GPS surveys, Real Time Kinematic (RTK), Precise Point Positioning (PPP), etc. each given the different levels of accuracy on the position. For subsidence monitoring, in order to achieve millimeter of accuracy, then the GPS survey method based on phase data should be implemented with stringent measurement and data processing strategies [3, 4]. GPS surveys relay on differential technique using minimum of two receivers and with this data differencing most of biases and error can be reduce significantly. PPP only use one receiver. In this case, the correction of clock and orbit is necessary. These two corrections can be downloaded from IGS community. The RTK is differential positioning in real-time mode with centimeter level of accuracy. In order to fulfill the need for real-time data differential correction, therefore data communication via radio, GPRS, or satellite communication is mandatory.

The principle of subsidence monitoring using repeated static method/GPS survey method is depicted in **Figure 4**. With this method, several points which are placed on the media covering

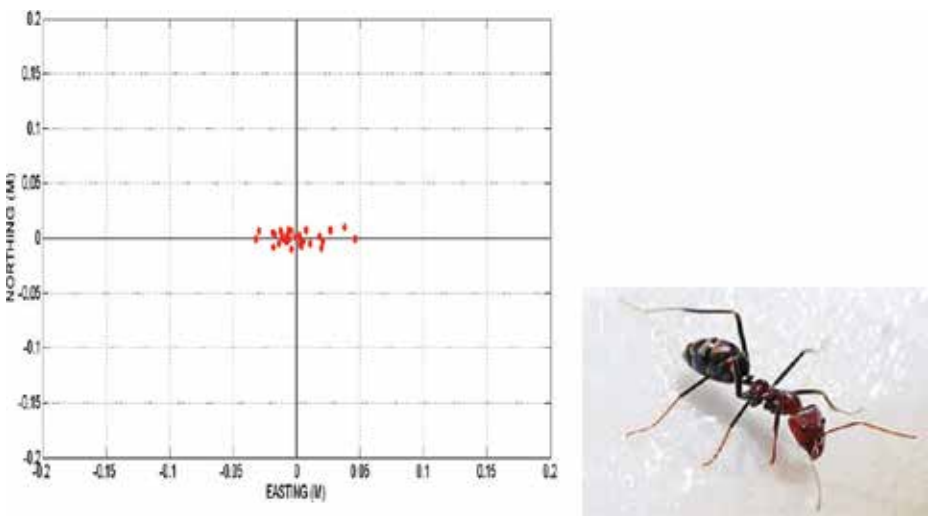

Figure 3. Graph of position repetition within millimeter variation derived from GNSS GPS measurement. An object as small as an ant can be positioned precisely.

http://dx.doi.org/10.5772/intechopen.73565

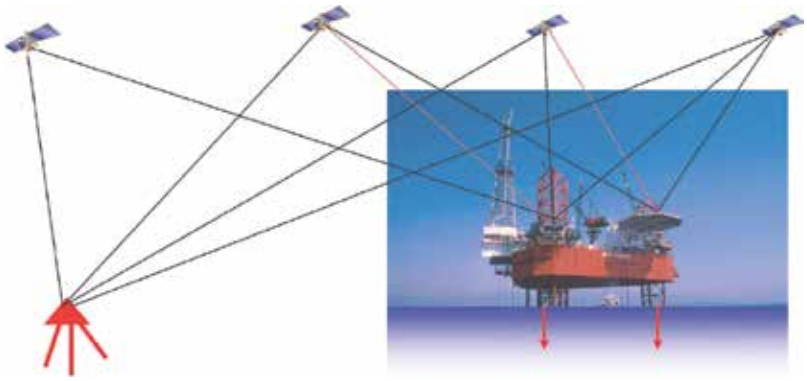

Figure 4. The principle of subsidence monitoring (e.g., platform subsidence) using repeated GNSS GPS survey method or CGPS (continuously operating the GPS receivers).

the area investigation are accurately positioned using GPS survey relative to a certain reference (stable) point. The precise coordinates of the points are periodically determined using repeated GPS surveys with certain time interval. With the same principle as GPS surveys, continuous determination of precise coordinate of point can be achieved by continuous observations. By studying the characteristics and rate of changes of the height component of coordinates from survey to survey or data to data in continuous mode, the subsidence characteristics can be derived. In the recent time, the capability of PPP is also promising to choose for subsidence monitoring.

In the case of studying the subsidence or other high-precision application, there are several advantages of using GNSS GPS survey method that should be noticed, such as the following: it provides the three-dimensional displacement vector with two horizontal and one vertical components, so it will give not only land subsidence information but also land motion in horizontal direction; it provides the displacement vectors in a unique coordinate reference system, so it can be used to effectively monitor land subsidence in a relatively large area like in offshore oil and gas field; the GPS can yield the displacement vectors with a several mm precision level which is relatively consistent in temporal and spatial domain, so it can be used to detect even a relatively small subsidence signal; and the GPS can be utilized in a continuous manner, day and night, independent of weather condition, so its field operation can be flexibly optimized.

The reference point is one important thing in order to have best monitoring of subsidence. We have to make sure the stability of reference point because it will be used to see relatively the subsidence at the monitoring point such as platform oil and gas. Approach of geological and geodetic can be applied. **Figure 5** shows the example of exercise to see stability over reference station by process time series of GNSS GPS data and plot the repeatability of their height component position. InSAR can also be used to see the stability of area where reference station took place. As from geology approach, the information of bed rock will help us on choosing the place for reference station.

To give clear description on how we measured in the investigation area (e.g., oil and gas platform), we give picture of documentation of real measurement in the field. The GNSS GPS receiver attached to the body of platform (usually on hand fence) is seen. Obviously to be

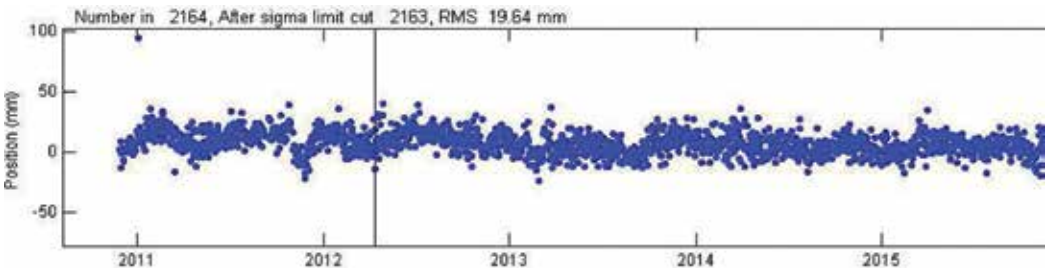

Figure 5. Example of stability of reference station from repeatability of their height component position through years of observation.

assured that it is stable for observation and visibilities to the satellite are good. It is needed also to define the best observation strategies, as it can be seen in **Table 1** (**Figure 6**).

Back to the reference station issue, for Indonesia case it can be interesting to discuss since Indonesia is an archipelago country. Most of the region is water, and many sources of oil and gas are taking place offshore (see **Table 2** and **Figure 7**). Scenario of choosing one reference station for whole Indonesia regions could be used, or we choose reference scenario by cluster. The baseline length will be crucial for both scenarios, since the accuracy theoretically depends on its length. Here we do data processing simulation for each scenario of long and even very long baseline, and the results can be found in **Tables 4** and **5** and **Figures 10–17** chapter data analysis.

Figure 7 shows map of onshore and offshore oil and gas area in Indonesian regions. There are six offshore regions as summarized in **Table 2**, and most of onshore oil and gas area is located in Sumatera, Java, Kalimantan, and Bird Head of Papua. In spite of these potential resources, the areas are prone to subsidence. Monitoring subsidence around these areas is necessary to make sure the safety on exploitation, etc.

Figure 8 shows long baseline concept using one stable reference station for subsidence monitoring (e.g., platform) along large offshore oil and gas area of Indonesia. The GNSS GPS stations with baseline length more than 1000 km are chosen for simulation and analyzed for their accuracy whether it can achieve the requirement for subsidence monitoring on the platform.

Figure 9 shows baseline concept using reference station at clustered offshore regions for subsidence monitoring (e.g., platform) along large offshore oil and gas area of Indonesia. The GNSS

Parameters observation	Observation strategy for millimeter accuracy
1. Receiver/observation signal	Geodetic dual phase L1/L2 obs and CODE
2. Observation times	Continuous or minimum 12 h session
3. Mas angle	15 degrees
4. Observation rate	30 s or higher rate

Table 1. Observation strategy that is generally used in order to derive millimeter accuracy of position such as for platform subsidence monitoring.

http://dx.doi.org/10.5772/intechopen.73565

Figure 6. Illustration of GNSS GPS data acquisition in the field for oil and gas platform subsidence monitoring.

Regions	Offshore oil and gas area block name
1. Offshore of East Coast of Sumatera	Aceh, Riau, Jambi, Lampung
2. Offshore of North Coast of Java	Bekasi, Blanakan, Gresik, Madura
3. Offshore of Natuna	East Natuna, West Natuna
4. Offshore of East Coast of Kalimantan	Bunyu, Tarakan, Mahakam, Balikpapan
5. Offshore of Maluku	Halmahera, East Maluku
6. Offshore of Bird head Papua	Sorong, Fakfak, Kai, Tanimbar, Biak

Table 2. Offshore oil and gas area in Indonesian regions.

GPS stations with baseline length less than 1000 km are chosen for simulation and analyzed for their accuracy whether it can achieve the requirement for subsidence monitoring on the platform.

All of GNSS GPS data are taken for investigation of the subsidence or other deformation phenomena that require millimeter accuracy usually processed by using scientific GPS software (e.g., Gamit, Bernese, Gypsy Software, etc.). This scientific software is commonly used for achieving the good accuracy level of relative coordinates or point positioning from GPS surveyed data [5]. All of errors and biases (e.g., ionosphere, troposphere biases, cycle slip, phase ambiguity, antenna phase center bias, etc.) will be estimated or modeled and leaving the residual mostly only in few millimeters. Since mostly the baseline from each combination of data will exceed typical of short baseline, in this case good handling of parameter errors

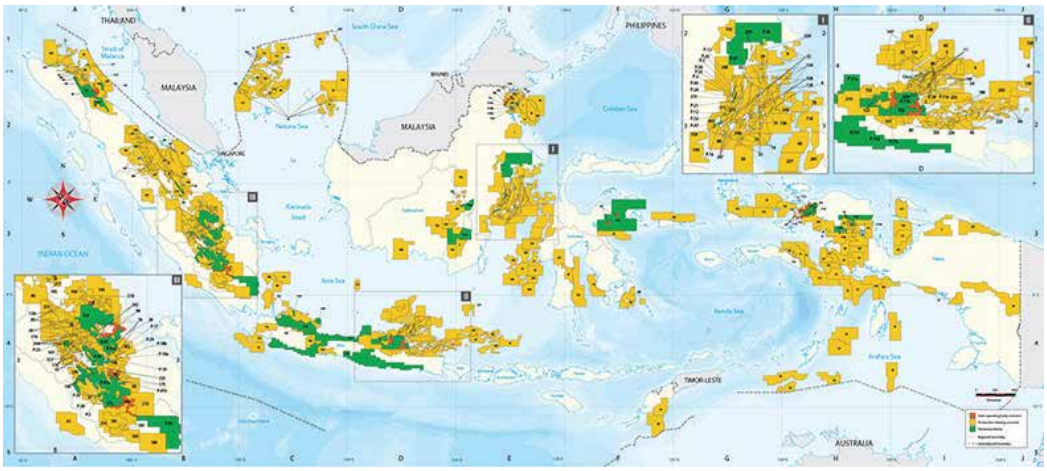

Figure 7. Onshore and offshore map of oil and gas area in Indonesian regions (images courtesy theoilandgasyear).

Figure 8. Baseline concepts using one stable reference station for subsidence monitoring along large offshore oil and gas area of Indonesia.

and biases is crucial for high accuracy requirements. **Table 3** shows parameter processing and processing strategy that are used on data processing using scientific software.

Final precise orbit from International GNSS Services (IGS) can be downloaded in every 2 weeks after the observation time, while earth rotation parameter can be downloaded either daily, every 2 weeks, or on yearly basis. As for phase center parameter, we can download from UNAVCO website or Bernese website. Many mirror addresses are also available for downloading GNSS GPS parameter data processing.

http://dx.doi.org/10.5772/intechopen.73565

Figure 9. Baseline concepts using reference station at clustered offshore regions for subsidence monitoring around offshore oil and gas area of Indonesia.

Parameter processing	Processing strategy using scientific software
1. Observations	Data phase, L1/L2. Data CODE
2. Earth rotation parameters	IGS. ERP
3. Orbits	Final precise orbit from IGS
4. Ionospheric and tropospheric biases	Data combination, parameter estimation
5. Antenna phase center	Antenna phase correction (PVC)

Table 3. Parameter data processing and processing strategy using scientific software in order to derive millimeter accuracy of position such as for platform subsidence monitoring.

4. Data analysis

Table 4 shows the result simulation of baseline concept using one stable reference station, while **Table 5** shows the result simulation of baseline concept using reference station at clustered offshore regions, for subsidence monitoring around offshore oil and gas area of Indonesia. On each figures we can see the baseline length and the average for height component from simulation result. For baseline with more than 1000 km, the average height component is around 1 cm. For baseline with less than 1000 km, less than 1 cm of average can be seen.

Results from data simulation show that the scenario using reference station at clustered offshore are given better result than scenario using only one stable reference station. Nevertheless with using scenario of only one stable reference station, generally it is sufficient enough for monitoring offshore oil and gas platform subsidence in such large offshore like in Indonesia.

Baseline ID	Baseline length (m)	Observation session	Average for height component from simulation (m)
1. BAKO-CSAB	1,868,631.008	24 h/31 days	0.021
2. BAKO-BTNG	2,207,624.866	24 h/31 days	0.014
3. BAKO-CNAB	3,163,103.652	24 h/31 days	0.011
4. BAKO-CMRE	1,707,364.779	24 h/31 days	0.011

Table 4. Result simulation of baseline concepts using one stable reference station for subsidence monitoring along large offshore oil and gas area of Indonesia.

Baseline ID	Baseline length (m)	Observation session	Average for height component from simulation (m)
1. CNAB-CFAK	359,191.773	24 h/31 days	0.007
2. CNAB-CMAN	319,811.751	24 h/31 days	0.011
3. BNOA-CBTU	934,272.232	24 h/31 days	0.005
4. BNOA-CDNP	100,619.250	24 h/31 days	0.004

Table 5. Result simulation of baseline concepts using reference station around clustered offshore regions for subsidence monitoring around offshore oil and gas area of Indonesia.

For baseline with more than 1000 km when we get 1 cm of accuracy, it is very good indeed. It may give the effectiveness and efficiency to the monitoring projects by the oil and gas company and others.

Figures 10–13 show graphs of repeatability on data simulation processing result for scenario using only one stable reference station for subsidence monitoring with baseline that varies more than 1000 km. A good repeatability on each graph can be discovered. A clear view of accuracy given by this scenario would be achieved. Generally it is sufficient enough for monitoring offshore oil and gas platform subsidence in such large offshore area like in Indonesia.

Figures 14–17 show graphs of repeatability on data simulation processing result for scenario using reference station at clustered area for subsidence monitoring with baseline that varies less than 1000 km. There is a good repeatability on each graph. A clear view of accuracy given

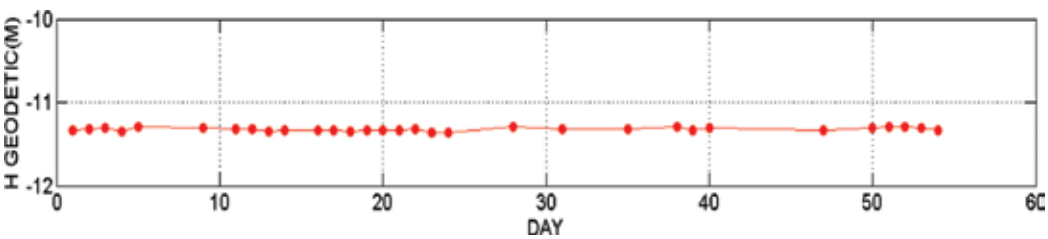

Figure 10. Repeatability of H result simulation baseline BAKO-CSAB 1,868,631.008 m.

http://dx.doi.org/10.5772/intechopen.73565

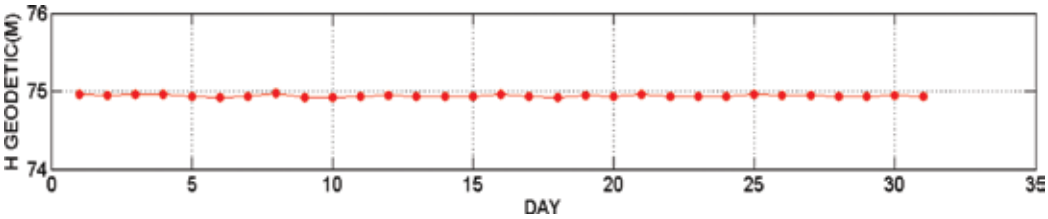

Figure 11. Repeatability of H result simulation baseline BAKO-BTNG 2,207,624.866 m.

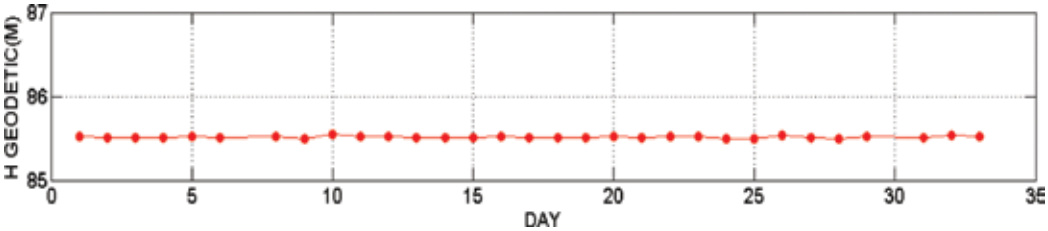

Figure 12. Repeatability of H result simulation baseline BAKO-CNAB 3,163,103.652 m.

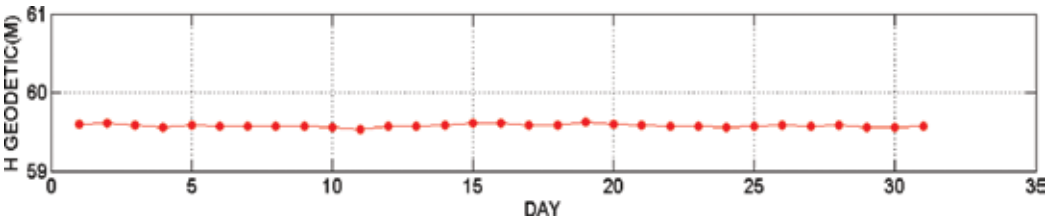

Figure 13. Repeatability of H result simulation baseline BAKO-CMRE 1,707,364.779 m.

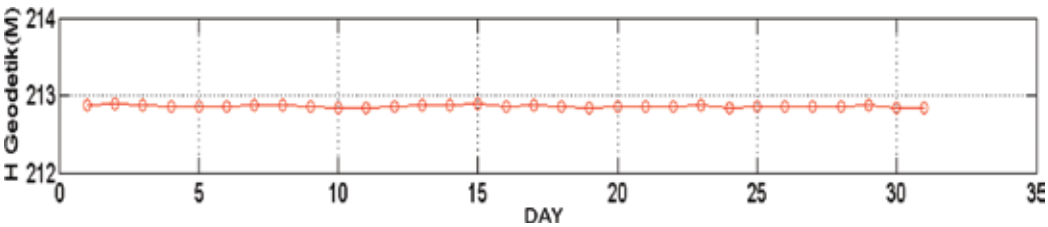

Figure 14. Repeatability of H result simulation baseline CNAB-CFAK 359,191.773 m.

by this scenario has been achieved. There is a high confident to use this scenario for monitoring offshore oil and gas platform subsidence.

From simulation results the capabilities of GNSS GPS technology on monitoring subsidence on oil and gas platform are proven. Indeed the real data observations are available in quite numbers of offshore oil and gas platforms around Indonesia. **Figures 18** and **19** show example of subsidence signal at Platform X and Platform Y somewhere located on classified area. Very

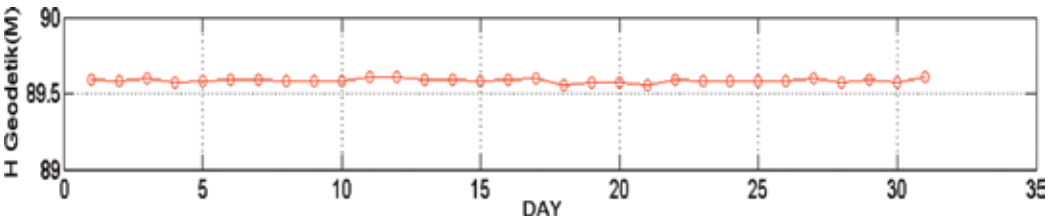

Figure 15. Repeatability of H result simulation baseline CNAB-CMAN 319,811.751 m.

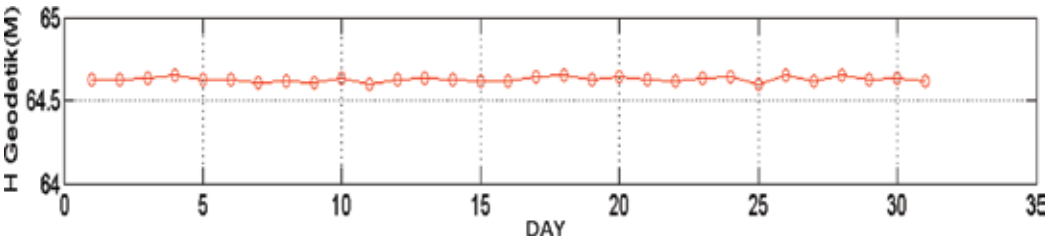

Figure 16. Repeatability of H result simulation baseline BNOA-CBTU 934,272.232 m.

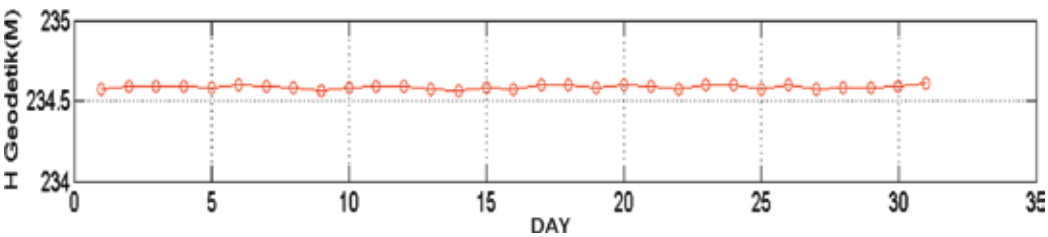

Figure 17. Repeatability of H result simulation baseline BNOA-CDNP 100,619.250 m.

Figure 18. Example of real data of platform subsidence in platform X offshore of Indonesia.

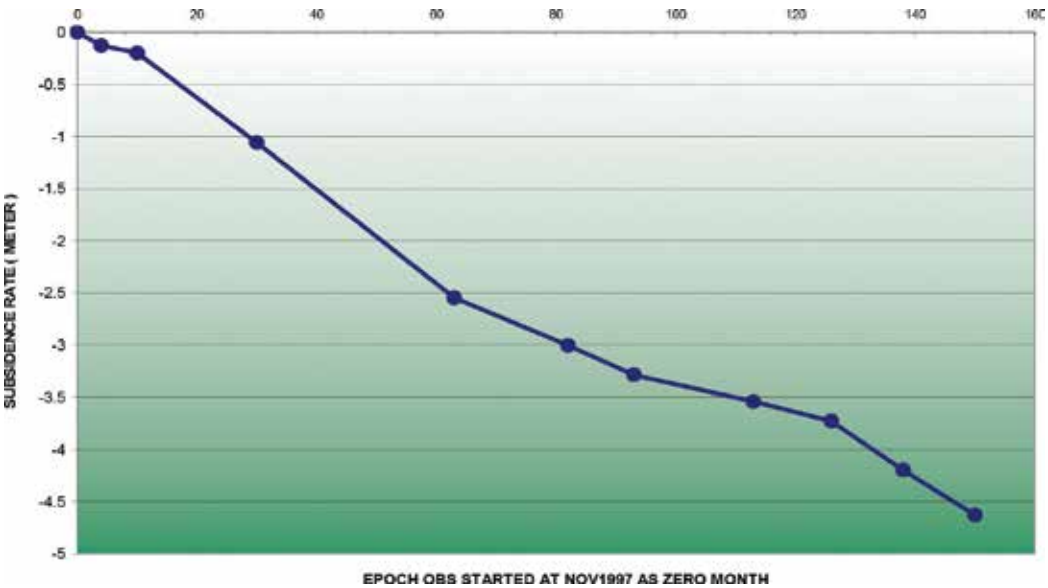

Figure 19. Example of real data of platform subsidence in platform Y offshore of Indonesia.

clear subsidence with rates of about 10–20 cm per year can be seen on the graphs. Some platforms have trend of few centimeters per year; it depends on how much oil and gas are being exploited, etc. In a detailed viewing, fluctuation on the trend can be seen. Sometimes it is accelerating, while in some cases, it is slowing or linier.

Large rates of subsidence are usually taking places in old oil and gas platform where depletion on reservoirs is more due to decrease in pore pressure, etc. There are already quite number for old oil and gas platform in Indonesia region. In this case monitoring program is quite important today. GNSS GPS is mostly the chosen technology for the programs. Nevertheless in many cases, the methodology on data acquisition and data processing is not correct. That is why it is necessary to write this kind of paper to help people on understanding more the capabilities of GNSS GPS technology on monitoring subsidence on oil and gas platform, as well as share the more correct concept and methodology. There are other methods that have been implemented together side by side with the GNSS GPS such as using altimeter and pressure gauge. They rely on identification the changing on MSL through times.

5. Closing remarks

Due to oil and gas exploitation, offshore oil and gas platform may experience subsidence. It has been observed from the real measurement that the rates can be varying from 1 to 10 centimeters per year and even more for certain places. In a detailed viewing, we can see fluctuation on the trend. Sometimes it is accelerating, while in some cases, it is slowing or linier. This situation will depend on how much oil and gas are being exploited and also how much pore pressure left, the fluid injection, etc. This subsidence information is mandatory for risk assessment and safety requirement. Continuing subsidence may deform the

platform infrastructures, adding the risk for any failure on the platform objects. With surrounding full of gases and oil, the failure may cause fatality.

The capabilities of GNSS GPS technology on monitoring subsidence on oil and gas platform have been proven. By observing enough satellites, and measuring their distance, in this case the coordinate on location at the earth can be calculated precisely and even with precision in the order of millimeter. This technology can measure accurately an object as small as an ant. To get information of subsidence signal or any deformation signal, we just repeatedly or continuously monitor accurate positions on the objects investigation, and the changing of positions is representing subsidence and/or deformation.

For Indonesia case it can be interesting to discuss about the reference station for monitoring subsidence on the platform since Indonesia is an archipelago country. Most of the region is water, and many sources of oil and gas are taking place offshore. The scenario of choosing one reference station for whole Indonesia regions or by cluster can be used. Results from data simulation show that the scenario using reference station at clustered offshore are given better result than scenario using only one stable reference station. Nevertheless with using scenario of only one stable reference station, generally it is sufficient enough for monitoring offshore oil and gas platform subsidence in such large offshore like in Indonesia. For baseline with more than 1000 km when we get 1 cm of accuracy, it is very good indeed. It may give the effectiveness and efficiency to the monitoring projects by the oil and gas company and others.

Acknowledgements

Many thanks and appreciation are given to Badan Informasi Geospatial for sharing CORS data for simulation. Appreciation is also given to Totok who processes the data using Bernese Software and also to Mohamad Gamal and students from Institute of Technology Bandung who helped the investigation in the field and PT LAPI who gives the project of monitoring platform subsidence for recent years.

Author details

Heri Andreas*, Hasanuddin Z. Abidin, Irwan Gumilar, Dina A. Sarsito and Dhota Pradipta

*Address all correspondence to: heri@gd.itb.ac.id

Geodesy Research Division, Faculty of Earth Science, Institute of Technology Bandung, Bandung, West Java, Indonesia

References

[1] Wells DE, Beck N, Delikaraoglou D, Kleusberg A, Krakiwsky EJ, Lachapelle G, Langley RB, Nakibogku M, Schwarz KP, Tranquilla JM, Vanicek P. Guide to GPS Positioning. Fredericton, N.B., Canada: Canadian GPS Associates; 1986

[2] Hofmann-Wellenhof B, Lichtenegger H, Walse E. GNSS Global Navigation Satellite Systems: GPS, GLONASS, Galileo, and More. Wien: Springer Verlag; 2007

[3] Abidin HZ. Penentuan Posisi Dengan GPS dan Aplikasinya. 2nd ed. Jakarta: P.T. Pradnya Paramita; 2000. 268 pp. ISBN: 979-408-377-1

[4] Leick A. GPS Satellite Surveying. 3rd ed. New York: Wiley; 2004

[5] Beutler G, Bock H, Brockmann E, Dach R, Fridez P, Gurtner W, Hugentobler U, Ineichen D, Johnson J, Meindl M, Mervant L, Rothacher M, Schaer S, Springer T, Weber R. Bernese GPS Software Version 4.2. University of Berne; 2001. 515 pp

Section 5

Earth Study With Space Technology Advances - Research of Natural Resources

Chapter 6

The Use of MODIS Images to Quantify the Energy Balance in Different Agroecosystems in Brazil

Antônio Heriberto de Castro Teixeira,
Janice F. Leivas, Carlos C. Ronquim and
Gustavo Bayma-Silva

Additional information is available at the end of the chapter

http://dx.doi.org/10.5772/intechopen.72798

Abstract

Sugarcane (SC) is expanding over coffee (CO), while both crops have replaced the natural vegetation (NV) in the northeastern side of São Paulo (SP) state, Southeast Brazil. Under these dynamic land-use changes, geosciences are valuable tools for evaluating the large-scale energy and mass exchanges between the vegetation and the lower atmosphere. For quantification of the energy balance components in these mixed agroecosystems, MODIS images were used throughout the Simple Algorithm for Evapotranspiration Retrieving (SAFER) algorithm, during the year 2015 in the main sugarcane- and coffee-growing regions of the state. Regarding, respectively, sugarcane, coffee, and natural vegetation, the fractions of the net radiation (Rn) used as latent heat flux (λE) were 0.68, 0.87, and 0.77, while the corresponding ones for the sensible heat (H) fluxes were 0.27, 0.07, and 0.16. Negative H values were noticed from April to July, because of heat advection raising λE values above Rn, but they were more often in coffee than in sugarcane. It was concluded that sugarcane crop presented lower evapotranspiration rates, when compared with coffee, which could be an advantage under the actual water scarcity scenario. However, sugarcane replacing natural vegetation means environmental warming, while the land use changes promoted by coffee crop represented cooling conditions.

Keywords: safer, land use changes, latent heat flux, sensible heat flux, soil heat flux

1. Introduction

Sugarcane (SC) (*Saccharum officinarum*) and coffee (CO) (*Coffea arabica* L.) crops are expanding in the northeastern side of the São Paulo (SP) state, Southeast Brazil. The first one is an annual crop, while the second one is a perennial crop, but both are replacing the natural vegetation (NV), composed by a mixture of Savannah and Atlantic Coastal Forest species. However,

sugarcane is also replacing the coffee areas [1], as consequences of both sugar and alcohol explorations, but also by stimulating renewable energy use [2].

The negative effects of the sugarcane expansion could be more serious when compared with those from the fossil fuel exploration, regarding greenhouse gas emissions [3, 4]. Aiming bio-energy production, a crop has to grow fast presenting high yield, but its energy output must exceed fossil fuel energy input. Considering these issues, sugarcane is a good candidate for energy crop [5]. However, its expansion could affect the large-scale energy balance further influencing the carbon cycle [6–8]. Anderson-Teixeira et al. [9] have reported energy balance alterations because of sugarcane expansion.

Under land-use and climate change conditions, the use of tools for quantifying the large-scale energy balance components is relevant for supporting policy planning and decision-makings about the water resources. The difficulties of measuring and analyzing these components throughout only field measurements highlighted the importance of coupling remote sensing and weather data, which have been successfully done in commercial crops under different environmental conditions [3, 10].

Several algorithms have been developed for acquiring the large-scale energy balance components. The Simple Algorithm for Evapotranspiration Retrieving (SAFER) is applied in this chapter in sugarcane and coffee crops comparing the results with those for natural vegetation. The algorithm was developed and validated in Brazil based on simultaneous field radiation and energy balance data from experiments and remote sensing under strongly water and vegetation contrasting conditions [11, 12].

Having cropland masks available, the energy balance components are analyzed in these mixed agroecosystems by the coupling MODIS images and weather data. The results may subsidize policies for a rational sugarcane and coffee water managements, being the analyses very useful under the actual scenario of water competitions between these crops and other sectors in the Southeast Brazil, as consequences of both climate and land use changes.

2. Materials and methods

2.1. Study region, crops, and agrometeorological data

Figure 1 shows the location of the study region in the northeastern side of São Paulo state, Southeast Brazil, together with the cropland masks and the agrometeorological stations used for the weather data gridding processes.

The agroecosystems are constituted by sugarcane (SC) and coffee (CO) interspaced with natural vegetation (NV). This last class is a mixture of Savannah and Atlantic Coastal Forest species. Some of the areas before occupied by coffee are nowadays being replaced by sugarcane crop.

The sugarcane areas present two well-defined seasons: the first one rainier and hotter and the other one drier and colder. According to Cabral et al. [13], the long-term maximum rainfall occurs in December (274 ± 97 mm month^{-1}), and the minimum one is between July and August

http://dx.doi.org/10.5772/intechopen.72798

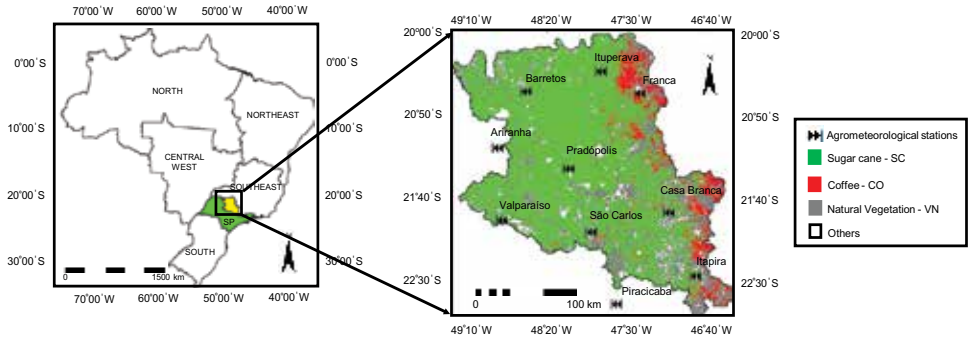

Figure 1. Location of the study region inside the northeastern side of the São Paulo state, Southeast Brazil, together with the cropland masks and the agrometeorological stations used for the weather data gridding processes.

(27 ± 34 mm month^{-1}); the annual value is 1517 ± 274 mm yr.$^{-1}$. The mean air temperatures in January and July are, respectively, 24 and 19°C, and the annual average is 22°C.

The sugarcane phases may be divided into four [14]: Phase 1: Germination and establishment, from January to February, are influenced by soil moisture, soil temperature, and soil aeration, denoting activation and subsequent sprouting of the vegetative bud. Phase 2: Tillering is influenced by variety, solar radiation, air temperature, soil moisture, and fertilization, starting from around 40 days after the initiation of the growing cycle and may last up to 120 days (February–April). Phase 3: Grand growth is from 120 days after the starting of the growing cycle lasting up to 270 days in a 12-month crop (May–September). Both high soil moisture and solar radiation levels favor better cane elongation during this phase. Phase 4: Ripening and maturation are characterized by slower growth activity, lasting for about 3 months starting from 270 to 360 days after the growing cycle initiation (September–December). High solar radiation levels and low soil moisture conditions are favorable during this last phase [15].

The coffee crop concentrates at the right side of the study area (see **Figure 1**). The region presents also a rainy season and a dry winter somewhat similar to the sugarcane areas; however, due to higher altitudes, between 700 and 1100 m, the long-term annual air temperature ranges are lower, from 18 to 20°C [16].

The coffee crop in Brazil, differently from sugarcane, which completes its average growing cycle in 12 months, takes 2 years for its all crop stages. Six coffee phases are considered, starting in September of each year [17, 18]: Phase 1: Vegetation with bud formation, during 7 months, is normally from September to March. Phase 2: Vegetation is between April and August, when the transformation of the vegetative to reproductive buds occurs, when at the end of this phase, from July to August, the plants enter in relative dormancy stage. Phase 3: Flowering and grain expansion are normally from September to December. Phase 4: Grain formation is normally from January to March, when water stress can be detrimental to the grain development. Phase 5: Grain maturation. Moderate water stress can benefit the grains. Phase 6: Senescence and death of the non-primary productive branches generally occur in July and August. In this last stage, the self-pruning process represented by senescence occurs, when the productive branches wither and die, limiting plant development.

2.2. Large-scale energy balance modeling

For the large-scale modeling, the MODIS images were used during the year 2015 together with 10 agrometeorological stations from the National Meteorological Institute (INMET) in the study area, considering the cropland classes. Weather data were used to calculate the reference evapotranspiration (ET0) by the Penman-Monteith method [19]. The weather input modeling parameters, global solar radiation (RG), air temperature (T_a), and ET_0 were up scaled for the 16-day period of the MODIS MOD13Q1 reflectance product (spatial resolution of 250 m) and gridded by using the moving average method generating pixels with the same spatial resolution as the satellite images.

Figure 2 shows the steps for modeling the energy balance throughout the SAFER algorithm with the MODIS MOD13Q1 product.

Following **Figure 2**, the surface albedo (α_0) was estimating according to Valiente et al. [20]:

$$\alpha_0 = a + b\alpha_1 + c\alpha_2 \quad (1)$$

where α_1 and α_2 are the reflectances from the bands 1 and 2, respectively, and a, b, and c are regression coefficients, considered as 0.08, 0.41, and 0.14, obtained under different Brazilian vegetation types and distinct hydrological conditions [10].

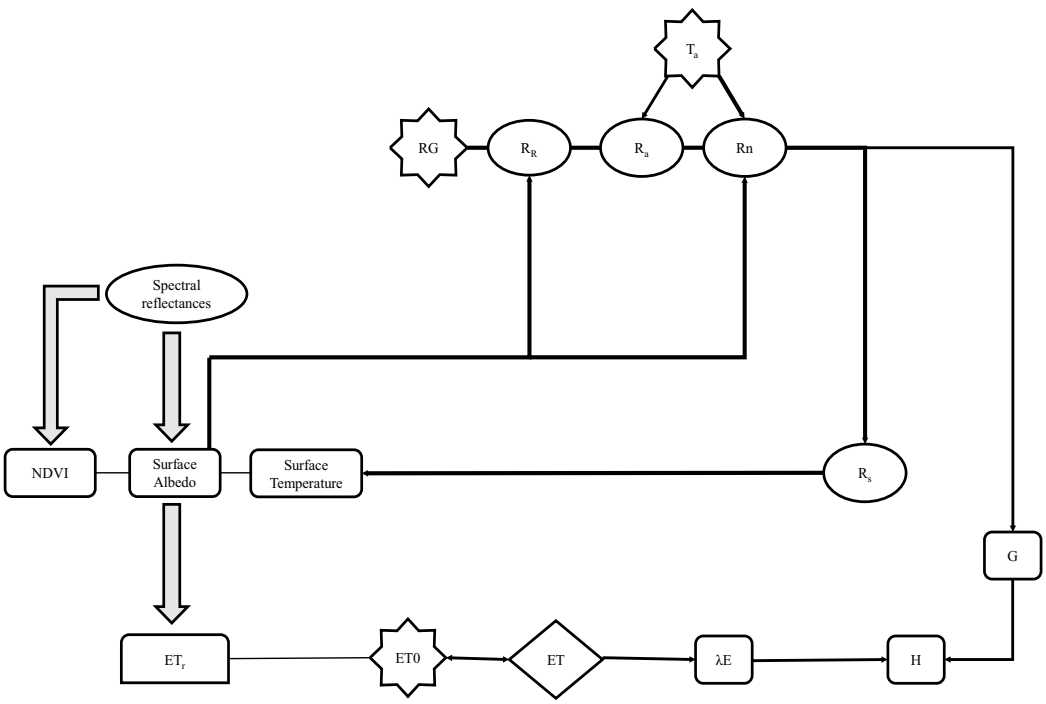

Figure 2. Flowchart for modeling the energy balance throughout application of the SAFER algorithm to the MODIS MOD13Q1 product.

http://dx.doi.org/10.5772/intechopen.72798

The normalized difference vegetation index (NDVI) is a measure of the amount of vegetation at the surface:

$$NDVI = \frac{\alpha_2 - \alpha_1}{\alpha_2 + \alpha_1} \quad (2)$$

The reflected solar radiation (R_R) was estimated as

$$R_R = \alpha_0 RG \quad (3)$$

The longwave atmospheric radiation (R_a) was calculated by applying the Stefan-Boltzmann low:

$$R_a = \sigma \varepsilon_A T_a \quad (4)$$

where ε_A is the atmospheric emissivity and σ is the Stefan-Boltzmann constant (5.67×10^{-8} W m^{-2} K^{-4}).

The parameter ε_A was calculated according to Teixeira et al. [21]:

$$\varepsilon_A = a_A (-\ln \tau)^{b_A} \quad (5)$$

where τ is the shortwave atmospheric transmissivity calculated as the ratio of R_G to the incident solar radiation at the top of the atmosphere and a_A and b_A are the regression coefficients 0.94 and 0.10, respectively.

Net radiation (Rn) can be described by the 24-hour values of net shortwave radiation, with a correction term for net longwave radiation [22]:

$$Rn = (1 - \alpha_0)RG - a_L \tau \quad (6)$$

where a_L is the regression coefficient of the relationship between net longwave radiation and τ on a daily scale.

Because of the thermal influence on longwave radiation via the Stephan-Boltzmann equation, a_L coefficient from Eq. (6) was correlated with the 24-hour T_a [11]:

$$a_L = dT_a - e \quad (7)$$

where d and e are the regression coefficients found to be 6.99 and 39.93, respectively.

Having estimated R_R, R_a, and Rn, the emitted surface longwave radiation (R_s) was acquired as residue in the radiation balance equation:

$$R_S = RG - R_R + R_a - Rn \quad (8)$$

Then, the surface temperature (T_0) was estimated by the residual method [22]:

$$T_0 = \sqrt[4]{\frac{R_s}{\sigma \varepsilon_s}} \tag{9}$$

where the surface emissivity (ε_S) was estimated as follows [22]:

$$\varepsilon_S = a_S(\ln \mathrm{NDVI}) + b_s \tag{10}$$

and a_S and b_S are the regression coefficients 0.06 and 1.00, respectively.

The SAFER algorithm is used to model water indicator represented by the ratio of the actual to the reference evapotranspiration (ET_r) based on the input remote sensing parameters, which is then multiplied by the 24-hour ET_0 values to estimate the daily ET large-scale rates which in turn are transformed into latent heat fluxes (λE):

$$ET_r = \left\{ \exp\left[f + g\left(\frac{T_0}{\alpha_0 \mathrm{NDVI}} \right) \right] \right\} \frac{ET\,0_{yr}}{5} \tag{11}$$

where f and g are the original regression coefficients, 1.8 and −0.008, respectively. The correction factor ($ET0_{yr}/5$) is applied, $ET0_{yr}$ being the annual grids of reference evapotranspiration for São Paulo state in the year 2015 and 5 mm is the ET_{0yr} value for the period of the original modeling in the Northeast Brazil [21].

For soil heat flux (G), the equation derived by Teixeira [12] was used:

$$\frac{G}{R_n} = a_G \exp(b_G \alpha_0) \tag{12}$$

where the regression coefficients a_G and b_G are 3.98 and −25.47.

The sensible heat flux (H) is acquired as residue in the energy balance equation:

$$H = R_n - \lambda E - G \tag{13}$$

3. Results and discussion

3.1. Thermohydrological conditions and crop stages

The driving weather variables for the surface energy balance are R_G, T_a, precipitation (P), and ET_0. They are presented in **Figure 3** on a 16-day time scale in terms of day of the tear (DOY), during 2015 as average pixel values for each agroecosystem class: sugarcane (SC), coffee (CO), and natural vegetation (NV).

Among the four weather parameters, P was the most variable along the year with the largest values occurring during the first and the last 3 months. The high-moisture conditions in the root zones during these periods affect the energy balance, increasing the latent heat fluxes (λE) for all agroecosystems. The rainfall annual totals were 1253, 1277, and 1245 mm yr^{-1} for the sugarcane (SC), coffee (CO), and natural vegetation (NV) with the range of standard

deviation (SD) staying between 11 and 12 mm yr^{-1}. These values are below the historical value of the study area, and they were not well distributed along the year. A period from July to October, with several rainfall 16-day values bellow 10 mm, was noticed for all analyzed agroecosystems. The short rainfall amounts occurred from Phase 3 to Phase 4 of the generalized sugarcane growing cycle, which should have caused some water deficit, when its water requirements are high. Cabral et al. [13] reported a 13% of sugarcane biomass reduction in relation to the regional average in São Paulo state, Brazil, because of the lower water availability observed during the initial 120 days of cane regrowth. For rainfed sugarcane crop, a well-distributed growing season total precipitation between 1100 and 1500 mm is considered adequate. However, the P dropping during Phase 3 should have caused some water deficit, when the crop water requirements are high, further affecting the energy partition, by reducing leaf area and the number of tillers and leaves per stalk [23]. During Phase 4, rains are not desirable for sugarcane, because they lead to poor juice quality [15], and then the high amounts at the end of the year, coinciding with this phase, were not favorable.

Taking into account the ET_0 values, one can see two atmosphere demand peaks with the smallest one happening at the middle of the year, however, with lower differences among the agroecosystems when compared with precipitation. The corresponding ET_0 annual values were 1321, 1297, and 1293 mm yr^{-1} for the sugarcane (SC), coffee (CO), and natural vegetation (NV) but with small SD from 3 to 4 mm yr^{-1}. The shortest ET_0 values in the middle of the year,

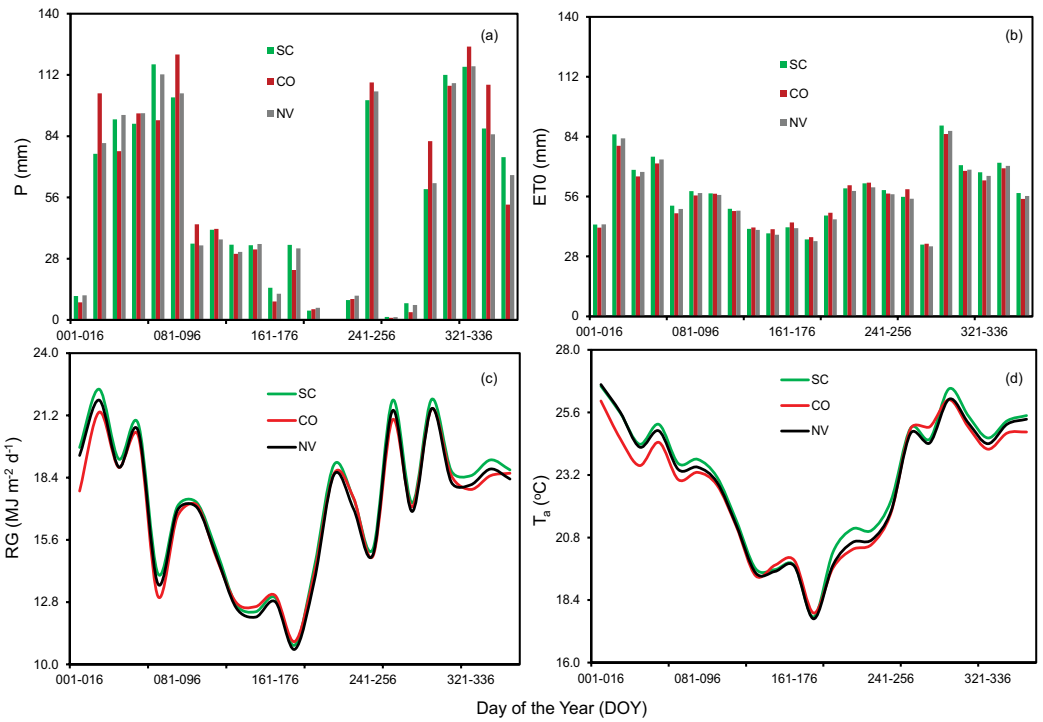

Figure 3. Average 16-day values for the weather variables during 2015 in areas with sugarcane (SC), coffee (CO), and natural vegetation (NV) in terms of day of the year (DOY), located at the northeastern side of São Paulo state, Brazil. (a) Precipitation (P), (b) reference evapotranspiration (ET_0), (c) incident global solar radiation (R_G), and (d) air temperature (T_a).

from May to July, coincide with the sugarcane Phase 3, favoring cane elongation reduction during this phase.

In relation to R_G and T_a, the differences among the agroecosystems were smaller than those for P and ET_0, with average annual values around 17 MJ m^{-2} day^{-1} and 23.0°C, respectively. Then, the highest atmosphere demands in sugarcane could be probably attributed to low air humidity and/or high wind speed conditions.

The thermohydrological conditions also strongly affect the coffee crop stages [17]. As the growing cycle takes 2 years, some coffee phases will coexist. Rainfall should be well distributed for good yield. At the start of the year, for the period involving Phases 1 and 4, there was only a 16-day (DOY 001–016) period with P lower than 10 mm in January. In Phase 2 rainfall is important for the transformation of the vegetative to reproductive buds. During this period, P declined until values close to zero at the end of July (DOY 209–224). In Phase 3 (September–November), some water stress is desirable, as the main flowering happens during a period of water stress following by good water availability. However, only two 16-day periods with low rainfall amounts are verified from September to October (DOY 257–288). In Phase 4, water stress may wilt the fruits, but only during the period from DOY 001 to 016 the rainfall amount was low, bellow 10 mm. In Phase 5 the water requirements declined, and some water deficit during this phase could have favored the coffee plant growth. The period with low rainfall amounts from May to June was also inside this phase.

Conditions of low R_G and ET_0 levels from May to August coincided with low P amounts, thus reducing water consumption in coffee areas. Air temperature (T_a) regulates the vegetative growth and reproductive buds, being high values associated with water deficit during booming the reason for flower abortion and growth reduction [23]. However, the higher values, above 23°C, occurred under conditions of good rainfall availability.

3.2. Agroecosystem energy balances

Figure 4 shows the composed average net radiation (Rn) values for sugarcane (SC), coffee (CO), and natural vegetation (NV) agroecosystems, during the year 2015, inside the northeastern side of São Paulo (SP) state, Southeast Brazil.

The lowest Rn pixel values are in the middle of the year, when reached close to 6.0 MJ m^{-2} d^{-1}, while the maximum ones were above 10 MJ m^{-2} d^{-1}. All ecosystems averaged 9.0 MJ $m^{-2}d^{-1}$; however, with small spatial variation, one can see from the SD values with range from 0.3 to 1.5 MJ m^{-2} d^{-1}. The highest end of this range was for the coffee (CO) class, in DOY 225–240 (August), period of the year coexisting plants inside Phases 2 and 6.

To see the energy availability in detail for the different agroecosystems along the year, **Figure 5** presents the Rn average values (a) and their fractions to RG (b) for sugarcane (SC), coffee (CO), and natural vegetation (CO), during the year 2015, in the northeastern side of São Paulo (SP) state, Southeast Brazil.

The strong dependence of Rn on RG is clear for all analyzed agroecosystems (see **Figures 3c** and **5a**). The Rn trends for the sugarcane (SC) and natural vegetation (NV) classes were similar, but values for coffee (CO) were a little lower, at the start and at the end of the year, during

http://dx.doi.org/10.5772/intechopen.72798

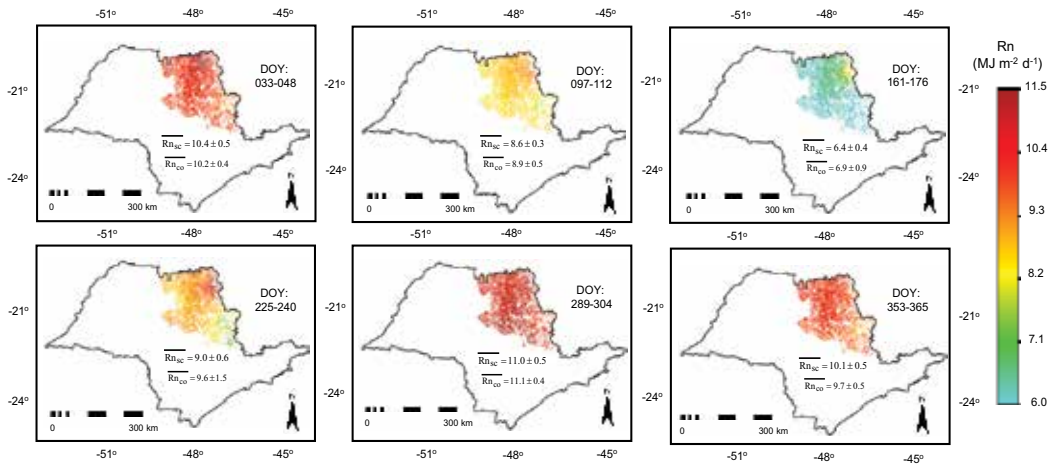

Figure 4. Composed net radiation (Rn) average values for sugarcane (SC), coffee (CO), and natural vegetation (NV) agroecosystems, during the year 2015, inside the northeastern side of São Paulo (SP) state, Southeast Brazil. The over bars mean averages showed together with standard deviations (SD).

Phases 1 and 4 of coffee plants. However, at the middle of the year, CO values were higher, when the plant stages were in mixed stages of the Phases 2, 5, and 6.

Regarding the ratio Rn/RG (**Figure 5b**), the higher mean pixel values were for the coffee (CO) class, mainly in the middle of the year. The values ranged from 0.49 to 0.55, from 0.50 to 0.57, and from 0.50 to 0.56, for, respectively, the SC, CO, and NV agroecosystems. The average annual Rn/RG of 50–55% is in agreement with field measurements in fruit crops and natural vegetation in the Northeast Region of Brazil [11] and with studies involving other distinct agroecosystems around the world [24, 25]. These results of similarities with national and international studies give confidence to the large-scale remote sensing methods tested here by coupling the MOD13Q1 product and agrometeorological stations.

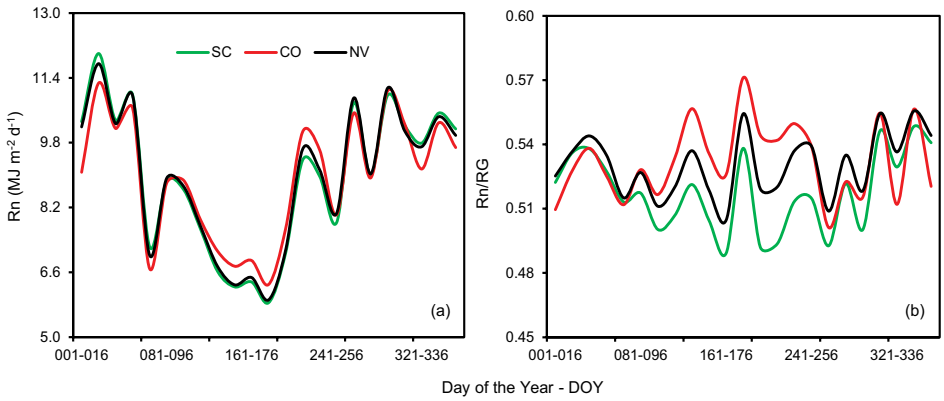

Figure 5. Daily net radiation (Rn) and their ratios to global solar radiation (RG) for sugarcane (SC), coffee (CO), and natural vegetation (NV) agroecosystems, during the year 2015, in the northeastern side of São Paulo (SP) state, Southeast Brazil. The over bars mean averages showed together with standard deviations (SD).

The composed latent heat flux (λE) values in the sugarcane (SC), coffee (CO), and natural vegetation (NV) agroecosystems, during the year 2015 inside the northeastern side of São Paulo (SP) state, Southeast Brazil, are shown in **Figure 6**.

Much more distinct of both λE and SD values among the agroecosystems are noticed than in the case of Rn, with λE ranging from close to zero to becoming higher than 13 MJ m^{-2} d^{-1}. The lowest values were for the sugarcane (SC) class, with an average λE of 6.1 ± 2.2 MJ m^{-2} d^{-1}, followed by natural vegetation (NV), 6.9 ± 1.8 MJ m^{-2} d^{-1}, and coffee (CO) with the highest average of 7.8 ± 1.8 MJ m^{-2} d^{-1}. Besides the lowest λE, the SC class presented also the largest spatial variation. Considering all agroecosystems, the highest and the lowest λE rates were, respectively, in January and at the end of October.

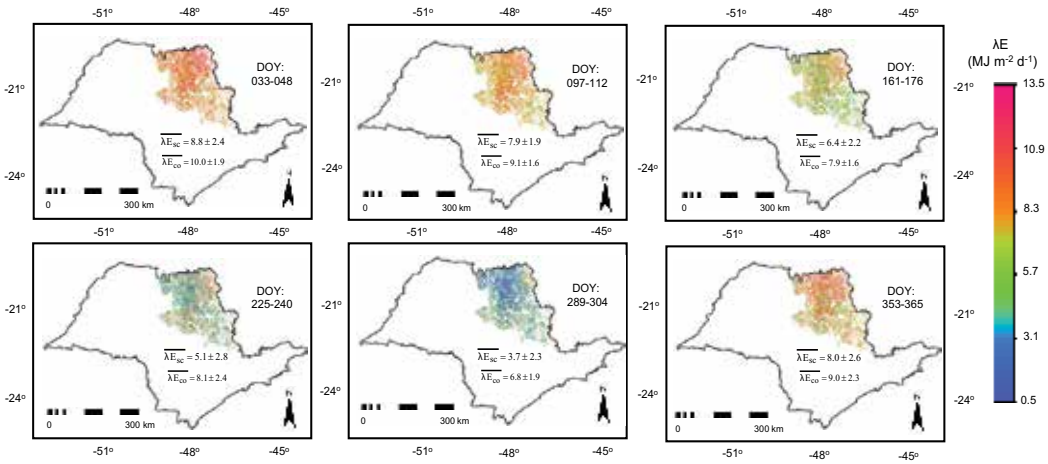

Figure 6. Composed latent heat flux (λE) values for the sugarcane (SC), coffee (CO), and natural vegetation (NV) agroecosystems, during the year 2015, inside the northeastern side of São Paulo (SP) state, Southeast Brazil. The over bars mean averages showed together with standard deviations.

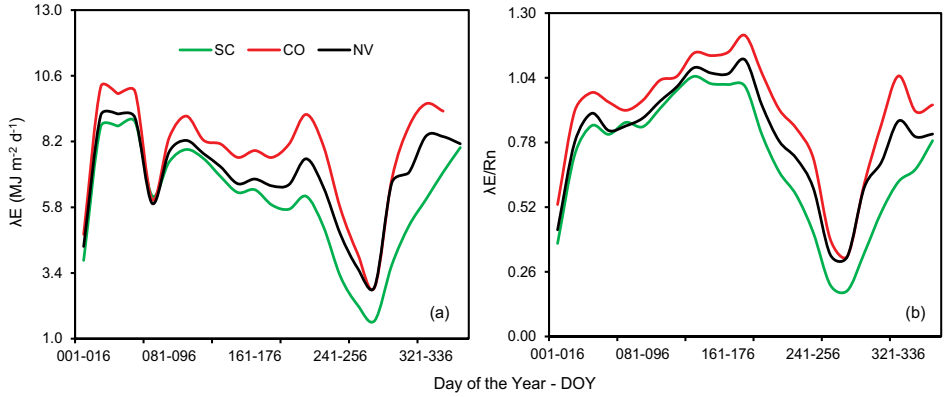

Figure 7. Average pixel values for the latent heat flux (λE) and their ratios to net radiation (Rn) for the sugarcane (SC), coffee (CO), and natural vegetation (NV) agroecosystems, during the year 2015, in the northeastern side of São Paulo (SP) state, Southeast Brazil.

Figure 7 presents the latent heat flux (λE) average values (a) and their fractions to Rn (b) for the sugarcane (SC), coffee (CO), and natural vegetation (NV) agroecosystems, during the year 2015.

Considering the three studied agroecosystems, the λE values started with short values, below 5.0 MJ m^{-2} d^{-1}, at the first half of January (2.0 mm d^{-1}), due to the low rainfall amounts (see **Figures 3a** and **7a**). After the first rains, λE followed the RG levels but dropping again in August because a short water scarcity spell. Clearly, one could see that in almost all periods of the year, for the coffee (CO) class, λE values were the highest ones, while for sugarcane (SC), they were the lowest ones. Natural vegetation (NV) presented intermediary λE values.

Energy balance differences among the agroecosystems were also noticed for the λE/Rn ratio. This last ratio is an index of the soil moisture in the root zones, and its behavior along the year evidenced two low-water availability periods in the root zones, with $\lambda E/R_n$ values below 0.60. One of these conditions was at the first half of January; however, for the sugarcane (SC) class, there was a longer period with low λE/Rn, from the first half of August to the end of October, dropping below 0.20.

Considering λE in terms of mm of waters, the evapotranspiration (ET) rates were from 0.7 to 3.6 mm d^{-1}, from 1.2 to 4.1 mm d^{-1}, and from 1.2 to 3.7 mm d^{-1} for the sugarcane (SC), coffee (CO), and natural vegetation (NV) agroecosystems, respectively. The corresponding annual average values were 2.5, 3.2, and 2.8 mm d^{-1}. Eksteen et al. [26] reported ET daily values for sugarcane (SC) between 1.6 and 2.9 mm d^{-1}, involving different varieties and soil moisture conditions, while in Florida (USA), Omary and Izuno [27] found a daily range from 0.7 to 4.6 mm d^{-1}. Regarding coffee (CO) crop, Vila Nova et al. [28] reported in Brazil, for the complete grain maturation, the mean ET rates of 3.5 mm d^{-1}, while Oliveira et al. [29] found an average of 2.9 mm d^{-1}. The ET values for the SC and CO agroecosystems in the current research are similar to these national and international studies.

The higher λE values for coffee (CO) than for sugarcane (SC) in the northeastern São Paulo state, Brazil, mean a larger annual water consumption for the first crop that should be considered under the conditions of water competition by agriculture and other sectors. Even with the cropland masks involving different stages of the agroecosystems in the current study, the similarity of our Rn and λE values with those from national and international literature provides confidence for the large-scale energy balance analyses by applying the SAFER algorithm throughout the MOD13Q1 product.

Considering the soil heat flux as a fraction of Rn, the sensible heat flux (H) was spatially retrieved by residue in the energy balance equation. The composed H values in sugarcane (SC), coffee (CO), and natural vegetation (NV) agroecosystems, during the year 2015 inside the northeastern side of São Paulo (SP) state, Southeast Brazil, are shown in **Figure 8**.

The sensible heat flux (H) values among the agroecosystems are also well differentiated according to the time of the year, but in this case with the highest values corresponding to the driest soil moisture conditions. They ranged from negative values as low as −3 MJ m^{-2} d^{-1} to high positive ones close to 13 MJ m^{-2} d^{-1}. The lowest ones were for the coffee (CO) class, which presented an average annual value of 0.6 ± 1.7 MJ m^{-2} d^{-1}, followed by natural vegetation (NV), 1.4 ± 1.8 MJ m^{-2} d^{-1}, and sugarcane (SC), with the highest average rate of 2.4 ± 2.2 MJ m^{-2} d^{-1}. Besides the highest H, the SC agroecosystem presented also the largest H spatial variation.

Taking into account all agroecosystem classes, the largest H values were during the driest conditions of the year, in the first half of January and from the second half of September to the end of October. The lowest ones, even negative, were at the end of the first rains, from April to the second half of July, when the root zones of the agroecosystems were moistier.

Figure 9 presents the H average values (a) and their fractions to Rn (b) for sugarcane (SC), coffee (CO), and natural vegetation (NV) agroecosystems, during the year 2015, in the north-eastern side of São Paulo (SP) state, Southeast Brazil.

In the middle of the year, negative H indicated horizontal heat advection from the drier and hotter natural areas to the wetter and colder cropped areas (**Figure 9a**). The highest positive

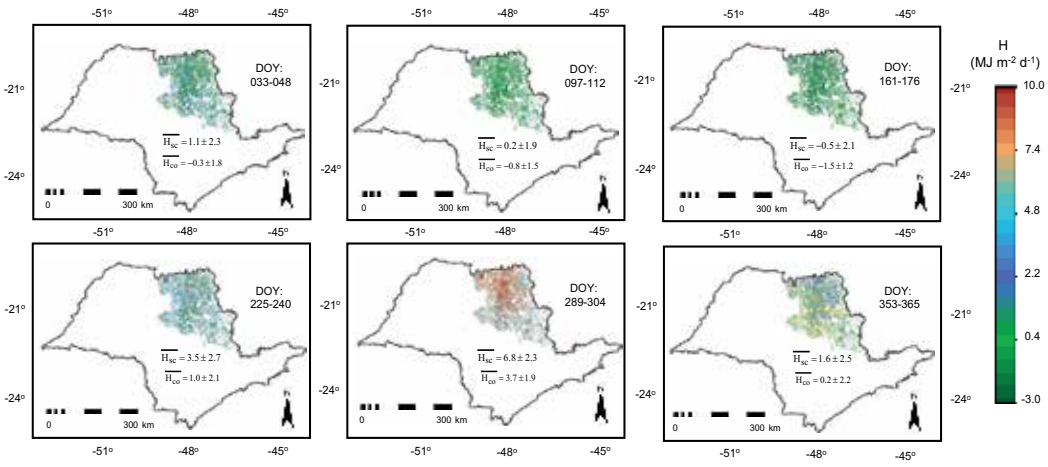

Figure 8. Composed sensible heat flux (H) values in sugarcane (SC), coffee (CO), and natural vegetation (NV) ecosystems, during the year 2015, inside the northeastern side of São Paulo (SP) state, Southeast Brazil. The over bars mean averages showed together with standard deviations (SD).

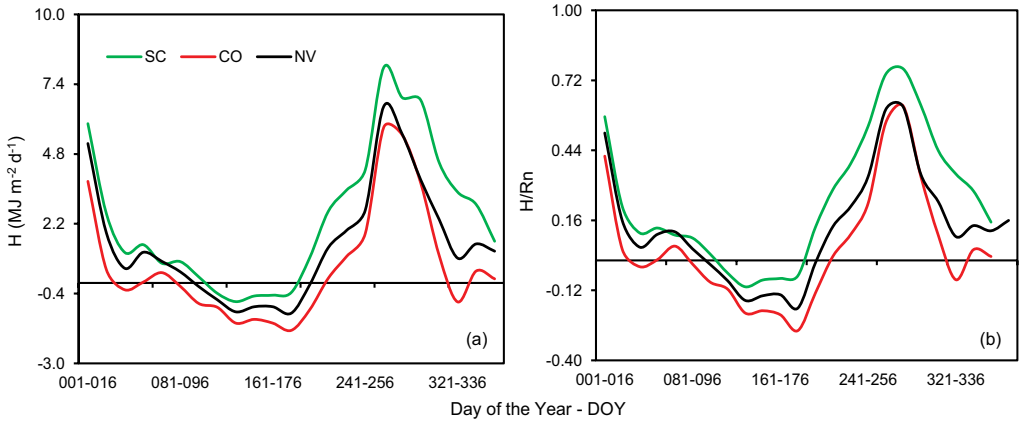

Figure 9. Average pixel values for the sensible heat flux (H) and their ratios to net radiation (Rn) in sugarcane (SC), coffee (CO), and natural vegetation (NV) ecosystems, during the year 2015, in the northeastern side of São Paulo (SP) state, Southeast Brazil.

values happened in the sugarcane (SC) class, reaching to the average of 8 MJ m^{-2} d^{-1} during the second half of September (DOY 257–252), when H represented 74% of Rn (**Figure 9b**). The lowest H values happened in the coffee (CO) class, during DOY 129–144, in May, when the average 16-day value was −1.5 MJ m^{-2} d^{-1}. During the year, the average annual H/Rn fractions were 0.07, 0.16, and 0.27 for coffee (CO), natural vegetation (NV), and sugarcane (SC), respectively. These results may represent cooling and warming microclimate effects as consequences of the replacement of the natural vegetation by coffee and sugarcane, respectively. Although sugarcane plants consume less water than the coffee ones, which is a positive aspect under the water scarcity conditions, the higher H rates for the sugarcane (SC) class have to be considered under the coupled effects of warming and land use change contexts.

Completing the energy balance, the composed ground heat flux (G) values in sugarcane (SC), coffee (CO), and natural vegetation (NV) agroecosystems, during the year 2015 inside the northeastern side of São Paulo (SP) state, Southeast Brazil, are shown in **Figure 10**.

Ground heat fluxes (G) among the agroecosystems are well distinct according to the time of the year, but with lower magnitudes than those for λE and H. The average pixel values ranged from 0.0 to 1.0 MJ m^{-2} d^{-1}. The spatial variations are low, with SD staying around 0.1 MJ m^{-2} d^{-1}. The average annual G values for sugarcane (SC) and coffee (CO) were the same (0.5 MJ m^{-2} d^{-1}), but for natural vegetation (NV), it was a little higher, with a mean value of 0.6 MJ m^{-2} d^{-1}.

Figure 11 presents the ground heat flux (G) daily average values (a) and their fractions to Rn (b) for sugarcane (SC), coffee (CO), and natural vegetation (NV) agroecosystems, during the year 2015.

The shapes of the curves pictured in **Figure 11** were somewhat similar of those for the latent heat flux (λE), but the values for the natural vegetation (NV) class moved from intermediary to the highest values. Lower G and of its ratio to net radiation (Rn) for the sugarcane (SC) class

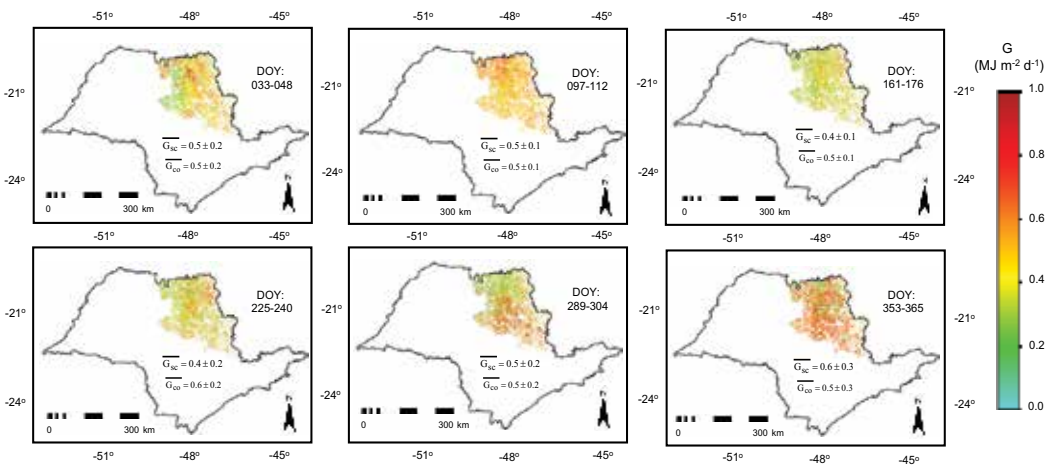

Figure 10. Composed ground heat flux (G) values for sugarcane (SC), coffee (CO), and natural vegetation (NV) agroecosystems, during the year 2015, inside the northeastern side of São Paulo (SP) state, Southeast Brazil. The over bars mean averages showed together with standard deviations.

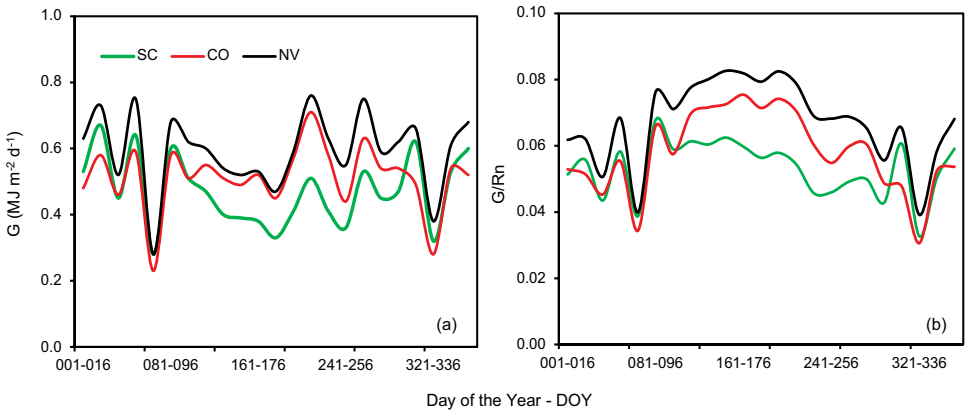

Figure 11. Ground heat flux (G) and their ratios to net radiation (Rn) in sugarcane (SC), coffee (CO), and natural vegetation (NV) agroecosystems, during the year 2015, in the northeastern side of São Paulo (SP) state, Southeast Brazil.

were found, mainly in the period of DOY 097–304 (April to the end of October). The average values of Rn partitioned as G were, respectively, 5, 6, and 7% for sugarcane (SC), coffee (CO), and natural vegetation (NV) agroecosystems.

4. Conclusions

The joint use of agrometeorological stations and the MODIS MOD13Q1 reflectance product allowed the large-scale energy balance quantification and analyses in the mixed agroecosystems composed by sugarcane, coffee, and natural vegetation along the year 2015 in the northeastern side of São Paulo state, Southeast Brazil. The strong dependence of net radiation (Rn) on the global solar radiation (RG) levels was clear for all classes, however, being lower for sugarcane and higher for coffee.

The daily values for the latent (λE), sensible (H), and ground (G) heat fluxes can be estimated in different kinds of vegetation from instantaneous measurements of the reflectances from the MODIS sensor, throughout the application of the SAFER algorithm. The lowest and the highest λE were, respectively, for sugarcane and coffee. Although sugarcane presents lower evapotranspiration rates than coffee crop in an annual scale, being a positive aspect under the actual water scarcity conditions, its higher H has to be considered under the conditions of the coupled effects of warming and land use changes.

Acknowledgements

The authors acknowledge the National Council for Scientific and Technological Development (CNPq) for the financial support to a project on large-scale radiation and energy balances in Brazil.

Author details

Antônio Heriberto de Castro Teixeira[1]*, Janice F. Leivas[2], Carlos C. Ronquim[2] and Gustavo Bayma-Silva[2]

*Address all correspondence to: heriberto.teixeira@embrapa.br

1 Embrapa Coastal Tablelands, Aracaju-SE, Brazil

2 Embrapa Satellite Monitoring, Campinas-SP, Brazil

References

[1] Satolo LF, Bacchi MRP. Impacts of the recent expansion of the sugarcane sector on municipal per per capita income in São Paulo state. ISRN Economics. 2013;**2013**:1-14. http://dx.doi.org/10.1155/2013/828169

[2] Mello CO, Esperancini MST. Análise econômica da eficiência da produção de cana-de-açúcar de fornecedores do Estado do Paraná. Revista Energia na Agricultura. 2012;**27**:48-60. http://dx.doi.org/10.17224/EnergAgric.2012v27n3p48-60s

[3] Rudorf BFT, Aguiar DA, Silva WF, Sugawara LM, Adami M, Moreira MA. Studies on the rapid expansion of sugarcane for ethanol production in São Paulo state (Brazil) using Landsat data. Remote Sensing. 2010;**2**:1057-1076. DOI: 10.3390/rs2041057

[4] Scharlemann JP, Laurance WF. How green are biofuels? Science. 2008;**319**:43-44. DOI: 10.1126/science.1153103

[5] Waclawovsky AJ, Sato PM, Lembke CG, Moore PH, Souza GM. Sugarcane for bioenergy production: An assessment of yield and regulation of sucrose content. Plant Biotechnology Journal. 2010;**8**:1-14. DOI: 10.1111/j.1467-7652.2009.00491.x

[6] Chooyok P, Pumijumnog N, Ussawarujikulchai AT. The water footprint assessment of ethanol production from molasses in Kanchanaburi and Supanburi province of Thailand. Procedia APCBEE. 2013;**5**:283-287. http://dx.doi.org/10.1016/j.apcbee.2013.05.049

[7] Beringer T, Lucht W, Schaphoff S. Bioenergy production potential of global biomass plantations under environmental and agricultural constraints. GCB Bioenergy. 2011;**3**:299-312. http://dx.doi.org/10.1111/j.1757-1707.2010.01088.x

[8] Cerri CC, Galdos MV, Maia SMF, Bernoux M, Feigl BJ, Powlson D, Cerri CEP. Effect of sugarcane harvesting systems on soil carbon stocks in Brazil: An examination of existing data. European Journal of Soil Science. 2011;**62**:23-28. http://dx.doi.org/10.1111/j.1365-2389.2010.01315.x

[9] Anderson-Teixeira KJ, Snyder PK, Twine TE, Cuadra SV, Costa MH, de Lucia EH. Climate-regulation services of natural and agricultural ecoregions of the Americas. Nature Climate Change 2012;**2**:177-181. http://dx.doi.org/10.1038/nclimate1346

[10] Teixeira AH de C, Hernandez FBT, Scherer-Warren M, Andtrade RG, Victoria D de C, Bolfe EL, Thenkabail PS, Franco RAM. Water productivity studies from earth observation data: Characterization, modeling, and mapping water use and water productivity. In: Prasad ST, editor. Remote Sensing of Water Resources, Disasters, and Urban Studies. 1st ed. Vol. III. Boca Raton: Taylor and Francis; 2015, pp. 101-126. ISBN 9781482217919

[11] Teixeira AH de C, Bastiaanssen WGM, Ahmad M–u–D, Bos MG, Moura MSB. Analysis of energy fluxes and vegetation-atmosphere parameters in irrigated and natural ecosystems of semi-arid Brazil. Journal of Hydrology. 2008;**362**:110-127. http://dx.doi.org/10.1016/j.jhydrol.2008.08.01

[12] Teixeira AH de C. Determining regional actual evapotranspiration of irrigated and natural vegetation in the São Francisco river basin (Brazil) using remote sensing and Penman-Monteith equation. Remote Sensing. 2010;**2**:1287-1319. DOI: 10.3390/RS0251287

[13] Cabral OMR, Rocha HR, Gash JH, Ligo MAV, Ramos NP, Packer AP, Batista ER. Fluxes of CO_2 above a sugarcane plantation in Brazil. Agricultural and Forest Meteorology. 2013;**182-183**:54-56. http://dx.doi.org/j.agrformet.2013.08.004

[14] da Silva TGF, Moura MSB, Zolnier S, Soares JM, Vieira VJ de S, Júnior WFG. Demanda hídrica eficiência do uso da água da cana-de-açúcar irrigada no semiárido brasileiro. Revista Brasileira de Engenharia Agrícola e Ambiental. 2011;**15**:1257-1265. http://dx.doi.org/10.1590/1807-1929/agriambi.v19n9p849-856

[15] Tejera NA, Rodes R, Ortega E, Campos R, Lluch C. Comparative analysis of physiological characteristics and yield components in sugarcane cultivars. Field Crops Research. 2007;**102**:64-72. http://dx.doi.org/10.1016/j.fcr.2007.02.002

[16] Camargo AP. Zoneamento de aptidão climática para a cafeicultura de arábica e robusta no Brasil. In: Fundação IBGE, Recursos, meio ambiente e poluição. 1977. pp. 68-76

[17] Camargo AP, Camargo MBP. Definição e esquematização das fases do cafeeiro arábica nas condições tropicais do Brasil. Bragantia. 2001;**60**:65-68. http://dx.doi.org/10.1590/S0006-87052001000100008

[18] Júnior AFC, Júnior OA de C, Martins E de S, Guerra AF. Phenological characterization of coffee crop (*Coffea arabica* L.) from MODIS time series. Revista Brasileira de Geofísica. 2013;**31**:569-578. http://dx.doi.org/10.22564/rbgf.v31i4.338

[19] Allen RG, Pereira LS, Raes D, Smith M. Crop Evapotranspiration: Guidelines for Computing Crop Water Requirements. Rome: Food and Agriculture Organization of the United Nations; 1998. p. 300

[20] Valiente JA, Nunez M, Lopez-Baeza E, Moreno JF. Narrow-band to broad-band conversion for Meteosat-visible channel and broad-band albedo using both AVHRR-1 and -2 channels. International Journal of Remote Sensing. 1995;**16**:1147-1166. http://dx.doi.org/10.1080/01431169508954468

[21] Teixeira AH de C, Leivas JF, Hernandez FBT, Franco RAM. Large-scale radiation and energy balances with Landsat 8 images and agrometeorological data in the Brazilian semiarid region. Journal of Applied Remote Sensing. 2017;**11**:016030. http://dx.doi.org/10.1117/1.JRS.11.016030

[22] Teixeira AH de C, Leivas JF, Silva GB. Options for using Landsat and RapidEye satellite images aiming the water productivity assessments in mixed agro-ecosystems. Proceedings of SPIE. 2016;**9998**:99980A-1-99980A-11. DOI: 10.1117/12.2240119

[23] Inman-Bamber NG, Smith D. Water relations in sugarcane and response to water deficits. Field Crops Research. 2005;**92**:185-202. http://dx.doi.org/10.1016/j.fcr.2005.01.023

[24] Hughes CE, Kalma JD, Binning P, Willgoose GR, Vertzonis M. Estimating evapotranspiration for a temperate salt marsh Newcastle, Australia. Hydrological Processes. 2001;**15**:957-975. http://dx.doi.org/10.1016/j.fcr.2005.01.023

[25] Yunusa IAM, Walker RR, Lu P. Evapotranspiration components from energy balance, sapflow and microlysimetry techniques for an irrigated vineyard in inland Australia. Agricultural and Forest Meteorology. 2004;**127**:93-107. http://dx.doi.org/10.1016/j.agrformet.2004.07.001

[26] Eksteen A, Singels A, Ngxaliwe S. Water relations of two contrasting sugarcane genotypes. Field Crops Research. 2014;**168**:86-100. http://dx.doi.org/10.1016/j.fcr.2014.08.008

[27] Omary M, Izuno FT. Evaluation of sugar-cane evapotranspiration from water table data in the everglades agricultural area. Agricultural Water Management. 1995;**27**:309-319. http://dx.doi.org/10.1016/0378-3774(95)01149-D

[28] Villa Nova NA, Favarin JL, Angelocci LR, Dourado Neto D. Estimativa do coeficiente de cultura do cafeeiro em função de variáveis climatológicas e fitotécnicas. Bragantia. 2002;**61**:81-88. http://dx.doi.org/10.1590/S0006-87052002000100013

[29] Oliveira PM, Silva AM, Castro Neto P. Estimativa da evapotranspiração e do coeficiente de cultura do cafeeiro (*Coffea arabica* L.). Irriga. 2003;**8**:273-282 ISSN: 1808-8546

Section 6

Space Technology in Environment

Chapter 7

Earth Observation for Urban Climate Monitoring: Surface Cover and Land Surface Temperature

Zina Mitraka and Nektarios Chrysoulakis

Additional information is available at the end of the chapter

http://dx.doi.org/10.5772/intechopen.71986

Abstract

The rate at which global climate change is happening is arguably the most pressing environmental challenge of the century, and it affects our cities. Climate change exerts added stress on urban areas through increased numbers of heat waves threatening people's well-being and, in many cases, human lives. Earth observation (EO) systems and the advances in remote sensing technology increase the opportunities for monitoring the thermal behavior of cities. The Sentinels constitute the first series of operational satellites for Copernicus, a program launched to provide data, information, services, and knowledge in support of Europe's goals regarding sustainable development and global governance of the environment. This chapter examines the exploitation of EO data for monitoring the urban climate, with particular focus on the urban surface cover and temperature. Two example applications are analyzed: the mapping of the urban surface and its characteristics, using EO data and the estimation of urban temperatures. Approaches, like the ones described in this chapter, can become operational once adapted to Sentinels, since their long-term operation plan guarantees the future supply of satellite observations. Thus, the described methods may support planning activities related to climate change mitigation and adaptation in cities, as well as routine urban planning activities.

Keywords: Earth observation, Copernicus Sentinels, urban climate, satellite remote sensing

1. Introduction

Global climate change is one of the most pressing environmental challenges of the century. Climate change is affecting cities and their residents, especially the poor ones, and more severe impacts are expected as climate extremes. Cities already face significant climatic and environmental challenges that are independent of climate change. They are generally warmer

than the surrounding non-urban areas, because of the higher heat absorption and the relatively limited cooling associated with vegetation and permeable surfaces. Urban areas suffer from air pollution, which is exacerbated by high temperatures. In conjunction with these existing issues, the impacts of climate change on cities will depend on the actual changes in climate, such as increased temperatures and rainfall.

The cities need to adapt and the climate change needs to be considered in all development plans and investments, local, national, and international. Local policy makers tend to see climate change as an environmental issue of global scale that is not of their concern. The majority of climate change specialists focus on reducing greenhouse emissions, without practically helping cities to learn how to change and adapt. Climate change science mainly deals with global and regional impacts, and it is less able to provide reliable assessments for the cities.

Datasets from Earth observation (EO) satellites are crucial for measuring key parameters relevant to the climate change. The use of satellites to observe the Earth provides the data necessary to improve our understanding of the Earth system and help predict future change. The satellite data and products may form the understanding of climate change and the quantitative estimates of its effects form the basis for policy-makers to build effective strategies for adapting to and mitigating the effects of a changing climate. Although EO data and products are mainly used for global and regional research studies, there is great potential in their use for monitoring the urban climate and thus allow cities to adapt to a changing climate.

1.1. The climate of cities and the urban scales

The urban climate refers to the specific climatic conditions in cities that differ from the surrounding areas, as an effect of the urban development. Urbanization tremendously changes the form of the natural landscape causing changes in the local climate, not only compared to the surrounding areas, but also inside the city. While some climatic elements differ only slightly from one city district to the other, like the precipitation for example, others differ significantly, like the temperature and the wind conditions.

In the case of conventional meteorological elements (temperature, humidity, wind, and precipitation), it is not as easy to establish the magnitude of modulation of the atmospheric boundary layer by a city, and it is even more challenging to assign causes for the observed changes. One of the main difficulties is the geographical setting of cities. The setting of a city is barely random and settlements are usually developed for specific reasons. Riverbeds, for example, offered good communications in earlier years; coastal cities were developed near natural harbors; others near to natural resources. In many developed countries, settlement sites were also selected because they were more readily defensible than others. In the majority of cases, the topography is rather complex and there were micro- and meso-climatic differences between the settlement sites and the surroundings even before the cities ever sprung up [1].

With the construction of buildings, parking lots, and houses, urban areas dramatically change the smoothness of a surface, the thermal conductivity, the hydraulic conductivity, the albedo,

the emissivity, and the fraction of vegetation cover. Thus, urban regions behave a lot different from natural ones and they cause unique physical processes, depending on many parameters like the heat retaining capacity of the construction materials, the sealing of the soil, a modified water balance and the waste heat. As a result, urban landscapes modify the original physical processes that govern any natural land surface, and also add new, unique biogeophysical and biogeochemical processes into the land surface–atmosphere, such as the storage heat flux, the canyon effect, and the anthropogenic heat flux [2].

The urban surface and morphology results in cities being relatively warmer than the rural surroundings, a phenomenon called urban heat island (UHI). The warmer city climate can have fatal consequences such as those witnessed during the summer heatwave of 2003 in Central Europe [3]. There are different kinds of UHIs, displaying different characteristics and controlled by different assemblages of energy exchange processes. These possess different scale manifestations and result from different processes. Air temperature varies with height, a phenomenon much complicated in the urban environments and the different atmospheric layers. Thermal remote sensing permits definition of an UHI named ground or surface UHI, which refers to the skin or surface temperature difference between the city and its surrounding areas.

The concept of scale is fundamental in the understanding of the surface-atmosphere interactions when it comes to urban environments. In building scale, for example, the walls and roof facets have different time-varying exposure to solar radiation, net longwave radiation exchange, and ventilation. Horizontal ground-level surfaces are a patchwork of elements, such as irrigated gardens and lawns, non-irrigated greenspace, and paved areas with contrasting radiative, thermal, aerodynamic and moisture properties, frequently including trees. These different surface elements possess diverse energy budgets that generate contrasts in surface characteristics (e.g., skin temperature), and lead to mutual interactions by radiative exchange and small-scale advection. These fundamental units may be aggregated hierarchically, as illustrated in **Figure 1**.

Distinctive energy balances characterize each scale that generally do not represent the area-weighted average of the budgets of individual elements. This happens because each unit interacts with adjacent ones in the same scale by advection. While spatial scale increases, the

Figure 1. Graphical illustration of the different scales in the city. The urban canyon scale includes building walls and elements between buildings. The city block scale includes a number of urban canyons and roofs of buildings. The neighborhood scale refers to a number of city blocks, while the land use scale refers to larger areas including many similar neighborhoods.

spatial variability is likely to be reduced and less difference is expected among two land-use classes in a city for example, than between a north and south-facing wall of an individual building. Urban climatology studies this heterogeneity and complexity, either explicitly, in terms of detailed mapping of urban morphology, or in interpreting observations at aggregate scales [4].

1.2. Urban surface and morphology

The urban surface is composed of a large number of man-made materials arranged in a complex three-dimensional (3D) structure. Cities are built with artificial materials, such as cement, asphalt, brick, pebbles, or aggregates, which absorb and store radiation throughout the day and slowly release heat through the night. Moreover, streets, sidewalks, and parking lots are generally impervious, meaning that they do not allow the water to infiltrate into the soil. Since the urban environment is predominantly covered by artificial pavement, it is important to study the types of materials used and their individual characteristics. Impervious surfaces not only absorb high heat loads, which increase air temperatures through heat convection, but also increase the rate and temperature of runoff during storms [5].

While land changes from forests, grasslands, and croplands to impervious surfaces, the energy balance changes. The larger amount of solar radiation reaching the Earth's surface is reflected, absorbed, and transformed into sensible and latent heat. A small percentage of the solar radiation is also used in photosynthesis. The atmosphere close to the surface is mainly heated by energy radiating off the Earth's surface and not by direct solar heating. The surface materials affect largely the amount of solar radiation reflected or absorbed and, thus, they affect the heat flux from the surface to the atmosphere. The impervious surfaces alter the local energy balances through changes in the albedo, the emissivity, the specific heat capacities, and the thermal conductivities of the surfaces, as well as the ratio of sensible to latent heat fluxes from the surface to the atmosphere. Therefore, this impacts the temperature and humidity of the overlying air. Cool pavements are made from advanced materials and surface types that are used for decreasing the surface temperature in urban environments. These are mainly based on the use of materials with high albedo combined and high emissivity or techniques that exploit the latent heat to decrease the surface and ambient temperature [6]. Nevertheless, not only the materials, but also the 3D structures of the city have important impact on its radiational balance and thus its temperature. The shape of the cities can be described by several measures, each of which has effect on the city climate. The buildings and trees height affects the reflectivity, the flow regimes, and the heat dispersion above ground. The surface properties as well as the 3D structure of the cities can both be assessed using remote sensing methods and EO data.

2. Urban remote sensing and urban climate

A variety of remote sensors, satellite and airborne, detect and measure energy patterns from different portions of the electromagnetic spectrum, which are useful to quantify several

parameters essential for urban studies. The great number of EO data from satellite and airborne systems presents an opportunity to extract a great wealth of information via remote sensing, relevant to the urban and peri-urban environments at various spatial, temporal, and spectral scales. With recent innovations in sensor technologies, urban applications of remote sensing, i.e., urban remote sensing, has rapidly gained popularity among a wide variety of communities.

Environmental scientists are increasingly relying upon EO data to derive, for example, urban land cover information as a primary boundary condition used in many spatially distributed models [7]. The climate change community has also recognized remote sensing as an enabling and acceptable technology to study the spatiotemporal dynamics and consequences of urbanization as a major form of global changes [8]. Lately, more urban researchers are also using remote sensing to extract information for studying the urban surface and geometry [9, 10]. Finally, urban and regional planners are increasingly using EO data to derive information on cities in a timely, detailed, and cost-effective way to accommodate various planning and management activities [11].

Urban remote sensing can help improve our understanding of cities and many benefits of using EO data for urban studies that can be identified. The largest benefit of remote sensing, its capability of acquiring images that cover a large area, applies also for urban studies, where synoptic views allow identifying objects, patterns, and human-land interactions. Identifying the urban processes that operate over a rather large area and quantifying the differences in an intra-urban level is essential for understanding the urban environment. Remote sensing provides a great asset on information gathering on the entire mosaic of an urban phenomenon, while knowledge and expertise from multiple disciplines can lead to full understanding and modeling the urban processes.

Remote sensing holds an advantage as well, and complements the field measurements. Field measurements in most cases in urban sites do not represent the broader area. To cover large areas a lot of field measurements are needed, dense in both temporal and spatial terms and this can become prohibitively expensive in most cases. Moreover, data collected from field surveys and measurements can suffer from biases in the sampling design. Remote sensors can collect data in an unbiased and cost-effective way and thus provide better insights on the spatial and temporal evolution of processes. Field measurement can complement the remote sensing ones and combined methods and products hold great potential in terms of accuracy, spatial, and temporal coverage.

A framework of monitoring, synthesis, and modeling in the urban environment can be achieved with synergies of EO data integrated with relevant geospatial technologies, like spatial analysis and dynamic modeling. This framework can then be used to support the development of a spatio-temporal perspective of the urban processes and phenomena across scales and also to relate the different human and natural variables for understanding the direct and indirect drivers of urbanizations.

Last, remote sensing is ideal for connecting different scales for urban studies. Urban science disciplines have their own preferred scales of analysis. For example, urban planners tend to

work at street and neighborhood scales, while regional planners deal with larger entities such as metropolitan areas, even a whole city, or country region. Urban ecologists work at many spatial scales defined by the ecological units, and so as urban geographers, depending upon the specific topics under investigation. Urban meteorologists define the scales by the different physiographical features of the city. EO data can provide global coverage with spatial resolution ranging from sub-meter to a few kilometers and with varying temporal resolutions. The different urban researchers use different temporal scales depending on their application, varying from hourly, daily, weekly, monthly, seasonally to annual or decal basis. EO data allow work at any scale depending on the urban phenomenon being examined and they also offer the unique potential for linking different scales.

Remote sensing improves our understanding of urban areas in several ways, although the complexity of the urban environment challenges the realistic potential for making these improvements. Despite the profound benefits of using EO data for urban studies, the great inhomogeneity of urban environments obstructs the applicability and robustness of remote sensing methods. The presence of manmade materials and structures and the variety of vegetation cover, along with the 3D nature of cities, cause substantial inter-pixel and intra-pixel variations, complicating the characterization of urban landscapes. A great scientific challenge lies in the combination of EO data from different sensors, both in terms of scales and type of measurements. Moreover, it is always a challenge to integrate satellite data with other types of geospatial data in urban environmental analyses, like field measurement data, and cope with the fundamental differences in data sampling and measurement.

The ability to map, monitor, and analyze the complex and dynamic attributes of urban environments from EO data greatly depends on the characteristics of the remote sensing imaging instrument. Operational satellite EO systems are designed for specific missions, and thus have different operational principles and technical characteristics depending on the specifications of the missions. Currently, no EO system is specifically designed for monitoring urban areas. Airborne imaging systems are more flexible, but the cost of airborne campaigns limits the frequency of acquisitions and the area of coverage.

2.1. Satellite data in urban studies

A large variety of satellite data can be used for urban studies. The selection of a particular data source is a compromise among data availability, costs, and the required spatial, spectral, and temporal resolution. The majority of urban phenomena are scale-dependent, which means that urban patterns change with the scale of observation. Urban processes appear to be hierarchical in pattern and structure [12]. Therefore, studies of the relationship between the patterns at different levels in the hierarchy are urgently needed in obtaining a better understanding of the scale and resolution requirements in urban areas and in finding the optimal scale for examining the relationship between urban landscape pattern and process.

Over the past decade, urban remote sensing has emerged as a new frontier in the EO technology by focusing primarily on mapping and monitoring of the urban land cover and its spatial extent. The line in **Figure 2** shows the number of journal articles (including review articles)

http://dx.doi.org/10.5772/intechopen.71986

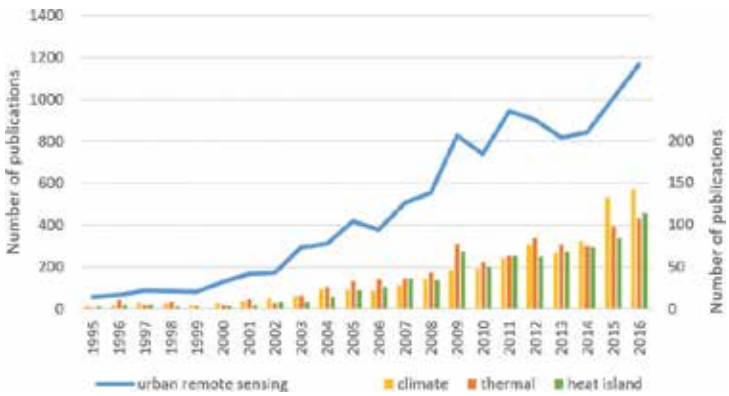

Figure 2. The number of journal articles (including review articles) including the key words urban remote sensing (line), urban remote sensing climate (first set of bars), urban remote sensing thermal (second set of bars), urban remote sensing heat island (third set of bars). Source: Scopus search on August 18, 2017.

on urban remote sensing, since 1995. There is a published literature on urban remote sensing since the 1970s, but a highly increasing rate is observed around 2002. This period coincides with the advent of very high spatial resolution satellite images (higher than 5 m) and the first spaceborne hyperspectral images. Thus, enhanced image processing techniques were developed such as the object-based image analysis, data mining, and data and image fusion of different sensors, wavelength regions and spatial, spectral, and temporal resolutions.

The same trend can be noticed in the literature of urban remote sensing for climate (first set of bars in **Figure 2**), which has been following similar rate of increase in these years. It is interesting though to observe that the pattern of urban thermal remote sensing (second set of bars in **Figure 2**) follows very close the one of urban heat island (third set of bars in **Figure 2**). Although expected, this graph is a strong indication that, so far, when referred to urban climate monitoring from space, the main focus is usually in thermal remote sensing. It is indeed true that thermal remote sensors provide indispensable information for the surface temperature, with their great advantage being the spatial cover of large areas. Yet, remote sensing can contribute much more than that into our understanding of the biophysical properties, the patterns and the processes of urban landscapes using all ranges of electromagnetic wavelength and active sensors as well. In fact, the last year (2015–2016) seems that the remote sensing community has started publishing studies related to urban climate, which are not necessarily using thermal data or are referring to the urban heat island.

From the wealth of available and upcoming EO data, detailed information on the urban surface cover and quantitative estimates of the biophysical parameters related to the urban climate can be extracted. Methodologies that exploit and combine satellite data from different sources and of various spatial, spectral, and temporal resolutions can give insights on the evolution in space and time of the urban climatic phenomena. Current and upcoming satellite sensors may provide great wealth of information for our understanding of the cities climate. Remote sensing provides a wealth of data of different spatial, spectral, and temporal resolutions that can cope with the spatial and temporal scale requirements of urban climate studies.

2.2. Spatial, spectral, and temporal resolutions for urban climate studies

Although the operating principles of various imaging instruments have changed over the years, the spectrum of applications and usability of imagery have been largely determined by their spatial, spectral, and temporal resolutions. Image resolution characteristics play a major role in determining the size and properties of the features or phenomena that can be discriminated in remotely sensed imagery.

The spectral signal is one of the most important properties of urban land surfaces measured with remote sensing. Most satellite sensors are multispectral systems, meaning they sense the earth surface with a few broad spectral bands. Urban environments possess a high spectral heterogeneity and they are characterized by a large diversity of materials. Therefore, increased spectral resolution is a requirement for urban remote sensing.

The spatial resolution of remote sensor is a function of the altitude of the platform relative to the earth surface and the resolving power of the sensor. The spatial resolution is often expressed as the ground sampling distance of the sensor at nadir. The spatial resolution required for a given study could be determined by the size of the smallest element to be mapped. However, due to several factors, the element spatial resolution is not sufficient to detect urban objects. The radiation measured for one pixel is affected by the radiation of its neighboring pixels, due to scattering effects that complicate the analysis. Moreover, an object can only be positively identified if it is represented by several pixels. The ideal spatial resolution of an image for a given application will, therefore, be several times smaller than the size of the smallest object that needs to be identified.

The Nyquist sampling theorem [13] establishes a sufficient condition for a sample rate that permits a discrete sequence of samples to capture all the information from a continuous-time signal of finite bandwidth and it is the theoretical basis for the spatial resolution needed to map individual objects. The Nyquist theorem suggests that an object should be of the order of one-tenth of the dimension of the pixel in order to ensure that it will be completely independent of its random position and orientation relative to the sampling scheme. A schematic representation of the relationship between the spatial resolution and the objects under consideration is given in **Figure 3**, although applicable thresholds are not easy to define. The three situations outlined in **Figure 3** require different approaches to unravel information for the underling objects. The urban surface objects (i.e., buildings, roads, etc.) have small spatial extent. Given the large amount of spatial heterogeneity, most analyses in urban areas rely upon high spatial resolution imagery usually from aerial photography or drones.

EO data and the advances in remote sensing techniques, though, can provide an alternative when working with larger scales than the objects to identify. The so-called sub-pixel classification methods resolve the radiance of a single pixel and identify percentages of separate components. These methods are particularly useful for material mappings when used with hyperspectral data [14], but there are examples in the literature of sub-pixel classification methods used with coarser spectral and spatial resolution data [15, 16].

http://dx.doi.org/10.5772/intechopen.71986

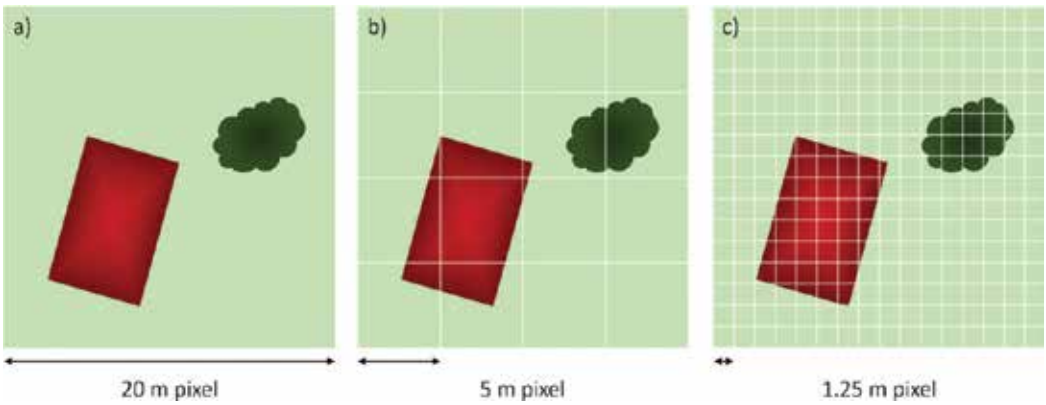

Figure 3. Relationship between objects under consideration and spatial resolution in urban sites: (a) pixels significantly larger than objects, (b) pixel and objects sizes are of the same order, and (c) pixels are significantly smaller than object.

The temporal resolution of a remote sensing system is the theoretical or the operational capability for acquiring repetitive imagery over some time interval. The spatial extent of images depends on the swath width, and influences the resulting temporal resolution.

A wide variety of EO systems acquiring data with various resolutions can be useful for urban studies. Medium resolution remote sensor data have been used to examine large dimensional urban phenomena or processes since early 1970s when NASA successfully launched the first Landsat. Over a period of nearly four decades, the Landsat program has acquired a scientifically valuable image archive unmatched in quality, details, coverage, and length, which has been the primary source of data for urbanization studies at the regional, national, and global scales. Since July 1982, with the launch of Landsat 4, thermal sensors are included in Landsat missions enabling surface temperature studies. The Advanced Spaceborne Thermal Emission and Reflection Radiometer (ASTER), a cooperative effort between NASA and Japan's Ministry of Economy Trade and Industry (METI), in orbit since December 18, 1999, includes a multispectral thermal instrument, which provides accurate estimates of emissivity and surface temperature in high spatial resolution. Yet, its on-demand acquisition mode limits the spatial resolution.

2.3. The Sentinels

The Sentinels constitute the first series of the ESA operational satellites for the Copernicus Programme. Copernicus is the continuity of the Global Monitoring for Environment and Security (GMES) Programme, which is launched to provide data, information, services, and knowledge that support Europe's goals regarding sustainable development and global governance of the environment. Copernicus is a European system for monitoring the Earth. It consists of a complex set of systems, which collect data from multiple sources: EO satellites and *in-situ* sensors and provides up-to-date information through a set of services related to environmental and security issues. The five Sentinel missions are based on constellations of two satellites to fulfill revisit and coverage requirements, providing robust datasets for Copernicus.

The Sentinel-2 mission provides continuity to services relying on multispectral high-spatial-resolution optical observations (like Landsat and SPOT satellites): it carries a Multispectral Instrument (MSI) covering the electromagnetic spectrum from the visible to the shortwave infrared with a pixel resolution from 10 to 60 m. Two satellites in orbit will provide data at a 5 days interval at the equator. Sentinel-2 combines a large swath, frequent revisit, and systematic acquisition of all land surfaces at high-spatial resolution and with a large number of spectral bands [17]. The pair of Sentinel-2 satellites routinely delivers high-resolution optical images globally, providing enhanced continuity of SPOT and Landsat type data.

Sentinel-3 mission represents the continuity of the ENVISAT sensors, i.e., MERIS (MEdium Resolution Imaging Spectrometer) and Advanced Along Track Scanning Radiometer (AATSR). In particular, the Sea and Land Surface Temperature Radiometer (SLSTR) will provide TIR data at 1 km resolution with daily revisit at the equator [18]. Among the Sentinel-3 mission objectives is to monitor the land surface temperature with high-end accuracy and reliability in support of climate monitoring.

3. Application for surface cover and land surface temperature

This chapter examines the exploitation of EO data for monitoring the urban climate, with particular focus on satellite data. The mapping of the urban surface and its characteristics, using spectral unmixing is examined in the first part. A method adjusted for urban studies is proposed which accounts for the non-linear mixture of spectral radiances in the urban canyon. The second part focuses on thermal EO data. To capture the intra-urban variations of temperature, EO data of high spatial and temporal resolution are necessary, but no current of forthcoming satellite provides them. Moreover, only one from the series of Sentinel satellites carries a thermal sensor of low spatial resolution. To overcome the limitations of the resolution trade-off, a synergistic methodology between high resolution optical and low resolution thermal satellite measurements with ultimate goal daily local-scale land surface temperature estimates.

3.1. Test area and data

The test area is in the city of Heraklion, Greece, and it covers an area of about 90 km^2. It is a typical Mediterranean city, characterized by mixed land-use patterns that include residential, commercial and industrial areas, transportation networks and rural areas. **Figure 4** shows the Urban Atlas land use map of Heraklion [19]. Apart from the Heraklion city core, the rest of the study area is featuring mixed urban and agricultural land cover pattern, mainly olive trees and vineyards.

Fourteen cloud-free Landsat 8 Surface Reflectance Climate Data Record (CDR) covering the test area corresponding to 1 year (April 1, 2013–April 30, 2014) were used in this study. The Landsat 8 CDR is a higher level data product of surface reflectance information for six bands,

http://dx.doi.org/10.5772/intechopen.71986

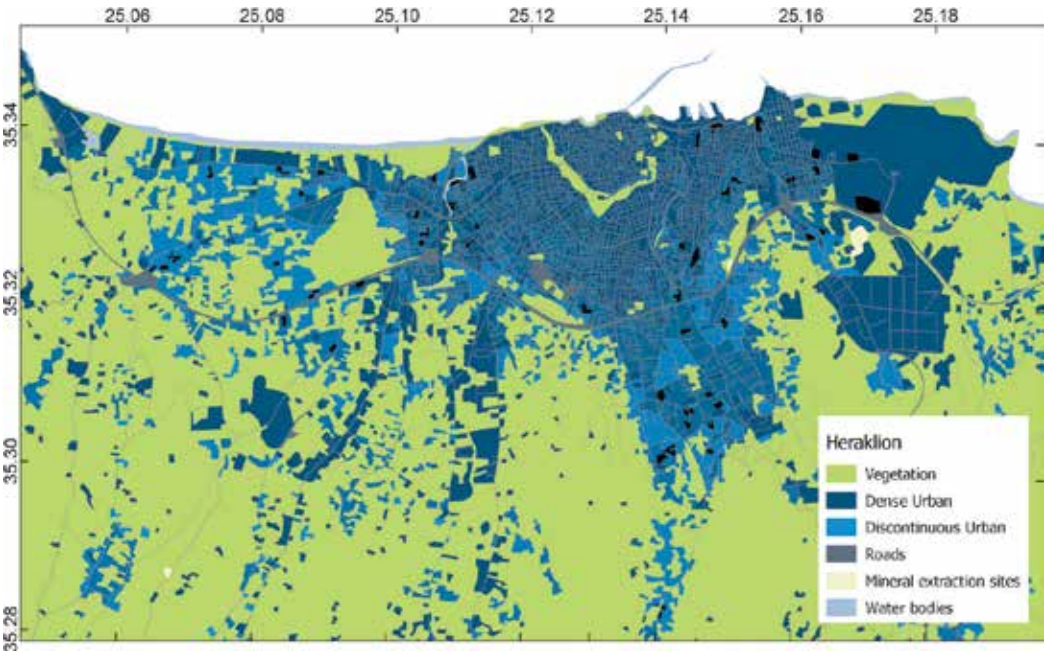

Figure 4. Urban Atlas land use polygons of the test site, the city of Heraklion, Greece.

generated from Landsat Ecosystem Disturbance Adaptive Processing System (LEDAPS) distributed by the U.S. Geological Survey [20].

Daily MODIS Level 1B (MOD021) data from both Terra and Aqua satellites for a period between April 1, 2013 and April 30, 2013 were acquired. The daily MODIS water vapor product (MOD05) was also used to provide ancillary atmospheric information on water vapor and cloud cover.

3.2. Urban surface cover mapping

The sub-pixel land cover information was estimated using spectral unmixing with a neural network, trained using endmember spectra collected from the image and synthetic spectra [21]. The methodology applied to produce the synthetic spectra and to estimate the surface cover fractions is briefly described below.

The urban surface is assumed to be composed of four land cover types: built-up surface, vegetation, non-urban bare surfaces, and water bodies. Using Landsat imagery, it is not easy to discriminate between different materials, but rather surface cover types, due to the medium spatial and low spectral resolution [22]. Thus, a redundant two-level hierarchy is assumed, as shown in **Figure 5**, including the four main surface cover types in the first level and a more detailed one in the second level, serving the endmembers collection.

Figure 5. The two-level hierarchical urban classification scheme used in this study.

Endmembers are collected from the image corresponding to the second level of the hierarchy. This ensures a variety of different endmember spectra in the library, representing different surface cover types, rather than a single category. It has to be noted here that the endmembers collected from medium resolution imagery do not correspond to material spectra, but rather spectra of large homogeneous surfaces. The spectral resolution of Landsat (30 m) is not enough to discriminate between types of the second level of hierarchy. The collected endmembers are then grouped to match the surface cover types of the first level.

The median value of each Landsat pixel surface reflectance for the total six images was estimated. The reason for doing this was to create a single image corresponding to the whole year and to avoid extreme reflectance values. The thermal and panchromatic bands were not included in the analysis. The median reflectance product is an image covering 1 year (April 1, 2013–April 30, 2014). This image is used for the collection of the endmember. The median is selected as a statistic to avoid extreme values, which might cause confusions in the network training and the unmixing process. A number of endmember spectra, corresponding to the cover types of **Figure 5**, is collected from the median reflectance product by visual inspection and using high resolution imagery from Google Earth as reference.

The endmember spectra are then used to produce synthetically mixed training data. These are generated using models corresponding to the first level of the classification scheme (**Figure 5**). Two- and three-endmemeber mixture models are considered, with repeated surface cover types allowed inside a model. **Table 1** shows the models that are considered for the spectral unmixing. No water endmembers are considered in the models and the generation of synthetic spectra, because water is generally dark and highly degenerate in terms of spectral mixture [15]. Both linear and non-linear mixture models are then considered for the generation of synthetic spectra.

The linear mixing model assumed is described by:

$$\rho_i = \sum_{j=1}^{M} a_j(i) \cdot \rho_j, \forall a_j(i) \geq 0 \; and \sum_{j=1}^{M} a_j = 1 \tag{1}$$

Three endmember	Two endmember
BU + VE + NB	BU + BU
BU + BU + VE	BU + VE
BU + BU + NB	BU + NB
BU + BU + BU	VE + NB

BU, Built-up; VE, Vegetation; NB, Non-urban bare.

Table 1. Mixture models assumed for spectral synthesis.

where ρ_i is the observed spectrum of pixel i, ρ_j is the representative spectrum of endmember j, and M is the number of endmembers in the mixture model. The abundance coefficients $a_j(i)$ represent the areal fraction of the endmembers ρ_j in the pixel i. The linear model assumes that the surface corresponding to a pixel is flat and uniformly irradiated. This simple model representing the spectrum ρ_i as a linear combination of the endmember spectra ρ_j is rather popular [23]. Using the endmember spectra for each cover type, for all the models in **Table 1** and assuming combinations of different mixture levels $a_j(i)$, mixed spectra ρ_i are produced.

Although many studies assume linear mixing effects, it has been known for some time that non-linear spectral mixing effects can be a crucial component in many real-world scenarios, including the urban scenes [24]. The buildings and the street canyons create a complicated 3D structure in the cities at a meter scale, which induces multiple scattering of light between surfaces. Recently, a physics-based approach of a spectral mixture model suitable for urban scenes was presented and validated against simulated urban scenes using a quadratic mixing model [25]:

$$\rho_i = \sum_{j=1}^{M} a_j(i) \cdot \rho_j + \sum_{j=1}^{M} \sum_{l=j}^{M} b_{j,l}(i) \cdot \rho_j \rho_l \tag{2}$$

where the $\sum_{j=1}^{M} a_j(i) \cdot \rho_j$ accounts for the linear mixing, while $\sum_{j=1}^{M} \sum_{l=j}^{M} b_{j,l}(i) \cdot \rho_j \rho_l$ accounts for the non-linear interactions in the urban structure. The abundance coefficients $a_j(i)$ represent the areal fraction of the endmember ρ_j in the pixel i and the endmember spectra are used, for all the models in **Table 1**, with randomly generated $b_{j,l}(i)$ coefficients to produce synthetic spectra.

A three-layer feed-forward neural network with a sigmoid activation function was used in this study. The input layer has six neurons, one for each Landsat band and four output neurons, one for each of the land cover types of the first level (**Figure 5**) and a hidden layer with 12 neurons. The number of hidden neurons is set to 12, because the network performance would not improve much by adding more neurons. The network is trained using a Levenberg-Marquardt backpropagation algorithm and endmember and synthetic spectra from the developed spectral library. The network training data output is set to a combination of values in the interval [0,1], matching the coefficients $a_j(i)$ used during the spectral synthesis. Once trained, the network is then applied to estimate the surface cover fractions individually for the Landsat scenes.

The developed spectral library contains 15 endmember spectra, 2 representing buildings/roofs bright materials, 2 representing buildings/roofs dark materials, 3 transportation areas (roads, parking lots, and airport runways), 1 sport infrastructure, 3 green vegetation, 1 non-photosynthetic vegetation, 2 bare soil, and 1 rocks. Synthetic spectra were generated from these endmembers using the two- and three-endmember models presented in **Table 1**. In the end, a set of 72,030 synthetic spectra were used to train the neural network. Randomly chosen 70% of the spectral library data were used for training, 15% for validation and 15% for testing the neural network. The topology of the network was determined to be 6-12-3 input-hidden-output neurons and the Levenberg-Marquardt backpropagation algorithm was used to estimate the weights and bias values of the network. Derived estimates were then applied independently in the series of 14 Landsat images, and cover fraction images for the four land cover types assumed in this study were generated.

An example of the resulting surface cover fraction maps for May and August is shown in **Figure 6**. The general pattern shown in **Figure 6** matches the Urban Atlas polygons (**Figure 4**). Moreover, the fraction image corresponding to May reveals more vegetation abundance than the one corresponding to August both in the outskirts as well as in the urban core.

3.3. Urban land surface temperature

Although LST is routinely derived by satellite TIR observations, currently there is no space-borne sensor capable of providing frequent thermal imagery at spatial resolution needed in urban studies. Current and forthcoming TIR remote sensing is confronting the trade-off between spatial and temporal resolution. A synergistic method that unmixes the low-resolution TIR measurements using high spatial information on the surface cover for estimating high spatial resolution LST is applied here [26]. The method is a multistep procedure described in detail along with its validation in Ref. [26]. For the method to be applied, information on the surface cover fractions is necessary. Representative emissivity values are then assigned to each of the cover types in **Figure 5**, using information derived from the ASTER Spectral Library [27]. Samples from the library, which are representative for the study area, are selected and convolved with the sensor's spectral response function and the emissivity $\varepsilon_k^{(H)}$ for each pixel high resolution (H) pixel i is estimated by:

$$\varepsilon_k^{(H)} = \sum_{i=1}^{n} \varepsilon_i \cdot a_{ik}^{(H)} \tag{3}$$

where n is the number of surface cover types, ε_i is the representative emissivity value for the surface cover type i, and $a_{ik}^{(H)}$ are the estimated fractions of surface cover types.

Spatial-spectral unmixing is then used to enhance the spatial resolution of the low resolution thermal bands. The contribution of the land cover components is estimated for each thermal pixel k, by summing the estimated fractions $a_{j_i}^{(H)}$:

$$A_{k_i}^{(L)} = \frac{1}{P} \sum_{j \in P} a_{j_i}^{(H)} \tag{4}$$

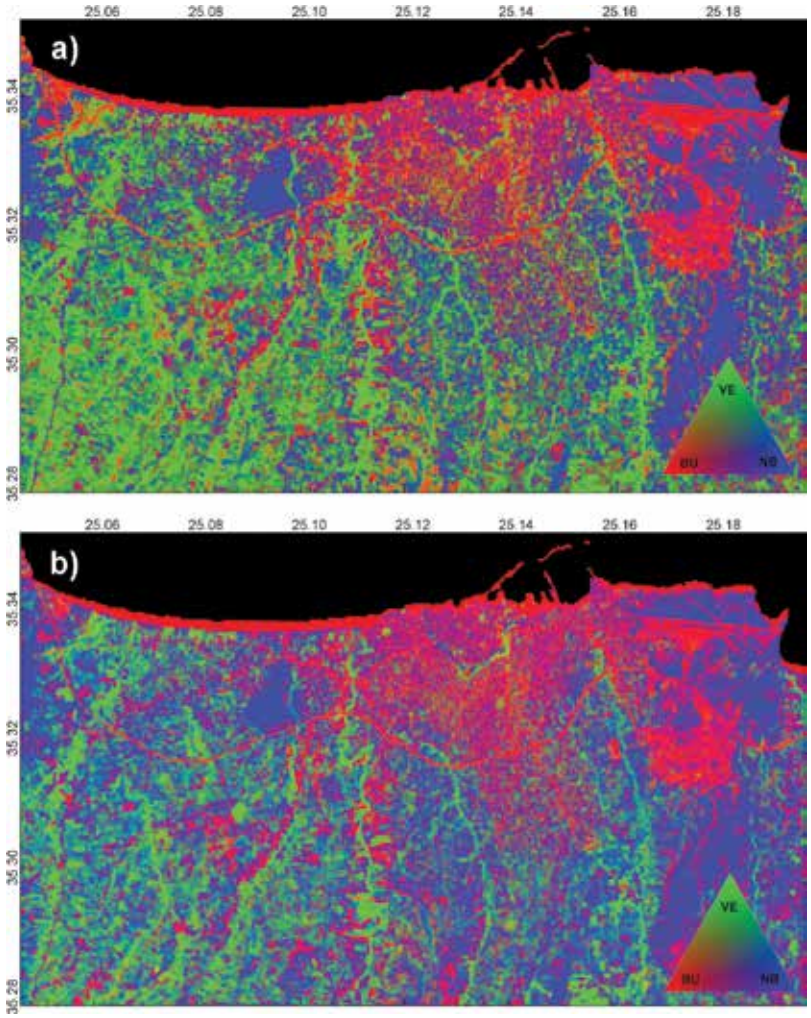

Figure 6. Pseudo color composition of the derived fraction images for the May 13, 2013 (a) and August 22, 2013 (b).

where P is the number of high resolution pixels ($j \in P$) corresponding to each low resolution one (k). Each low resolution pixel is then unmixed, using the contextual information of the neighboring pixels in a window (a window of size w):

$$\underset{w\times 1}{\underbrace{\boldsymbol{S}^{(L)}}} = \underset{w\times n}{\underbrace{\boldsymbol{A}^{(L)}}} \cdot \underset{n\times 1}{\underbrace{\boldsymbol{E}}} + er \tag{5}$$

where $S^{(L)}$ is a vector of the thermal radiances of the pixels in the window, $A^{(L)}$ is a matrix of the contributions of surface types to those pixels, and E is the thermal radiances under consideration. A regularization term is also used to prevent large deviations in optimization:

$$min_E \left\| \boldsymbol{S}^{(L)} - \boldsymbol{A}^{(L)} \cdot \boldsymbol{E} + b \frac{w^2}{n} (\boldsymbol{E} - \boldsymbol{S}'^{(L)}) \right\|_2^2 \quad (6)$$

where $\overline{S}^{(L)}$ are predefined spectra corresponding to surface cover types and b is a regularization parameter to ensure small spectral variations. The high spatial resolution thermal band is then constructed by applying Eq. (5) for high resolution (H).

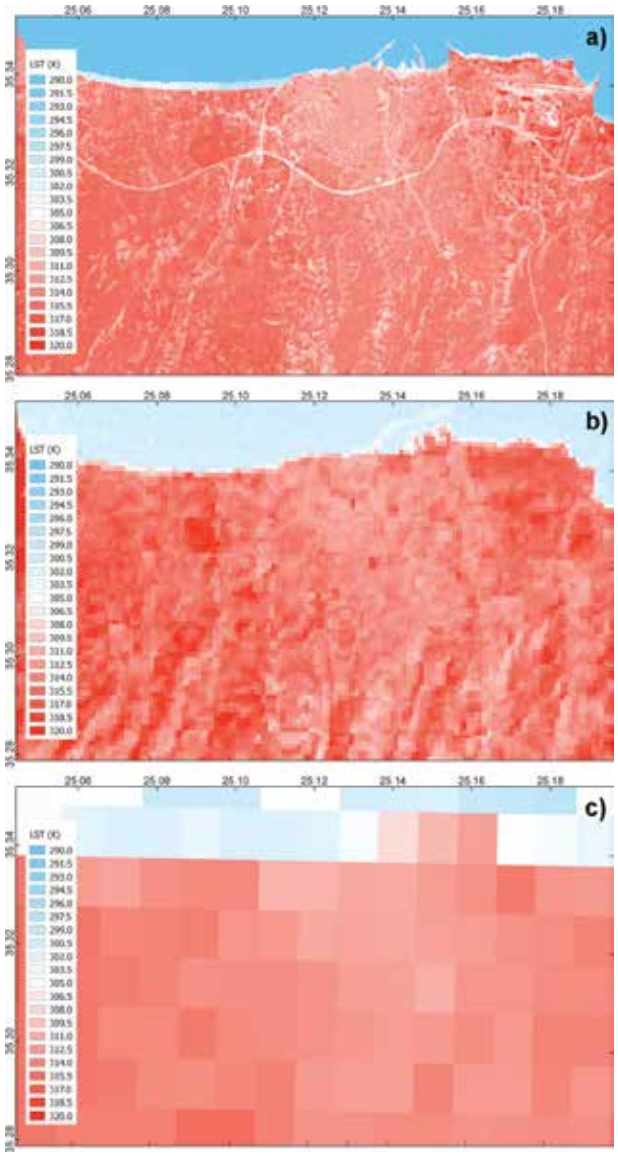

Figure 7. An example of downscaled LST (K) for the August 30, 2013 (a). The ASTER (b) and MODIS (c) LST products corresponding to the same date are also presented for comparison.

Given high resolution brightness temperature products for two thermal bands (T_i, T_j) and the respective emissivity products (ε_i, ε_j), LST is derived in high spatial resolution using a split-window algorithm [28]:

$$LST = T_i + c_0 + c_1 \Delta T + c_2 \Delta T^2 + (c_3 + c_4 WV)(1 - \varepsilon) + (c_5 + c_6 WV)\Delta\varepsilon \quad (7)$$

where WV is the atmospheric water vapor content, $\varepsilon = (\varepsilon_i + \varepsilon_j)/2$, $\Delta\varepsilon = \varepsilon_i - \varepsilon_j$, and c_0-c_6 are the split-window coefficients determined from the algorithm calibration.

The LST downscaling method was applied to the series of daily MODIS and a time series of daily high resolution LST (90 m) was derived for the case study. **Figure 7** shows an example of the methodology application for a cloud-free day (30 August, 2013) for which the ASTER LST product was also available. **Figure 7a** shows the high resolution LST, derived using the above-described downscaling procedure. The ASTER (**Figure 7b**) and MODIS (**Figure 7c**) LST products corresponding to the same date are also presented for comparison. The general temperature pattern of the downscaled LST product is similar to the ASTER LST product. The level of detail that appears in the downscaled product (**Figure 7a**) compared to the ASTER LST product (**Figure 7b**) is because the downscaled product is of 30 m spatial resolution (matching the Landsat-derived surface cover fractions), while the ASTER LST product is of 90 m spatial resolution.

4. Discussion

Medium spatial resolution satellite data have been used in the past with spectral unmixing methods for mapping the urban surface cover [15]. This chapter demonstrated the use of image endmember and synthetic spectra to estimate sub-pixel information on the urban surface cover. The proposed methodology is fast in terms of computational time and affordable to implement and apply for urban studies. It is also easy to reproduce for other cities, if the relevant data are available. It is, thus, suitable for monitoring the surface cover and it can be used for change detection and time series analysis. The products are useful for various studies, related to surface cover properties, urban climate, urban climatology, and urban expansion.

An example use of this detailed urban surface cover information is the LST downscaling method. The method described and applied in this chapter is highly dependent on accurate surface cover information. It has been demonstrated than the uncertainty in the downscaled LST estimation is closely linked to the uncertainty related to the surface cover fractions [29]. The methodology for mapping the urban surface cover is applicable to Sentinel-2 imagery. The enhanced spatial and spectral resolution of Sentinel-2 compared to Landsat is expected to advance the method. The optical bands of Sentinel-2 are similar to the ones of Landsat 8, but the enhanced spatial resolution of 10 m provides better insights on the underlying objects. Further advances may include analysis of the 10 m bands for identifying pure spectra to be used as endmembers for spectral unmixing techniques. Moreover, the additional bands

in the near-infrared compared to Landsat, for example, provide more spectral information necessary for unmixing techniques. Although these bands are designed for detecting and discriminating between different vegetation types, and their main advantage lies in this kind of applications, they can be proven useful for differentiating between urban materials as well. Further analysis is, though, needed to come to conclusions on using the red-edge bands for urban monitoring. Finally, Sentinel-2A and Sentinel-2B will provide frequent acquisitions with a revisit of 5 days in the equator and, in combination with the large swath of 290 km, the potential of updating the surface cover information is significantly increased. Thus, the increased temporal resolution substantiates the urban surface cover monitoring even in areas with persistent cloud cover.

The application of the downscaling method described in this chapter was demonstrated through an example using MODIS thermal data. With the use of the Sentinel-2 imagery, the surface cover characterization is expected to be improved significantly as discussed earlier. Moreover, the OLCI spectral bands measuring in VNIR share some common bands with Sentinel-2 MSI and this may allow further exploitation for updating the surface cover. Since, the Sentinels are developed for synergies [30], algorithms that exploit the common bands of OLCI and MSI may increase the accuracy of surface characterization and emissivity estimation.

5. Conclusions

The urban surface cover and the urban LST are essential to map and monitor in urban climate studies. This chapter demonstrates the use of satellite Earth observation geo-spatial data to assist the study of urban climate. The methods proposed here can be easily adapted to the Sentinels, which will have high revisit rate, and thus to provide high spatial and temporal resolution LST products for urban areas. Approaches like the ones described in this chapter can become operational once adapted to Sentinels, since their long-term operation plan guarantees the future supply of satellite observations. Thus, the described methods may support planning activities related to climate change mitigation and adaptation in cities, as well as routine urban planning activities. It is therefore expected to advance the current knowledge of the impacts of the intra-urban LST variability on urban energy budget and hence on both urban heat island and energy consumption in cities.

Acknowledgements

The project leading to this application has received partial funding from the European Union's Horizon 2020 research and innovation program under grant agreement No. 637519 (URBANFLUXES) and partial funding from the project SEN4RUS (MIS T3EPA-00101) which is funded by the Operational Programme "Competitiveness, Entrepreneurship and Innovation" (NSRF 2014–2020) and co-financed by Greece and the European Union (European Regional Development Fund).

Author details

Zina Mitraka* and Nektarios Chrysoulakis

*Address all correspondence to: mitraka@iacm.forth.gr

Foundation for Research and Technology Hellas, Heraklion, Greece

References

[1] Landsberg HE. The Urban Climate. New York: Academic Press; 1981

[2] Chrysoulakis N, Marconcini M, Gastellu-Etchegorry J-P, Grimmond CSB, Feigenwinter C, Lindberg F, Del Frate F, Klostermann J, Mitraka Z, Esch T, Landier L, Gabey A, Parlow E, Olofson F. Anthropogenic heat FLUX estimation from Space. In: Proceedings of 2017 Joint Urban Remote Sensing Event, JURSE 2017; Dubai, United Arab Emirates; 6-8 March 2017. DOI: 10.1109/JURSE.2017.7924591

[3] Khamsi R. Human activity implicated in Europe's 2003 heat wave. news@nature. 2004. DOI: 10.1038/news041129-6

[4] Arnfield AJ. Two decades of urban climate research: A review of turbulence, exchanges of energy and water, and the urban heat island. International Journal of Climatology. 2003;**23**:1-26. DOI: 10.1002/joc.859

[5] Barnes KB, Morgan JM, Roberge MC, Roberge M. Impervious Surfaces and the Quality of Natural and Built Environments. Baltimore, Maryland: Towson University; 2002

[6] Santamouris M. Using cool pavements as a mitigation strategy to fight urban heat island—A review of the actual developments. Renewable and Sustainable Energy Reviews. 2013; **26**:224-240. DOI: 10.1016/j.rser.2013.05.047

[7] Hepinstall JA, Alberti M, Marzluff JM. Predicting land cover change and avian community responses in rapidly urbanizing environments. Landscape Ecology. 2008;**23**:1257-1276. DOI: 10.1007/s10980-008-9296-6

[8] Grimm NB, Faeth SH, Golubiewski NE, Redman CL, Wu J, Bai X, Briggs JM. Global change and the ecology of cities. Science. 2008;**319**:756-760. DOI: 10.1126/science.1150195

[9] Batty M. The size, scale, and shape of cities. Science. 2008;**319**:769-771. DOI: 10.1126/science.1151419

[10] Rashed T, Weeks JR, Stow D, Fugate D. Measuring temporal compositions of urban morphology through spectral mixture analysis: Toward a soft approach to change analysis in crowded cities. International Journal of Remote Sensing. 2005;**26**:699-718. DOI: 10.1080/01431160512331316874

[11] Bhatta B. Analysis of Urban Growth and Sprawl from Remote Sensing Data. Berlin, Heidelberg: Springer Science & Business Media; 2010

[12] Weng Q, editor. Global Urban Monitoring and Assessment through Earth Observation. 1st ed. Boca Raton, Florida, USA: CRC Press Taylor & Francis Group; 2014. 387 p. ISBN: 9781466564497

[13] Shannon CE. Communication in the presence of noise. Proceedings of the IRE. 1949; **37**:10-21

[14] Roberts DA, Quattrochi DA, Hulley GC, Hook SJ, Green RO. Synergies between VSWIR and TIR data for the urban environment: An evaluation of the potential for the Hyperspectral infrared imager (HyspIRI) decadal survey mission. Remote Sensing of Environment. 2012;**117**:83-101. DOI: 10.1016/j.rse.2011.07.021

[15] Powell R, Roberts D, Dennison P, Hess L. Sub-pixel mapping of urban land cover using multiple endmember spectral mixture analysis: Manaus, Brazil. Remote Sensing of Environment. 2007;**106**:253-267. DOI: 10.1016/j.rse.2006.09.005

[16] Weng Q, Hu X, Liu H. Estimating impervious surfaces using linear spectral mixture analysis with multitemporal ASTER images. International Journal of Remote Sensing. 2009;**30**:4807-4830. DOI: 10.1080/01431160802665926

[17] Drusch M, Del Bello U, Carlier S, Colin O, Fernandez V, Gascon F, Hoersch B, Isola C, Laberinti P, Martimort P, Meygret A, Spoto F, Sy O, Marchese F, Bargellini P. Sentinel-2: ESA's optical high-resolution mission for GMES operational services. Remote Sensing of Environment. 2012;**120**:25-36. DOI: 10.1016/j.rse.2011.11.026

[18] Berger M, Moreno J, Johannessen JA, Levelt PF, Hanssen RFESA. S missions in support of earth system science. Remote Sensing of Environment. 2012;**120**:84-90. DOI: 10.1016/j.rse.2011.07.023

[19] Meirich S. Mapping Guide for a European Urban Atlas. Available from: http://ec.europa.eu/regional_policy/sources/tender/pdf/2012066/annexe2.pdf [Accessed: 2017-11-29]

[20] Masek JG, Vermote EF, Saleous N, Wolfe R, Hall FG, Huemmrich F, Gao F, Kutler J, Lim TK. LEDAPS Calibration, Reflectance, Atmospheric Correction Preprocessing Code, version 2. Model product. 2013. Available from: http://daac.ornl.gov/cgi-bin/dsviewer.pl?ds_id=1146 [Accessed: 2017-11-29]

[21] Mitraka Z, Del Frate F, Carbone F. Nonlinear spectral Unmixing of Landsat imagery for urban surface cover mapping. IEEE Journal of Selected Topics in Applied Earth Observations and Remote Sensing. 2016;**9**(7):1-11. DOI: 10.1109/JSTARS.2016.2522181

[22] Small C. The Landsat ETM+ spectral mixing space. Remote Sensing of Environment. 2004; **93**:1-17. DOI: 10.1016/j.rse.2004.06.007

[23] Keshava N, Mustard JF. Spectral unmixing. IEEE Signal Processing Magazine. 2002;**19**: 44-57

[24] Heylen R, Parente M, Gader P. A review of nonlinear hyperspectral unmixing methods. IEEE Journal of Selected Topics in Applied Earth Observations and Remote Sensing. 2014;**7**:1844-1868. DOI: 10.1109/JSTARS.2014.2320576

[25] Meganem I, Déliot P, Briottet X, Deville Y, Hosseini S. Linear-quadratic mixing model for reflectances in urban environments. IEEE Transactions on Geoscience and Remote Sensing. 2014;**52**:544-558. DOI: 10.1109/TGRS.2013.2242475

[26] Mitraka Z, Chrysoulakis N, Doxani G, Del Frate F, Berger M. Urban surface temperature time series estimation at the local scale by spatial-spectral Unmixing of satellite observations. Remote Sensing. 2015;**7**:4139-4156. DOI: 10.3390/rs70404139

[27] Baldridge AM, Hook SJ, Grove CI, Rivera G. The ASTER spectral library version 2.0. Remote Sensing of Environment. 2009;**113**:711-715. DOI: 10.1016/j.rse.2008.11.007

[28] Jimenez-Munoz J-C, Sobrino JA. Split-window coefficients for land surface temperature retrieval from low-resolution thermal infrared sensors. IEEE Geoscience and Remote Sensing Letters. 2008;**5**:806-809. DOI: 10.1109/LGRS.2008.2001636

[29] Mitraka Z, Doxani G, Del Frate F, Chrysoulakis N. Uncertainty estimation of local-scale land surface temperature products over urban areas using Monte Carlo simulations. IEEE Geoscience and Remote Sensing Letters. 2016;**13**(7):1-5. DOI: 10.1109/LGRS.2016.2553367

[30] Gastellu-Etchegorry J-P, Lauret N, Yin T, Landier L, Kallel A, Malenovsky Z, Al Bitar A, Aval J, Benhmida S, Qi J, Medjdoub G, Guilleux J, Chavanon E, Cook B, Morton D, Chrysoulakis N, Mitraka Z. DART: Recent advances in remote sensing data modeling with atmosphere, polarization, and chlorophyll fluorescence. IEEE Journal of Selected Topics in Applied Earth Observations and Remote Sensing. 2017;**10**:2640-2649. DOI: 10.1109/JSTARS.2017.2685528

Section 7

Space Technology in Natural Disaster

Chapter 8

Pre-earthquake Anomaly Detection and Assessment through Lineament Changes Observation Using Multi-temporal Landsat 8-OLI Imageries: Case of Gorkha and Imphal

Biswajit Nath, Zheng Niu and Shukla Acharjee

Additional information is available at the end of the chapter

http://dx.doi.org/10.5772/intechopen.72735

Abstract

Pre-earthquake anomaly detection and assessment was performed in the present study through lineament changes observation by using multitemporal Landsat 8 OLI satellite imageries. These data found convincing results to identify relevant anomalous variations prior to the two recent earthquakes, that is, Gorkha of Nepal 7.8 M_w (major) (25 April 2015) and Imphal of Manipur (eastern India) 6.7 M_w (strong) (4 January 2016) compared with normal behavior in the absence of earthquake. Epicenter-based single tile of five multitemporal Landsat 8 OLI data was considered for each case, where one image was considered to show the normal behavior of lineament (in the absence of earthquake) and three for anomalous behavior prior to earthquake (in the presence of earthquake), and the rest one used to represent post-earthquake behavior (in the absence of earthquake), respectively. The derived lineament data were used further in different forms to observe pre-earthquake anomalies. The research results witnessed major changes of lineaments and observed anomalies prior to the two impending earthquakes while it was observed normal behavior in the absence of earthquake event. The results obtained using the automated and geo-integrated techniques help us to detect earthquake in advance prior to its strike could be used an alternative method in worldwide for future earthquake monitoring.

Keywords: pre-earthquake anomaly, lineament change, multitemporal, Landsat 8 OLI, Gorkha, Imphal

1. Introduction

In the modern geoscientific time frame, remote-sensing and GIS techniques have been tremendously used for obtaining reliable information from satellite imageries at macro- to microscale investigations. Studies of linear geologic features (lineaments) from macro- to microlevel have been increasing rapidly. Lineament extraction from satellite imagery either by visual or automatic interpretation has been a long interest of geologists, where the character and extent of these features have been realized and lineament analysis of remotely sensed data using automatic extraction, is a valuable source of information for studying the structural settings of an area. The term "Lineament" has been widely used in the field of geology, and literally, it expresses by different scientists through their research work in different ways. The term lineament was first described as significant line of landscape within the basement rocks [1]. The lineament defines as linear features in a landscape identified on satellite images and aerial photographs, most likely have a geological origin. Generally, lineaments are underlying by structural zone, fractured zone, a series of fault or fold aligned hills zone of localized weathering and zone of increased permeability, porosity, seismicity, landslide formation [2], active erosion, and karst development [3].

Lineament extraction and analysis have been studied by different distinguished scientists [4–11]. Besides these, lineament analysis has been used extensively for geologic interpretation, particularly from the 1930s with the advent of photogeology [12]; because satellite data provide quick and useful baseline information on the parameters controlling the occurrence and movement of groundwater like geology, lithology/structural, geomorphology, soils, land use/land cover, and lineaments. With the advancement of remote sensing techniques, identifications of lineaments for earthquake have become a rapid and cost-effective procedure. One of the main features of geological interpretation of satellite imagery has been the recognition of lineaments varying in length from a few kilometers to hundreds of kilometers [13]. The lineament is a mappable linear or curvilinear feature of a surface whose parts align in a straight or slightly curving relationship [14], which differs from the pattern of adjacent features and reflects some subsurface phenomena [15].

Moreover, lineament mapping and analyses have been gaining popularity with the increasing availability of satellite images [16]. Since satellite images are obtained from varying wavelength intervals of the electromagnetic spectrum, they are considered to be a better tool to discriminate the lineaments and to produce better information rather than conventional aerial photographs. Recently, two earthquakes were badly hit in the geologically complex regions, that is, Gorkha region of Nepal (7.8 M_w) on 25 April 2015 and Imphal region of Manipur, Eastern India (6.7 M_w) on 4 January 2016, respectively. By observing the severity of the two earthquakes, these two study areas have been considered for our present research.

The main objective of this study is to extract lineament features through automatic approaches by using Landsat 8 Satellite imageries, which further used to calculate lineament length and directional change measurement through rose diagram and to know the pre-earthquake anomaly through lineament changes observation in the presence and the absence of an earthquake. Therefore, vector overlay technique was performed on lineament temporal data considered for the two impending earthquakes (major and strong). The earthquake occurrence signals were noticed in individual case by interpreting five satellite scenes of Landsat 8 OLI sensors.

http://dx.doi.org/10.5772/intechopen.72735

2. Materials and methods

2.1. Study area

The study area for each case covers 370 km^2 in size of each single satellite scene. The first study case is Nepal, which lies toward the southern limit of the diffuse collisional boundary where the Indian plates under thrusts the Eurasian plate, occupying the central sector of the Himalayan arc [17]. In Gorkha of Nepal case, the northern part of the satellite scene is covered by parts of China. Gorkha earthquake in Nepal (7.8 M_w) is a shallow earthquake occurred on 25 April 2015 (epicenter position: 28.147° N and 84.708° E) at a depth of 15 km created massive destruction. This earthquake was caused by a sudden thrust or release of built up stress along the major fault line [18].

On the other hand, the second case study is Imphal earthquake (6.7 M_w), which occurred in northeast regions of India in the state of Manipur. This earthquake was struck on 4 January 2016 at a depth of approximate 55.0 km (measured by United States Geological Survey, USGS) and about 15 km west of the fault coinciding with the edge of the Imphal valley. The epicenter (position: 24.804° N and 93.651° E) was in Manipur's Tamenglong district, and bordering area with Myanmar is in the right section of that corresponding image. According to Gahalaut V.K., and Kundu B., this earthquake was occurred on steep plane due to typical intraslab type movement within Indian plate, which predominantly moves toward north, and developed crack which was N-S oriented along with oblique motion (1–2 cm), and it was observed during field visit [19]. The regional plate boundary in eastern India-the Indo-Burmese Arc is oriented approximately in south-southwest-north-northeast direction (see [20]). The location of study areas is shown in **Figure 1**.

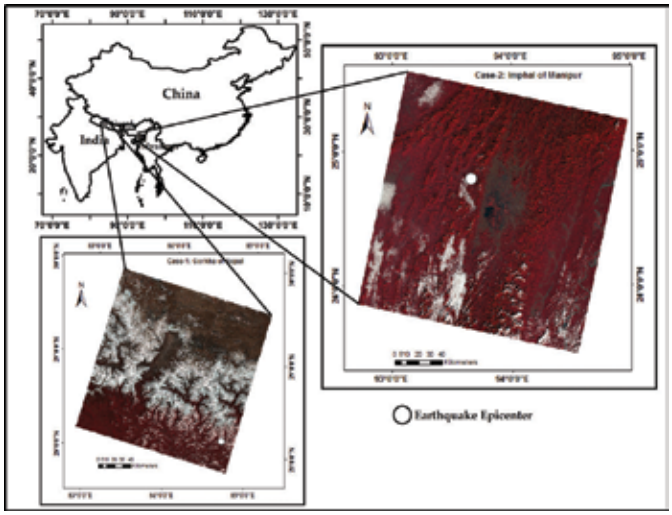

Figure 1. Location of study area.

2.2. Data

Datasets utilized for the present study included Landsat 8 Operational Land Imager Images. The details of data sources of Landsat 8 OLI imageries for both regions are shown in **Figure 2**: 2A and 2B, respectively, which were acquired from USGS Landsat archives (OLI, http://earthexplorer.usgs.gov/) path: 142, row: 40 for case 1, considering snow and partial cloud coverages and path: 135, row: 35 for case 2, considering partial cloud coverage.

The data product considered for the present research has a 30-m spatial resolution based on different days' interval prior to earthquake occurrence, the absence of earthquake and after the earthquake event. Detailed descriptions regarding the datasets used for this research are shown in **Table 1**.

These satellite images are a digital representation of the Earth's surface for the identification of lineament and its corresponding directional change that may represent the surface expression of geological structures [21, 22]. The digital image processing, thematic mapping of lineament, overlay operation and directions of lineament were obtained using the ENVI 5.3, PCI Geomatica 9.1, ArcGIS 10.5, and Rock Works 16 software, respectively. To investigate the normal behavior of lineament in the absence of earthquake, it has been found suitable imagery of 31 January 2015 only for case 1 (85 days before earthquake strike). From 31 January 2015 to 20 March 2015, all the available imageries suffer with extensive cloud; thus, they were neglected. Meanwhile, in case 2, from 19 March to 30 November 2015, three earthquakes (low category: 4.1–4.3 M_w) were struck in the study area, and most of the available imageries also suffer with cloud; thus, those

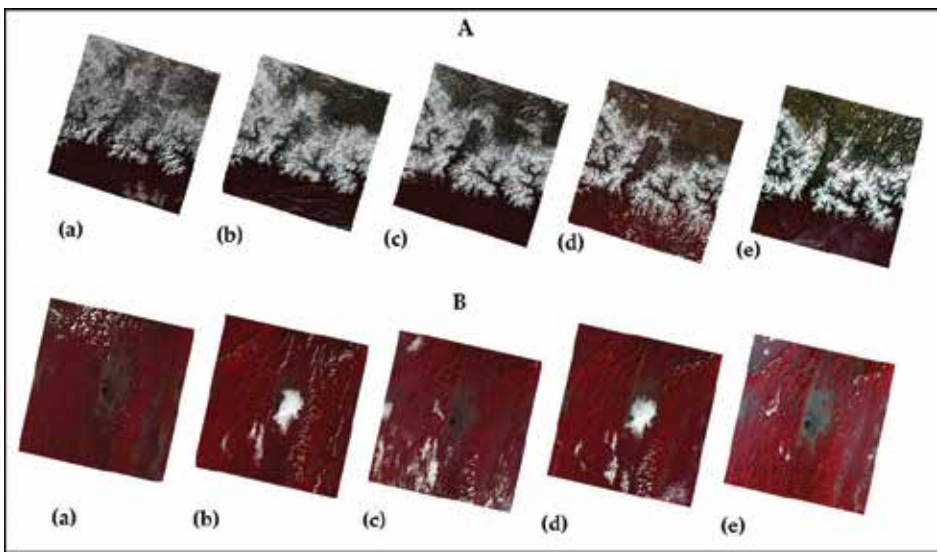

Figure 2. The details of data sources of Landsat 8 OLI imageries for two study areas: (A) Nepal and part of China shown in different time series Landsat 8 OLI data (FLAASH atmospheric corrected image): (a) 31 January 2015 (absence of EQ); (b) 20 March 2015 (presence of EQ); (c) 5 April 2015 (presence of EQ); (d) 21 April 2015 (presence of EQ); and (e) 7 May 2015 (post EQ); (B) Manipur and part of Myanmar shown in different time series Landsat 8 OLI data (FLAASH atmospheric corrected image): (a) 19 March 2015 (absence of EQ); (b) 30 November 2015 (presence of EQ); (c) 16 December 2015 (presence of EQ); (d) 1 January 2016 (presence of EQ), and (e) 17 January 2016 (post EQ).

Satellite sensors	Date of image acquisition	Days interval	Path/row	Resolution (m)
Gorkha of Nepal (case 1): category: major				
Landsat 8 OLI	31 January 2015 (absence of EQ)	85 days (before)	142/40	30
Landsat 8 OLI	20 March 2015 (presence of EQ)	36 days (before)	142/40	30
Landsat 8 OLI	5 April 2015 (presence of EQ)	20 days (before)	142/40	30
Landsat 8 OLI	21 April 2015 (presence of EQ)	4 days (before)	142/40	30
Landsat 8 OLI	7 May 2015 (post-EQ)	12 days (after)	142/40	30
Imphal of Manipur (case-2): category: strong				
Landsat 8 OLI	19 March 2015 (absence of EQ)	292 days (before)	135/43	30
Landsat 8 OLI	30 Nov 2015 (presence of EQ)	36 days (before)	135/43	30
Landsat 8 OLI	16 Dec 2015 (presence of EQ)	20 days (before)	135/43	30
Landsat 8 OLI	1 Jan 2016 (presence of EQ)	4 days (before)	135/43	30
Landsat 8 OLI	17 Jan 2016 (post-EQ)	13 days (after)	135/43	30

Brackets terminology in the 1st column OLI refer Operation Land Imager and 2nd column EQ refer Earthquake. *Source*: USGS-Earth explorer Landsat 8 Archive.

Table 1. Details of data used in this research.

imageries automatically neglected like case 1. Therefore, looking forward, it has been found that suitable imagery of 292 days before earthquake strike contains very less percentage of cloud.

From the visual observation of datasets, it has been confirmed that all considered Landsat 8 OLI images used for the automatic lineament feature extractions were partially covered by snow and cloud in case 1 and only by cloud in case 2, which did not affect too much of the lineament data volume. The present test has been conducted based only on satellite data without giving any importance of ground validation data. Traditional research application always required field surveys with ground validation data to match properly with satellite data. However, in this test, it has been used popular traditional technique of automatic line algorithm of PCI Geomatica for lineament data extraction, which clearly highlights the lineament changes in the study areas. The automatic LINE algorithm technique generates sufficient number of lineament data over the two study regions, which were used to know the pre-earthquake anomaly detection and assessment by considering multi-dates Landsat 8 OLI imageries. Though, very limited errors have been observed in extracted lineament data which is further checked by overlaying the highways, railroads, etc. These identified errors were checked with available vector shapefiles of those regions, thus finally neglected and removed from extracted lineament database. The present results which have derived automatically from satellite imageries clearly defined lineament datasets and do not need further validation, as the technique was commonly used by numerous researches. However, if validation required, the extracted data can be verified with superposition of layers with geological map of the specific areas. These are the scientific achievements of space technology application over the traditional surveys, as each satellite scene covered in large area in a single acquisition time, where ground surveys need longer period of time and sometimes not possible due to high rugged terrain or any other natural obstacles present in the Earth's surface.

2.3. Methodology

Satellite images (multispectral or digital elevation models) and aerial photography are broadly used to extract lineaments for different purposes, like defining geological structures and tectonics fabrics. Each image consists of 11 spectral bands and scene size is 185 km north-south by 185 km east-west, which enables the delineation of the geological lineaments in the study area. In this experiment, automatic extraction of geologic lineament performed through different steps including from raw satellite imagery pre-processing like DN value conversion into radiance, radiance to reflectance and later atmospheric correction using the FLAASH (Fast Line-of-sight Atmospheric Analysis of Hypercubes) module. Thereafter, enhancement-linear 5% stretch performed over R, G, B (5, 4, 2) band combinations respectively to get the better visualization image and at the end of this stage, all images were assigned to WGS 1984 datum with projection parameter of UTM zone 45 N (case 1) and 46 N (case 2), respectively.

In the next stage, principal component analysis (PCA) was performed on each atmospheric corrected image and each PC-1 image was created by considering best band selection, based on Eigen number and Eigen value, thus finally help to enhance image discontinuties corresponding to structural lineaments. For the present research, at initial stage, we have developed the theoretical model (**Figure 3**) to demonstrate whether the results are coherent with the theoretical model based on the different output of images.

Lineament distribution maps of Nepal and Manipur were prepared from Landsat 8 OLI satellite imageries by using four different remote sensing and GIS software's integration, where one software output was used by other to obtain the final lineament results. The OLI spectral band in gray scale was used to extract lineament. Out of five images of each case, one image used to observe the normal behavior in the absence of earthquake event, three images for "anomaly" observation (pre-earthquake stage), whereas another single image was used for after earthquake lineament change observation of Nepal and Manipur earthquake, respectively. Before the methodological description breakdown, the overall workflow of the present research is shown in **Figure 4**.

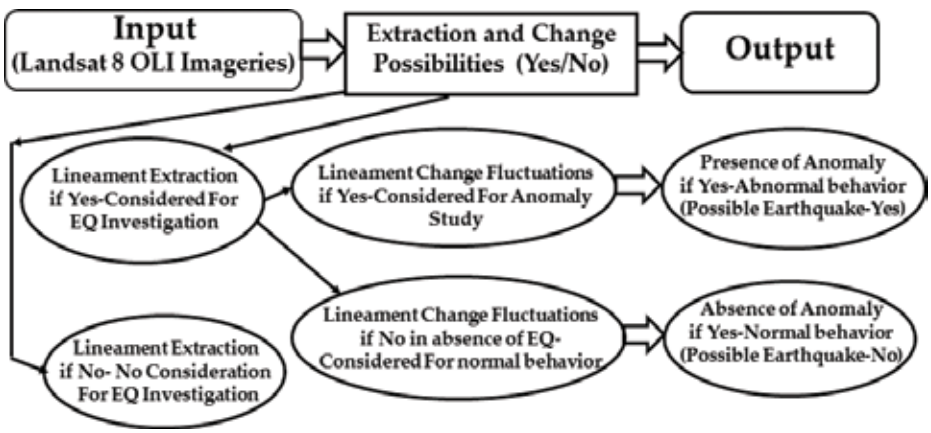

Figure 3. Theoretical model developed for the present research.

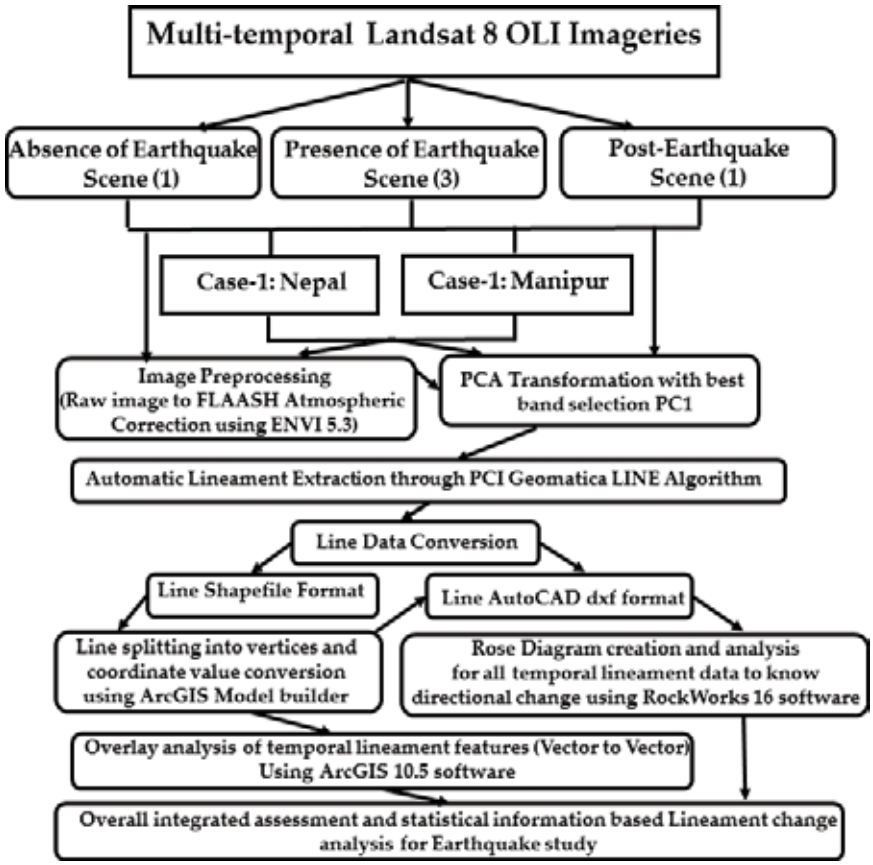

Figure 4. Flowchart of methodology used in this research.

2.3.1. Lineament extraction, line splitting, and length analysis method

There are two common methods for the extraction of lineaments from satellite images: visual extraction and automatic extraction. Most popular traditional methods based on edge filtering techniques, that is, Sobel, PCA, ICA, MNF, band rationing, RGB band combinations with high contrast, different stretch and directional filters are used worldwide for lineament extraction. In this research, PCA is considered, and the most widely used software is deployed for the automatic lineament extraction with the most common popular traditional method, that is, LINE algorithm of PCI Geomatica 9.1 v software [23], which consists of three stages [24] has accentuated and facilitated the detection of lineament in the satellite images. Various computer-aided methods such as edge detection, thresholding, and curve extraction steps [25] were carried out over derived principal component analysis (PCA) image (i.e., PC1) of the study area under default parameter windows, where user defined modification of values can be done using this software. For processing and extraction of lineaments, the following algorithm parameters and its corresponding values were used such as RADI-Radius of the filter in pixels (10), GTHR-Threshold for edge gradient (50), LTHR-Threshold for Curve length, in

pixels (30), FTHR-Threshold for Line fitting error in pixels (3), ATHR-Threshold for Angular difference in degrees (30), and DTHR-Threshold for linking distance in pixels (20).

In the first stage, RADI parameter (filter radius) specifies the size of the Gaussian kernel used as a filter during edge detection. The edge strength image was threshold to obtain a binary image. Therefore, the choice of RADI value depends on the condition, like as, the greater the value, the less noise and detail appear in the edge detection image. In the second stage, this image was defined by the GTHR parameter (edge gradient threshold) value after testing with different values, and the suitable one was considered. In the third stage, curves are extracted from binary edge image, which have several substeps. First, a thinning algorithm was applied to the binary edge image to generate pixel-wise skeleton curves, then sequence of pixels for each curve was extracted from that corresponding image. Any curve with the number of pixels less than parameter value LTHR was discarded automatically from further processing. Thereafter, extracted pixel curve was converted to vector form by fitting piece wise line segments to it. The resulting polyline was an approximation to the original pixel curve where the maximum fitting error distance between the two was specified by the FTHR parameter. Finally, the algorithm links pairs of polylines, which satisfy the last two parameters, where the angle between the two segments was less than the parameter ATHR and the distance between end points was less than the parameter DTHR. The lineament extraction algorithm takes these problems into account to extract linear features from the corresponding image.

The main geometric characteristics of a single linear line are orientation and length (continuity) and in case of curved line, curvature [26]. For line split generation, ArcGIS 10.5 Model builder was used to automate GIS processes by linking data input, tools/functions, and data output, which saved into shapefile format. These lineament features extracted as a compound line, which splitted into a single line at their vertices and recorded the polylines in a vector layer.

Thereafter, lineament line length analysis was performed using the ArcGIS 10.5 software through conversion of meters into kilometer unit. The most important factor was that the lineaments in an automated one were shorter in length, so that a few of them could be combined to form one long lineament. In this stage, we are getting lineament length of all the attribute values based on the derived products of lineaments of the two study areas.

2.3.2. Lineament fluctuations change observation method

To observe the lineament fluctuation change over the two study areas, satellite image-derived vector output, that is, lineaments were considered to perform overlay technique on each temporal data, helps to prepare corresponding lineament fluctuations maps. However, the criteria have the following conditions, if fluctuations of lineament persist over the study areas in the presence of earthquake, those are considered as "anomaly." These anomalous changes of lineament data represent fluctuations over the two study areas in three different phases, that is, initial, middle, and strong phase. On the other hand, if lineament observed less in number along with other statistical information in the absence of earthquake event, it is considered as normal behavior and categorized as "no anomaly" and finally, to know lineament situation after the earthquake, it is indicated as post-earthquake phase. However, the lineament increases or decreases at this phase does not matter, and this has been done only for comparison.

For overlay change detection, day wise comparison of temporal lineament data has been performed, which ultimately help to monitor the lineament changes of the study areas.

2.3.3. Lineament direction analysis method

The processing of the orientation of lineaments simply produces a directional diagram, which shows the distribution of lineament features. For lineament direction trend analysis, previously saved lineament data as dxf format was used in the RockWorks 16v software environment, where lineament computation was performed to measure bearing (unidirectional: 0–360°), length (m), line start and ending values, respectively, ultimately helps to create rose diagram. The directional diagram that depicts the orientation of the linear features finally saved it in the required format as a tiff file. Later, following the same process, remaining rose diagrams were prepared for the two study areas to figure out the directional change of lineaments based on three different stages (i.e., in the absence, presence, and after earthquake event, respectively).

2.3.4. Statistical analysis method

The statistical approach of the geometric parameters (number of lineaments and lengths variation) of lineaments is required to describe the structure of a region. The length parameters (i.e., total number of lineament, minimum, maximum, mean, total sum, and standard deviation) are generated based on all attributes of corresponding temporal lineament data of the two impending earthquakes in the absence and the presence of earthquake event. As, the lineament data variations observed in different places, the total number of lineament and length variations, that is, mean and standard deviation values were considered for anomalies identification of the study areas, which also further compare with post-earthquake data.

For statistical comparison, the demarcated line has been drawn over the line graph to represent the change behavior of lineament in three different situations with respect to earthquake occurrence day. The left black vertical dotted line used to represent the absence of earthquake marked as “no anomaly” and the second black point dash line considered to represent “extreme anomaly” prior to strike, and black solid line indicates the earthquake occurrence day in the corresponding study areas, whereas black dash line plotted in both the graphs to indicate the anomaly still present representing post-earthquake scenario. The X-axis represents the days which considered for earthquake observation and Y-axis represents the number of extracted lineaments and lineament length (mean and standard deviation value in km), respectively. However, number of lineament and mean value of lineament length were further used to justify the lineament change, observed through scatter diagram.

3. Results and discussion

The focused study areas both are tectonically active in nature, and there is no previous research conducted in the two earthquake-stricken areas considering lineament change. This research has been tried to test using Landsat 8 OLI dataset for the first time based on the newly developed theoretical model. To quantitatively evaluate the present methods, lineaments were automatically extracted from each image after principal component analysis

(PCA). Epicenter-based single tile images were considered to observe the changes of the lineaments related to both the earthquakes.

The following sections (3.1–3.4) represent the present research derived results, based on three different situations. First, results highlight automatic extraction of lineaments data along with lineament length information; second, temporal data-based lineament fluctuations observed by applying vector overlay technique of ArcGIS 10.5 software, and third, rose diagram was created to know the directional changes. Finally, the overall integrated assessment and statistical information-based lineament change comparison were performed for the two impending earthquakes. The present significant contribution of the lineament data suggests that data have potential enough to detect pre-earthquake anomaly in advance without having integration of processed satellite imageries, geological map and field validation data.

3.1. Number of lineaments and line length analysis

The resultant lineament maps produced for all temporal images of the two study areas. Thereafter, line length information was calculated (converted in kilometer) and phase wise lineament behavior changes were observed in the presence (prior to strike) and the absence of earthquake event. The spatial distribution of lineaments of Gorkha-Nepal from 31 January 2015 to 7 May 2015 and of Imphal-Manipur from 19 March 2015 to 17 January 2016 are generated and used in overlay analysis purpose, representing with two distinct black lines (light and solid) with line weights values 0.50 and 1.25, respectively are used for each anomaly phase detection. In each phase of anomaly, every initial image was highlight with light black line and afterwards image is displayed with solid black line. In the same way, different phases were represented as normal (absence of Earthquake), initial (presence of Earthquake), middle (presence of Earthquake), strong phase (presence of Earthquake), and post-earthquake phase, respectively. In addition, corresponding statistical information of lineaments for both study areas was generated and presented in **Table 2** for case 1 and **Table 3** for case 2.

The extracted data prior to the earthquake suggest that a major number of lineaments and total number of lineaments vary from 31,613 on 20 March 2015 to 34,641 on 21 April 2015 (earthquake strike on 25 April 2015). The total lineament was certainly dropped to 27,025 in number in just 4 days before the main event. This anomaly was quite high in respect with the

Date of image acquisition	Days (b/a)	No. of lineament	Length (km)-min	Length (km)-max	Mean value (km)	Sum value (km)	SD value (σ)
31 Jan 2015 (anomaly-no)	85 (b)	11,080	0.001	11.476	1.627	18025.26	0.808
20 Mar 2015 (anomaly-yes)	36 (b)	31,613	0.030	31.658	0.677	21409.09	0.613
5 Apr 2015 (anomaly-yes)	20 (b)	27,025	0.030	31.666	0.670	18116.14	0.680
21 Apr 2015 (anomaly-yes)	4 (b)	34,641	0.060	17.426	0.634	21973.44	0.397
7 May 2015 (anomaly-yes)	12 (a)	25,917	0.030	31.666	0.632	16382.09	0.681

Brackets terminology in the 1st column refers that lineament anomaly-no means normal behavior of lineaments, and anomaly-yes means abnormal behavior of lineaments; in the 2nd column, b refers before earthquake and a refers after earthquake (earthquake occurrence date: 25 April 2015). Source: data extracted using PCI Geomatica-9.1, ArcGIS 10.5.

Table 2. Statistical information of the extracted lineament of Gorkha of Nepal and its adjoining areas.

Date of image acquisition	Days (b/a)	No. of lineament	Length (km)-min	Length (km)-max	Mean value (km)	Sum value (km)	SD value (σ)
19 March 2015 (anomaly-no)	292 (b)	14,524	0.015	5.031	0.326	4734.38	0.184
30 Nov 2015 (anomaly-yes)	36 (b)	34,018	0.030	31.411	0.676	23014.35	0.750
16 December 2015 (anomaly-yes)	20 (b)	29,358	0.030	31.398	0.670	19678.25	0.658
1 January 2016 (anomaly-yes)	4 (b)	42,840	0.030	31.423	0.688	29462.89	0.674
17 January 2016 (anomaly-yes)	13 (a)	62,332	0.030	31.404	0.673	41938.37	0.558

Brackets terminology in the 1st column refers lineament anomaly-no, means normal behavior of lineaments and anomaly-yes, means abnormal behavior of lineaments and in the 2nd column b refers before and a refers after earthquake (earthquake occurrence date: 4 January 2016). Source: data extracted using PCI Geomatica-9.1, ArcGIS 10.5.

Table 3. Statistical information of the extracted lineament of Imphal, Manipur and its surrounds, Eastern India.

absence of earthquake, where only 11,080 lineaments observed (85 days before) (**Table 2**), whereas the number of lineaments was found decreasing (25,917) in post-earthquake phase (12 days after the earthquake) probably due to the release of strain and structural damage done by the high magnitude earthquake (7.8 M_w), compared to its three-preceding anomaly phases. The real cause is unclear till now regarding why the change was occurred prior to earthquake strike. However, simple explanations have been given only based on the experimental output from the extracted lineament results.

The lineament changes and anomalous behavior also observed through line length statistics (**Table 2**). Total line length was observed 18025.26 km, the minimum and maximum values were found quite low and the SD value was observed the highest in the absence of earthquake event. The anomaly phases were observed in the presence of earthquake event, where the maximum length and the SD value were found almost similar in 36, 20 days before earthquake (20 March and 5 April 2015), but not similar in 4 days before earthquake (21 April 2015). The mean length was dropped 0.043 km along with the maximum and SD length of lineament (in km) was sharply decreased (**Table 2**), representing high abnormal behavior (strong anomaly) prior to earthquake event. The same variables of lineament were found increased after the earthquake event (12 days later), as high magnitude of earthquake already ruptured in this region. There was a tendency of lineament to return to its original status but failed completely to return to its initial situation.

On the other hand, similar method applied over Imphal, Manipur (6.7 M_w) earthquake assessment. The total number of lineaments observed 14,524 in number (**Table 3**), representing "no anomaly" in the absence of earthquake event (292 days before). However, the lineament distribution during 30 November 2015 to 17 January 2016 represents the abnormal behavior. The number of lineaments was sharply decreased (4660) from initial to middle phase (30 November 2015 to 16 December 2015). The total number of lineaments found the highest in number (62,332) than its all four preceding values, observed in the post-earthquake stage (**Table 3**).

3.2. Lineament fluctuations observation through overlay analysis

As mentioned in Section 2.3.2 under Section 2.3 (on methodology), lineament fluctuations changes were observed based on temporal data. **Figures 5(a–g)** and **6(a–g)** represent temporal lineament fluctuations over Gorkha of Nepal and Imphal of Manipur regions, respectively.

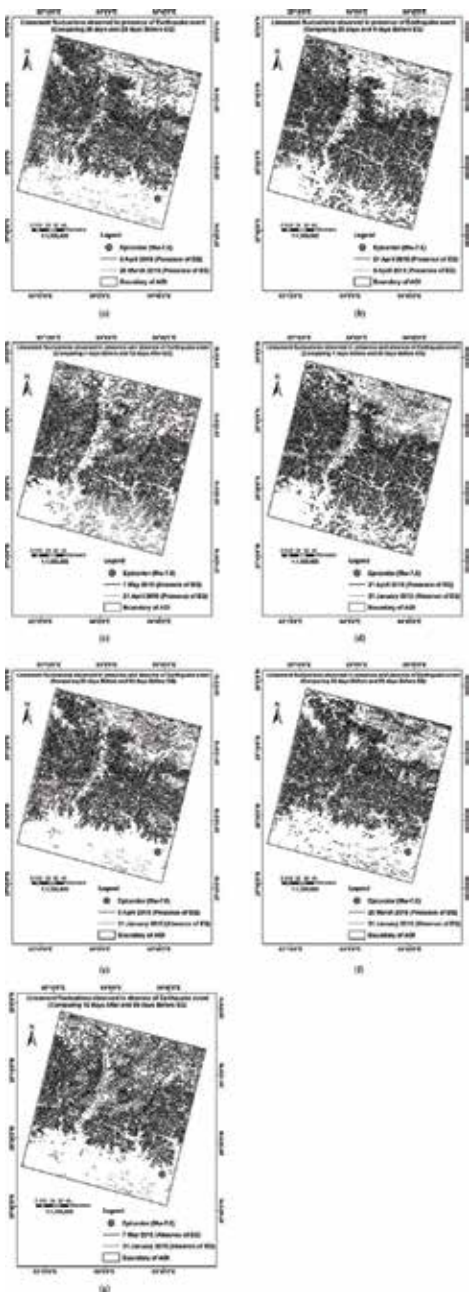

Figure 5. Lineaments fluctuations observed through overlay analysis of Gorkha of Nepal regions: (a) lineament fluctuations observed in the presence of earthquake event (comparing 36 and 20 days before earthquake), (b) same as observed in 36 days and 4 days before earthquake, (c) 4 days before and 12 days after), (d) highly observed fluctuations representing strong phase (4 days and 85 days before), (e) 20 days and 85 days before earthquake (in the presence and the absence of earthquake), (f) same fluctuations comparison between 20 March 2015 and 31 Jan 2015 (the presence and the absence of earthquake event) and (g) lineaments fluctuations in between 7 May 2015 (post-earthquake) and 31 January 2015 (in the absence of earthquake event). The earthquake epicenter was marked with the black dotted circle point symbol.

Figure 5a represents the fluctuations of the lineaments on 20 March 2015 (36 days before: light black color) to 5 April 2015 (20 days before: solid black color) in the presence of earthquake event. Thereafter, the abovementioned data overlay with 21 April 2015, where significant fluctuations of lineaments were observed around epicenter regions 4 days before earthquake strike (see southern part of image, **Figure 5b**). These data were further overlay with post-earthquake lineament data, which try to return to its earlier position (**Figure 5c**).

However, **Figure 5d** illustrates the lineament fluctuations in the presence (4 days before) and the absence of earthquake event (85 days before) and highlights with pink color to ensure that anomaly exists over this region. Sudden increase of lineaments around epicenter region represents the abnormality over this region. This means that anomalous and unexpected fluctuations observed in lineament data on this particular date. **Figure 5e** also represents the lineament fluctuations in the presence (20 days before) and the absence of earthquake (85 days before). The fluctuations were also slightly noticed in the initial phase (36 days before) compared with the absence of earthquake event (**Figure 5f**). In the final stage, it compares fluctuations both in the absence of earthquake, though observed lineaments try to readjust but not matched exactly with the normal condition (see **Figure 5g**).

On the other hand, similar technique was applied to know the lineament fluctuations for the Imphal-Manipur earthquake, and according to USGS, it was categorized as strong earthquake (6.7 M_w). **Figure 6** represents the lineament fluctuations over these areas in the absence and the presence of earthquake event, later compares with post-earthquake data. **Figure 6a** represents lineament fluctuations observed from 36 days (30 November 2015) and 20 days (16 December 2015) before earthquake, clearly noticed from epicenter and adjoining areas. However, it is mentioned here that, at this stage, few lineaments didn't observe due to presence of clouds on image. In the same way, fluctuations were observed comparing with 20 days and 4 days before lineaments data (**Figure 6b**). Five different colors were used for fluctuation comparison in the Imphal-Manipur regions similar to Gorha-Nepal regions. The unusual lineament behaviors were observed when compared 4 days before earthquake with 13 days after earthquake (**Figure 6c**). Thereafter, anomaly observed when it has been compared 36 days before (solid black color) (in the presence of earthquake event) with 292 days before data (light black color) (in the absence of earthquake event) (**Figure 6d**). The number of lineaments observed high in number, representing anomalous behavior around epicenter and its near adjoining areas. However, the sudden lineament fluctuations were also observed 20 days before compared to 292 days before in the absence of that event (**Figure 6e**).

The highest number of variations of lineaments observed prior to 4 days before earthquake (solid black color) compared to 292 days before earthquake (light black color) in the absence of earthquake event and detected the highest anomalies for the Imphal-Manipur earthquake epicenter and adjoining regions in the presence of earthquake event (**Figure 6f**). Whereas, the lineament data anomaly still present and found extreme number of lineaments probably due to massive geological activities done by this earthquake. This unexpected behavior was noticed only after the earthquake event (**Figure 6g**) compare to normal time lineament data (292 days before: showing in light black color), indicate another probable strong earthquake will immediately occur.

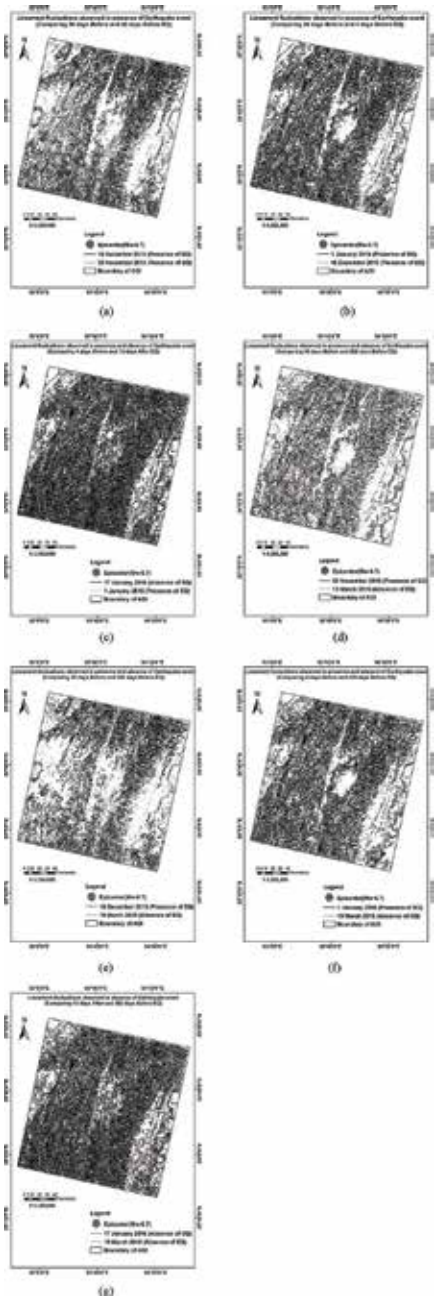

Figure 6. Similar overlay change analysis performed as **Figure 5** but for of Imphal of Manipur regions. Data representing changing behavior of lineament in the absence and presence of earthquake event. The panel represents (a) lineament fluctuations observed comparing 36 and 20 days before earthquake, (b) 20 days and 4 days before earthquake, (c) 4 days before and 13 days after, (d) highly observed fluctuations in the presence and the absence of earthquake (36 days and 292 days before), (e) 20 days and 292 days before earthquake (in the presence and the absence of earthquake), (f) fluctuations comparison between 4 days and 292 days before (presence and absence of earthquake event) and (g) lineaments fluctuations between 17 January 2016 (post-earthquake) and 19 March 2015 (in the absence of earthquake event).

3.3. Lineament orientation change observation through rose diagram

In this section, the lineament direction change has been observed in the absence and presence of earthquake event along with post-earthquake directional change, based on the method discussed on Section 2.3.3 under Section 2.3 (methodology). The case wise interpretation results based on lineament length data show normal and unusual behavior of lineament directions change ((**Figure 7(a–e)**—Gorkha and **Figure 8(a–e)**—Imphal). **Figure 7a** represents the direction of lineament during normal behavior (82 days before) with mean strike orientation of NE-SW direction (59.3 degrees-239.32 degrees), along with E-W and SE-NW directions also observed in the absence of earthquake. Whereas, the direction was start to move from 36 days before (20 March 2015) clearly represent that its mean strike line (101.8 degrees-281.85 degrees) was rotated enough (42.5 degrees) (**Figure 7b**) from normal condition (**Figure 7a**). **Figure 7c** represents directions were in ESE-WNW, E-W, NNE-SSW and N-S positions, where the mean strike direction (81.7 degrees-261.73 degrees) was rotated back and stay around 90° position (20 days before). Major direction was observed in ESE-WNW and NNE-SSW and another one N-E directional change firstly notice at this stage. Whereas, the direction was further rotated 23.7 degrees down

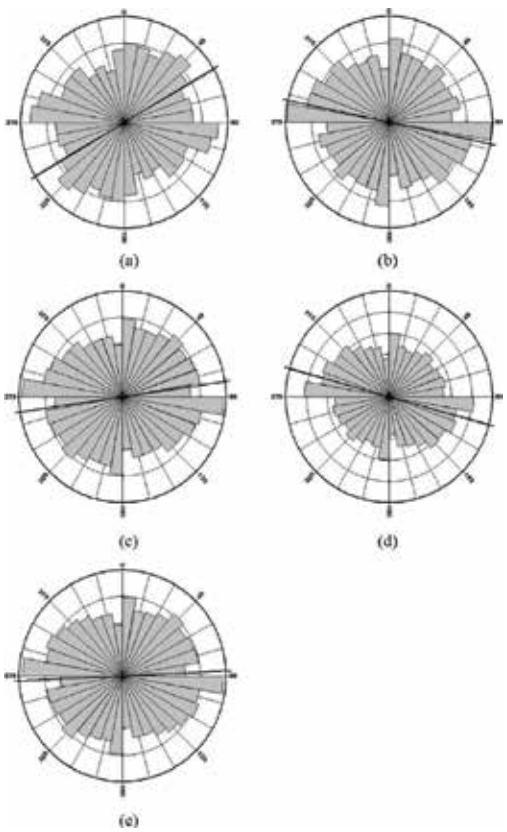

Figure 7. Directional change measurement through rose diagrams for Gorkha, Nepal earthquake: (a) 31 January 2015, (b) 20 March 2015, (c) 05 April 2015, (d) 21 April 2015, and (e) 7 May 2015 (all diagrams based on temporal lineament data).

from middle phase representing 4 days before earthquake scenario, and two major trends ESE-WNW and N-S directions clearly be interpreted from this rose diagram (**Figure 7d**).

The unusual behavior of lineaments clearly seen from these three phases of rose diagrams which shows an anomaly prior to earthquake strike. Whereas, lineament direction was trying to reach its original state but failed to adjust its original position due to internal geodynamic activities that occurred by this high magnitude (7.8 M_w) earthquake. The mean strike position was in E-W and along with two other directions NNE-SSW and SSE-WNW were observed in the post-earthquake phase (**Figure 7e**), though still there exist anomaly compare to normal phase in the absence of earthquake event. Subsequently, all these lineaments directional change were correlated and related within the regional context of the Gorkha-Nepal and its adjoining areas which is a great indication of any structural change and considered as a vital clue to know that impending earthquake.

On the other hand, **Figure 8** illustrates the lineament directions movement around Imphal, Manipur regions from 19 March 2015 to 17 January 2016 (**Figure 8(a–e)**). In order to analyze the lineaments directional change, the present analysis has been performed in the absence

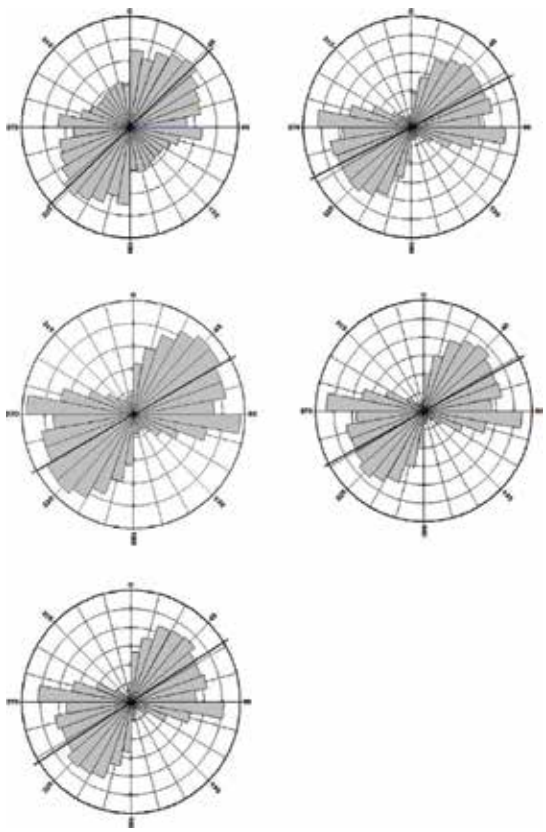

Figure 8. Directional change measurement through rose diagrams for Imphal-Manipur earthquake: (a) 19 March 2015, (b) 30 November 2015, (c) 16 December 2015, (d) 1 January 2016, (e) 17 January 2016 (all diagrams based on temporal lineament data).

and the presence of earthquake data. **Figure 8a** illustrates the lineament directions of normal condition in the absence of earthquake event where major lineament positions were in NNE-SSW and minor lineament positions were in SE-NW and mean strike was in NE-SW directions with 46.8 degrees – 226.79 degrees angle. **Figure 8b**, 30 November 2015 (36 days before earthquake), suggests, ESE-WSW direction and mean strike (63.4 degrees – 243.43 degrees) was move forward 16.6 degrees advanced from normal position.

Figure 8c represents 20 days before scenario (16 December 2015), it showed a major trend to be ESE-WNW (61.1 degrees – 241.11 degrees) with 2.3 degrees rotated back along with considering bin lengths another trend of NE-SW can also be exists. Besides those, on 1 January 2016 (prior to 4 days of earthquake events) two major trends NE-SW (61.7 degrees to 241.65 degrees) and ESE-WSW were identified by interpreting the lineament data (**Figure 8d**). Finally, **Figure 8e** represents the post-earthquake lineament direction (13 days after earthquake) which showed NE-SW (57.8 degrees – 237.83 degrees) from its immediate mean strike position data.

3.4. Statistical analysis based on lineament data

After fluctuations analysis of lineament data as shown in Section 3.2, few statistical test were performed in this section against number of lineament and length change. This statistical analyses were done based on the method discussed in Section 3.2.4 under Section 3.2, by using box-whisker for number of lineament and line trend by considering mean and SD value (**Figures 9** and **10**) in the absence and the presence of earthquake event.

The automatic extraction of lineament data values of both tables (**Tables 2** and **3**) suggests anomaly presence over the two study areas prior to earthquake strike, which was also observed even after the earthquake. On the other hand, the scenario was quite normal in the absence of earthquake event. The derived result illustrates different number of lineaments as observed through box plot and whiskers line chart (**Figure 9a**: Gorkha of Nepal; **Figure 10a**: Imphal of Manipur). However, line length value also differs in both cases (**Figure 9b**: Gorkha and **Figure 10b**: Imphal). These changes were noticed in our two cases, and probably due to

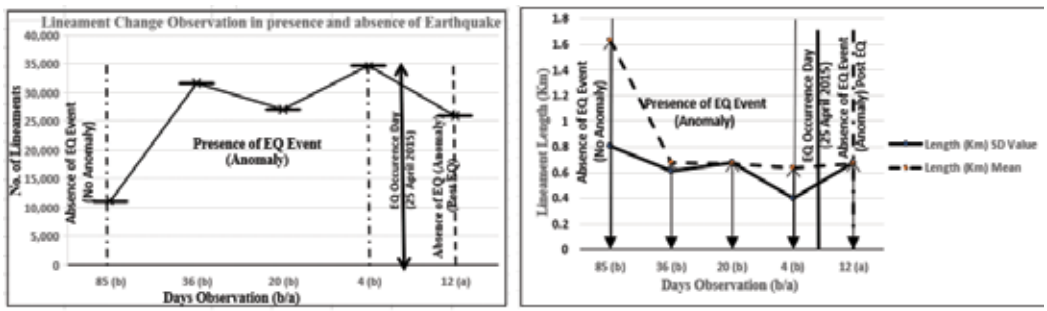

Figure 9. Results of number of lineament and lineament length change observed in the absence and the presence of Gorkha-Nepal earthquake (25 April 2015), from 31 January 2015 (85 days before) to 7 May 2015 (12 days after). (a) Number of lineament variation is represented by box-whisker with black line and (b) lineament mean length change (measured in kilometers) is represented by black dash line and solid black line with dot and light black arrow headed lines showing standard deviation (SD) value, respectively based on number of days observation.

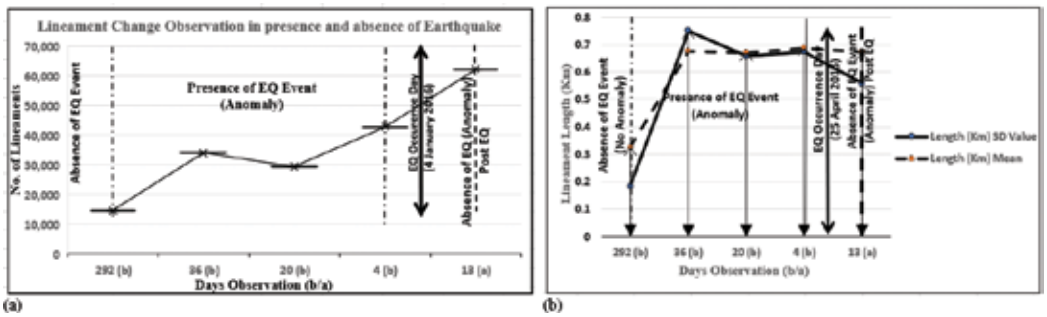

Figure 10. Results of number of lineament and lineament length change observation in the absence and the presence of Imphal-Manipur earthquake (4 January 2016) from 19 March 2015 (292 days before) to 17 January 2016 (12 days after). The internal details of data representations of both figures are the same as **Figure 9**.

different geologic condition, structural arrangements, depth, and magnitude variations of the mentioned two earthquakes.

The earthquake occurrence day is represented as a vertical solid black line. The left black vertical dotted line represents the absence of earthquake event (no anomaly) at this stage, and the second black point dash line represents extreme anomaly of 4 days prior to strike and black dash line line indicates the anomaly still present representing post-earthquake scenario. In both cases, the X-axis represents the days, which considered for lineament change observation during the corresponding earthquake, and Y-axis represents the number of extracted lineaments (**Figures 9a** and **10a**), and lineament length (km) represents with the SD and mean value (**Figures 9b** and **10b**).

Figures 9 and **10** represent data anomaly of two study areas in the presence of earthquake event (prior to earthquake). However, the number of lineament was found stable (in the absence of earthquake event) when the days observed 85 days before the earthquake event (case 1: Gorkha-Nepal) compared to the highest anomalous behavior present prior to earthquake strike (4 days before) and recorded approx. three times higher number of lineaments (**Figure 9a**). However, lineament anomaly was observed 2.5 times higher than stable condition (20 days before strike).

In **Figure 10** (Imphal-Manipur case), anomaly exists in the absence of earthquake event, and when the observation day's progresses from initial anomaly stage, lineaments were increased (4 days before: highest abnormality presence in the anomaly stage) than two other anomaly phases (**Figure 10a**), whereas other two phases were also showing anomaly.

On the other hand, lineament length (km) mean value was recorded as higher (**Figure 9b**). However, the mean length can be shorter or longer and it can be varied due to different geological settings and underlying geological activities. Furthermore, the SD value of lineament length of the two study areas represents (solid black line with dot symbol) different trend, which is decreasing-increasing-decreasing trend in strong earthquake case (Gorkha of Nepal: 7.8 M_w) compared to the absence of earthquake (**Figure 9b**). Whereas, in major earthquake case (Imphal of Manipur: 6.7 M_w), it follows increasing-decreasing-increasing trend (**Figure 10b**).

The results, which observed in each stage based on different analyses method, have individual credit, but all these data are integrated with each other in a sense, like that, first it generated number of lineaments, then measured the lineament length and its overall statistical values. Thereafter,

overlay analyses were performed to observe the abnormal and normal behavior of those lineaments, next directional change measurement by creating rose diagrams considering the lineament number and length. Finally, statistical comparisons were performed and presented under the three phases of lineament behavior changes in respect of earthquake day. The exact epicenter, magnitude, depth, and time of occurrence of earthquake on particular strike day are quite challenging to predict through this present study, but observing lineament data anomalies from the two case studies (prior to earthquake) suggests that pre-earthquake anomaly detection is possible.

Landsat 8 OLI satellite sensors-based time series data show its credit to extract lineament data through most popular traditional automatic LINE algorithm techniques found suitable for this research and help to identify the pre-earthquake anomaly of lineaments in two earthquake prone areas. Though few lineament extractions were obstructed due to the presence of cloud around the epicenter and its adjoining areas, but the outcome showed that it has less effect on the extracted data.

The research results from both study areas suggest that, as the time progresses, the lineament behavior also changed, which identified and confirmed through the experimental results based on the theoretical model and related methods. However, this change was obvious and probably occurred during that time due to movement of the underlain structure and several unknown internal activities. Through the present analyses method, this study assessed successfully of the two earthquakes in two different locations, that is, Gorkha of Nepal (7.8 M_w with 15-m depth, major category) and Imphal of Manipur, eastern India (6.7 M_w with 56-m depth, strong category) earthquakes, respectively. The existing unusual lineament anomalies appeared all over the images in the pre-earthquake stage, especially highly observed close to the epicenter area in both cases (epicenter marked in red asterisks).

4. Conclusions

In this study, based on the Landsat 8 OLI satellite-derived lineament data of the two earthquake regions from 2015 to 2016, the spatial fluctuations of lineaments data and their behavioral changes were analyzed in the presence and absence of earthquake event, which categorized into three phases, that is, in the absence of earthquake (no anomaly), the presence of earthquake event (anomaly) and post-earthquake phase, respectively.

The Gorkha earthquake of Nepal was a result of thrusting along the Main Himalayan Thrust (MHT) [27], and the analysis of the SAR interferograms led to the interpretations that the event was a blind thrust and seismogenic fault [28–30]. However, for Imphal the existing literature suggest that the regional plate boundary in eastern India-the Indo-Burmese Arc is oriented approximately south-southwest-north-northeast directions, see [31], matching the orientation of extracted lineaments.

Present research is the first kind of study conducted and applied in both the earthquake prone areas based on the theoretical model concept. This study creates a breeze in between all four softwares, which were deployed from preprocessing to final stage output performed through geo-integration techniques of ENVI—PCI Geomatica—ArcGIS-RockWorks software's, respectively. These combined techniques were successfully applied on Landsat 8 OLI optical imageries, which

used traditional popular automatic methods and clearly showed its ability to extract different kinds of information based on lineament data.

The automatic lineament delineation using the LINE module of PCI Geomatica was deployed and found great ability of data extraction capacity, as it extracts sufficient numbers of lineaments from Landsat 8 OLI imageries. Different types of information extracted from the lineaments data of the two study areas, where number of lineaments, lineament length change, that is, mean and SD value, and directional change were observed. In both cases, their behavior is abnormal in the presence of earthquake event regarded as anomaly.

The present results also identified that the highest lineament fluctuations and abnormality exist within the anomaly phase, which marked as the highest anomaly (strong phase) just 4 days before earthquake strike. Lineaments behavior was observed quite normal (no anomaly, compared with abnormal situation) in 85 days before (Gorkha of Nepal) and 292 days before (Imphal of Manipur) the earthquake event.

However, data comparison method and lineament fluctuations successfully identified the lineament anomaly change over the two study areas. Due to progress of Earth observing satellites in different parts of the world, similar experiments can also be tested and compared with another high-resolution imagery. From this analysis, the exact position of earthquake epicenter, magnitude, and timing of occurrences was quite difficult to predict, but the extracted data can only able to identify the abnormality before the earthquake strike at least 4–36 days before. Thereafter, this lineament abnormality along with cloud presence in the images over such time period can help to target the zone of probable earthquake epicenter.

Overall, the experimental results have shown positive output, as it has been observed anomaly in pre-earthquake stage. Therefore, the first output concept was considered which developed by theoretical model and regarded as possible earthquake. On the other hand, no abnormal behavior of lineament presents in before, compared to anomaly presence prior to earthquake strike; thus, it is considered as no anomaly and declared as no possible earthquake, which supports the second concept of theoretical model. From this research, it has been observed that Landsat 8 OLI data have some power to extract lineament and helpful for pre-earthquake anomaly detection through lineament change observation. That is the only reason of acceptance of those images for the present study, which also supports the theoretical model. However, present lineament change observation technique using Landsat 8 OLI time series data is found effective for pre-earthquake anomaly study and can be used as an alternative approach for future earthquake monitoring.

Acknowledgements

This work was supported by the Major State Basic Research Development Program of China (no. 2013CB733405) and the National High Technology Research and Development Program of China (863 Program) (no. 2014AA06A511) and received fellowship fund for PhD Program by Chinese Academy of Sciences and the World Academy of Sciences (CAS-TWAS) under CAS-TWAS President's Fellowship-2015 (no. 2015CTF024) awarded by the University of Chinese Academy of Sciences (UCAS) and give our sincere thanks to USGS earth explorer committee for freely acquisition of Landsat 8 Imageries from their archive. Finally, our special thanks to In Tech

Open Publishing manager for inviting us to write a book chapter, and book editor, anonymous reviewer for their insightful comments and suggestions which helps to improve the manuscript.

Author details

Biswajit Nath[1,2,3]*, Zheng Niu[1,2]* and Shukla Acharjee[4]

*Address all correspondence to: nath.gis79@gmail.com and niuzheng@radi.ac.cn

1 The State Key Laboratory of Remote Sensing Science, Institute of Remote Sensing and Digital Earth (RADI), Chinese Academy of Sciences (CAS), Beijing, China

2 College of Resource and Environmental Studies, University of Chinese Academy of Sciences (UCAS), Beijing, China

3 Department of Geography and Environmental Studies, University of Chittagong, Chittagong, Bangladesh

4 Department of Applied Geology, Dibrugarh University, Dibrugarh, Assam, India

References

[1] Hobbs WH. Repeating patterns in the relief and in the structure of land. Geological Society of America Bullet. 1911;**22**:123-176

[2] Pradhan B, Singh RP, Buchroithner MF. Estimation of stress and its use in evaluation of landslide prone regions using remote sensing data. Advances in Space Research. 2006;**37**:698-709

[3] Elmahdy SI, Mohamed MM. Mapping of tecto-lineaments and investigate their association with earthquakes in Egypt: A hybrid approach using remote sensing data. Geomatics Natural Hazards & Risk. 2016;**7**:600-619

[4] Masoud AA, Koike K. Auto-detection and integration of tectonically significant lineaments from SRTM DEM and remotely-sensed geophysical data. ISPRS Journal of Photogrammetry and Remote Sensing. 2011;**66**:818-832

[5] Caponera F. Remote sensing applications to water resources: Remote sensing image interpretation for ground water surveying. Food and Agricultural Organization of the United Nations, Rome. 1989. 234 pp

[6] Koike K, Nagano S, Ohmi M. Lineament analysis of satellite images using a segment tracing algorithm (STA). Computers and Geosciences. 1995;**21**:1091-1104

[7] Mah A, Taylor GR, Lennox P, Balia L. Lineament analysis of Landsat thematic mapper images, northern territory, Australia. Photogrammetric Engineering & Remote Sensing. 1995;**61**:761-773

[8] Karnieli A, Meisels A, Fisher L, Arkin Y. Automatic extraction of geological linear features from digital remote sensing data using a Hough transform. Photogrammetric Engineering and Remote Sensing. 1996;**62**:525-531

[9] Kim GO, Lee JY, Lee KK. Construction of lineament maps related to groundwater occurrence with ArcView and avenue TM scripts. Computer and Geosciences. 2004;**30**: 1117-1126

[10] Park Y, Lee K, Kim SH. Effects of highly permeable geological discontinuities upon groundwater productivity and well yield. Mathematical Geology. 2000;**32**:605-615

[11] Costa JBSC, Bemerguy RL, Hasui Y, Borges MS, Soares AAV Jr. Tectonics and paleogeography along the Amazon River. Journal of South American Earth Sciences. 2001;**14**: 335-347

[12] Lattman IH. Techniques of mapping geologic fracture traces and lineaments on aerial photographs. Photogrammetric Engineering. 1958;**19**:538-576

[13] Onyedim GC, Ocan OO. Correlation of SPOT imagery lineaments with geological fractures in parts of Ilesha area, southwestern Nigeria. Journal of Mining and Geology. 2001;**37**:15-22

[14] Hung LQ, Batelaan O, De SF. Lineament extraction and analysis, comparison of Landsat ETM and ASTER imagery. Case study: Suoimuoi tropical karst catchment, Vietnam. Proceedings of SPIE. 2005;**5983**:1-12

[15] O'Leary DW, Friedman JD, Pohn HA. Lineament, linear, lineation: Some proposed new standards for old terms. Geological Society of America Bullet. 1976;**87**:1463-1469

[16] Casas AM, Cirtes AL, Maestro A, Soriano MA, Riaguas A, Bernal J. A program for lineament length and density analysis. Computers and Geosciences. 2000;**26**:1011-1022. DOI: 10.1080/19475705.2014.996612

[17] Jonathan A. Why Nepal is so vulnerable to quakes. BBC. 2015 Retrieved 27 April 2015 [Accessed: 25 January 2016]

[18] USGS. Poster of the Nepal Earthquake of 25 April 2015-Magnitude 7.8. USGS Earthquake Hazards Program. 2015, 25 April. https://earthquake.usgs.gov/earthquakes/eqarchives/poster/2015/20150425.php [Accessed: 22 March 2016]

[19] Gahalaut VK, Kundu B. The 4 January 2016 Manipur earthquake in the indo-Burmese wedge, an intra-slab event. Geomatics Natural Hazards & Risk. 2016;**7**:1506-1512

[20] USGS Tectonic Summary. Earthquake Hazards Program, Tectonic Summary, M 6.7-30 km W of Imphal, India, reported on 2016-01-03, 23:05:22 UTC. 2016. http://earthquake.usgs.gov/earthquakes/eventpage/us10004b2n#executive [Accessed: 5 January, 2016]

[21] Pena SA, Abdesalam MG. Orbital remote sensing for geological mapping in southern Tunisia: Implication for oil and gas exploration. Journal of African Earth Sciences. 2006;**44**:203-219. http://doi.org/10.1016/J-Jafrearsci.2005.10.011

[22] Michaela F, Mohamed GA, Nicolas B. Remote sensing applications to geological problems in Africa. Journal of African Earth Sciences. 2006;**44**:vii-vix

[23] Kocal A, Duzgun HS, Karpuz C. Discontinuity mapping with automatic lineament extraction from high resolution satellite imagery. ISPRS Proceedings-XXXV. 2004 www.isprs.org/proceedings/XXXV/congress/comm7/papers/205.pdf

[24] PCI Geomatica Training Manual. 2015. www.pcigeomatics.com/training-manual-downloads

[25] Abdullah A, Akhir J, Abdullah I. Automatic mapping of lineaments using shaded relief images derived from digital elevation model (DEM) in the Maran-Sungi Lembing area, Malaysia. Web-EJGE**.** 2010;**15**:949-957. http://ejs-agri.com/uploads/pdf

[26] Jordan G, Csillag G, Szucs A, Qvarfort U. Application of digital terrain modelling and GIS methods for the morphotectonic investigation of the Kali Basin, Hungary. Zeitschrift für Geomorphologie. 2003;**47**:145-169

[27] USGS. Poster of the Nepal Earthquake of 25 April 2015-Magnitude 7.8.: USGS Earthquake Hazards Program. 2015, 25 April

[28] Angster S, Fielding EJ, Wesnousky S, Pierce ID, Chamlagain D, Gautam BN, et al. Field reconnaissance after the 25 April 2015 M 7.8 Gorkha earthquake. Seismological Research Letters. 2015;**86**:1506-1513. http://ariashare.jpl.nasa.gov/publications/Angster-et-al-SRL-v86-p1506.full.pdf. DOI: 10.1785/0220150135

[29] Kobayashi T, Morishita Y, Yarai H. Detailed crustal deformation and fault rupture of the 2015 Gorkha earthquake, Nepal, revealed from ScanSAR based interferograms of ALOS-2. Earth, Planets and Space. 2015;**67**:201. DOI: 10.1186/s40623-015-0359-z

[30] Lindsey E, Natsuaki R, Xu X, Shimada M, Hashimoto H, Melgar D, et al. Line of sight deformation from ALOS-2 interferometry: M_w 7.8 Gorka earthquake and 7.3 aftershock. Geophysical Research Letters. 2015;**42**:1-7. DOI: 10.1002/2015GL065385 http://topex.ucsd.edu/sandwell/publications/159_GRL_Lindsey.pdf

[31] USGS 2016 Imphal Earthquake-Wikipedia [Internet]. 2016. Available from: https://en.wikipedia.org/wiki/2016_imphal_earthquake [Accessed: 2016-01-15]

Section 8

Earth Observation with Use of Space Technology

Chapter 9

Optimization of an Earth Observation Data Processing and Distribution System

Jonathan Becedas, María del Mar Núñez and David González

Additional information is available at the end of the chapter

http://dx.doi.org/10.5772/intechopen.71423

Abstract

Conventional Earth Observation Payload Data Ground Segments (PDGS) continuously receive variable requests for data processing and distribution. However, their architecture was conceived to be on the premises of satellite operators and, for instance, has intrinsic limitations to offer variable services. In the current chapter, we introduce cloud computing technology to be considered as an alternative to offer variable services. For that purpose, a cloud infrastructure based on OpenNebula and the PDGS used in the Deimos-2 mission was adapted with the objective of optimizing it using the ENTICE open source middleware. Preliminary results with a realistic satellite recording scenario are presented.

Keywords: Earth Observation, distributed systems, cloud computing, ENTICE project, gs4EO

1. Introduction

Traditionally, Earth Observation systems have been operated by governments and public organizations; the primary investors being US, China, Russia, Japan and Europe mainly because of worldwide common objectives such as climate change, sustainable development and objectives at national level.

However, from 2015 to 2016, the Earth Observation from space paradigm is changing with the globalization of the market, the evolution of the information and communication technologies and the high investment of private entities in the field.

This boost of commercial interest in Earth Observation can be explained because of the parallel evolution of three main pillars, as stated by Denis et al. in [1]:

1. Increased performance of commercial satellites with defence needs in the range of very high resolution products, i.e. resolutions between 0.25 and 1 m.
2. The development of hybrid procurement schemes between private and public customers.
3. Appearance of the New Space scheme started in Silicon Valley, which attracted the interest of investors and contributed to the creation and entrance of new actors in the space sector.

To these, we would add the dedicated budget of new countries, such as Kazakhstan, Venezuela and Vietnam, in EO; increased budget in new EO programmes for India, China and South Korea [2] and fast evolution of information and communication technologies, which facilitated the creation of new applications requiring availability of lots of information in the shortest time possible. This contributed to the evolution of the space sector in two manners: (a) the evolution of the sensors to provide highest performance at a lower cost and (b) the launch of more satellites to cover the demand of information. This last explains the increase in the launch of satellites during the last years and interest of satellite operators to operate satellite constellations in order to reduce the revisit time and offer more coverage of the land surface. A proof of this is the number of EO satellites launched between 2006 and 2015: 163 satellites over 50 kg were launched for civil and commercial applications, generating $18.4 billion in manufacturing market revenues, whereas 419 satellites are expected to be launched over the next decade (2016–2025), generating $35.5 billion in manufacturing revenues. In terms of EO data sales, the market reached $1.7 billion in 2015 and it is expected to reach $3 billion in 2025. This is $12.2 billion total revenue in the decade 2006–2015 and $24 billion in the decade 2016–2025 [3]. The amount of generated data is used, for instance, to accumulate spatial and temporal records of the world itself, of the events and changes that occur in it in a diverse number of applications: security, maritime, agriculture, energy and emergency, among others [4].

However, the infrastructures used to manage EO data are still based on traditional EO systems, which (because of their previous ambit of application) make use of on-site traditional infrastructures or data centers. Their architecture was designed to be monolithic in a localized single infrastructure.

Now, the process of recording data from Earth observations generates massive amounts of spatiotemporal geospatial information that has to be intensively processed for a variable and increasing demand. This is a handicap for traditional data centers since they are not designated to manage variable amounts of data. They were designed and sized to operate a certain data volume. They are then limited in terms of flexibility and scalability [5]. The storage of increasing amounts of data over time is also a challenge, since the recordings are also maintained by their owners over time as well [6].

Traditional Earth Observation Payload Data Ground Segments (PDGS) present the following limitations to cover the demands of the current EO market:

i. Traditional infrastructures are not flexible or easily scalable to operate.
ii. There is a risk of oversizing/undersizing the infrastructure to offer services when highly variable demand exists.
iii. They make the cost of acquiring recent images of the Earth very high.

iv. The customers cannot access directly neither fast to the information they need because this has to be processed and ad-hoc distributed.

However, the use of cloud computing technology can eliminate the previous drawbacks to improve EO services because it is elastic, scalable, it works on demand through virtualization of resources, offers virtually unlimited storage and computation capability, it is worldwide connected and it is based on a pay per use model [7, 8].

Nevertheless, the current cloud computing technology still presents some limitations:

i. The virtual machine images (VMIs) are not optimized, being highly oversized, impacting in the costs of using the infrastructure and in the dynamic resources provisioning.

ii. The deployment of virtual machines (VM) in cloud is not in real time. The deployment normally takes between 10 and 20 minutes, which directly affects to the flexibility and dynamic scalability of the system.

iii. Although the pay per use model should intrinsically have reduced costs, since the customer only pays for what he uses, the costs of using cloud computing are still high.

iv. There are some major worldwide champions in the offer of cloud services such as Amazon, Google, Microsoft and IBM, which make difficult the migration of a system from a cloud infrastructure to another different cloud infrastructure, existing vendor lock-in. This limits the democratization of these services and makes an entrance barrier for new cloud providers.

Within the ENTICE H2020 project (project no. 644179), we intend to demonstrate that processing the data recorded from Earth observations in a cloud environment with the middleware ENTICE optimizes the efficiency and overcomes the critical barriers of cloud computing and data processing needs. Among other advantages, ENTICE provides independence from a specific infrastructure provider and facilitates the distribution of VMs in distributed infrastructures.

In this work, we present the implementation of the Earth Observation Data (EOD) pilot, which mainly consists of the implementation in cloud of the already commercial Ground Segment for Earth Observation (gs4EO) suit, commercialized by Deimos [9], which is currently operational in the Deimos-2 satellite mission [10].

For this purpose, we simulate a real scenario with the Deimos-2 satellite running in a federated cloud infrastructure, in which we obtain real performance metrics and present real system requirements for normal operations with the satellite. Through this experimentation, we demonstrate the EOD concept as a solution for the new EO market paradigm.

2. Earth Observation Data Processing and Distribution Pilot

2.1. ENTICE environment

In order to facilitate the implementation in cloud, the EOD pilot makes use of the ENTICE middleware [11], which facilitates autoscaling and flexibility to the ingestion of satellite imagery, its

processing and distribution to end users with variable demands. Kecskemeti et al. [12] introduced the ENTICE approach to solve these problems. The ENTICE environment consists of a ubiquitous repository-based technology, which provides optimised virtual machine (VM) image creation, assembly, migration and storage for federated clouds. The webpage of ENTICE can be found in [13].

ENTICE facilitates the implementation of cloud applications by simplifying the creation of lightweight virtual machine images (VMIs) by means of functional descriptors. These functional descriptors define at high and functional levels the VMIs and contribute to define the system Service Level Agreement (SLA) to facilitate the optimization of the VMIs in terms of performance, costs, size and quality of service (QoS) needed. Then, the VMIs are automatically decomposed and distributed to meet the application runtime requirements. In addition, ENTICE facilitates elastic autoscaling. The benefits of using ENTICE are the following:

- Reduction of up to 80% storage.
- 95% elastic Quality of Service.
- VMIs creation 25% faster.
- Reduction on the costs of deployment.
- VMIs optimization up to 60%.
- VMIs delivery 30% faster.
- Scalability and elasticity.
- Elimination of cloud infrastructure vendor lock-in.

In the EOD pilot, ENTICE is used as middleware between the federated infrastructure described in Section 3.1 and the gs4EO application software.

2.2. EOD pilot description

The Earth Observation Data Processing and Distribution Pilot (EOD) consists of the implementation of the Elecnor Deimos' geo-data processing, storage and distribution platform of Deimos-2 satellite using cloud technologies. The main functionalities of the system are the following:

- **Acquisition of raw data:** When the imagery data are ingested from the satellite into the ground station, the system is notified and the ingestion component automatically ingests the raw data into the cloud for its processing.
- **Processing of data:** Once the data are ingested, it is processed in the product processors. There are several processing levels to provide different products.
- **Archiving and cataloguing geo-images:** The different products obtained from the processing of raw data are archived and catalogued in order to provide these images or high added value services to end users.
- **Offering user services:** This is the front-end of the system. It allows end users to select the product that they want to visualize or to download.

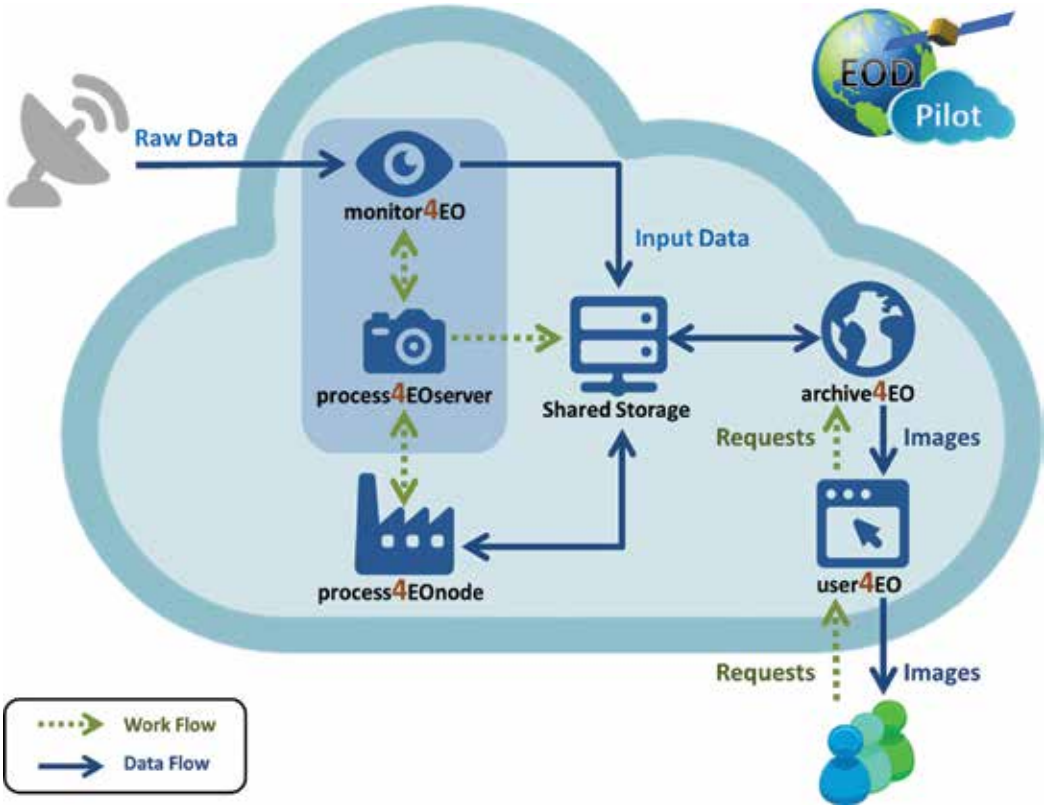

Figure 1. Earth Observation Data Processing and Distribution pilot (EOD)'s architecture.

2.2.1. EOD architecture

The main objectives of the EOD pilot is to process real data of Deimos-2 satellite in a realistic scenario of normal operation and the validation of the processing chain module as part of the cloud infrastructure. Ramos and Becedas [14] proposed an original architecture of the gs4EO suit to be implemented in cloud. Based on that work, the architecture for the EOD pilot has been redesigned and implemented, see **Figure 1**.

The architecture is composed of the following components:

- **monitor4EO:** It is a ground station monitor, which ingests the available raw data from the ground stations to the cloud system. It contains an Orchestrator, which manages the tasks of the different modules.
- **process4EO server:** It is the Orchestrator, which is the component that manages the tasks to be done by all the modules of the architecture computed in the cloud infrastructure. The Orchestrator has the following functions:
  - To identify which outputs shall be generated by the processors.
  - To generate the Job Orders. They contain all the necessary information that the processors need. Furthermore, these eXtensive Markup Language (XML) files include the interfaces

and addresses of the folders in which the input information to the processors is located and the folders in which the outputs of the processors have to be sent. They also include the format in which the processors generate their output.

- To find data in the ground stations (pooling) to be ingested in a shared storage unit in the cloud for its distribution to the processing chain.
- To control the processing chain by communicating with the product processors.
- To manage the archive and catalogue.

- **process4EO node:** Constituted of different software modules, which are in charge of the processing of the raw data and the products of previous levels to produce image products. **Figure 2** depicts the pipeline of the image processing process. The four most important operations are the following:
  - Calibration: (L0 and L0R processing levels) to convert the pixel elements from instrument digital counts into radiance units.
  - Geometric correction: (L1A processing level) to eliminate distortions due to misalignments of the sensors in the focal plane geometry.
  - Geolocation: (L1BR processing level) to compute the geodetic coordinates of the input pixels.
  - Orthorectification: (L1C processing level) to produce orthophotos with vertical projection, free of distortions.

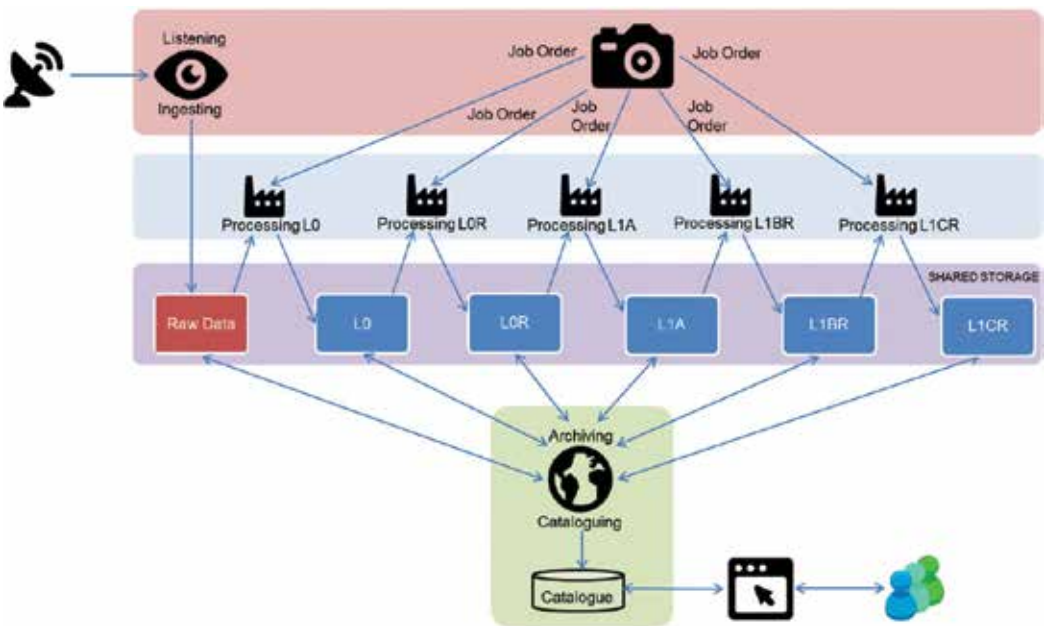

Figure 2. EOD's pipeline.

- **archive4EO:** In this module, the processed images are stored and catalogued for their distribution. It offers a Catalogue Service for the Web (CSW) interface.
- **user4EO:** It is a web service in which the end users can access to the products.
- **Shared storage:** It is a storage module shared by all the modules of the architecture in which all the inputs and outputs of the different modules of the architecture are stored.

3. Experiment setup

3.1. Testing infrastructure

The testing infrastructure used in the experiment is formed by hardware deployed in three different locations and managed in a federated manner: DMU infrastructure (in Deimos UK in United Kingdom), DMS infrastructure (in Deimos Space in Spain) and DME infrastructure (in Deimos Engenharia in Portugal). The hardware resources deployed in every location are described in **Table 1**. The ENTICE middleware was installed in the DMU infrastructure, which is acting as master. It also contains an object store with interface to Amazon Simple Storage Service (Amazon S3) for cloud bursting. DMS and DME infrastructures are slaves of DMU infrastructure and contain object stores also with interfaces to Amazon S3. A block diagram describing the interrelations of the testing infrastructure is depicted in **Figure 3**. The virtualization of the infrastructure was done with OpenNebula. Kernel-based Virtual Machine (KVM) was used as hypervisor. The creation of the virtual machines was done with Packer, whereas the automatic deployment of the virtual machines was done with Ansible. **Figure 4** shows a diagram describing the logic process of automatic generation of the virtual machines that constitute the EOD software. The image building process takes advantage of

Location	Name	Model	CPU	RAM (GB)	HD (GB)	OS
DMU	Node-1	Dell Optiplex790	Intel Core i7–2600 3.4 GHz	8	160	CentOS 7.2.1511
	Node-2	Dell Optiplex790	Intel Core i7–2600 3.4 GHz	16	250	CentOS 7.2.1511
	OpenNebula-fe	Dell Optiplex745	Intel Core 2 6300 1.86 GHz	4	250	CentOS 7.2.1511
DMS	Node-2	Dell	Intel 8 Core 2.37 GHz	16	2048	CentOS 7.2.1511
	Node1	Dell	Intel 2 Core 3 GHz	6	230	CentOS 7.2.1511
DME	Node1	HP	AMD Athlon 64 X2 Dual Core 3800+	4	256	CentOS 7.2.1511

Table 1. Hardware resources in the testing infrastructure.

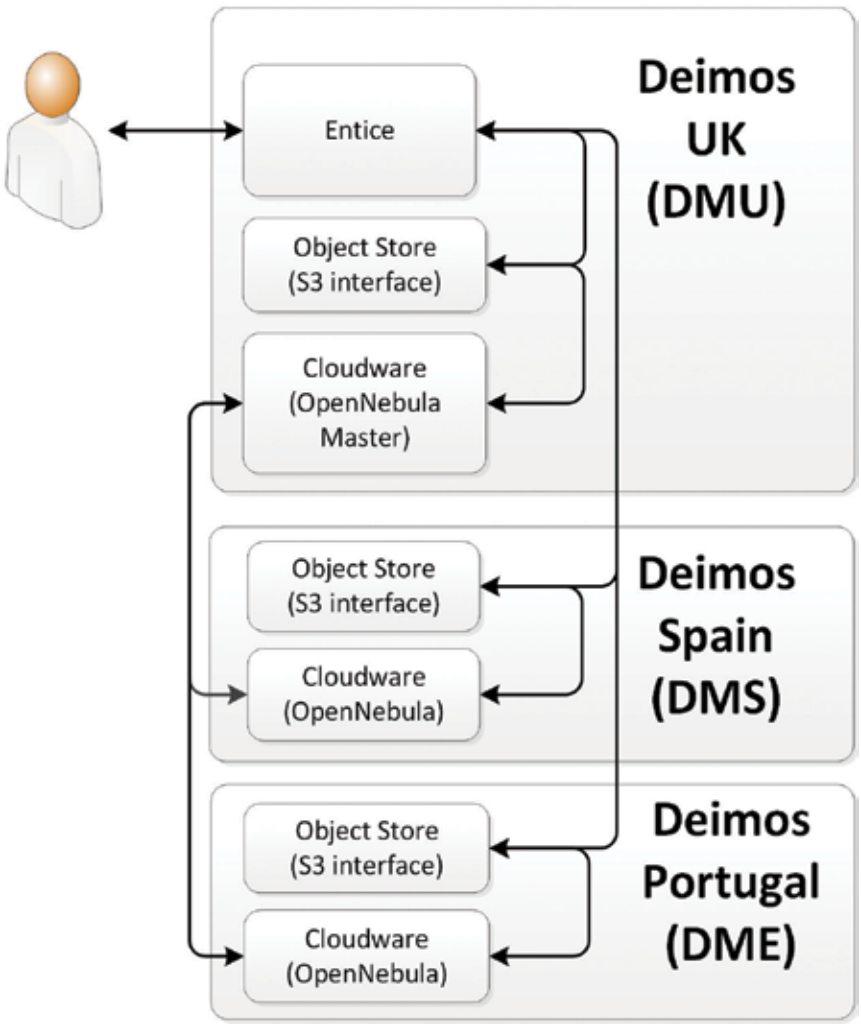

Figure 3. Block diagram of the testing infrastructure.

the functionalities provided by Packer and Ansible to build KVM images. The virtual images are based on CentOS 6 Linux distribution and are stored in qcow2 format. This automation step comprises several files:

- Execution script: This script, developed in Python, launches the creation of the machine image with Packer. It receives a JSON file with all the variables that will be used in the building process, e.g. the user configuration, software repositories, Kickstart file and Ansible playbook, and configures all the required fields in the Kickstart file. It can build all the types of VMIs required to deploy the EOD software: archive4EO, monitor4EO and process4EO. The type of virtual machine to generate is specified in the content of the configuration file.

- Packer template: It is a JSON file that provides all the information to create the virtual machine in Packer. It contains the format, the instructions and the parameters on how to build a VMI using KVM. The provisioners define the scripts or recipes in Ansible for configuring the machine and installing the applications.
- Ansible playbook: These files are "recipes" to install the EOD software in the virtual machines. This is a YAML file with the commands expressed in a simplified language, describing a configuration or a process. It contains the information to configure the system, install the EOD software and the functionalities to work in the cloud environment (contextualization).

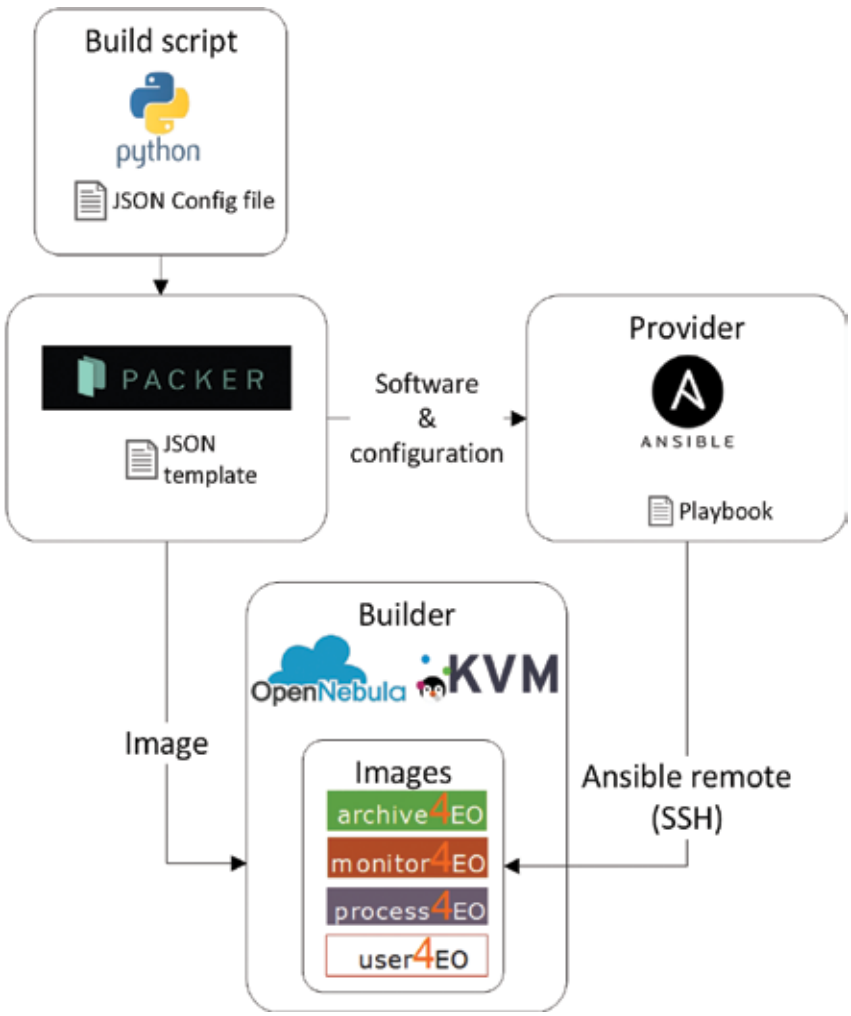

Figure 4. Diagram of the automatic generation of the EOD virtual machines.

The Python script receives the configuration file and launches the Packer command after configuring some parameters in the Kickstart file. The Packer command takes the template and runs all the builds within it in order to generate a set of artefacts and build the image in KVM. Once the image is built, Packer launches all the provisioners (Ansible) contained in the template. Ansible carries out several steps: it configures all the repositories, installs all the dependencies and software packages of the EOD modules, configures the EOD software and installs a context package to deploy the VMI in OpenNebula.

The recording of the experiment data was done with Jmeter™ [15] and Nagios® [16]. Jmeter™ is installed in the Node and Nagios® in a virtual machine inside the federated cloud. It is used for the monitoring of the cloud resources and status and to extract the experimental data.

3.2. Experiment description

The aim of this experiment is to demonstrate the feasibility of implementing the EOD system in cloud and how its behavior improves after the optimization done by ENTICE over the process4EO node.

The experiment is that of a realistic recording with Deimos-2 satellite in which a real acquisition is ingested into the EOD pilot. Then, the processing of the raw data is carried out with the EOD pilot before and after the optimization process. The results are compared to evaluate the functionality of the optimized system with regard to the nonoptimized system and validate the implementation of the gs4EO modules in cloud.

VMI size, VMI creation time, VMI delivery time and VMI deployment time are the evaluated metrics selected to compare the performance of the system before and after the optimization process.

The following are the evaluated metrics to demonstrate that the functionality of the system remains the same after the optimization: processing time, imagery products size, CPU use per process and memory use per process.

The raw data used in the experiment have 3 MB size, four multispectral bands (R, G, B and NIR) and one panchromatic. The recorded area of the land surface is a rectangle of 8.86 × 16.59 km^2.

The raw data are managed and processed to automatically obtain the following products:

- L0: raw data decoded.
- L0R: transformation of L0 into image.
- L1A: geolocated and radiometric calibrated image.
- L1BR: resampled image and more precise geolocation.
- L1CR: orthorectification.

The virtual resources used in the experiment were the following: a virtual machine with 300 GB, a RAM of 10 GB, four CPUs of 32 bits, a shared storage with 99 GB and an additional storage volume with 50 GB. This hardware was used for both experiments (EOD before and after optimization) in order to facilitate comparison.

4. Experiment results

First, the virtual machine images of the EOD pilot were created, delivered and deployed in the cloud. Then, the virtual machine of the proces4EO was optimized and its VMI was again created, delivered and deployed. The time spent in every step is depicted in **Table 2**.

In these results, one can see the increase in the performance of the system before the runtime, i.e. up to the deployment of the system: this is a reduction of 30% in VMI size, a reduction of 37.3% in the VMI creation time, a reduction of 34.53% in the VMI delivery time and a reduction of 54.05% in the deployment time.

Next, the raw data recorded with the satellite were ingested in both the original EOD pilot and the optimized EOD pilot. The response of both optimized and nonoptimized systems were measured in the runtime. The processing time of the satellite imagery in the original EOD pilot and the EOD pilot with the optimization of the processing chain is shown in **Figures 5** and **6** respectively. It can be noticed that the processing time of the different levels is similar in both experiments, so as to the time to process the raw data up to the orthorectification level (L1CR): 33.95 and 35.75 s in the nonoptimized and optimized systems, respectively. This difference is not substantial and can be produced by some OpenNebula processes, or the cloud has used

	VMI size (GB)	VMI creation time (hh:mm:ss)	VMI delivery time (hh:mm:ss)	VMI deployment time (hh:mm:ss)
Nonoptimized VM	2	00:19:42	00:20:25	0:06:47
Optimized VM	1.4	00:12:21	00:13:22	0:03:07
Reduction (%)	30	37.31	34.53	54.05

Table 2. Metrics of the optimized and nonoptimized EOD pilot.

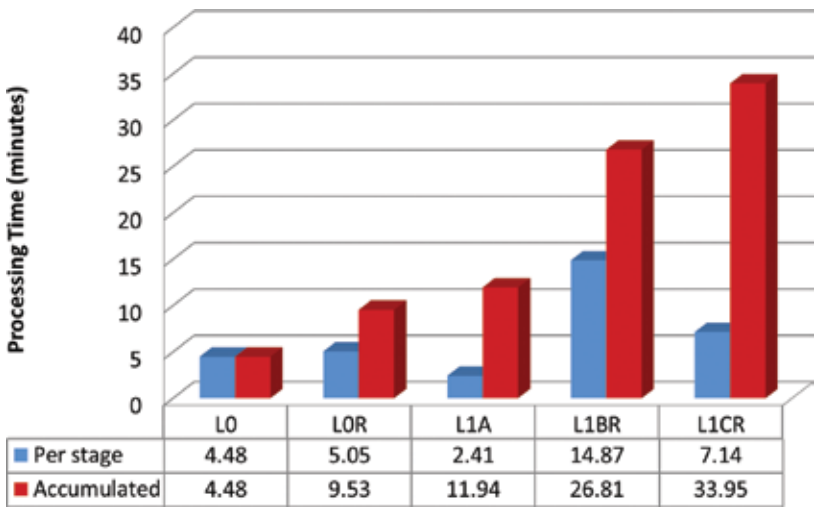

Figure 5. Processing time of the satellite imagery with nonoptimized EOD system.

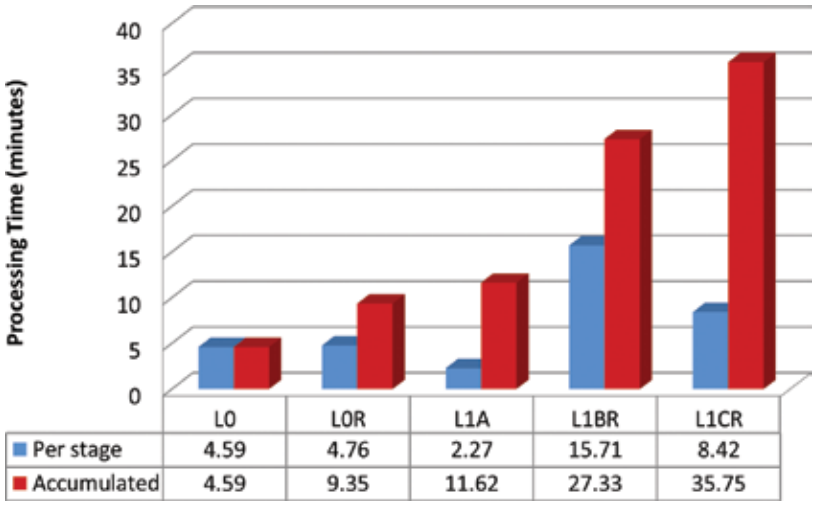

Figure 6. Processing time of the satellite imagery with optimized EOD system.

Data type	Raw data	L0	L0R	L1A	L1BR	L1CR	Total Products
Size of the products obtained with the non-optimized system (MB)	3090	764	789	749	1140	1130	4572
Size of the products obtained with the optimized system (MB)	3090	764	789	749	1140	1130	4572

Table 3. Imagery product sizes obtained with both the nonoptimized and the optimized EOD system.

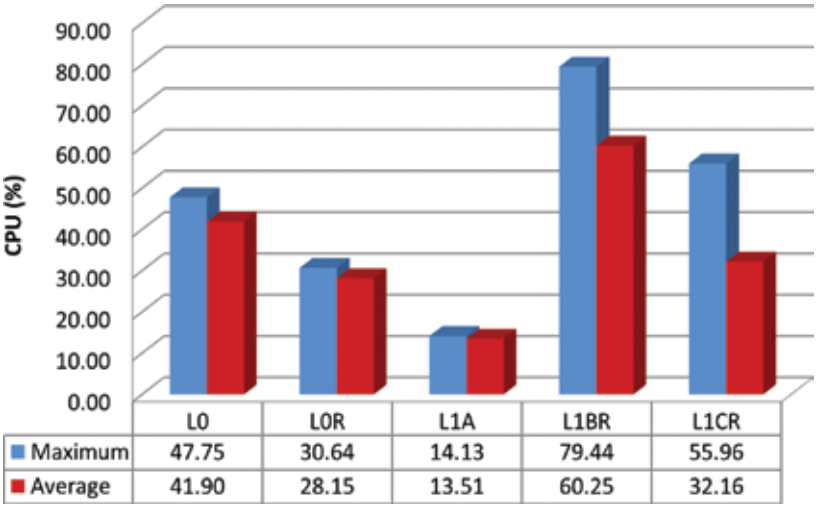

Figure 7. CPU use per process in the nonoptimized EOD system.

http://dx.doi.org/10.5772/intechopen.71423

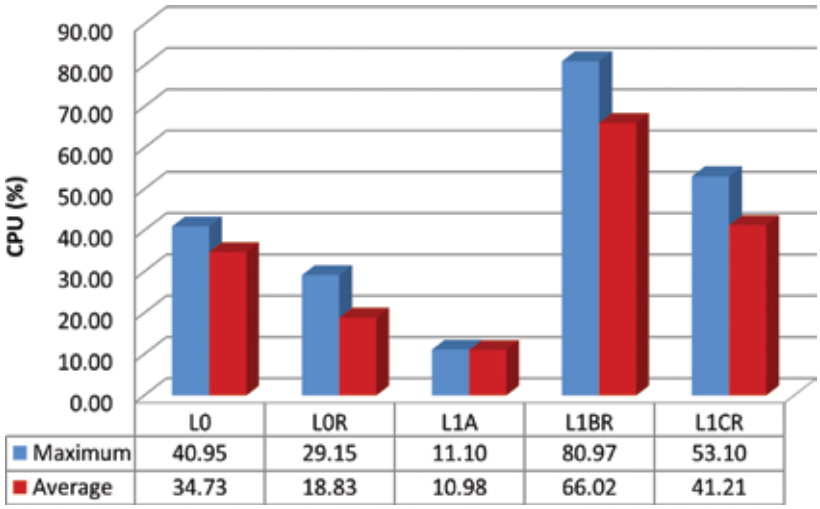

Figure 8. CPU use per process in the optimized EOD system.

some resources while executing the experiments. In addition, the size of the different imagery products in both experiments is depicted in **Table 3**. Notice that the size of the different products remains the same in both experiments. These demonstrate that the functionality of the system is intact after the optimization process, while the optimization provides benefits in storage, creation, delivery and deployment of the system.

Furthermore, the CPU and memory used in both experiments are similar for all the processing stages: in **Figure 7**, the CPU used in the processing of the satellite imagery with the nonoptimized system is shown; in **Figure 8**, the CPU used in the optimized system is depicted.

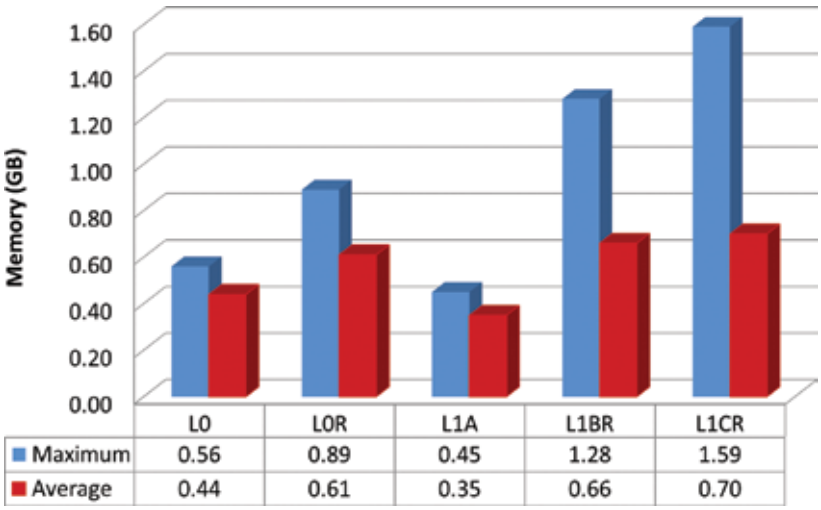

Figure 9. Memory use per process in the nonoptimized EOD system.

Besides, the memory used by the optimized system was lower: the memory use per process in the nonoptimized system can be seen in **Figure 9**, while the memory used in the optimized system can be seen in **Figure 10**.

These results obtained with the EOD pilot can be related with the new paradigms of the Earth Observation market stated in [1]. **Table 4** describes how an approach of a PDGS system similar to the EOD pilot could cover the main requirements of the new EO market.

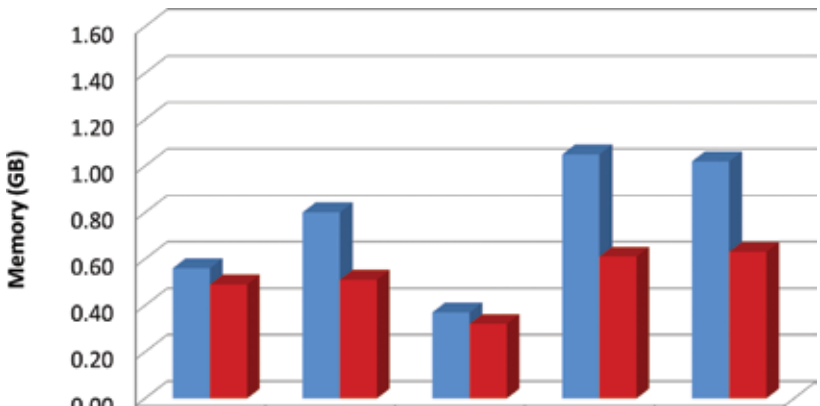

Figure 10. Memory use per process in the optimized EOD system.

New paradigm requirements	EOD pilot
Costs optimization	Cost reduction by means of reduced storage of optimized VMIs, reduced creation time, reduced delivery time and reduced deployment time
Multi sensors ground processing systems	Ground stations, ground control centers and data processing centers would take advantage of a rapid, agile, resilient and secure interconnected computer system in cloud
Vertical integration	Global distributed infrastructure connecting all the stakeholders in an operational environment
Scalability	Elastically autoscale applications on cloud resources based on their fluctuating load with optimized VM interoperability across cloud infrastructures and without provider lock-in

Table 4. New paradigm requirements vs. EOD pilot approach.

5. Conclusions and future work

In this work, the successful implementation of the EOD pilot in an experimental cloud infrastructure with the middleware ENTICE was demonstrated. The pilot was tested and

promising results were obtained. These results indicated that real scenarios of satellite imagery managing and processing can be carried out in cloud with many advantages with respect to traditional infrastructures. Furthermore, an optimization of the EOD pilot was carried out, demonstrating a reduction of 30% in VMI size, 37.3% in the VMI creation time, 34.53% in the VMI delivery time and 54.05% in the deployment time, while maintaining the functionality of the system intact. This indicates that a PDGS system implemented in cloud in a similar manner to that of the EOD pilot can fulfill the requirements of the new Earth observation market paradigm. Specifically, these EOD pilot results demonstrate that the deployment of an optimized PDGS system in cloud can reduce the costs of storage and reduce the time to user by reducing the creation time, the delivery time and the deployment time of the system. Besides, ground stations can take the advantage of rapid, agile, resilient and secure interconnected system when are cloud-based. In addition, the global operational environment provided by a cloud infrastructure facilitates both global acquisition and distribution of data, improving the market efficiency. Finally, the system improves its scalability without vendor lock-in, covering the needs of recent on demand markets.

In future research, different realistic scenarios with variable demand of services will be tested. With these scenarios, we will evaluate the elastic behaviour in the ingestion of raw data in the system, the processing and the distribution of imagery products to users. Furthermore, a complete optimization of the system will be tested to evaluate the complete repository storage size reduction, which was not evaluated in this work. In addition, new metrics will be measured to validate the implementation of the system for its commercial implementation in the next future.

Acknowledgements

This work has received funding from the European Union's Horizon 2020 research and innovation programme under grant agreement no. 644179.

Author details

Jonathan Becedas*, María del Mar Núñez and David González

*Address all correspondence to: jonathan.becedas@deimos-space.com

Elecnor Deimos Satellite Systems, Puertollano, Spain

References

[1] Denis G, Claverie A, Pasxo X, Darnis JP, de Maupeou B, Lafaye M, Morel E. Towards disruptions in Earth observation? New Earth Observation systems and markets evolution: Possible scenarios and impacts. Acta Astronautica, 2017;**137**:415-433. DOI: 10.1016/j.actaastro.2017.04.034

[2] Keith A. Emerging programs, markets drives earth observation growth. Earth Imaging Journal [Internet]. 21 February, 2015. Available from: http://eijournal.com/print/articles/emerging-programs-markets-drive-earth-observation-growth [Accessed: 2017-08-24]

[3] Keith A, Larrea Brito N, Manjunath S. Satellite-Based Earth Observation: Market Prospects to 2025. 9th ed. Euroconsult, Paris, France; September 2016

[4] Samsó L, Quirce J, Becedas J. Distributed Satellite Systems: The Next Big Thing is Already Here. In: Small Satellite Systems and Services Symposium (4S'2014); 26-30-05-2014, Majorca, Spain: ESA; 2014. p. 1-14

[5] Farres J. Cloud Computing and Content Delivery Network Use within Earth Observation Ground Segments: Experiences and Lessons Learnt [Internet]. 2012. Available from: https://earth.esa.int/documents/1656065/1664726/11-Cloud_computing_content_delivery.pdf [Accessed: 2017-08-30]

[6] Yang C, Goodchild M, Huang Q, Nebert D, Raskin R, Xu Y, Bambacus M, Fay D. Spatial cloud computing: How can the geospatial sciences use and help shape cloud computing? International Journal of Digital Earth. 2011;**4**(4):305-329. DOI: 10.1080/17538947.2011.587547

[7] Armbrust M, Fox A, Griffith R, Joseph AD, Katz R, Konwinski A, Lee G, Patterson D, Rabkin A, Stoica I, Zaharia M. A view of cloud computing. Communications of the ACM. 2010;**53**(4):50-58. DOI: 10.1145/1721654.1721672

[8] Botta A, Donato W, Persico V, Pescapé A. Integration of cloud computing and internet of things: A survey. Future Generation Computer Systems. 2016;**56**:684-700. DOI: 10.1016/j.future.2015.09.021

[9] gs4EO. Complete Suite of Ground Segment Products [Internet]. 2017. Available from: http://www.elecnor-deimos.com/wp-content/uploads/2017/07/gs4EO-EN-1.pdf [Accessed: 2017-08-30]

[10] Deimos-2 Minisatellite Mission [Internet]. 2017. Available from: https://directory.eoportal.org/web/eoportal/satellite-missions/d/deimos-2 [Accessed: 2017-08-30]

[11] Prodan R, Fahringer T, Kmovski D, Kecskemeti G, Csaba A, Stankovski V, Becedas J, Ramos JJ, Sheridan C, Whigham D, Rodrigo C. Use cases towards a decentralized repository for transparent and efficient virtual machine operations. In: 25th Euromicro International Conference on Parallel, Distributed and Network-based Processing (PDP'2017); 6-08-03-2017; St. Petersburg, Russia. IEEE; 2017. p. 478-485

[12] Kecskemeti G, Csaba A, Kertesz A. The ENTICE approach to decompose monolithic services into microservices. In: International Conference on High Performance Computing & Simulation (HPCS'2016); 18-22-07-2016; Innsbruck, Austria. IEEE, 2016. p. 591-596

[13] ENTICE – dEcentralized repositories for traNsparent and efficienT vIrtual maChine opErations [Internet]. 2017. Available from: http://www.cloudwatchhub.eu/entice-decentralized-repositories-transparent-and-efficient-virtual-machine-operations [Accessed: 2017-08-30]

[14] Ramos JJ, Becedas J. Deimos' gs4EO over ENTICE: A cost-effective cloud-based solution to deploy and operate flexible big EO data systems with optimized performance. In: Proceedings of the 2016 Conference on Big Data from Space (BiDS'16); Santa Cruz de Tenerife, Spain. ESA; 2016. p. 107-110

[15] Apache Jmeter™ [Internet]. Available from: http://jmeter.apache.org/ [Accessed: 2017-09-01]

[16] Nagios. The Industry Standard in IT Infrastructure and monitoring [Internet]. Available from: https://www.nagios.com/ [Accessed: 2017-09-01]

Chapter 10

Multi-purposeful Application of Geospatial Data

Chattopadhyay Nabansu, Chandras Swati and
Tidke Nivedita

Additional information is available at the end of the chapter

http://dx.doi.org/10.5772/intechopen.74217

Abstract

Agriculture is the backbone of the Indian economy. Any changes in weather and climate in short term as well as long- term adversely affect the agricultural productivity and the production of food grain production. In order to minimise the adverse impact of weather and climate on crops, the use of agrometeorological information and agromet services has already been proved to be highly beneficial. Agrometeorological services rendered by India Meteorological Department (IMD), Ministry of Earth Sciences, are a step to contribute to weather information-based crop/livestock management strategies and operations dedicated to enhance crop production and food security. IMD is operating a project 'Gramin Krishi Mausam Sewa' (GKMS) with an objective to serve the farming community at different parts of the country. Different states of technologies including the application of geospatial technology are being used in India for further refinement of the Agromet Advisory Services. The application of geospatial technology in generating agrometeorological information and products is very necessary for preparing need-based advisories at a high-resolution scale for the farmers in the country. In this chapter, elaborate discussion has been made on how the Geographical Information System (GIS) is being used for generating information and products using ground observations as well as satellite observations.

Keywords: geospatial technology, agromet products, agrometeorology

1. Introduction

Weather and climate play an important role in agricultural production. It has a profound influence on crop growth, development and yields; on the incidence of pests and diseases; on water needs; and on fertiliser requirements. Weather aberrations may cause physical damage

to crops and soil erosion. The provision of need-based climate information to farmers can support the management of agricultural resources (land, water and genetic resources). India Meteorological Department (IMD), Ministry of Earth Sciences (MoES), is operating Gramin Krishi Mausam Seva (GKMS) project at the district level in India, which represents a small step towards agriculture management in rhythm with weather and climate variability, leading to weather proofing for farm production. In order to minimise the adverse impact of malevolent weather, GKMS project provides a very special kind of inputs to the farmer as advisories that can make a tremendous difference to the agriculture production. The primary role of combating the negative impact of extreme events under the Agromet Advisory Services (AAS) is to find out the basic requirement to generate ways and means of adjusting crop cultivation plans/practices depending on the time of occurrence of the extreme events. Farmers are using these advisories for sowing and transplantation of crops, fertiliser application, predictions regarding pests and diseases and measures to control them, weeding/thinning, irrigation (quantities and timing) and harvest of crops.

Under the GKMS project, a number of activities were carried out during the last couple of years particularly in the generation of weather forecast, agromet advisories and its dissemination, capacity building, awareness, outreach, and so on in collaboration with 130 Agromet Field Units (AMFUs) located at State Agricultural Universities, Institutes of Indian Council of Agricultural Research (ICAR), Indian Institute of Technology (IITs) and also other collaborating organisations. At present, quantitative weather forecast in medium-range scale is being used in the preparation of agromet advisories at the district level for the farmers in the country. In addition to that, state composite and national level Agromet Advisory Service advisories are also prepared for state and national levels for planners and other users in macro-level planning and particularly under contingent plan. Efforts have also been made for the preparation of accurate medium-range weather forecast by value addition from Regional Meteorological Centres (RMCs)/Meteorological Centres (MCs). To help the farmers to cope with climate risks and uncertainties and also effectively use seasonal to inter-annual climate forecasts, IMD in collaboration with Central Research Institute for Dryland Agriculture, Hyderabad, also issued AAS Bulletins based on Extended Range Weather Forecast and Monthly Weather Forecast during southwest monsoon 2017 to fulfil the needs of different users including planners at state and national levels and farmers.

Among others, the generation and use of different agromet information and products are important initiatives to deliver crop- and location-specific agromet advisories to the farmers in the country. Here, GIS has an important role to play. Agrometeorological products are derived parameters from meteorological/agrometeorological or other interdisciplinary information. It deals with the application of weather- and climate-derived information in agricultural management. Timely availability and appropriate use of this information are vital for successful farming operations. These products serve as an important step for improving the agromet advisories and ultimately in the quality of bulletin. The first and foremost consideration is user requirements. Thus, agromet products are crop and location specific. At present, integrated approaches are being adopted by combining ground data, satellite data along with the high-resolution models and GIS technology to provide crop and location specific even at

district/sub-district level agromet advisories for meeting individual demand of the farmers. In this chapter, an elaborate discussion has been made regarding how the GIS is being used and what are the future plans to improve the services for the farmers in the country by exploiting the modern geospatial technology.

2. Application of GIS in agrometeorology

GIS is extensively used in modern science of operational agrometeorology. Under GIS platform, diverse data sources like real-time weather data including climatological data, land surface data and satellite data are fed into advanced system along with the algorithms for the visualisation of information and also products.

A GIS provides an organised method of storing spatial data. It stores the characteristics of features (the attribute component) in a database and then links the attributes to features (the spatial component) that it displays on a map. According to Refs. [1, 2], technology is an expansion of Cartographic Science, which takes advantage of computer science technologies, enhancing the efficiency and analytic power of traditional methodologies.

In a GIS, all the information can be linked and processed simultaneously, thus creating a syntactical expression of the changes induced in the system by the variation of a parameter. Using GIS improves data integration and usability, spatial analysis, and increases potential for broader applications. GIS could also make weather and climate information more usable in different allied fields of meteorological community. GIS is an essential tool to understand complex processes at different scales: local, regional and global. It is being extensively used in the science of agrometeorology. In GIS, the information coming from different disciplines and sources, that is, from traditional or digital maps, databases and remote-sensing, can be combined in models that simulate the behaviour of complex systems. Some common applications are relative to the control of industrial cycles, the simulation of urban and natural systems, the evaluation of specific procedures and the analysis of environmental impact (Refs. [3–5]).

Under the climate service programme, GIS is used extensively using the long period data. It also helps in the development of climate service tools for different sectors like agriculture, health, disaster risk reduction, and so on. These days, GIS is also used in the visualisation of weather pattern and other areas of interests of the common man. Most of the feature of GIS mentioned earlier is being considered in improving the operational agrometeorological advisory services across the world.

3. Ground data used in GIS application

Under the GKMS project, GIS is used extensively by utilising the weather information from the conventional as well as the automatic weather stations (AWS) including crop state and stage, soil information pests and diseases, and so on. The information/products so far obtained are

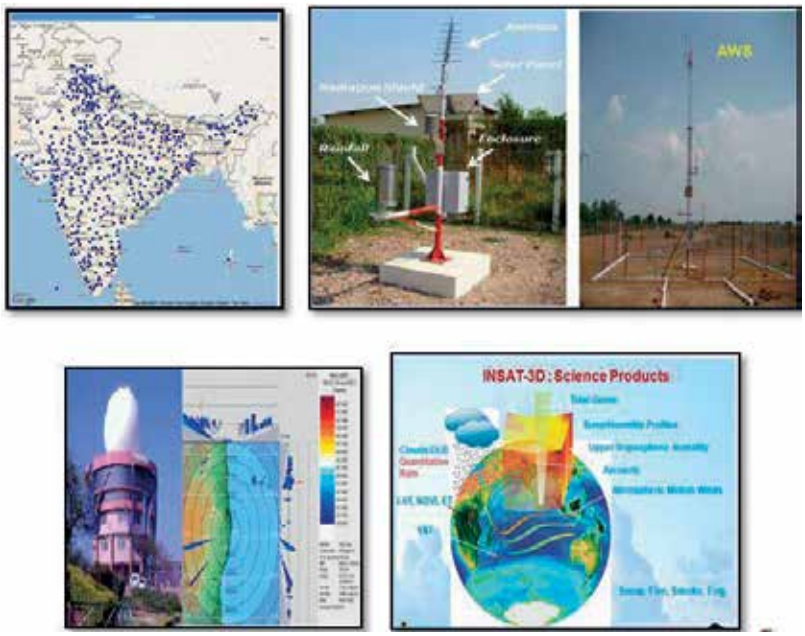

Figure 1. Observational network of IMD.

utilised at the time of sowing of crops, irrigation scheduling, fertiliser application, pesticides application, and so on.

IMD is establishing a number of observatories like surface, agromet, and so on to provide operational and R&D on atmospheric sciences. IMD is having different kinds of networks of observatories in India to monitor and assess the extreme events which are conventional observational network, automatic weather stations (AWS), buoy/ship observations, cyclone detection radars, Doppler weather radars and satellite observations. Satellite and radar observations are very crucial for monitoring and assessment of hazards, especially the Himalayan region and North Indian Ocean.

Figure 1 shows the weather observational network in India. At present, there are surface (532), automatic weather stations (593), automatic rain-gauge stations (1352), agromet observatory (264) and DRMS (3500). Maintenance and strengthening of atmospheric observational network is absolutely required to sustain and improve the skill of weather forecasts. IMD has been augmenting its observing system networks over the past years. At present, geospatial technology is used to convert discreet data into continuous data. Using interpolation technique, the data are converted to spatial spread. These data cover each and every district of India at a high-resolution scale which can be used for the betterment of agro-advisory.

4. Use of GIS in agrometeorological products in India

At present, under the GKMS project, extensive data on crop, weather and satellite data are being used to prepare the advisories at different temporal and spatial levels. In view

http://dx.doi.org/10.5772/intechopen.74217

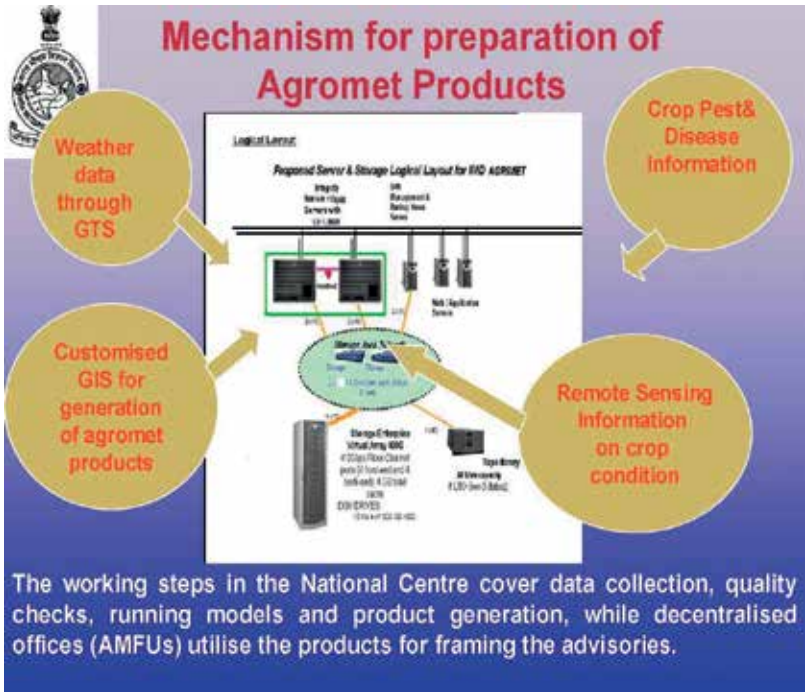

Figure 2. The mechanism for the preparation of agromet products.

of that, geospatial technology is being used in generating a number of products using ground-based data as well as the satellite data. To provide these services on a pan India mode, station-wise point data are not enough to generate the required products at the desired level. The present system helps IMD to compile data from various monitoring stations, analyse, generate advisories and disseminate information through online in near real-time basis. Since information is broadcasted in the form of maps and tables, it also helps users to extract various advisories and other information specific to the location of interest. Under the present system, it is possible to compile meteorological data from various monitoring stations along with geographic data from other sources, analyse, generate maps related to weather information, hydrology, agromet advisories, and so on and disseminate information through state-of-art communication system in near real-time basis. Since information will be broadcasted in the form of map and tables it helps users to extract various advisories and other information specific to location of interest. The software accommodates various algorithms and models to generate agromet, climatological and hydrological products.

It covers the following aspects:

- study of existing data including maps,
- preparation of guidelines for data standards and formats to be followed,
- preparation of mechanism to collect data/information from various field stations and linking with decision support system (DSS),

- study of interpolation techniques to be used,
- study of algorithm for agromet advisory.

The digital data are being collected from different authorised agencies through IMD for the preparation of digital database. The mechanism for the preparation of agromet products is given in **Figure 2**.

5. Product generations from the ground observations using GIS

In the context to the Indian agriculture, advisories have been given to farmers using weather information at the district level. Weather information and their departure from normal value at different temporal and spatial scales are useful for the preparation of agromet advisories. In view of that, daily, weekly, fortnightly, monthly and seasonal contours (**Figure 3**) are being generated utilising the realised weather observations for the parameter temperature (maximum temperature, minimum temperature and diurnal temperature variation), maximum and minimum relative humidity, cloud and wind speed. Synoptic observatory data received through Global Telecommunication System (GTS) are used to generate contours on a pan India mode. Weather information and their departure from normal value at different temporal and spatial scale is useful information for preparation of agromet advisories. In view of that daily, weekly, fortnightly, monthly and seasonal contours are being generated utilising the realised weather observations for the parameters temperature (maximum temperature, minimum temperature diurnal temperature variation), maximum and minimum relative humidity, cloud and wind speed. Synoptic observatory data received in GTS is used to generate contours on pan India mode. Using GIS software, the data are converted to spatial spread.

5.1. Daily spatial rainfall

Gridded rainfall data generated daily over India at a grid resolution of 0.25° × 0.25° of measured rainfall from the large number of rain-gauge stations distributed over India are interpolated using IDW interpolation at 0.25° × 0.25°, and the spatial district rainfall is generated using GIS software. The daily spatial rainfall maps are given in **Figure 4**.

5.2. Realised and forecast soil moisture on a pan India mode

The daily soil moisture (**Figure 5**) has been computed by soil water balance (SWB) based on the method given in Ref. [6]. The spatial district rainfall values extracted in GIS are used as data source to generate the daily realised soil moisture using SWB model. Soil moisture generated from SWB model is further interpolated using Gaussian interpolation technique under Krigging to generate spatial soil moisture maps. In addition to daily soil moisture data, the cumulative difference between two consecutive days for soil moisture is also made using GIS software. Dynamic potential evapotranspiration (PET) computed from Indian Geostationary Satellite (INSAT 3D) interpolated in GIS is used in this model.

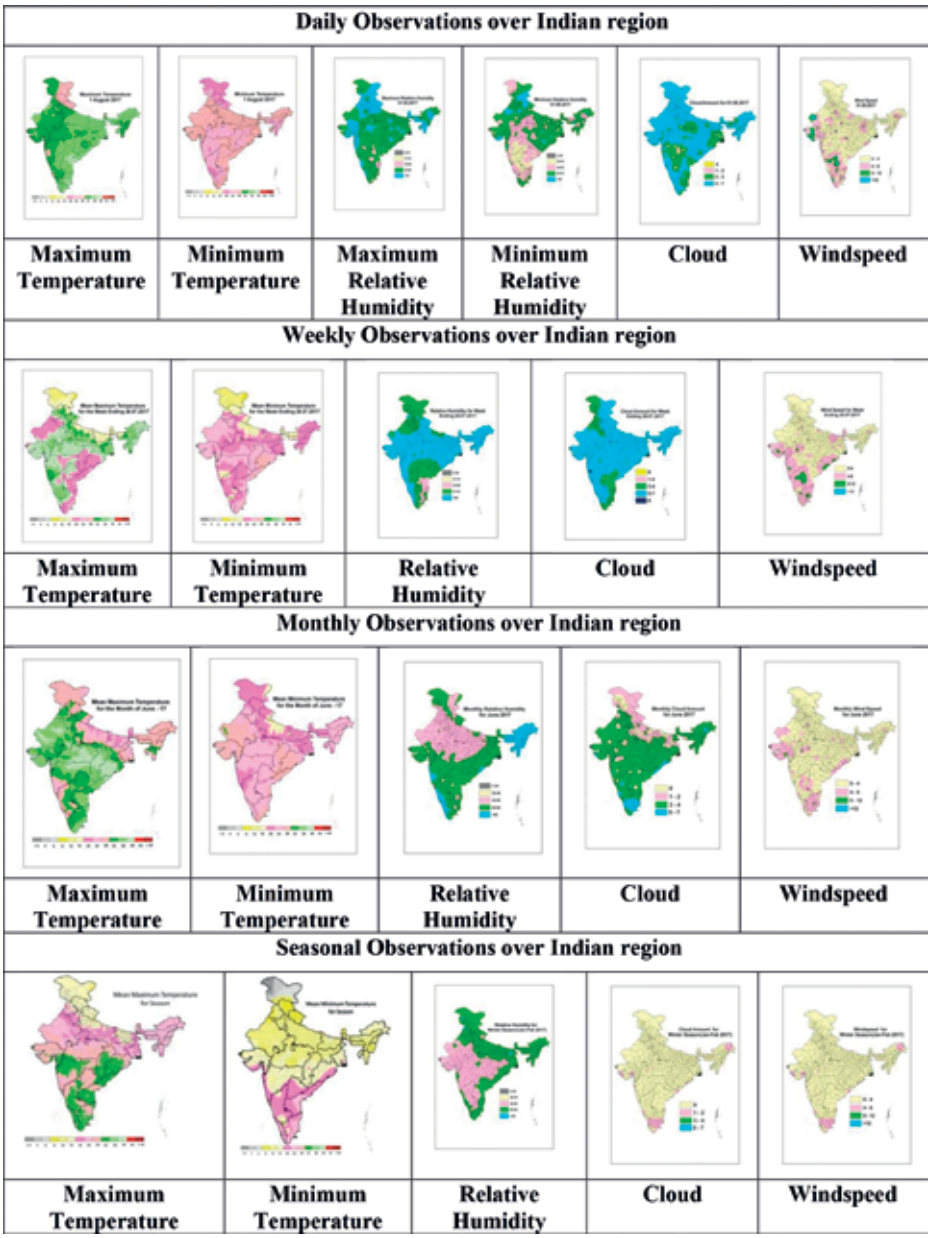

Figure 3. Spatial spread of daily, weekly, monthly and seasonal weather parameters over India.

Soil moisture forecast (**Figure 6**) is made based on the quantitative rainfall forecast (NWP model output of T 1534). NWP model output (rainfall) values added by different Regional Meteorological Centres/Meteorological Centres of India on every Tuesday and Friday are being used as district level rainfall in SWB model to generate soil moisture forecast.

Figure 4. Daily spatial rainfall.

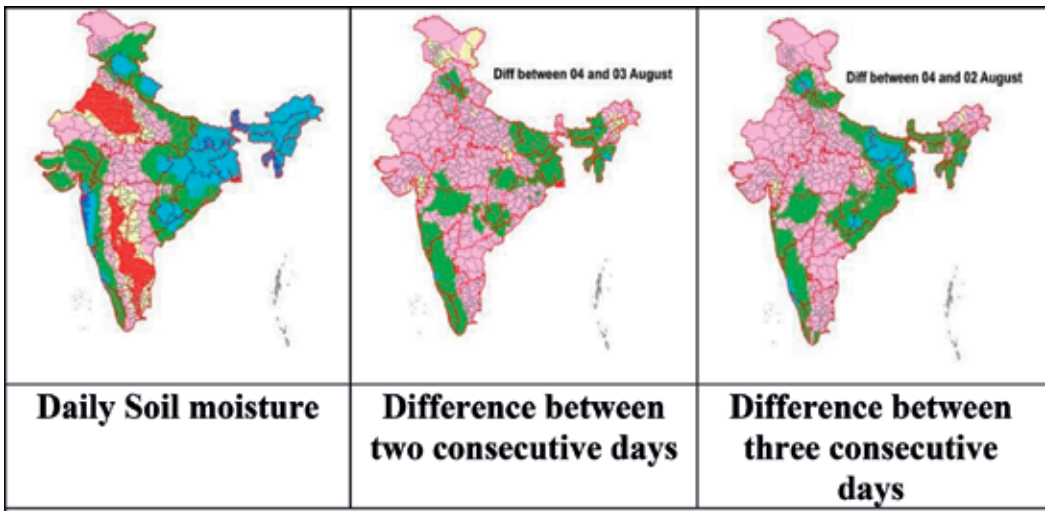

Figure 5. Realised soil moisture on a pan India mode.

5.3. Soil temperature and its anomaly at different depths

Presently, 153 stations are recording soil temperature at different depths at 07 LMT and 14 LMT. Soil temperatures recorded at these stations are used for spatial spread on a pan India mode using GIS software at different depths (5, 10 and 20 cm) which are depicted in **Figure 7**.

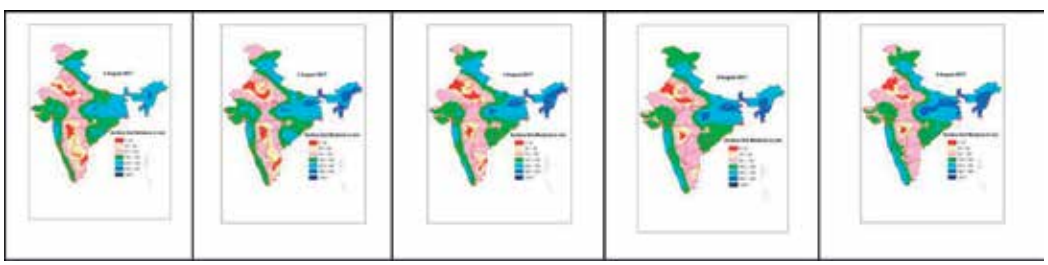

Figure 6. Forecast soil moisture on a pan India mode.

http://dx.doi.org/10.5772/intechopen.74217

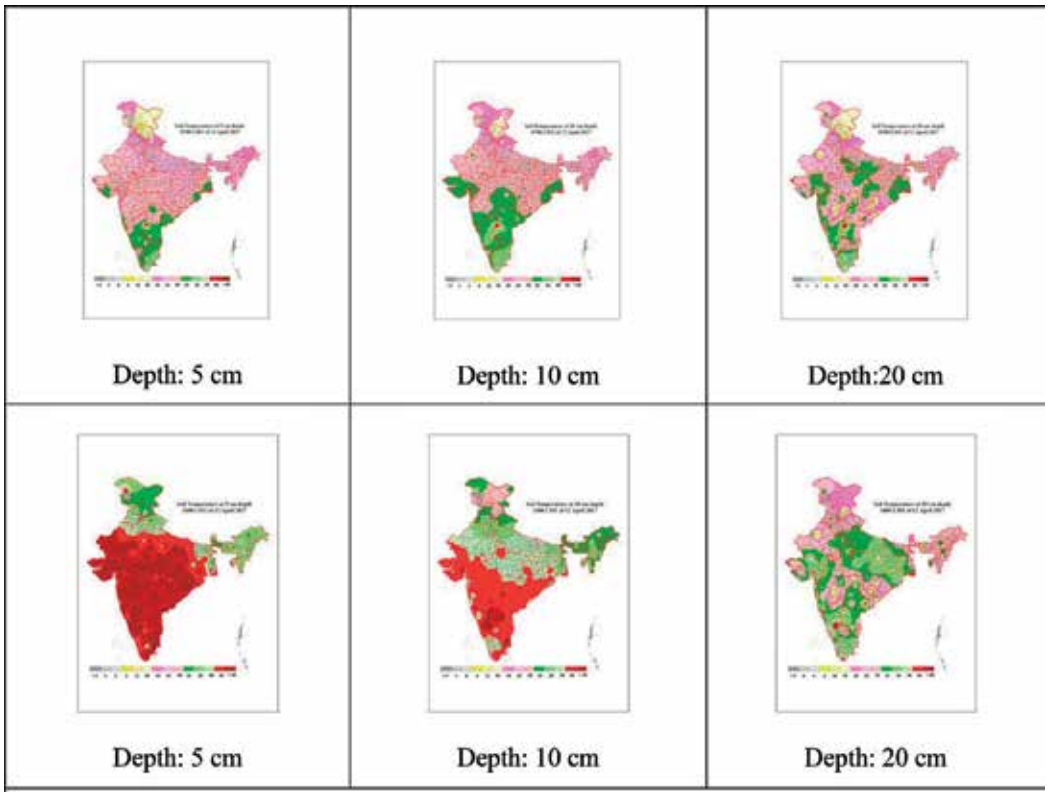

Figure 7. Soil temperature and its anomaly at different depths.

6. Web-GIS-based spatial decision support system development

An interactive web-GIS-based spatial decision support system (SDSS) is being developed to cater to various requirements of IMD in the field of agriculture, hydrology, weather forecasting, pest and disease forecasting. This software has the facility for digitisation, editing, interpolation and advisory generation and dissemination. The system has the following modules:

a. spatial database generation.

b. weather information map preparation,

c. hydrological analysis,

d. agromet advisories preparation.

The details of the modules are mentioned as follows:

a. Spatial database generation

This module has tools for

- digitisation of point, line and polygon feature,
- editing of digitised features,
- entry of attribute (non-spatial) information,
- linking of external non-spatial data,
- data import/export,
- linking of GTS (global telecommunication satellite) data with GIS.

b. Weather information map preparation

This module includes tools for

- generation of forecast maps based on forecasts/warnings issued for various weather parameters like rainfall, temperature, and so on,
- generation of weather anomaly maps (pressure, wind, temperature (maximum, minimum and dew point) and extreme meteorological event maps like heat wave, cold wave, etc.),
- generation of climatological maps of rainfall, maximum temperature and minimum temperature all over India.

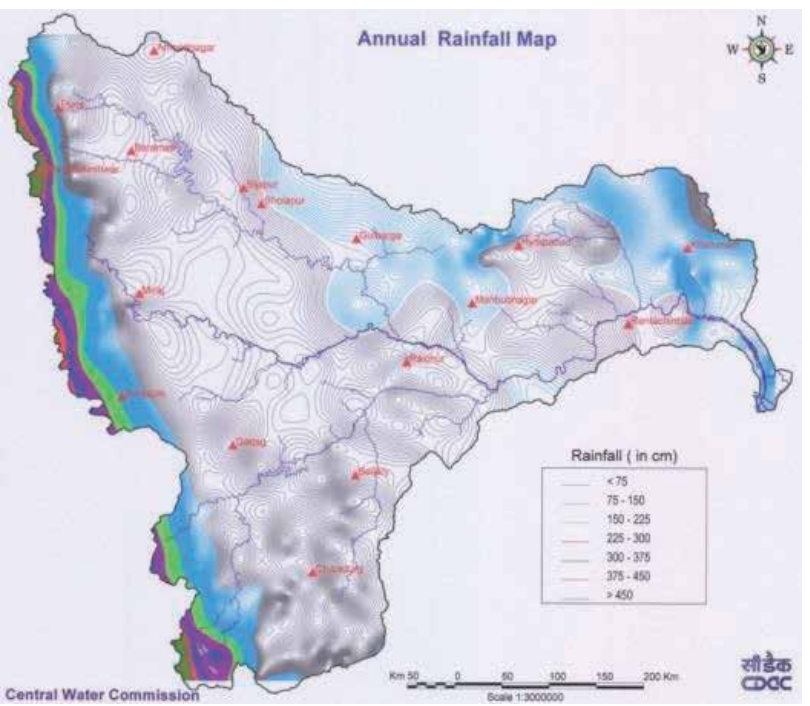

Figure 8. Annual rainfall map (with Isohyet) of Krishna Basin.

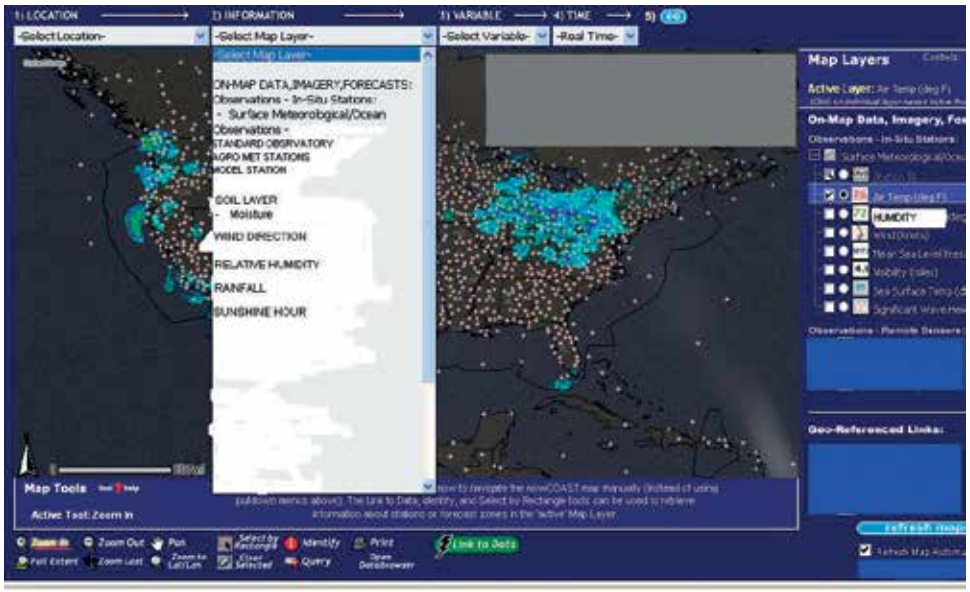

Figure 9. An example of an interactive web-GIS portal.

c. Hydrological analysis

This module includes tools for

- importing point data such as rainfall, temperature, relative humidity, and so on, with respect to geographic locations,
- interpolation of point data to generate surface map of rainfall, temperature, and so on,
- generation of isoline maps: this tool is used to generate isolines of different weather parameters like temperature (isotherm), and so on as shown in **Figure 8**.

d. Agromet advisory preparation

This module includes tools for

- Field data entry: a form is designed to facilitate field station user to enter field data such as crop, crop condition, soil moisture, location, and so on.
- Importing field data from the data entry form.
- Map generation for parameters like soil type, soil moisture, soil temperature, air temperature, humidity, rainfall, wind, cloud, bright hours of sunshine, crop condition (biotic and abiotic stress) and pest-disease infestation status, drought and aridity along with textual and data information.
- Generation of real-time agromet products (crop and location specific) like pest forecasting, irrigation scheduling, fertiliser application, and so on, using requisite meteorological

data, crop data and soil data. Preparation of agromet advisories (crop and location specific) for different agro-climatic zones (a total of 127) in the country addressing to intra-zonal variability at the district level (about 640).

e. Data collection and organising

- Accuracy check: the accuracy of the individual map will be assessed in terms of topology, digitisation error and attribution.
- Map projection: all collected maps will be brought into a standard projection system as per the SRS.
- Mosaicking and edge matching: the individual map with a desired accuracy will be processed further for edge matching and mosaicking to prepare seamless datasets.
- Data attribution: each feature of the digitised map will be linked with its attribute data.

Figure 9 depicts an example of an interactive Web-GIS portal for operational agrometeorology.

7. Application of GIS in product generation with satellite observations

As climatic variability and climate change will shortly throw huge challenges to agricultural productivity and agricultural production in the country, the days are not very far that farmers of the country will need personalised services on their farm management. Here, remote-sensing/satellite information will play a great role when the country does not have an ideal network of weather observatories, or if at all there will be more observatories, it will take more number of years and the management of weather observatories will also be a herculean task for a country like India. Satellite offers a unique source of information for many agricultural applications. Recent advances in satellite technology in terms of high-resolution, multi-spectral bands provide useful information for agricultural operations. The integrated use of satellite data and conventional meteorological observations are found to be very useful to extract information relevant to agriculture in India. Agricultural meteorology is one of the fields of hydrometeorology for which satellite data are very important. Agrometeorological parameters are very variable in time and space. Ground observations do not provide end users with the required spatial and temporal resolution. **Figure 10** shows the current Indian Geostationary Meteorological Satellite. Information about large areas can only be obtained by remote-sensing. The flow of data from new satellites such as Meteosat-8, Terra, and so on is much more informative which opens new areas for agrometeorological applications. Satellite remote-sensing technology is increasingly gaining recognition as an important source of operational agrometeorological services. The regular and national-scale agrometeorological monitoring of the physiological processes and growth indicators require the retrieval of basic land surface variables using spatial observations. The challenge for research therefore is to develop new systems extracting this information from remotely sensed data, giving to the final user's near-real-time information. Satellite-based agrometeorological products and the interpretation of

http://dx.doi.org/10.5772/intechopen.74217

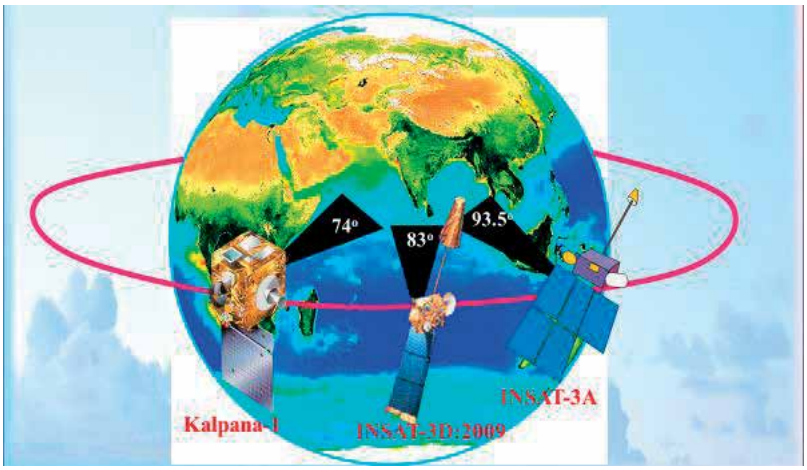

Figure 10. Current Indian geostationary meteorological satellites.

the same in terms of crop and soil moisture status will help the experts to frame the advisories in a better way and ultimately improve the quality of the advisories. In order to extend the support of the ongoing operational AAS, the generation of satellite products for the generation of location-specific agromet advisories is required to meet the end-user requirement.

Besides, the remote-sensing technology helps to provide information for monitoring the pest and disease, drought and flood conditions along with the remedies to the farming community before the situation turns into a disaster affecting the crop yield and productivity. The potential zone for agriculture activities can be identified by studying the climatic variability, and localised services may be provided to the farmers to increase productivity. The yield productivity can be estimated using the remote-sensing technology where information can be further used for the crop insurance services. Remote-sensing methods can be integrated with crop growth models and statistical models to estimate better result in a spatial format. The great challenges would be to the meteorologists/agrometeorologists and space scientists to develop bias-free meteorological/agrometeorological information at its proper application at a local scale to further increase agricultural production to the huge population of the country in the coming years. In order to provide high-resolution information at a ground level, it is almost mandatory to use the remote-sensing data into the GIS hub under the advanced operational Agromet Advisory Services. At present, utilising the information of geostationary and polar satellite, a number of information like soil moisture index, land surface temperature (LST), Normalised Difference of Vegetation index and vegetative condition (VCI) are used to generate a number of information particularly when the plants are in stress conditions.

All information produced by the satellite is elaborated for the extraction of the desired information. There are many methods, algorithms and procedures to derive fundamental data for agrometeorological application from remote-sensing. Among the existing indices, the most extensively used are the land surface temperature (LST) which is a good indicator of climatic and microclimatic conditions prevailing close to the surface, as well as the frost or the moisture in the soil.

In developing countries, GIS use can be promoted through the transfer of technologies and information from the developed ones. This requires generalisation of the knowledge and studies carried out elsewhere. Moreover, frequently in developing countries, data used for the production of the informative layers are often unreliable or even lacking. Besides, the models used in these systems are the results of studies and projects, realised at different scales. Implementation of a GIS requires a great effort to collect and organise the available information on the territory. This important activity requires a period of validation for the operational use of the system. In any case, many projects have started to implement GIS in a number of different environmental and economic systems, mainly using information derived from remote-sensing to complete the direct observations. The common advantage is the definition of the state of the art and a first study of the particular problems, with the suggestion of innovative specific solutions. At this level, the products often are already used for practical applications, and the operators find it sufficiently powerful and reliable.

The data collected and the different information layers are organised in a database, and all the information about the territory is integrated in a GIS. Each layer is composed of different archives (numeric data, text and images), which were preliminarily controlled and evaluated. The archives are completed with graphical representations of the main data trends and synthetic information, obtained by means of spreadsheet and statistical software. The most important information is extracted to describe the territory and then combined for understanding the possible relationships between the different factors. The representation of these data can be made for discrete or continuous values, to obtain thematic maps or territorial representation of the spatially distributed parameters. Satellite data are for agricultural monitoring as monitoring land condition and also for within-season forecasting.

Under GKMS project in India, a joint initiative has been taken up by the Indian Space Research Organisation (ISRO), Indian Council of Agricultural Research (ICAR), India Meteorological Department, National Centre for Medium Range Weather Forecasting (NCMRWF), Noida, Mahalanobis National Crop Forecasting Centre (MNCFC), New Delhi, under DAC (Department Agriculture and Cooperation) to prepare a roadmap for using satellite-based information to augment services to farmers. The ISRO centres include Space Applications Centre, Ahmedabad, National Remote Sensing Centre, Hyderabad, ISRO HQ, Bangalore, Indian Institute of Remote Sensing, Dehradun, and ICAR. With the launching of INSAT 3D, it is expected that Agromet Advisory Services would be further strengthened by providing customised information to the farmer at smaller areas.

A number of studies are being made with the geostationary satellite launched in India, that is, INSAT 3D. INSAT 3D has two kinds of payloads 'Imager' and 'Sounder'. The 'Imager' has six bands consisting of broad visible (VIS), short-wave infrared (SWIR), middle infrared (MIR), water vapour (WV) and two split-thermal infrared (TIR) bands. The optical (VIS, SWIR, MIR) and thermal bands (TIR) from 'Imager' are able to capture reflective and emissive signatures in cloudless skies at half-hourly interval with a single snapshot over the entire country and South-East Asian continent. The combination of all these products from 3D, improved weather forecasts, vegetation index product from INSAT 3A CCD and in situ data are valuable ingredients to generate real-time value-added information for enhanced operational agromet advisory services in the country. The long-term datasets from INSAT suite will be able to aid in

http://dx.doi.org/10.5772/intechopen.74217

digital agro-climatic characterisation. A large scope of advanced research exists to explore the INSAT data, to develop advanced algorithm, to improve the accuracy of scheduled product and develop new products. The Imager data would be able to provide satellite meteorological (sat met) products such as rainfall, land surface temperature (LST), land surface albedo, incident solar radiation, cloudiness, upper troposphere humidity (UTH) and outgoing long-wave radiation (OLR). The occurrence and progress of fire, fog and smoke can also be monitored by INSAT 3D data. IMD and SAC have jointly started the incorporation of satellite-based agrometeorological component, particularly NDVI composite image, developed from INSAT 3A CCD image for generating information on crop vigour and agricultural progress. This information along with the rainfall data are being used in stress monitoring and track the crop growth from sowing to harvesting of the major crops in the country. Besides, some studies on crop stress detection through the estimation of evapotranspiration using satellite data have also been attempted in the past along with pest-disease studies based on weather and satellite data.

It is planned for the effective usage of satellite observations, particularly Indian satellites, to improve the initial conditions of Numerical Weather Prediction (NWP). The Research and Development (R & D) activity for the optimal use of the satellite data is being carried out,

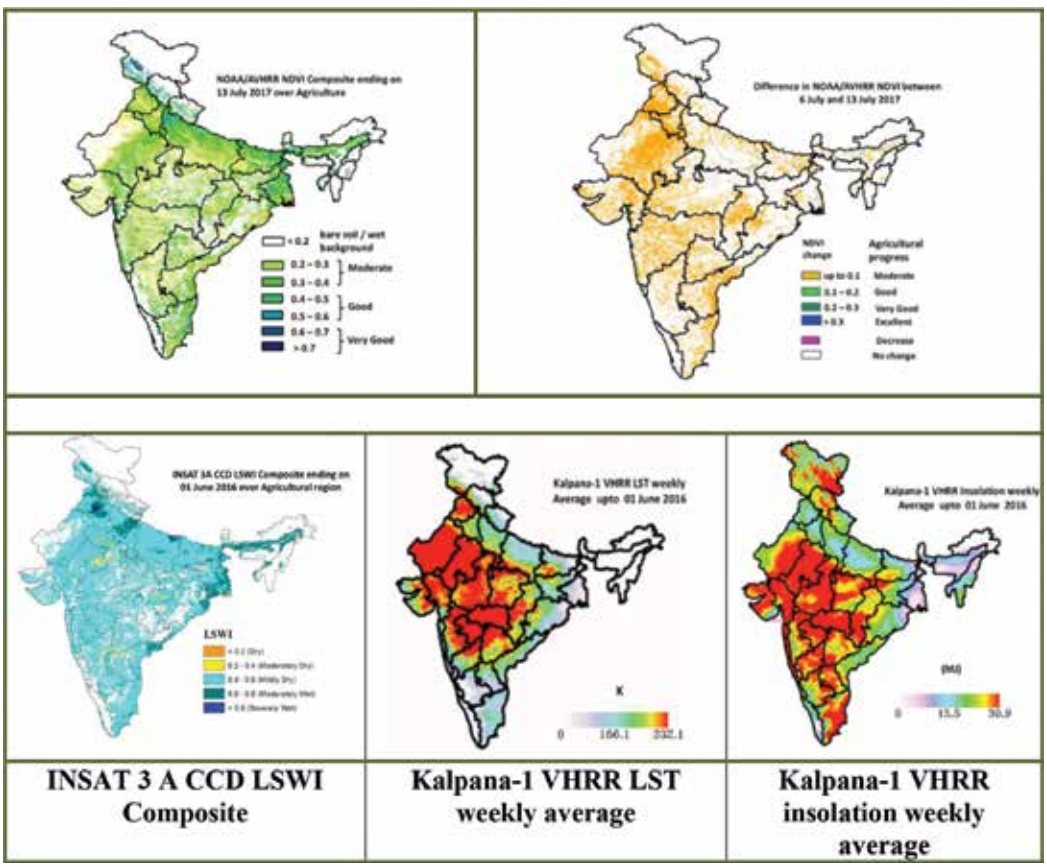

Figure 11. NOAA/AVHRR NDVI composite and difference.

and subsequently, improved assimilation system for the optimal use of the satellite is implemented. The implementation plans are given as follows:

- Operationalise the assimilation of SAPHIR and INSAT-3D radiances in the Multi-Model Ensemble (MME) for improvement of weather forecast.
- Assimilation system to assimilate different land surface products such as soil moisture, vegetation and snow fraction, land surface temperature and albedo.
- Development of RAPID system (www.rapid.gov.in). This system is a geoportal for satellite meteorology and forecasts with different Web-GIS facilities. This system should be modified and adapted for agrometeorological applications and agro-advisory purposes so that any official engaged in Agromet Services can utilise this facility.

The data from suite of INSAT satellites are being received and processed on real-time basis through an operational chain known as INSAT Meteorological Data Processing System (IMDPS), New Delhi, as well as mirror site in IMDPS, SAC, Ahmedabad. The images and digital products at different time scales (half-an-hour to daily) from IMDPS on real-time basis have great potential for use in the preparation of advisories for Agrometeorological Services on an operational basis and ensuring the availability of data on a requirement basis.

There are specific requirements to derive some specialised products such as surface insolation, LST, albedo and reference evapotranspiration from INSAT 3D 'Imager'. It is proposed to develop algorithms of all these products and will be implemented at IMDPS, New Delhi, for generation of these products on an operational basis. Validated global 7-day composite of

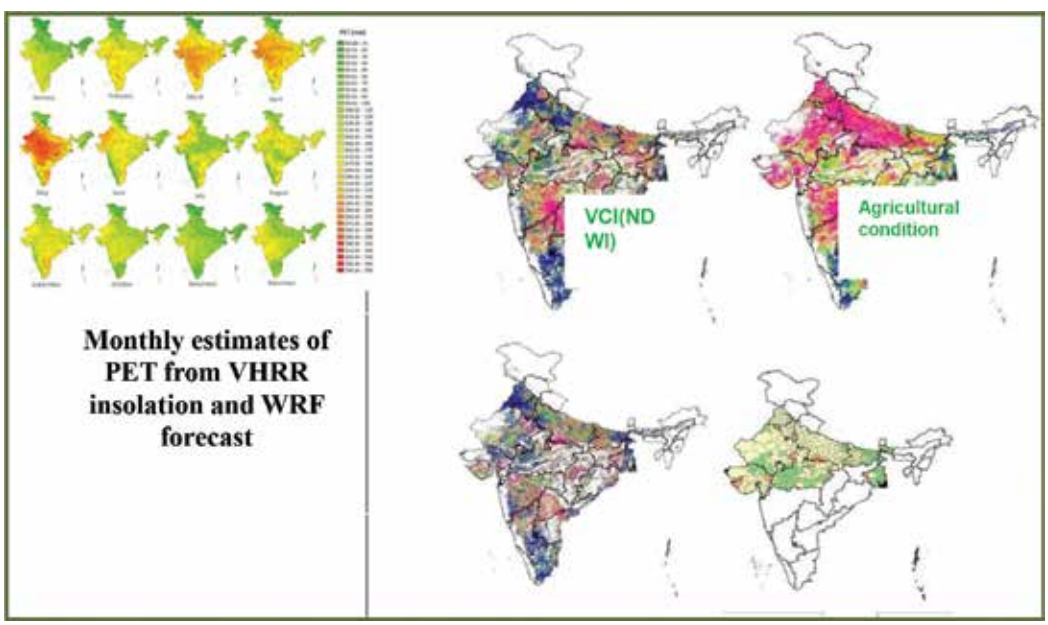

Figure 12. Different remote-sensing products.

SMN data at 4 km is derived from no noise NDVI (Normalised Difference Vegetation index). Gridded weekly global vegetation indices (SMN, VCI, TCI and VHI) are derived from NOAA VHRR satellites. These datasets can be used to estimate the vigour and stress on vegetation, start of growing season and its phonological phages. Weekly NDVI products and composite maps are being operationally generated for the Indian region (**Figures 11** and **12**).

In order to provide large-area updates by using finer-scale low-repeat RS data and products over land, data from IRS, OCM, AWiFS, MODIS and RISAT-1 are being created weekly composite of vegetation indices, snow cover and snow/water fraction. Surface insolation and land surface temperature (LST) from INSAT 3D are being operationalised in India. Besides, efforts are being made to operationalise products of land surface albedo and reference evapotranspiration at IMDPS, New Delhi. The generation of potential crop maps for rice (*kharif, rabi*), wheat, mustard, cotton, potato, sugarcane, jute and *rabi* sorghum at 100–200 m spatial resolution all over India coverage for all the above crops once in a season is in process including advanced operational agromet products such as actual evapotranspiration, aridity index and water requirement satisfaction index (WRSI). These products are made available subjected to the success of other core agromet products to be generated from INSAT 3D. Different remote-sensing products for agrometeorology are depicted in **Figure 12**.

8. Other projects on use of satellite information in operational Agromet advisory services

8.1. Determination of soil moisture over India using space-borne passive microwave sensors on board SMOS

Soil moisture is being estimated for three states, Uttar Pradesh, Madhya Pradesh and Gujarat (**Figure 13**), by the satellite products, namely SMOS (soil moisture and salinity) launched by European Space Agency (ESA), MODIS (NDVI and LST from Terra/Aqua) and SSMIS (Special Sensor Microwave Imager/Sounder) by NASA for (LST) using Beam 4.9 software.

Satellite data-based fusion approach to develop soil moisture monitoring system in India: Methodology has been developed for the estimation of soil moisture using SAR data from PALSAR (phase array L-band synthetic aperture radar) and NDVI from MODIS using NEST and POLSAR-PRO software. On experimental mode, soil moisture maps have been generated in Moga, Hissar, Roorkee, Saharanpur, Meerut, Dhanbad and Moradabad with the resolution of 25 m.

8.2. Optimum sowing suitability for *kharif* (June and July), *rabi* (November and December) seasons and general agricultural health based on edaphic factors

Activities on the use of satellite data have been initiated in collaboration with different organisations (Space Applications Centre, ISRO), to strengthen the Agromet Advisory Services (AAS). One important activity, that is, sowing suitability of crops during *kharif* season, has been started using the satellite data (AMSR-2 (Advanced Microwave Scanning Radiometer sensor), soil moisture content (SMC at 10 km available from Japan Aerospace Exploration

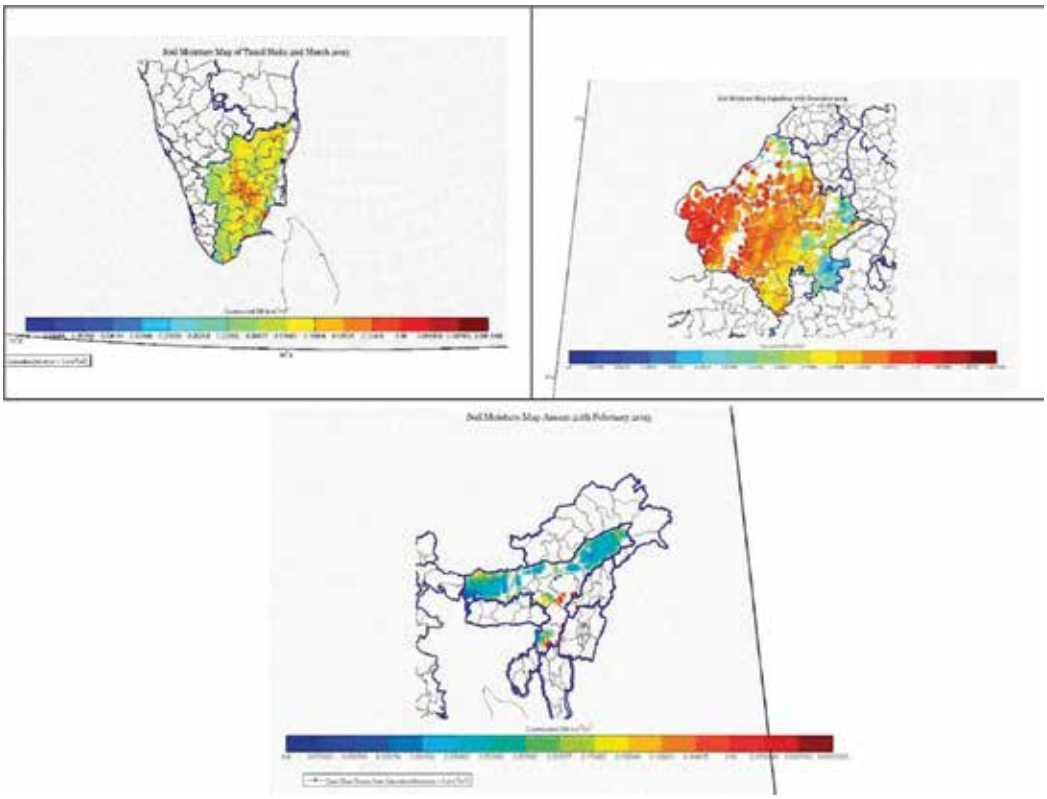

Figure 13. Estimation of soil moisture using SMOS.

Agency) and (Indian Geostationary satellite) INSAT 3A CCD NDVI (1 km) data). In order to provide large-area updates, the weekly mean of AMSR-2 surface soil moisture (SSM) and the weekly composite of INSAT Normalised Difference Vegetation Index (NDVI) are used. The geospatial integration of these two was carried out after putting desired thresholds. It is known that the optimum surface soil moistures of 0.1–0.15 m^3 m^{-3} maintained at least for a week or 2 weeks are ideal at the start of the growing seasons if soil temperature and other meteorological conditions are conducive. Spectral emergence is evident when NDVI crosses 0.3. In *kharif* season, the weekly accumulated rainfall and their thresholds determine sowing. These thresholds vary from crop to crop and according to different agro-climatic settings. Using this information, the current week and the previous week SSM were applied a threshold of 0.1–0.15 and the current week NDVI was applied a threshold of 0.3 to extract the area suitable for sowing. Further thresholds were applied to determine the already sown area. The maps in **Figure 14** show the sown area and area conducive for sowing. The corresponding weekly rainfall maps also show the area with normal or excess rainfall in two consecutive weeks that are probably sown or conducive for sowing.

Presently, the satellite and modelled rainfall maps are the source used for the prediction of area suitable for sowing. The abovementioned maps, which use the soil moisture condition and vegetation

http://dx.doi.org/10.5772/intechopen.74217

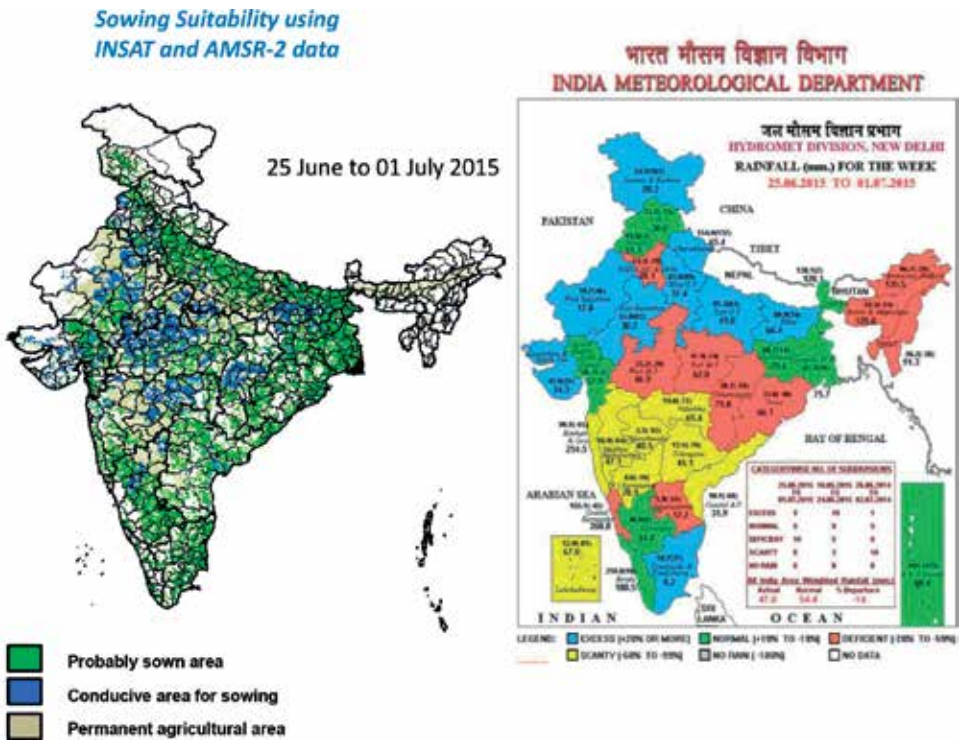

Figure 14. Sowing suitability map.

condition, can act as promising maps for prediction areas suitable for sowing. The technique to generate this map has been prepared and the satellite data used can be made available freely. Thus, this methodology to generate sowing suitability maps can be made operational and can be shared with different AMFUs by providing state-level sowing suitability maps.

8.3. Development of methodology for forecasting spatial crop age/phenology

Response to abiotic stresses and quality of advice to farmers depends on the crop type and crop growth stages. The crop age or phenological stages depend on spectral emergence date/sowing date and subsequent ambient temperature and sunshine hours expressed through thermal and helio-thermal units. The length of the growing season is determined from spectral emergence date and the date of physiological maturity.

Temporal profiles of vegetation index from satellite remote-sensing observations are modelled to trace back spectral emergence date. Early detection could be possible if high temporal vegetation index with a resolution varying from 200 to 1000 m depends on the crop type and coverage. The potential crop mask is an essential input to this. This work is being attempted for six major crops for which the potential crop masks are expected to be available. Superimposition of extended-range or medium-range weather forecasts with spectral emergence dates would provide crop age if agro-climatic zone-wise thermal thresholds are known.

8.4. Development and validation of crop water requirement satisfaction index (WRSI)

Stage-wise crop water requirement satisfaction index is a function of potential, actual ET and crop age. This determines the level and persistence of water stress. The development of WRSI from available ET products from MODIS/INSAT or other sources is made for *rabi* crops such as wheat, mustard, potato and *rabi* rice. The validation is being carried out based on Eddy covariance, ISRO-AMS and scintillometer data available in India.

8.5. Inter-comparison of different abiotic stress indicators

Different satellite-based abiotic stress indicators have been reported over the past. These are Temperature Vegetation Dryness Index (TVDI), Vegetation Temperature Condition Index (VTCI), water deficit index (WDI), combined deficit index (CDI) and vegetation health index (VHI). These indices use various approaches such as triangle, trapezoid, lag correlation and anomaly that use satellite-based VI, land surface temperature (LST) and rainfall. Study is being carried out on comparing the efficiencies of these indices in both *kharif* and *rabi* especially over semi-arid regions or regions having history of persistent water scarcity such as Anantpur (Andhra Pradesh), Bundelkhand region (Uttar Pradesh), Saurashtra region (Gujarat) and Jodhpur-Jaisalmer region (Rajasthan).

8.6. Development of digital agro-climatic atlas for improved crop planning

The improved crop planning provides economic security to farmers. The improvement in crop planning for 'smart agriculture' depends on knowledge or information base from systematic historical data records on several agro-climatic databases valid for 127 agro-climatic regions. The long-term databases on satellite-based surface insolation, near-surface Tmax, Tmin, RHmax, RHmin, rainfall, LST, NDVI, ET_0, AET, surface and root-zone soil moisture on monthly, seasonal and annual scales are generated after bias correction and temporal filtering at 5–10 km. The ancillary databases on soil physical and chemical properties are superimposed. Geospatial analysis can be carried out to bring out national-scale digital agro-climatic atlas.

8.7. Development of methodology for tracking of major pests and diseases

The foremost step of spatial forewarning of pests and diseases is to obtain highly accurate and high spatial-resolution weather products. Different satmet products such as OLR, insolation, UTH, wind vectors and near-surface atmospheric temperature and humidity are available from IMDPS at a resolution varying from 5 to 30 km. These data are being obtained at 30 min to 1 h temporal resolution. Some analysed fields are also being available. Standardisation of these satmet products or analysed fields with reference to in situ surface weather data will be carried out to adapt these to develop alarm zone for major candidate pests and diseases.

The work is initiated in mustard crop for Alternaria blight and Aphid, SATMET product (LST, SpH and sunshine hour/rainfall) near-surface (2–3 m) utilised for weekly progress of pest (incl. diseases) infestation, and then tracking the pest (incl. diseases) through a suitable growth model can be attempted. In this study, growth model is constructed for tracking of pest (incl. diseases) infestation on mustard crop with the combination of remote-sensing information.

Hyper-spectral data using spectroradiometer in field and remote-sensing approach in reflectance for many continuous narrow wavelength bands in visible–near infrared (VNIR) and short-wave infrared (SWIR) region of electromagnetic spectrum are used for the detection and growth of Alternaria and aphid infestation in mustard crop within a year. Different spectral indices like NDVI, RVI, AI, SIPI, and so on are calculated for the identification of Alternaria infection and aphid infestation or stress on crop using remote-sensing.

9. Conclusion

Under the observed and projected climate change along with the climatic variability, productivity and production of major crops in India are expected to reduce substantially. Besides, weather and climate extremes during the last one and half decades damaged standing crops extensively. Under these scenarios, operational agrometeorological services play a great role. National Meteorological & Hydrological Services in collaboration is another organisation providing services to the marginal and small farmers at present at the district level and shortly at the sub-district level for increasing the crop production.

Among others, the generation and use of different agromet information and products are important initiatives to deliver crop- and location-specific agromet advisories to the farmers in the country. Here, GIS has an important role to play. Agrometeorological products are derived parameters from meteorological/agrometeorological or other interdisciplinary information. At present, under the GKMS project, extensive data on crop, weather and satellite data are being used to prepare the advisories at different temporal and spatial levels. In view of that, geospatial technology is being used in generating a number of products using ground-based data as well as the satellite data. To provide these services on a pan India mode, station-wise point data are not enough to generate the required products at a desired level. At present, geospatial technology is used to convert discreet data into continuous data. Using interpolation technique, the data are converted to spatial spread. These data cover each and every district of India at a high-resolution scale which can be used for the betterment of agro-advisory. An interactive Web-GIS-based spatial decision support system is being developed to cater to various requirements of IMD in the field of agriculture, hydrology, weather forecasting, pest and disease forecasting. With the launching of a series of geostationary satellite, at present, vast information and products are available in India. The challenge for research is to develop new systems extracting this information from remotely sensed data, giving to the final user's near-real-time information. Satellite-based agrometeorological products and the interpretation of the same in terms of crop and soil moisture status will help the experts to frame the advisories in a better way and ultimately improve the quality of the advisories. In order to extend the support of the ongoing operational AAS, the generation of satellite products for the generation of location-specific agromet advisories is required to meet the end-user requirement. Under the operational Agromet Advisory Services, using GIS, a number of products like NDVI, VCI and PET (potential evapotranspiration) are being used to capture stress condition of crops for providing appropriate advisories. Besides, the generation of a number of information and products is in the pipeline. It is expected that with the ground data, satellite information and products and with the geospatial technology, more appropriate high-resolution and crop-specific agromet advisories will be provided in the near future

and ultimately it will be possible to minimise the crop loss due to aberrant weather and also improve the economic conditions of small and marginal farmers in the country.

Acknowledgements

The authors are thankful to the Centre for Development of Advanced Computing (C-DAC), Pune, and Space Application Centre (SAC), Ahmedabad, for sharing the information in the preparation of this chapter.

Author details

Chattopadhyay Nabansu*, Chandras Swati and Tidke Nivedita

*Address all correspondence to: nabansu.nc@gmail.com

India Meteorological Department, Pune, Maharashtra, India

References

[1] Ballestra G, Bertozzi R, Buscaroli A, Gherardi M, Vianello G. Applicazioni dei sistemi informativi geografici nella valutazione delle modificazioni ambientali e territoriali. Milano, Italy: Franco Angeli; 1996

[2] Coulson RN, Lovelady CN, Flamm RO, Spradling SL, Saunders MC. Intelligent geographic information systems for natural resource management. In: Turner MG, Gardner RH, editors. Qualitative Methods in Landscape Ecology. New York: Springer Verlag; 1991. pp. 153-172

[3] Mueksch MC. Monitoring and assessing natural lake and environments for lake-GIS. In: Proc. GIS/LIS'96, Annual Conf. and Exposition, Denver, Colorado. 1996. pp. 30-36

[4] Bouman BAM, Nieuwenhuyse A, Hengsdijk H, Jansen HGP, Schipper RA. An integrated methodology for sustainable land use exploration using GIS. In: Proc. 1st Int. Conf. Geospatial Information in Agriculture and Forestry. Lake Buena Vista, FL, USA. 1998. pp. 230-237

[5] Taylor JD, Burger LW. Wild life habitat evaluation and planning using GIS. In: Proc. 1st Int. Conf. Geospatial Information in Agriculture and Forestry. Lake Buena Vista, FL, USA. 1998. pp. 215-220

[6] Thornthwaite CW, Mather JR. The Water Balance. Publ. in Climatology. Vol. 8, No. l. Centerton, New Jersey: C.W. Thornthwaite & Associates; 1955

Edited by Rustam B. Rustamov, Sabina Hasanova and Mahfuza H. Zeynalova

This book is dedicated toward space technology application in Earth studies based on the use of a variety of methods for satellite information classification and interpretation. Advantages of geospatial data use in a large-scale area of observation and monitoring as a source of decision-making stage have been demonstrated.

The book describes navigation systems providing data estimation method and review of existing data in the literature relevant to remote sensing sensors delivering main information electromagnetic spectrum and a variety of sensor applications. This aspect is important when combining/integrating satellite data processing into the field measurements.

Satellites and satellite data application for the study of Earth features have been demonstrated as the next step of geospatial data application.

The use of different purposeful processing technology applications of satellite data is one of the vital aspects of space technology advances. The use of GNSS GPS technology in industry and MODIS images and data interpretation for agriculture purposes has been presented.

It was the aim of the book to create an attractive environment by presenting space technology application in the wide areas of Earth study. For this purpose, some of the book chapters are dedicated toward space technology advances in climate monitoring, natural disaster factor detection, satellite data processing optimization, and GIS technology for meteorology information with the aim of agriculture developments.

Published in London, UK

IntechOpen

ISBN 978-1-83881-410-6